

The Pennsylvania State University
APPLIED RESEARCH LABORATORY
P.O. Box 30
State College, PA 16804

**ACOUSTIC EMISSIONS FROM UNSTEADY
TRANSITIONAL BOUNDARY LAYER
FLOW STRUCTURES**

By

R. C. Marboe
G. C. Lauchle

Technical Report No. TR 00-002
October 2000

Supported by:
Applied Research Laboratory

L. R. Hettche, Director
Applied Research Laboratory

Approved for public release; distribution unlimited

DTIC QUALITY INSURED 4

20001116 081

REPORT DOCUMENTATION PAGE

Form Approved
OAGB No. 0704-0108

Public reporting burden for this collection of information is estimated to average 1 hour per response, including the time for reviewing instructions, searching existing data sources, gathering and maintaining the data needed, and completing and reviewing the collection of information. Send comments regarding this burden estimate or any other aspect of this collection of information, including suggestions for reducing this burden, to Washington Headquarters Services, Directorate for Information Operations and Reports, 1215 Jefferson Davis Highway, Suite 1204, Arlington, VA 22202-4302, and to the Office of Management and Budget, Paperwork Reduction Project (0704-0108), Washington, DC 20503.

1. AGENCY USE ONLY (Leave blank)		2. REPORT DATE October 2000		3. REPORT TYPE AND DATES COVERED Ph.D. Dissertation / Acoustics	
4. TITLE AND SUBTITLE Acoustic Emissions from Unsteady Transitional Boundary Layer Flow Structures				5. FUNDING NUMBERS	
6. AUTHOR(S) R. C. Marboe, G. C. Lauchle					
7. PERFORMING ORGANIZATION NAME(S) AND ADDRESS(ES) Applied Research Laboratory The Pennsylvania State University P.O. Box 30 State College, PA 16804-0030				8. PERFORMING ORGANIZATION REPORT NUMBER TR00-002	
9. SPONSORING/MONITORING AGENCY NAME(S) AND ADDRESS(ES) Applied Research Laboratory The Pennsylvania State University P.O. Box 30 State College, PA 16804-0030				10. SPONSORING/MONITORING AGENCY REPORT NUMBER	
11. SUPPLEMENTARY NOTES					
12a. DISTRIBUTION/AVAILABILITY STATEMENT Distribution Unlimited, Approved for Public Release				12b. DISTRIBUTION CODE	
13. ABSTRACT (Maximum 200 words) <p>The research described critically examines the popular approaches to modeling the radiation mechanisms and attempts to bring some degree of closure to the physical and practical significance of noise and pseudo-noise originating in the laminar-to-turbulent transition zone within a natural boundary layer. Several refinements were made to theoretical models for directly radiated noise based upon the Liepmann analogy for fluctuating displacement thickness including the incorporation of a semi-empirically derived space-time correlation function for the intermittency indicator.</p> <p>A quiet airflow facility was developed to measure the direct acoustic radiation from a naturally transitioning boundary layer. Real-time acoustic intensity measurement instrumentation was developed if measurements of isolated spots in otherwise laminar flow had been necessary. This technique uses a hot film signal from the transition structure to obtain the coherent output intensity (COI). Model predictions are compared to the measured acoustic radiation from a naturally transitioning boundary layer.</p>					
14. SUBJECT TERMS acoustic radiation, turbulent spots, boundary layer transition, acoustic intensity measurement, displacement thickness fluctuations				15. NUMBER OF PAGES 302	
				16. PRICE CODE	
17. SECURITY CLASSIFICATION OF REPORT UNCLASSIFIED	18. SECURITY CLASSIFICATION OF THIS PAGE UNCLASSIFIED	19. SECURITY CLASSIFICATION OF ABSTRACT UNCLASSIFIED	20. LIMITATION OF ABSTRACT UNLIMITED		

ABSTRACT

The true acoustic radiation contribution of boundary layer flow structures has been the subject of debate for many years. The research described here critically examines the popular approaches to modeling the radiation mechanisms and attempts to bring some degree of closure to the physical and practical significance of noise and pseudo-noise originating in the laminar-to-turbulent transition zone within a natural boundary layer. This includes improving models to include recent computational and experimental statistics, an evaluation of model sensitivities to input parameters, and the applicability significance for situations of engineering relevance.

There have been significant efforts over the last twenty years to model the statistics of the wall pressure fluctuations resulting from flow structures within the laminar-to-turbulent boundary layer transition zone. Models for the directly radiated noise from these structures have, in turn, depended upon these statistics. Measurements of the space-time statistics for these pressures allow further development of prediction codes. Several refinements have been made to a theoretical model for the directly radiated noise based upon the Liepmann analogy for fluctuating displacement thickness including the incorporation of a semi-empirically derived space-time correlation function for the intermittency indicator and a dipole source description for the induced wall normal velocity. A similar model exists consisting of a Lighthill acoustic analogy using a two-fluids model. An additional model for radiation by vortex structures within the transition zone is qualitatively reviewed. The predominant effort in the last eight years has been to

apply direct numerical simulation methods to solving for acoustic radiation. These efforts are reviewed to help define their useful role in predicting sound radiation from transition. The role of pressure gradient in axisymmetric body flows, flat plate flows, and over air- and hydrofoils is investigated for incorporation into the model through a sensitivity analysis on affected flow parameters.

A quiet airflow facility was developed and refined to measure the direct acoustic radiation from a naturally transitioning boundary layer using time-averaged acoustic intensity. Real-time acoustic intensity measurement instrumentation was developed in case measurements of isolated turbulent spots in otherwise laminar flow had been necessary. This technique uses a hot film signal from the transition structure to obtain the coherent output intensity (COI).

Comparisons are made of model predictions to the measured acoustic radiation from a naturally transitioning boundary layer. Radiated noise measurements isolating the direct radiation from a transition zone demonstrated similar dependence with axial location within the transition zone as previous wall pressure measurements. This included radiated noise levels near mid transition zone that were higher than the noise level produced by a fully turbulent boundary layer by 2-3 dB. The levels measured suggest that the radiation from transition flow structures is multipolar and has a higher radiation efficiency than the quadrupole TBL sources. Transition noise per unit area is greater than TBL noise per unit area. Thus, the contribution to overall directly radiated flow noise from the transition zone in typical engineering applications is negligible compared to the radiation from the much larger area of fully turbulent flow.

TABLE OF CONTENTS

	<u>Page</u>
LIST OF FIGURES	x
LIST OF TABLES	xix
LIST OF SYMBOLS	xx
ACKNOWLEDGMENTS	xxii
CHAPTER 1 INTRODUCTION	1
1.1 Background	1
1.2 Boundary Layer Transitional Flows	2
1.2.1 Boundary Layer Flow Structures	3
1.2.2 Transitional Flows	3
1.3 Goals and Scope of the Present Investigation	6
CHAPTER 2 MODELS FOR BOUNDARY LAYER TRANSITION ZONE ACOUSTIC RADIATION	16
2.1 Fluctuating Shear Stress Using a Lighthill Analogy	17
2.2 Fluctuating Boundary Layer Displacement Thickness Using a Liepmann Analogy	20
2.2.1 Formulation Based on Lauchle Theoretical Space-Time Correlation Function	20
2.2.2 Formulation Based on Josserand-Lauchle Measured Space-Time Correlation Function	22
2.2.3 Chase Statistical Modification	23
2.3 Two Fluids Model Using a Lighthill Analogy	24
2.4 Vortex Motions	27
2.5 Direct Numerical Simulation	28

TABLE OF CONTENTS (continued)

	<u>Page</u>
2.6 Direct and Indirect Radiation from Complex Geometries	32
2.6.1 Vicinity of Half-Plane Leading Edge	32
2.6.2 Bodies of Revolution	35
2.6.3 Airfoils and Hydrofoils	37
2.7 Need for Refining the Fluctuating Boundary Layer Displacement Thickness Model in a Natural Transition Region	38
2.7.1 Example Applications of Fluctuating Displacement Thickness Model	41
2.7.2 Study Objectives: Acoustic Emissions from Isolated Transition Flow Structures and Natural Transition Zone. .	42
 CHAPTER 3 MODEL REFINEMENTS	 55
3.1 Fluctuating Boundary Layer Displacement Thickness Using a Liepmann Analogy - Theoretical Space-Time Correlation Function	56
3.1.1 Computational Model Refinements	57
3.1.2 Incorporation of Measured Normal Velocity Fluctuations .	61
3.2 Fluctuating Boundary Layer Displacement Thickness Using a Liepmann Analogy - Empirical Space-Time Correlation Function	63
3.2.1 Integration of Josserand-Lauchle Correlation Function . .	63
3.2.2 Chase Statistical Modification	65
3.3 Two Fluids Model with Refined Normal Velocity	66
3.4 Accounting for Vortical Motion	66
3.5 Incorporation of Green's Function for Transition Zone Near Half-Plane Leading Edge	68
 CHAPTER 4 RADIATED SOUND POWER PREDICTIONS	 80
4.1 Model Comparisons	80
4.1.1 Comparisons of Models for Air Flows	82
4.1.2 Comparisons of Models for Water Flows	83

TABLE OF CONTENTS (continued)

	<u>Page</u>
4.2 Role of Rise Time, t_i	83
4.3 Effects of Pressure Gradient	84
4.4 Effects of Scattering by a Plane Leading Edge	86
4.5 General Assessment of Models	86
CHAPTER 5 EXPERIMENTAL APPARATUS	103
5.1 Quiet Airflow Facility	104
5.1.1 Flow-Through Anechoic Chamber	104
5.1.2 Air Source	105
5.1.3 Flow Management	107
5.1.4 Test Section	108
5.1.5 Half-Plane	109
5.1.6 Diffuser	110
5.2 Instrumentation and Signal Processing	111
5.2.1 Hot Wire Anemometry	111
5.2.2 Sound Pressure	115
5.2.3 Acoustic Intensity	116
5.2.4 Coherent Output Intensity	119
5.2.5 Other Processing Hardware and Software	120
CHAPTER 6 MEASUREMENT RESULTS	142
6.1 Test Section Flow	142
6.2 Intensity Measurement Calibration	143
6.3 Flat Plate Natural Transition Zone	145
CHAPTER 7 CONCLUSIONS AND FUTURE WORK	179
7.1 Conclusions	179
7.2 General Observations on Transition Noise	180
7.3 Recommended Future Work	183

TABLE OF CONTENTS (continued)

		<u>Page</u>
	BIBLIOGRAPHY	185
APPENDIX A	MATHCAD MODEL FILES	201
A.1	Fluctuating Shear Stress Using a Lighthill Analogy	202
A.2	Fluctuating Boundary Layer Displacement Thickness Using a Liepmann Analogy - Theoretical Space-Time Correlation Function	212
A.3	Fluctuating Boundary Layer Displacement Thickness Using a Liepmann Analogy - Theoretical Space-Time Correlation Function with Krane Dipole Source Model.	222
A.4	Fluctuating Boundary Layer Displacement Thickness Using a Liepmann Analogy - Empirical Space-Time Correlation Function	234
A.5	Noise Generated by Boundary Layer Transition on Symmetric Hydrofoils - Howe Formulation	240
A.6	Calculation of Boundary Layer Descriptors - Air.	253
A.7	Calculation of Boundary Layer Descriptors - Water	258
A.8	Calculation of Nozzle Contours	263
A.9	Calculation of Measurement Errors from a Two Microphone Intensity Probe	268
APPENDIX B	QUIET AIRFLOW FACILITY DEVELOPMENT	271
B.1	Power Source Improvements	271
B.2	Blower Noise Improvements	272
B.3	Noise Reduction at the Test Plate	273
B.4	Relocation of Test Section and New Nozzle Design	275

TABLE OF CONTENTS (continued)

	<u>Page</u>
B.5 Diffuser Design	276
APPENDIX C REAL-TIME ACOUSTIC INTENSITY SIGNAL PROCESSING	288
C.1 Time-Averaged Intensity Processing	289
C.2 Real-Time Intensity Processing	289
C.3 Conditioning with a Shear Stress Sensor	291

LIST OF FIGURES

<u>Figure</u>	<u>Page</u>
1.1 General features of the wavevector-frequency spectrum of the wall pressure fluctuations under a turbulent boundary layer where $k_z=0$ and k_x is the independent variable for constant frequency	10
1.2 Photograph of flow on a heated body showing transition flow structures [from Lauchle 1991]	11
1.3 Schematic views of a turbulent spot and its growth with downstream distance [from several sources]	12
1.4 System of coordinates	13
1.5 Representative sketch of $I(x_i, t)$, where $\gamma(x_i)$ is the intermittency function and N is the average burst frequency function [from Lauchle 1981]	14
1.6 The modified indicator function $I(t)$ is shown in (a) and its first time derivative in (b) [from Lauchle 1981]	15
2.1 Vortex view of a turbulent spot [from Audet et al. 1989a]	45
2.2 The normalized rms wall pressure fluctuations in the transitional boundary layer measured and predicted for a flat plate. The curves are predictions which account for spatial and frequency filtering of the sensors. Curve 1 is γp_r , Curve 2 is the radiated acoustic source term, and Curve 3 is their sum. The symbols are measured data for 3 velocities. [from Audet et al. 1989a,b]	46
2.3 Comparison of instantaneous isolines of spanwise vorticity (solid lines) and normal velocity component (dashed lines) at $z=0$: (a) $t=10T$; (b) $t=10.4T$. Local maxima and minima of normal velocity are indicated.[from Rist and Fasel, 1995]	47
2.4 Measured flow noise levels on modified ellipsoidal nose. Δ , $U_\infty=10.0$ m/s; \circ , $U_\infty=10.9$ m/s; \square , $U_\infty=12.2$ m/s [from Arakeri et al. 1991]	48

LIST OF FIGURES (continued)

<u>Figure</u>	<u>Page</u>
2.5 Verification of the proposed scaling law with the Haddle and Skudrzyk (1969) results. —, IISc model results with $U_{\infty}=12.2$ m/s and diameter $D=0.075$ m; o, model results extrapolated to Haddle and Skudrzyk conditions of $U_{\infty}=18.5$ m/s and $D=0.42$ m without corrections; - - -, extrapolated results corrected for diffraction loss scaled on two different power laws; Δ , the Haddle and Skudrzyk experimental results [the 5 th power law is from Arakeri et al. 1991; the 7.5 power law is from Lauchle 1992]	49
2.6 Comparison of radiated 1/3 octave levels predicted by Equation (2.13) for the Haddle and Skudrzyk (1969) test conditions using a flat plate (0.15 m) and a hemispherical noise prediction (0.061 m) for transition zone length Δx	50
2.7 Two cross-sections through a spot: a comparison of criteria, $U_{\infty}=9.4$ m/s, (a) elevation, (b) plan. -x-, Coles and Barker (1974); ---, Wygnanski et al. (1976). Shape based on 2% elevation in U: ●●●●, LE ensemble average; ----, TE ensemble averaged [from Wygnanski et al. 1976]	51
2.8 Spanwise variation for normal velocity for $x/U_{\infty}\nu=1.93\times 10^5$: (a) $y/h_o=0.325$, $0.0\leq z/\text{span}\leq 0.941$; (b) $y/h_o=0.54$, $z/\text{span}=0.0$ [from Wygnanski et al. 1976]	52
2.9 Pressure spectral densities measured under the laminar boundary layer on an axisymmetric body in the CEPRA 19 wind tunnel and comparison with computational model results [from Perraud 1989]	53
2.10 Measured and predicted radiated noise spectra for the Haddle and Skudrzyk (1969) buoyant bodies operating at 15.44 m/s [from Lauchle and Brungart, 1988]	54
3.1 Theoretical model refinements for directly radiated noise from a transitioning boundary layer	70
3.2 Turbulent spot with substructure vortices [from Sankaran et al.1988] ...	71
3.3 Instantaneous velocity vectors and sectional streamlines [from Sankaran et al. 1991]	72
3.4 Comparison of empirically derived intermittency functions	73

LIST OF FIGURES (continued)

<u>Figure</u>	<u>Page</u>
3.5 Comparison of empirically derived normalized burst rate functions	74
3.6 Effect of substitution of refined empirically derived equations for the intermittency function, $\gamma(\eta_x)$, and turbulent spot burst frequency, $N(\eta_x)$, for CEPRA 19 axisymmetric body in air, $U_\infty=50$ m/s, $u_{ct}/\Delta x=0.15$, $\Delta\delta^*=0.25$ mm and $\Delta x=0.2$ m (data from Perraud 1989)	75
3.7 Mass flux deficit and derived normal velocity fluctuations at $x=1.13$ m, $z=0$, and $U_\infty=40.6$ cm/s in water with spot edge denoted by 2% velocity disturbance contour [from Krane 1992]	76
3.8 Proposed multipole source distribution for the measured normal velocity distribution above a passing turbulent spot, $v_n(\eta_x)$ [from Krane 1992]	77
3.9 Comparison of Krane (1992) measured nondimensional rise time, $u_{ct}/\Delta x$, and function $TK(Z_x)$ fit to the data	78
3.10 Comparison of correlation surface, $R_f(\eta_x, \xi_x, 0, \tau)$, for empirical space-time correlation function for original Josserand form and with Chase first exponential term statistical modification for $U_\infty=11.8$ m/s, $\Delta x=1.83$ m, with $\eta_x/\Delta x=0.50$	79
4.1 GLPROG80 predicted radiated pressure levels for a zero pressure gradient flat plate in air for $9 \text{ m/s} < U_\infty < 27 \text{ m/s}$	90
4.2 GLPROG81 predicted radiated pressure levels for a zero pressure gradient flat plate in air for $9 \text{ m/s} < U_\infty < 27 \text{ m/s}$	91
4.3 KMTRANS00 predicted radiated pressure levels for a zero pressure gradient flat plate in air for $9 \text{ m/s} < U_\infty < 27 \text{ m/s}$	92
4.4 JLTRANS99 predicted radiated pressure levels for a zero pressure gradient flat plate in air for $U_\infty = 24 \text{ m/s}$	93
4.5 MSHTRANS99 predicted radiated pressure levels for a zero pressure gradient flat plate half-plane in air for $U_\infty = 24 \text{ m/s}$	94

LIST OF FIGURES (continued)

<u>Figure</u>	<u>Page</u>
4.6 Comparison of models for radiated pressure levels for a zero pressure gradient flat plate in airflow, $U_{\infty}=24$ m/s, $\Delta\delta^*=0.243$ cm, $\Delta x=0.32$ m, $u_c/U_{\infty}=0.7$, $r=1.0$ m	95
4.7 GLPROG80 predicted radiated pressure levels for a zero pressure gradient flat plate in water for 3 m/s $< U_{\infty} < 21$ m/s	96
4.8 GLPROG81 predicted radiated pressure levels for a zero pressure gradient flat plate in water for 3 m/s $< U_{\infty} < 21$ m/s	97
4.9 KMTRANS00 predicted radiated pressure levels for a zero pressure gradient flat plate in water for 3 m/s $< U_{\infty} < 21$ m/s	98
4.10 JLTRANS99 predicted radiated pressure levels for a zero pressure gradient flat plate in water for $U_{\infty} = 21$ m/s	99
4.11 MSHTRANS99 predicted radiated pressure levels for a zero pressure gradient flat plate half-plane in water for $U_{\infty} = 21$ m/s	100
4.12 Comparison of models for radiated pressure levels for a zero pressure gradient flat plate in water, $U_{\infty}=21$ m/s, $\Delta\delta^*=0.021$ cm, $\Delta x=0.028$ m, $u_c/U_{\infty}=0.7$, $r=1.0$ m	101
4.13 Comparison of models for radiated pressure levels for a zero pressure gradient flat plate in airflow, $U_{\infty}=21$ m/s, $\Delta\delta^*=0.278$ cm, $\Delta x=0.9$ m, $u_c/U_{\infty}=0.7$, $r=1.0$ m	102
5.1 Quiet Airflow Facility configuration for present experiment	122
5.2 Flow-through anechoic chamber	123
5.3 Anechoic chamber background noise relative to balanced noise criterion (NCB) curves	124
5.4 Blower and sound/vibration isolation box	125
5.5 Flow source enclosure, plenum, and silencer	126
5.6 Flow source noise attenuation plenum	127

LIST OF FIGURES (continued)

<u>Figure</u>	<u>Page</u>
5.7 Buffalo Forge blower and motor	128
5.8 Elbow and conduit pipe for flow into anechoic chamber	129
5.9 In-flow silencer and diffuser into acoustic settling chamber	130
5.10 Flow management plenum, diffuser, screens and settling sections prior to nozzle	131
5.11 New nozzle contracting to 15.2 cm x 30.5 cm	132
5.12 View of test section	133
5.13 Test section view showing drilled holes for hot film probe or spot generation excitation	134
5.14 View of nozzle, plenum, and diffuser	135
5.15 Stethoscope burst probe	136
5.16 Half-plane plate designed for test section	137
5.17 Looking upstream through diffuser to the test section and the added diffuser resistance	138
5.18 Intensity probe calibration tubes, (a) high frequency and (b) low frequency	139
5.19 Processing diagram for coherent output intensity	140
5.20 Anemometer and microphone amplifier	141
5.21 Test instrumentation	141
6.1 Boundary layer profile for $U = 23.1$ m/s, $x = 7.6$ cm, $y = 2.54$ cm from centerline	149
6.2 Spanwise uniformity of the test section streamwise velocity for $U = 23.1$ m/s, $x = 7.6$ cm, at 25, 50, and 75% of test section height	150

LIST OF FIGURES (continued)

<u>Figure</u>	<u>Page</u>
6.3 Spanwise uniformity of the test section streamwise velocity for $U=23.1$ m/s, $x = 77.5$ cm, at 25, 50, and 75% of test section height . . .	151
6.4 Comparison of boundary layer profiles and turbulence intensity profiles tripped, fully turbulent flow for nominal $U=23.9$ m/s near end of test section	152
6.5 Calibration configuration	153
6.6 Magnitude and phase of microphone mismatch as measured in small calibration tube	154
6.7 Intensity estimate bias errors due to point monopole and dipole source fields for microphone separation of 2.54 cm	155
6.8 Comparison of (a) P-P time-averaged intensity measurement to far field intensity at 0.8m above speaker, and (b) P-P time-averaged intensity measurement with and without mylar to open far field intensity at 0.5m above speaker in 1.6 Hz bands.	156
6.9 Comparison of P-P time-averaged intensity measurement with and without mylar to open far field intensity at 0.5m above speaker in (a) 50 Hz bands and (b) 1/3 octave bands	157
6.10 Intensity probe gain over a single microphone	158
6.11 Configuration of P-P intensity probe for transition zone measurements	159
6.12 Locations and levels of hot film measurements for intermittency compared to Josserand intermittency function and locations of intensity measurements	160
6.13 Examples of spectrum smoothing achieved through wider band processing	161
6.14 Active intensity in 1.6 and 50 Hz processing bands measured for natural transition region of 21 m/s in zero pressure gradient above mylar wall for $-0.03 < Z_x < 0.60$	162

LIST OF FIGURES (continued)

<u>Figure</u>	<u>Page</u>
6.15 Active intensity in 1.6 and 50 Hz processing bands measured for natural transition region of 21 m/s in zero pressure gradient above mylar wall for $Z_x = -0.03, 0.45$ and 0.53 259.	163
6.16 Boundary layer trip of 50 grit sandpaper in 6 cm long strip at $x = 20$ cm and boundary layer stimulation of 150 grit sandpaper in two 10mm long strips at $x = 12$ and 15 cm	164
6.17 Active intensity in 1.6 and 50 Hz processing bands measured for tripped turbulent flow at 21 m/s in zero pressure gradient above mylar wall for $-0.03 < Z_x < 0.60$	165
6.18 Active intensity in 1.6 and 50 Hz processing bands measured for tripped turbulent flow at 21 m/s in zero pressure gradient above mylar wall for $Z_x = -0.03, 0.45$ and 0.53	166
6.19 Active intensity in 1.6 and 50 Hz processing bands measured for stimulated transition region at 21 m/s in zero pressure gradient above mylar wall for $-0.03 < Z_x < 0.60$	167
6.20 Active intensity in 1.6 and 50 Hz processing bands measured for stimulated transition region at 21 m/s in zero pressure gradient above mylar wall for $Z_x = -0.03, 0.45$ and 0.53	168
6.21 Comparison of active intensity in 1.6 and 50 Hz processing bands measured for natural and stimulated transition and tripped turbulent flow at 21 m/s in zero pressure gradient above mylar wall for $Z_x = -0.03$	169
6.22 Comparison of active intensity in 1.6 and 50 Hz processing bands measured for natural and stimulated transition and tripped turbulent flow at 21 m/s in zero pressure gradient above mylar wall for $Z_x = 0.09$	170
6.23 Comparison of active intensity in 1.6 and 50 Hz processing bands measured for natural and stimulated transition and tripped turbulent flow at 21 m/s in zero pressure gradient above mylar wall for $Z_x = 0.20$	171
6.24 Comparison of active intensity in 1.6 and 50 Hz processing bands measured for natural and stimulated transition and tripped turbulent flow at 21 m/s in zero pressure gradient above mylar wall for $Z_x = 0.31$	172

LIST OF FIGURES (continued)

<u>Figure</u>	<u>Page</u>
6.25 Comparison of active intensity in 1.6 and 50 Hz processing bands measured for natural and stimulated transition and tripped turbulent flow at 21 m/s in zero pressure gradient above mylar wall for $Z_x = 0.45$	173
6.26 Comparison of active intensity in 1.6 and 50 Hz processing bands measured for natural and stimulated transition and tripped turbulent flow at 21 m/s in zero pressure gradient above mylar wall for $Z_x = 0.53$	174
6.27 Comparison of active intensity in 1.6 and 50 Hz processing bands measured for natural and stimulated transition and tripped turbulent flow at 21 m/s in zero pressure gradient above mylar wall for $Z_x = 0.60$	175
6.28 Fluctuating wall pressure measurements made in air by Dufourq (1984).	176
6.29 Comparison of transition noise model predictions with measured directly radiated sound pressure levels	177
6.30 Comparison of intermittency weighted measured turbulent boundary layer noise with measured transition zone directly radiated sound pressure levels	178
B.1 Original orientation of Quiet Airflow Facility to the flow-through anechoic chamber	278
B.2 Comparison of narrowband signature of Borg-Warner inverter and replacement ABB inverter for (a) upstream plenum and (b) airborne levels in control room	279
B.3 Original semi-circular wall jet over flat plate configuration	280
B.4 Addition of suction manifold below test plate	281
B.5 Views of suction manifold ports and rods with cones	282
B.6 Measured sound pressure level for assembly in control room running at $U_\infty = 11.8$ m/s compared to GLPROG81 predictions for $u_{ct}/\Delta x = 0.15$ and $u_{ct}/\Delta x = 0.05$	283
B.7 GLPROG81 sound pressure level predictions for $U_\infty = 11.8$ m/s and several $u_{ct}/\Delta x$ values otherwise matching Figure B.6	284

LIST OF FIGURES (continued)

<u>Figure</u>	<u>Page</u>
B.8 Relocation of facility and addition of moving wall test plate [from Brungart 1997]	285
B.9 Diffuser design iterations versus stall design criterion [stall curve from Kline 1959]	286
B.10 Possible flow conditions in diffuser	287
C.1 General processing diagram	294
C.2 Traditional method of FFT processing of a P-P intensity probe	295
C.3 Processing diagram for analog and digital calculation of intensity from a P-P probe	296
C.4 Processing diagram for integrator	297
C.5 Circuit diagram for real-time processing of a P-P intensity probe	298
C.6 Component layout for real-time active intensity circuit	299
C.7 Residual intensity measured for same signal input to channels 1 and 2 compared to input signal	300
C.8 Comparison of real-time intensity circuit output to time-averaged intensity method for a fully turbulent flow condition	301
C.9 Processing diagram for conditioning a real-time processing of a P-P intensity probe with a hot film probe	302

LIST OF TABLES

<u>Table</u>	<u>Page</u>
4.1 Common Constants for Model Exercising	81
4.2 Calculated Model Inputs	82
5.1 Sound Absorption Coefficients of Foam and Wedges Used in QAF	107
5.2 Equipment List for Time-Averaged Acoustic Intensity Measurement	118
5.3 Calibration Tube Characteristics	118
5.4 Equipment List for Coherent Output Intensity	121

LIST OF SYMBOLS

$B(Z)$	normalized turbulent spot formation (burst rate), $N(Z)\Delta x / u_o$
c_o	speed of sound in the medium, m/s
$I(x,t)$	indicator function, a zero-one function
M	Mach number, U_∞ / c_o
N	spot formation rate (also known as burst frequency), 1/s
r	measurement distance from acoustic source,
R_I	correlation function for the intermittency indicator
$Re_{\Delta x}$	Reynolds number based on transition zone length
Re_{x_o}	Reynolds number based on streamwise location where spots first appear
S_o, S	Source terms in the two fluids model
t_i	time constant for growth of the laminar boundary layer displacement thickness into the turbulent displacement thickness, s
u_c	turbulent spot convection velocity through transition zone (typically equal to $0.7U_\infty$), m/s
U_∞, u_o	freestream velocity, m/s
W	spanwise width of transition zone, m
x_o	location of leading edge of transition zone, m
Z_x	normalized longitudinal coordinate in the transition zone, $\eta_x / \Delta x$
Z_z	normalized transverse coordinate in the transition zone, $\eta_z / \Delta x$
α^*	flare parameter
Δx	streamwise length of the transition zone, m

LIST OF SYMBOLS (continued)

$\Delta\delta^*$	change in boundary layer displacement thickness between laminar and turbulent states, m
$\gamma(x)$	intermittency factor, increases monotonically from zero at the first spot formation to one at fully turbulent flow
$\delta^*(t)$	time dependent boundary layer displacement thickness, m
$\eta_{x(z)}$	streamwise (transverse) coordinate within transition zone, m
ρ, ρ'	fluid density (steady, fluctuating), kg/m ³
ϕ	acoustic field due to flow intermittency in two-fluids model, m ² /s
$\xi_{x(z)}$	streamwise (transverse) separation distance between correlation points in transition zone, m
θ	angle from the dipole source axis to the receiver
$\sigma(x)$	$\tau_T(x) - \tau_L(x)$, dynes/cm ²
$\tau_{T(L)}$	wall shear stress under a turbulent (laminar) boundary layer, dynes/cm ²

ACKNOWLEDGMENTS

I gratefully acknowledge the mentoring, support, and patience of my advisor, Prof. G. C. Lauchle as well as the contributions of my other committee members, Prof. G. H. Koopmann, Prof. D. K. McLaughlin and Prof. F. S. Archibald. I am also appreciative of the opportunity to work with Prof. M. S. Howe during his sabbatical period at Penn State.

I am also indebted to faculty and staff colleagues at the Applied Research Laboratory for their support throughout this research effort. In particular, Bob Grove provided superb construction support over the development lifetime of the Quiet Airflow Facility. Eric Riggs provided hot wire anemometry support. I am also thankful for the long standing collaboration in aeroacoustic problems with Dr. Tim Brungart.

My family has both sustained and distracted me throughout this long process, but I wouldn't have it any other way. So this work is dedicated to my wife, Rose, children, Teresa and Paul, and my parents, Robert and Evelyn Marboe.

Portions of this work were supported by a grant from the Office of Naval Research, Code 1125 OA and the Fundamental Research Initiatives Program at the Applied Research Laboratory managed by Dr. R. Stern.

CHAPTER 1

INTRODUCTION

1.1 Background

Much debate exists over the true acoustic radiation contribution of boundary layer flow structures. Is the near- and far-field noise significant? Current knowledge is based on analytical theories and a very limited database of measured data where it is believed that transition noise exists. Unfortunately, much of the data from these measurements are questionable due to possibility of contamination by other noise sources. It seems that sonar self-noise is affected by transition and that a radiation noise field exists, but a refined theoretical or computational model and subsequent experimental verification is required.

The research described in this dissertation critically examines the popular approaches to modeling the radiation mechanisms and brings a degree of closure to the physical and practical significance of noise and pseudo-noise originating in the laminar-to-turbulent transition zone within a natural boundary layer. This effort includes updating of models to include computational and experimental statistics plus an evaluation of model sensitivities, applicability, and significance for situations of engineering relevance.

There have been significant efforts over the last twenty years to model the wall pressures resulting from flow structures within the laminar-to-turbulent boundary layer transition zone. Knowledge of the wavevector-frequency spectrum of the wall pressures

can be used to predict indirect radiation from excitation of the structure over which transition occurs.

Josserand and Lauchle (1990) showed that the transition zone wall pressure fluctuation wavevector-frequency spectrum, near the convective wavenumber domain, is equal to the wavevector-frequency spectrum for wall pressure fluctuations under a fully turbulent boundary layer (Figure 1.1) multiplied by an intermittency factor, γ . This factor varies monotonically from zero at the beginning of transition to unity for the fully turbulent boundary layer. The transition zone wavevector-frequency spectrum is:

$$\Phi_{trans}(\lambda_x, k_x, k_z, \omega) = \gamma(\lambda_x) \Phi_{TBL}(k_x, k_z, \omega). \quad (1.1)$$

Here, $\lambda_x = (x - x_o)/\Delta x$ and the function Φ_{TBL} used by Josserand and Lauchle (1990) was developed by Chase (1980). However, this equation is not valid over the low wavenumber or sonic region. It is thus the intent of this dissertation to refine equation (1.1) with emphasis on the prediction of the direct radiation from transition flow structures at sonic and supersonic wavenumbers.

1.2 Boundary Layer Transitional Flows

Since the scope of this dissertation is limited to the modeling of direct radiation from the transition zone, it is best to refrain from detailing all of the fundamental work that has been done to determine the fluid mechanics of transition mechanisms and the measurements of turbulent flow structures which form the basis for the described models. The reader is directed to the review articles of Tani (1969), Gad-el-Hak (1989), and

Lauchle (1991). Some of the more important prior developments relevant to the present research will be discussed briefly in the next two sections.

1.2.1 Boundary Layer Flow Structures

Much of the modeling of flow structures in the transitional boundary layer has been based on the modeling of flow structures found in the fully developed turbulent boundary layer (TBL). The characterization of these structures has come predominately through experimental measurements, particularly from those utilizing laser doppler velocimetry. The models are highly empirical.

The description of flow structures and characteristics within the TBL are found in Bershadskii and Tsinobar (1994), Honkan and Andreopoulos (1999), Klebanoff et al. (1992), Koh (1993), Krogstad and Antonia (1994), Schlichting (1979), and White (1974). Wall pressure models for the TBL are given by Corcos (1963), Chase (1991), Capone and Lauchle (1995), Graham (1997), Keith and Abraham (1997), and Singer (1997). Radiated noise models are found in Powell (1960), Chase (1987), Barker (1974), Bergeron (1973), Howe (1998), Lauffer et al. (1964), Pierce (1981), and Tam (1975).

1.2.2 Transitional Flows

As laminar flow over a flat or curved surface approaches a critical Reynolds number, hydrodynamic instabilities occur. Examples are Tollmien-Schlichting, Rayleigh, and Kelvin-Helmholtz for different flow regimes. [See Huerre and Monkewitz (1990), Panton, (1984), Schlichting (1979), or White (1974) for more details.] For the flat plate,

two-dimensional Tollmien-Schlichting waves form in the boundary layer. These instabilities become non-linear and three-dimensional. Bursting occurs, followed by the formation of Emmons spots (Emmons, 1951). These spots are turbulent regions within an otherwise laminar flow (Figures 1.2 and 1.3) which grow and coalesce to become fully turbulent flow. The transition region, of length Δx beginning at x_o , is usually defined as the zone in which distinct Emmons spots exist.

Therefore, within this transition region, the flow can be thought of as a classical mixture of turbulent and laminar flow zones with concentrations determined by the intermittency function $\gamma(\eta_x)$ and $1-\gamma(\eta_x)$, respectively. Here, $\gamma(\eta_x)$ is the time average value of $I(x,t)$, the intermittency indicator function which has the value of zero for a laminar state and unity for a turbulent state. The system of coordinates and relevant flow characteristics are shown in Figure 1.4. This function is typically used for $y=0$. For infinite span, we expect $I(\eta_x, \eta_z, t)$ to be statistically homogeneous in the η_z direction but non-homogeneous in the η_x direction. So, the time average value will be independent of η_z and vary from 0.0 at $\eta_x=0$ to 1.0 at $\eta_x=\Delta x$. The burst frequency, $N(\eta_x)$, describes the mean number of Emmons spots which pass a point per unit time. The general behavior of these functions through the transition zone can be seen in Figure 1.5. While the ideal indicator function is constructed with step functions, a physically realizable indicator includes rise times as shown in Figure 1.6. This rise time accounts for the time for the flow to change from a laminar flow value to a turbulent flow one and conversely (Lauchle, 1989). As shown in Figure 1.6, the rate of change of the indicator function is described by $e^{-\eta_x/\tau}$. If this change in flow state, with inherent increase in displacement

thickness from laminar to turbulent, were considered as a piston movement, then a shorter time, t_i , would result in higher source surface velocity and a higher radiated noise. This time should be a function of the flow velocity and other characteristics of transition zone which are fluid dependent.

The transition zone length can be predicted from empirical formulae of the form

$$Re_{\Delta x} = C Re_{x_0}^n \quad (1.2)$$

where the Reynolds numbers are based on the subscripted length and freestream velocity, U_∞ . Chen and Thyson (1971) found $C=60$ and $n=2/3$ for blunt nosed bodies which accounted for positive pressure gradients and Mach number. However, values have been derived from the flat plate experimental data of Dhawan and Narasimha (1958): $C=15$ and $n=0.8$, and from Josserand and Lauchle (1990): $C=17$ and $n=0.8$. Narasimha et al. (1984) argued that, because the spots do not propagate at consistent speeds proportional to freestream velocity, every pressure gradient results in a unique intermittency distribution, and Equation (1.2) must be adjusted accordingly.

Once again, there have been many investigations covering transition mechanisms and flow structures described in the literature. The following are some representative references that were found to be helpful. Modeling of transition mechanisms is described by Barenblatt (1990), Gogineni and Shih (1997), and Stewart and Smith (1992).

Definitions of the characteristics of turbulent spots themselves can be found in Barrow et al. (1984), Gad-el-Hak and Fazle Hussain (1986), Henningson and Alfredsson (1987), Jahanmari et al. (1996), and Van Atta et al. (1982). A description of vortices in

spots is available in Haidari and Smith (1994). Details on spot intermittency through the transition zone is provided by DeMetz and Casarella (1973), Farabee et al. (1974), Krane (1992), Krane and Pauley (1992), Narasimha (1957), Schneider (1995), and Zhang et al. (1995). The wall pressures resulting from turbulent spot formation, growth, and convection are well documented in Bowles and Smith (1995), Ching and LaGraff (1995), Gedney (1979), Gedney and Leehey (1989), Josserand and Lauchle (1989), and Mautner (1982). Studies on the interaction of turbulent spots are given by Cherny and Pauley (1994), and Coles and Savas (1979). The growth and convection of turbulent spots varies with the pressure gradient over the transition zone. Several investigations have addressed the variations with both favorable and adverse pressure gradients. These include Bandyopadhyay and Ahmed (1993), Blair (1992 a,b), Clark et al. (1996), Dey and Narasimha (1991), Jeon and Kang (1995), Katz et al. (1990a,b), Ramesh et al. (1996), Seifert and Wygnanski (1995), and Walker and Gostelow (1990).

1.3 Goals and Scope of the Present Investigation

This investigation was begun under a three year Office of Naval Research Fundamental Research Initiatives Program: Hydroacoustics of Boundary Layer Transition. The overall objective was to identify the physical mechanisms that cause sound radiation from intermittent (particularly transitional) boundary layer flows over rigid surfaces. Specifically this requires:

1. evaluation of existing theoretical and semi-empirical models and new developments or modifications based on new or refined space-time statistics;

2. experimental determination of the statistics of the unsteady fluid mechanics of these flow structures, in particular:

- develop scalar descriptors of turbulent spot growth,
- measure space-time development of transition zone fluctuating displacement thickness (for individual and multiple interacting spots),
- relate spot growth descriptors to sound production including the characteristic time constants associated with the acoustic radiation model;

3. obtain unambiguous measurements of the acoustic emissions from isolated boundary layer flow structures including natural transition and/or individual turbulent spots; and

4. use the existing experimental database to validate the theoretical and semi-empirical models.

The second goal was the basis for an associated investigation which is reported in the Ph.D. dissertation by Krane (1992) and complements the measurements by Josserand (1986). The first, third, and fourth items were the basis for the present investigation. If this research were viewed from a verification and validation process (Coleman and Steele, 1999) perspective, the models have undergone verification to assure correct implementations of equations and address computational limitations but the validation is really more of an early evaluation of the applicability of the many models. We are still in the discovery phase of the physical mechanisms which are contributing to the transition zone radiated noise which has been experimentally determined for the first time.

The structure of this dissertation is as follows. Important boundary layer parameters and definitions are covered in Chapter 1. Five approaches to modeling the radiated noise from a transition zone are covered in Chapter 2.. These include: a fluctuating shear stress model [Lauchle 1980], a fluctuating displacement thickness model using the Liepmann analogy [Lauchle 1981,1989], a two-fluids model using the Lighthill analogy [Sornette and Lagier 1984a,b, Lagier and Sornette 1986, and Audet, et al. 1989a,b], direct numerical simulation [Wang, Lele, and Moin, 1996a], and a vortex motions model [Kambe 1986 and Hardin 1991]. Recent activity has focused on the use of direct numerical simulation (DNS) using full Navier-Stokes equations solvers to predict statistical quantities relevant to a Lighthill approach. The problem statement then evolves from examining some predictive comparisons for three test cases for which experimental data are believed to be influenced by transition. These include a flat plate in air, an axisymmetric body in air, and an axisymmetric body in seawater. It is apparent that pressure gradient plays an important role in the pressure fluctuations and its effect will also be discussed.

The computational model refinements are detailed in Chapter 3. Based on the results of Josserand and Lauchle (1990), it is possible to make refinements to Lauchle's (1981) model by incorporating the empirically derived space-time correlation function. In addition, several other refinements can be made using measurements by Krane and Pauley (1993), correlation simplifications, plus accounting for retarded time differences and vortical motions. Predictions for several relevant flow conditions are presented in Chapter 4.

It is important for any model to have experimental validation. The direct radiation from transition flow structures (distinct from measured wall pressures) has not previously been measured in isolation. Chapter 5 contains a description of the quiet airflow facility modified for these measurements and the flow-through anechoic chamber of the Applied Research Laboratory at The Pennsylvania State University. Acoustic intensity instrumentation and signal processing was employed to overcome facility noise. Time-averaged acoustic intensity measurement techniques were used successfully for the measurements of directly radiated noise from a natural transition zone. This measurement includes the interactions of multiple spots. These measurements are described in Chapter 6. In anticipation of a possible need for additional noise rejection, real-time acoustic intensity measurement instrumentation was developed. A process was developed to use a hot film signal from the transition flow structure to obtain coherent output intensity (COI). This technique would have been necessary for measurements of the radiated noise from individual spots generated and convecting in otherwise laminar flow. Conclusions and recommendations for further investigation are provided in Chapter 7.

Mathcad ® software from Mathsoft, Inc was used for the computational modeling. Printouts of the worksheets are provided in Appendix A. A chronology of the development of the Quiet Airflow Facility is detailed in Appendix B. Finally, details of the electronics developed for the real-time acoustic intensity measurement are given in Appendix C.

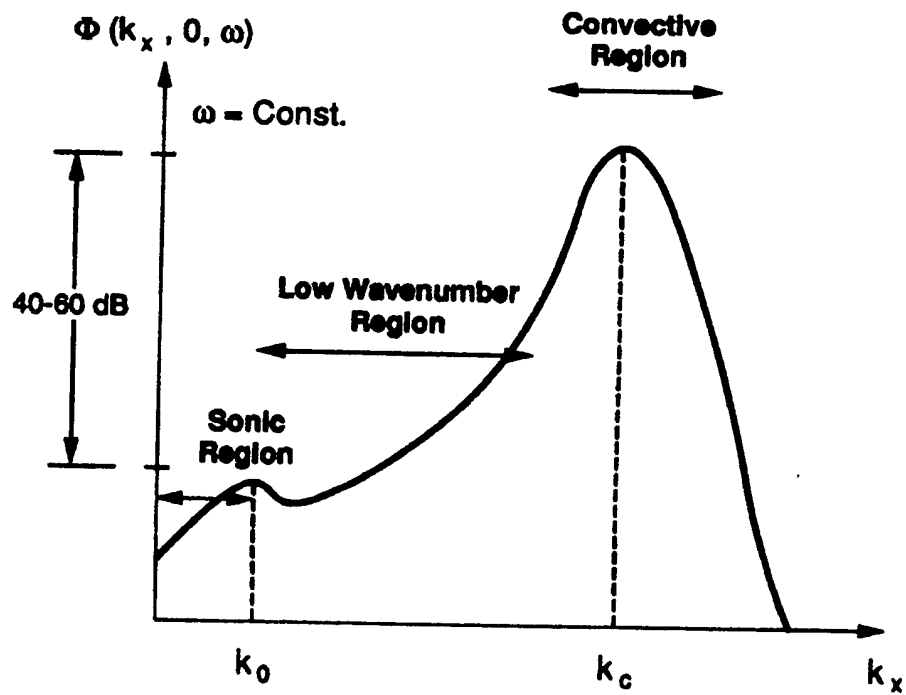


Figure 1.1 General features of the wavevector-frequency spectrum of the wall pressure fluctuations under a turbulent boundary layer where $k_z=0$ and k_x is the independent variable for constant frequency.

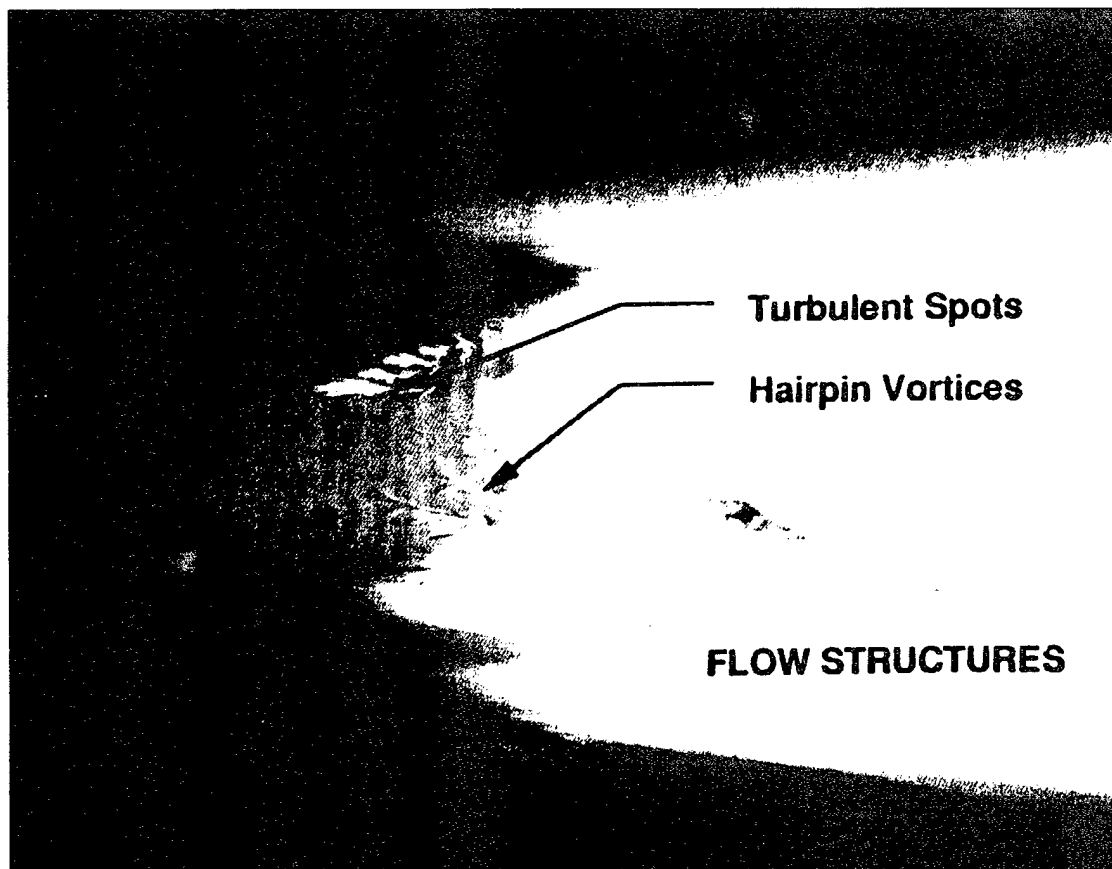


Figure 1.2 Photograph of flow on a heated body showing transition flow structures
[from Lauchle 1991].

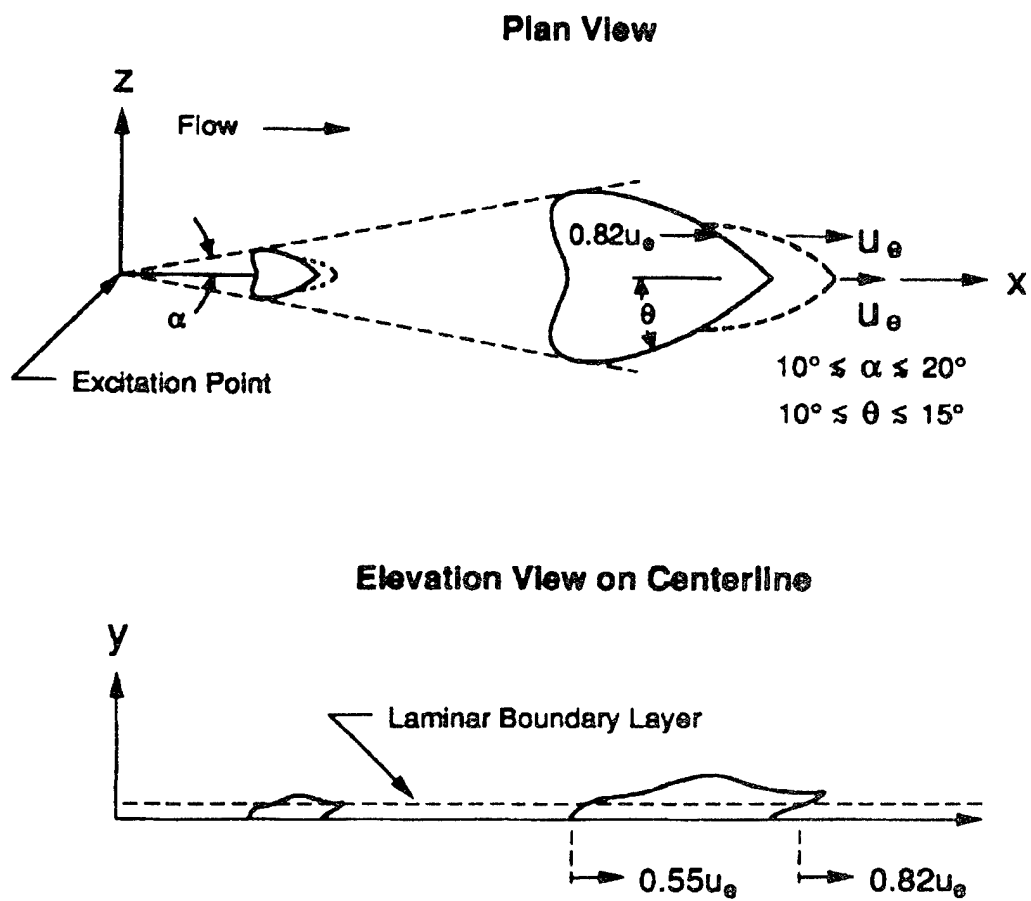
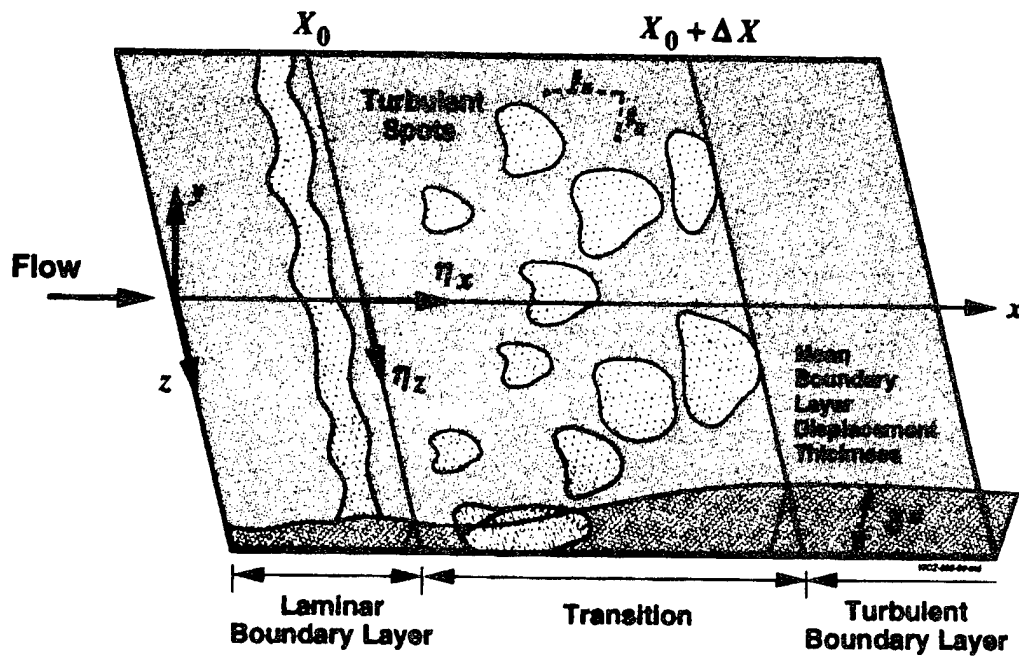


Figure 1.3 Schematic views of a turbulent spot and its growth with downstream distance [from several sources].



$$Z_x = \eta_x / \Delta x$$

Figure 1.4 System of coordinates.

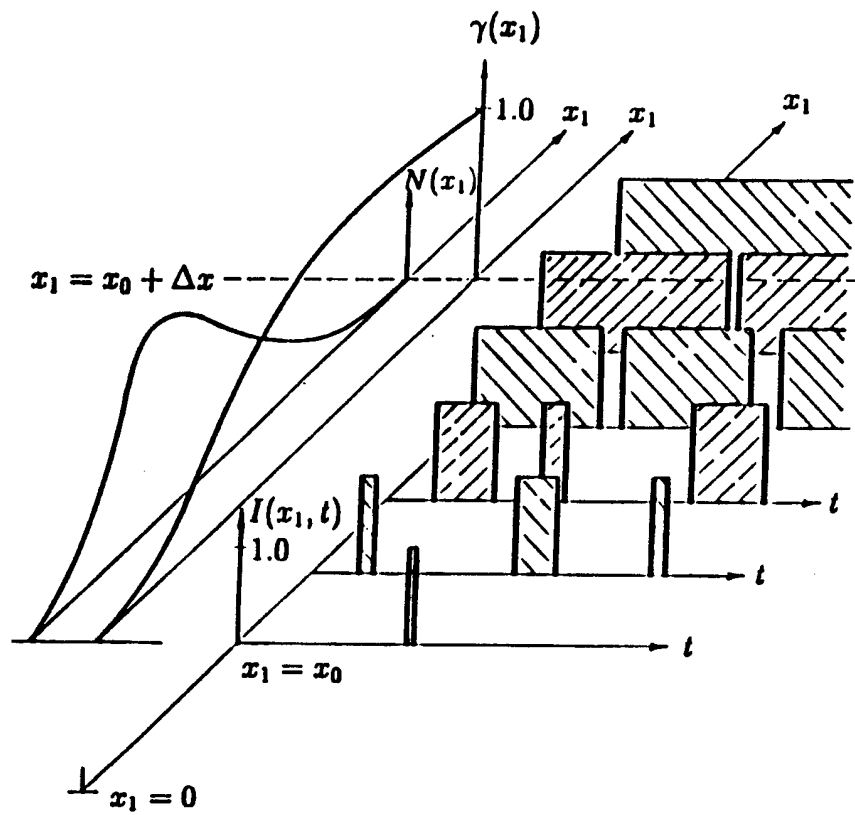
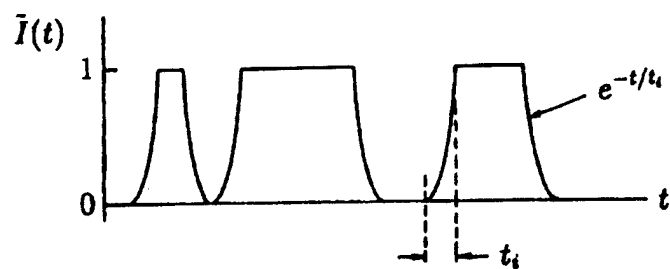
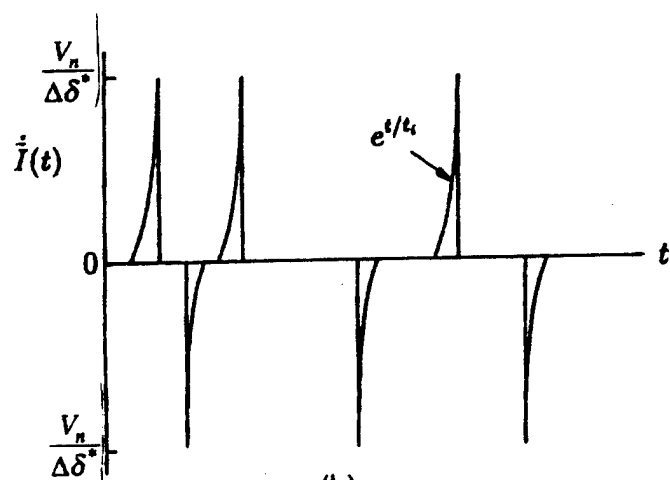


Figure 1.5 Representative sketch of $I(x, t)$, where $\gamma(x_1)$ is the intermittency function and N is the average burst frequency function [from Lauchle 1981].



(a)



(b)

Figure 1.6 The modified indicator function $\tilde{I}(t)$ is shown in (a) and its first time derivative in (b) [from Lauchle 1981].

CHAPTER 2

MODELS FOR BOUNDARY LAYER TRANSITION ZONE ACOUSTIC RADIATION

The modeling of flow-induced noise from boundary layer flows has been well researched for many years. Several papers are significant and form the basis for investigation of transition noise. The works of Lighthill (1952, 1954), Ffowcs Williams (1967, 1969, 1977, 1982), Curle (1955), Crighton (1975), and Blake (1986), and Howe (1998) provide a good general background.

Several approaches have been taken to model the unsteady pressures due to boundary layer transition processes. These have predominately used the Lighthill analogy as a basis. Lauchle (1981) took a more phenomenological approach by modeling the displacement thickness change due to transition as a piston motion with non-uniform velocity distribution. This was later supported through a Lighthill approach by Sornette and Lagier (1984a). Audet et al. (1989a) then claimed the experimental appearance of monopole-like acoustic sources. While the gross fluctuations of the growth in displacement thickness seem to be modeled well by the piston-like sources, there is also much interest in modeling the acoustic sources due to the vortical structures of the spots. In this chapter, four of these models will be presented. Direct numerical simulation efforts will be discussed briefly.

2.1 Fluctuating Shear Stress Using a Lighthill Analogy

Lauchle (1980) used the Lighthill acoustic analogy to find dipole, quadrupole, and octupole components of radiated noise from transition. He assumed radiation efficiencies scale on Mach number according to M^3 and M^5 for the dipole and quadrupole sources respectively. Since a low Mach number flow was also assumed, he neglected the quadrupoles and octupoles due to the fluctuating Reynolds stresses and their images. However, their large amplitudes, relative to those of the wall shear stresses that form the dipole contribution may compensate for the lower radiation efficiency and make this a poor assumption.

The Lighthill equation for sound radiation from fluid dynamic sources is:

$$\frac{\partial^2 p'}{\partial t^2} - c^2 \frac{\partial^2 p'}{\partial x_i^2} = \frac{\partial T_{ij}}{\partial x_i \partial x_j} \quad (2.1)$$

where T_{ij} is Lighthill's stress tensor given by:

$$T_{ij} = \rho u_i u_j - \sigma_{ij} + (p' - \rho' c^2) \delta_{ij} \quad (2.2)$$

It should be noted that Fraudeiplonika (2000) suggests that this stress has an additional contribution, $\vec{\nabla}(\mu u_i)$, but that was not considered in the context of this development. The tensor of Equation (2.2) consists of the fluctuating Reynolds stress tensor, $\rho u_i u_j$, the fluctuating viscous shear stress tensor, σ_{ij} , and a "correction" term which is essentially zero for hydrodynamic flows.

Employing Curle's equation and Powell's (1960) extension for image flow with a rigid, planar surface, Lauchle derived an estimate of the acoustic pressure due to shear stress fluctuations only:

$$p(\mathbf{r}, t) \approx \frac{\cos \theta}{2 \pi r c_o} \frac{\partial}{\partial t} \iint_s \tau_o \left(\eta_i, t - \frac{r}{c} \right) dS(\eta_x), \quad M \ll 1 \quad (2.3)$$

where θ is the angle from the x axis to the observation point. This, of course, assumes that the contribution of the longitudinal and lateral quadrupoles is insignificant based on a M^{-2} reduction in radiation efficiency for low Mach number flows.

Using intermittency to model the wall shear stress in a mix of laminar and turbulent states, $\partial \tau / \partial t$ reduces to $(\tau_T - \tau_L) dl/dt = \sigma(x_i) \dot{I}(x_i, t)$. This results in an equation for the power spectral density of the sound radiated per unit spanwise width of transition:

$$\frac{\partial G(r, \omega)}{\partial z} = \frac{\omega^2 \cos^2 \theta \sigma^2(x_o)}{4 \pi^2 r^2 c_o^2} \iiint \eta_x R_x(\eta_x, \xi_x, \tau) e^{i\omega \tau} d\eta_x d\xi_x d\tau \quad (2.4)$$

This assumes that the space-time correlation function for the indicator can be separated, the same as Corcos (1963) did for the homogeneous, fully developed turbulent boundary layer. This requires that:

$$\langle II \rangle = R_x(\eta_x, \xi_x, \tau) R_z(\eta_z, \xi_z) \quad (2.5)$$

It is assumed that the indicator function, $I(x_3, t)$, is stationary in time and homogeneous in x_3 . A longitudinal space-time correlation function was then formulated based on physical notions of the transition process. The details will not be presented here.

Incorporation of this correlation, which is itself a function of the intermittency, spot burst frequency rate, and a flare parameter (α^*) (defining the decay envelope), yields a final form of Equation (2.4) reduced to a single integration:

$$\frac{\partial G(r, \omega)}{\partial z} = \frac{\cos^2 \theta \sigma^2(x_o) u_o (\Delta x)^2}{2 \pi^2 r^2 c_o^2} F(k_c \Delta x, \alpha^* \Delta x, \frac{u_c}{u_o}) \quad (2.6)$$

with

$$F(k_c \Delta x, \alpha^* \Delta x, \frac{u_c}{u_o}) = (k_c \Delta x)^2 \int_0^1 \frac{1.272 Z^2 (1 - e^{-4.185 Z^2}) e^{-4.185 Z^2}}{[6.472 (u_o/u_c)^2 Z^2 e^{-8.37 Z^2} + (k_c \Delta x)^2] [(\alpha^* \Delta x)^2 + (k_c \Delta x)^2]^{1/2}} \cdot \left(\frac{2 \alpha^* \Delta x}{[(\alpha^* \Delta x)^2 + (k_c \Delta x)^2]^{1/2}} - e^{-\alpha^* \Delta x Z} \sin(k_c \Delta x Z - \varphi) + e^{-\alpha^* \Delta x (1-Z)} \sin[k_c \Delta x (1-Z) - \varphi] \right) dZ \quad (2.7)$$

where $\varphi = \tan^{-1} (\alpha^* \Delta x / k_c \Delta x)$, $k_c = \omega/u_c$ and $Z = \eta_x / \Delta x$. Based on limited experimental data, this model appears to significantly under-predict the transition zone radiated noise.

This led to a search for a more efficient mechanism which would produce the higher

measured levels. It does not appear to be advantageous to pursue any further modifications to this model that uses only the wall shear stresses as the source term.

2.2 Fluctuating Boundary Layer Displacement Thickness Using a Liepmann Analogy

In order to account for the previously neglected terms for the fluctuating velocities, Lauchle (1981,1989) used the Liepmann (1954) analogy rather than calculating the Reynolds stresses in transition as required by the Lighthill equation.

The Liepmann analogy uses the fluctuations in the boundary layer displacement thickness to describe the normal velocity of a vibrating surface. This is the "surface" that the potential outer flow feels as it is displaced by the boundary layer. A wave equation is then solved for the acoustic radiation of this vibrating surface. The results of this approach differ from Lighthill's analogy only in that the unknown source is described in the boundary condition and not in the source terms of the Lighthill inhomogeneous wave Equation (2.1). The use of displacement thickness fluctuations in acoustic modeling was also recognized by Lighthill (1958) and Howe (1981).

2.2.1 Formulation Based on Lauchle Theoretical Space-Time Correlation Function

A solution for the Helmholtz equation is obtained using the Green's function, G_o , for an infinite half space with a Neumann boundary condition (essentially a baffled "piston" with velocity $v_n(\eta_x, \eta_z, t)$):

$$p(\mathbf{x},t) = \frac{1}{2\pi} \int_S \frac{\partial p(\mathbf{x},t)}{\partial n} G_o(\mathbf{x},\mathbf{y};t,\tau) dS \quad (2.8)$$

with boundary conditions of

$$\left. \frac{\partial p}{\partial n} \right|_{y=0} = \rho \frac{\partial v_n}{\partial t}, \quad (2.9)$$

$$v_n(\mathbf{x},t) = \left(\frac{\partial \Phi}{\partial y} \right) \Big|_{y=0} = \frac{\partial \delta^*(\mathbf{x},t)}{\partial t} = \frac{\partial}{\partial t} \tilde{I}(\eta_x, \eta_z, t) \Delta \delta^* \quad (2.10)$$

where n represents the direction normal to the surface, v_n is the fluctuating normal velocity and

$$\delta^*(\eta_x, \eta_z, t) = [1 - \tilde{I}(\eta_x, \eta_z, t)] \delta_L^*(\mathbf{x}) + \tilde{I}(\eta_x, \eta_z, t) \delta_T^*(\mathbf{x}). \quad (2.11)$$

A power spectral density formula was derived as

$$G(r, \omega) = \frac{\rho^2 (\Delta \delta^*)^2 W \omega^4}{8 \pi^2 [1 + (\omega t_i)^2]} \int_{-\infty}^{\infty} \int_0^{\Delta x} \int_{-\eta_x}^{1-\eta_x} \int_{-\infty}^{\infty} \frac{1}{|\mathbf{x} - \mathbf{y}|} \frac{1}{|\mathbf{x} - (\mathbf{y} + \boldsymbol{\xi})|} R_I(\eta_x, \xi_x, \xi_z, t) e^{i\omega \tau} d\xi_z d\xi_x d\eta \quad (2.12)$$

With an estimated space-time correlation function for the intermittency indicator, the far-field solution for the power spectrum of the radiated pressure per spanwise width

becomes

$$\frac{\partial G(r, \omega)}{\partial z} = \frac{\rho^2 (\Delta \delta^*)^2 u_o u_c^2}{8 \pi^2 r^2} F^*(k_c \Delta x, \alpha^* \Delta x, \frac{u_c t_i}{\Delta x}, \frac{u_c}{u_o}) \quad (2.13)$$

where

$$F^* = \frac{(k_c \Delta x)^2}{[1 + (k_c \Delta x)^2 (\frac{u_c t_i}{\Delta x})^2]} F(k_c \Delta x, \alpha^* \Delta x, \frac{u_c}{u_o}) \quad (2.14)$$

with $F(k_c \Delta x, \alpha^* \Delta x, u_c/u_o)$ given by Equation (2.7).

More generally, the normal velocity in Equation (2.10) is created both by flow over the spot and the spot's growth itself. Wygnanski, et al. (1976) found that the normal velocity is directed toward the plate at the spot leading interface and outward over the rest of the spot. This is shown in Figure 2.1.

The opportunity exists to make several modifications to this model based on recent experimental results. These are described in general in Lauchle (1991), Marboe and Lauchle (1992, 1994) and in detail in Chapter 3.

2.2.2 Formulation Based on Josserand-Lauchle Measured Space-Time Correlation Function

Theoretical forms for the space-time correlation function were the only functions that could be employed prior to the actual measurements of these statistics in the transition zone by Josserand (1986). This is now suggested for substitution into Equation (2.12).

The development of a semi-empirical space-time correlation function was performed by Josserand (1986) using a zero pressure gradient, natural transition zone on a flat plate in the ARL Penn State 1.22 m wind tunnel. From Josserand and Lauchle

(1990):

$$R_f(\eta_x, \xi_x, \xi_z, \tau) = \gamma_u \gamma_d + \gamma_u (1 - \gamma_d) \exp \left\{ -5 \left(4 + 200 \left| \tau - \frac{\xi_x}{u_c} \right| \right) \left| \tau - \frac{\xi_x}{u_c} \right| \right\} \cdot \exp \left(\frac{20 |\Lambda_x|}{0.014 + |\Lambda_x|} \left| \tau - \frac{\xi_x}{u_c} \right| \right) \cdot \exp \left(- \left| 15.75 \Delta x - \frac{1260 \left| \tau - \frac{\xi_x}{u_c} \right|}{1 + 71 |\Lambda_z|} \right| \frac{|\Lambda_z|}{1 + 14.2 |\Lambda_x|} \right) \cdot \exp \left[- \frac{A |\Lambda_x|}{0.0014 + |\Lambda_x|} \frac{1}{1 + 1300 \left| \tau - \frac{\xi_x}{u_c} \right|^2} \right] , \quad (2.15)$$

where $A = -\ln[1 - \exp(-4.27/\Delta x)]$, (units of Δx are in meters),

$$\Lambda_i = \xi_i / \Delta x ,$$

$\gamma_u = \gamma(\eta_x)$ and $\gamma_d = \gamma(\eta_x + \xi_x)$ when the reference location is upstream of the second location,

$\gamma_u = \gamma(\eta_x + \xi_x)$ and $\gamma_d = \gamma(\eta_x)$ when the reference location is downstream of the second location.

2.2.3 Chase Statistical Modification

Chase (1989) has suggested that the first exponent term in Equation (2.15) can be replaced by a more general term based on the probability of state transition to turbulence of form:

$$\exp \left\{ - \frac{N_d}{\gamma_d (1 - \gamma_d)} \left| \tau - \frac{\xi_x}{u_c} \right| \right\} . \quad (2.16)$$

However, Josserand found that both terms predict the measured correlation values well for $0.3 \leq \gamma \leq 0.7$; but, that outside of these limits, the Chase theoretical term tended to over-predict the measured correlation. Both terms are available as options in the

computational codes developed for this dissertation.

2.3 Two-Fluids Model Using a Lighthill Analogy

The two-fluids model was first proposed by Sornette and Lagier (1984a,b), further developed with Lagier and Sornette (1986), and applied by Audet et al. (1989a,b). A Lighthill approach was used to validate Lauchle's phenomenological approach. The acoustic radiation described by the two-fluids (states) model is also analogous to a fluctuating piston powered by: (1) fluctuations due to turbulence (vorticity) below the interface, and (2) "growth" processes due to the laminar-turbulent transition (accounted for by Lauchle (1981)). The normal quadrupole terms are found plus one monopole due to entropy production by viscous dissipation (dependent upon the time derivatives of the intermittency indicator function) and another monopole due to kinetic energy dissipation (dependent upon the spatial derivatives of the indicator function).

Following the Lighthill analogy, the fluctuating density is found to be $\rho' = \gamma \rho_T + \Phi$ with "acoustic potential", Φ

$$\frac{\partial^2 \Phi}{\partial t^2} - c_o^2 \nabla^2 \Phi = S_o + S \quad (2.17)$$

and the two source terms, S_o and S , given by

$$S_o = c_o^2 \left(2 \nabla \gamma \cdot \nabla \rho_T + \rho_T \nabla^2 \gamma \right) - \left(\rho_T \frac{\partial^2 \gamma}{\partial t^2} + 2 \frac{\partial \gamma}{\partial t} \frac{\partial \rho_T}{\partial t} \right) \quad (2.18)$$

$$\begin{aligned}
S(\mathbf{r}, t) = & \rho_0 \left[\frac{\partial^2 v_i v_j}{\partial x_i \partial x_j} - \gamma \frac{\partial^2 v_i^T v_j^T}{\partial x_i \partial x_j} - (1-\gamma) \frac{\partial^2 v_i^L v_j^L}{\partial x_i \partial x_j} \right] \\
& - 2 \frac{\partial \gamma}{\partial x_i} \frac{\partial}{\partial x_j} (\tau_{ij}^T - \tau_{ij}^L) - \frac{\partial^2 \gamma}{\partial x_i \partial x_j} (\tau_{ij}^T - \tau_{ij}^L) \\
& - \frac{\partial^2 \Theta_{ij}}{\partial x_i \partial x_j} + 2 \nabla \gamma \cdot \nabla (p^T - p^L) + (p^T - p^L) \nabla^2 \gamma
\end{aligned} \tag{2.19}$$

where v_{ij} is the fluid particle velocity component, τ_{ij} is the fluctuating viscous stress tensor, and with θ_{ij} defined by (using shear viscosity, η , and volume viscosity, ζ)

$$\theta_{ij} = \eta \left[\frac{\partial \gamma}{\partial x_j} (v_i^T - v_i^L) + \frac{\partial \gamma}{\partial x_i} (v_j^T - v_j^L) \right] + \left(\zeta - \frac{2}{3} \eta \right) \delta_{ij} (v^T - v^L) \cdot \nabla \gamma \quad . \tag{2.20}$$

(In this notation, $\gamma(x, t) \equiv I(x, t)$). The S_0 term comes from the wall pressure fluctuations that are due to a fully turbulent flow and whose amplitude is weighted by the intermittency indicator. It contains monopole, dipole, and quadrupole terms. The second term, S , represents the incompressible part of the velocity fluctuations in the transitioning boundary layer. These are monopole sources. The ratio of S_0/S is proportional to Mach number, so S_0 could be neglected in hydrodynamic cases.

Audet et al. (1989a,b) developed a model for the wall pressure spectrum using the two fluids theory to get a fluctuating pressure field of $\gamma p_T + p_{acoustic}$ accounting for the contribution of the turbulent wall pressure modified by the intermittency and the radiated

acoustic field (calculated using the Lauchle (1981) theoretical intermittency indicator correlation). This acoustic pressure is given by

$$p_{acoustic} = \frac{\rho}{\pi} \int_S \frac{1}{|r-r_o|} \Delta\delta^* \frac{\partial^2 \tilde{I}(r_o, t - \frac{|r-r_o|}{c})}{\partial t^2} dS. \quad (2.21)$$

An example of this calculation is shown in Figure 2.2. Equation (2.21) has the advantage over Equation (2.13) (Lauchle 1981) of predicting radiation as a function of $\eta_x/\Delta x$ because of accounting for retarded time differences in the surface integral for $v_n(x, t)$. However, Audet, et al. (1989a,b) used simplifying assumptions for their calculations such as assuming a far field receiver and separation of spatial dependence from temporal dependence which limits the usefulness of this approach.

Certainly the two-fluids model pioneered by Lagier and Sornette provides a more rigorous model of possible transition-induced pressure fluctuations, which contribute to both the nearfield and the farfield. However, using this method to get an estimate of acoustic radiated pressures becomes an almost intractable problem for the engineer. This would seem to be better suited to use with direct numerical simulation and staggering amounts of computer time and memory. When the sufficient simplifications are made to allow a calculable estimate, it provides little benefit when compared to the fluctuating displacement thickness approach.

2.4 Vortex Motions

Kambe and Minota (1981) and later Kambe (1984, 1986) used the viscosity terms for vortices to predict quadrupole and low amplitude monopole-like radiation from vortex motion particularly vortex-edge interaction. According to Kambe (1986), the transition process evolves from Tollmien-Schlichting waves which are amplified and become associated with the concentration of vorticity along discrete lines. These lines distort into vortex loops which continue to distort and grow as turbulent spots until coalescence. The stresses at the vortex interface become a significant sound source.

Hardin (1991) argues that, by a process of elimination, the major source of sound in the turbulent boundary layer is the formation of horseshoe vortex structures by the interaction of the streamwise vorticity with the primary spanwise vorticity. This may be an important source of sound, in addition to the normal velocity of the fluctuating displacement thickness.

There have been many advocates of vortex noise generation modeling. The leaders have been Powell (1964, 1995), Obermeier (1977, 1979, 1980, 1985), Mohring (1978), Howe (1998a,b, 1999a,b), and Mohring et al. (1983). The dynamic response of a vortex to interaction with a sound field [Lund, 1989], a surface [Kambe, Minota, and Ikushima, 1985], and another vortex [Kambe and Minota, 1983] have all been measured experimentally. Two additional experiments have yielded good qualitative data for vortex formation behind a vortex generator [Littell and Eaton, 1991] and in boundary layer transition [Williams, Fasel, and Hama, 1984] .

While some aspects of vortex motions are incorporated in the fluctuating

displacement thickness and two-fluids models, they probably have not been fully accounted for in the computational approximations for the normal velocity and therefore warrant being highlighted as an additional modeling possibility.

The contribution of vortex sound could also play more of a role in flows with non-zero pressure gradients due to growth and stretching.

2.5 Direct Numerical Simulation

The state of the art in computational fluid dynamics application to solution of the acoustic problem in fluid flow can be best summarized with a quote from Crighton (1975):

"Lack of knowledge of features of the flow does not entitle us to make assumptions and approximations except with the greatest care. We are dealing with a small by-product, and approximations which may be quite safe as far as the flow dynamics are concerned may be fatal for the by-product. Vast errors may easily be incurred in this way through apparently harmless approximations, especially in underwater flows, where the Mach numbers are always extremely small, and the acoustic energy is a correspondingly minute fraction of the total energy.... Highly accurate numerical predictions are simply not to be expected - a reflection of the fact that noise levels usually vary far more widely than do the parameters which describe the noise-producing flow."

Having read that, it is important to state that significant progress has been made in

the last eight years. Some of the best work has been done by Wang, Lele, and Moin (1994, 1996a, 1996b). Their modeling focuses on the quadrupole source functions in the solution of the full incompressible Navier-Stokes equations. They find that negligible sound is created during primary and secondary instability stages but that disintegration of the detached high shear layer and vortex shedding near the boundary layer edge results in amplification of the Reynolds stress quadrupoles, particularly at the frequency of vortex shedding. Their conclusion is that the acoustic quadrupoles and images dominate up through the formation of spots and then in-plane dipoles, due to surface shear stress, dominate in late transition. [Note that this is the modeling approach of Lauchle (1980) discussed in section 2.1]. The small scale features and large convected eddies are considered to be inefficient acoustic sources despite larger amounts of energy. They also show that small structures traveled faster than the lambda vortex which elongates the disturbance region yet neighboring spot interaction is negligible. This group has also developed a hybrid technique for low Mach numbers that uses a Navier-Stokes solver for incompressible hydrodynamic terms and a Lighthill analogy for the acoustic contribution. Notably, an exit boundary correction is also been developed for the quadrupole source calculated in the truncated domain, V_o

$$\ddot{Q}_{ij}(t) = \frac{\partial^2}{\partial t^2} \int_{V_o} T_{ij}(y,t) d^3y + \frac{\partial}{\partial t} \int_{S_o} U_c T_{ij}(y,t) d^2y \quad (2.22)$$

given by the second term which is equal to the time derivative of the Lighthill stress fluxes carried by convecting eddies across the exit surface. In contrast, Kloker,

Konzelmann, and Fasel (1993) use a "re-laminarization" zone downstream of transition before passing through the outflow boundary to suppress reflected flow disturbances in direct numerical simulation (DNS).

A very important part of any DNS modeling effort is the introduction of a disturbance to cause breakdown to turbulence. An excellent overview is provided in Rist and Fasel (1995). They discuss the use of temporal vs. spatial models. They recommend that most "real life" cases should only use a spatial model, but the penalty is in processing resources. They also discuss a mean flow which is obtained from a time averaged disturbance flow. This quantity is like what Krane (1992) measured. This is contrasted with a steady base flow that is obtained from numerical solution of the Navier-Stokes equations before the unsteady flow field is calculated. They also found a high shear layer structure that sat on top of the lambda vortex structure and instantaneous maps of normal velocity (see Figure 2.3) that show a pushing of the flow structures away from the wall.

A number of computational studies have achieved results which may contribute to our qualitative understanding of transitional flow structures. Coherent structures, similar to bursts in the fully developed TBL, were calculated by Rempfer and Fasel (1994). There is a spike stage in their result which yields fluctuating velocities that are significant for acoustic modeling. Ducros et al. (1996) performed a large eddy simulation (LES) of boundary layer transition. This took 80 hours (CRAY YMP) using LES (compared to 800 hours using DNS, Rai and Moin (1993)) and a filtered structure function on the velocity field to eliminate large scale oblique perturbations. Their results show qualitative progress and could aid in interpretation of the role of vorticity in the acoustic

signature. But obviously, this is not a time effective means for prediction or design.

Yang, et al. (1992) performed computational analyses for natural transition in an adverse pressure gradient. Similarly, the works of Goldstein et al. (1992), Goldstein and Leib (1993), plus Henningson and Kim (1991) show results which provide some insight into the roles of vorticity, local separations, and spot growth. Wilde and Rose (1997) concluded from their use of a temporal model of K-type transition and spatial model of bypass transition that the generated sound comes from the streamwise dipole of the wall shear stress.

The work of Joslin (1991) on the modeling of the effects of compliant walls on primary and secondary instabilities in boundary layer transition warrants further investigation relative to efficient numerical simulation compared to DNS. This may also have some applicability in further refining the fluctuating displacement thickness model.

Abraham and Keith (1997) have shown that DNS simulations for the fully developed TBL can produce a reasonable estimate for wall pressure events associated with sweeps and bursts. They also show that the number of positive and negative events occur in comparable densities and that their average spectra are lower in level by 3 to 7 dB than their peak spectral amplitudes. This is significant in light of the positive and negative normal velocity distributions sensed for the passage of for turbulent spots described in Krane and Pauley (1995).

2.6 Direct and Indirect Radiation From Complex Geometries

The research described here is intended to critically examine the popular approaches to modeling the radiation mechanisms and bring some degree of closure to the physical and practical significance of noise and pseudo-noise originating in the laminar-to-turbulent transition zone within a natural boundary layer. This effort includes updating of models to include recent computational and experimental statistics plus an evaluation of model sensitivities, applicability, and significance for situations of engineering relevance such as for the noses of bodies of revolution and for airfoils.

Although little has yet been done to model transition noise for transition zones specifically on curved surfaces, Howe (1981) has made some generalizations. He contends that displacement thickness fluctuations will give efficient sound radiation in the regions of a surface or body where the local radius of curvature is smaller than the acoustic wavelength. For an airfoil, this would be in the leading and trailing edge regions under compact conditions.

2.6.1 Vicinity of a Half-Plane Leading Edge

The effect of scattering of near-field energy due to the surface geometry near the leading edge or trailing edge of a plane is to enhance the shear stress dipole sources in the transition region based on formulations by Howe (1999a,c). These sources may be less important for flat walls compared to the quadrupole sources in the turbulent spots but, for a curved leading edge, tend to contribute to the low frequency signature following a U^6 velocity scaling. Two factors play into this. First, due to the curvature of the leading

edge, the transition tends to occur in a region of adverse pressure gradient which will accelerate the transition. Second, the nearfield of the transition region hydrodynamic unsteadiness will extend forward to the leading edge and diffract around the curved surface.

Howe models the transition region with an 'upwash' velocity on the body surface using the Biot-Savart formula giving the (time dependent) distributed vorticity induced instantaneous velocity field as though the surface was not present. He uses the proportional local blocked surface pressure to represent the spectrum of the upwash velocity. The fully developed TBL spectrum is used with the addition of an intermittency weighting factor.

The assumptions for this model include:

- very low Mach number, 2-D flow;
- symmetric, finite thickness plane (better termed a hydrofoil);
- hydrofoil chord is acoustically non-compact;
- hydrofoil span is much greater than the boundary layer thickness;
- hydrofoil thickness is acoustically compact, and that the leading edge is within the nearfield of the transition zone;
- zero angle of attack and boundary layer fluctuations on opposite sides of the foil are equal and independent so an estimate of one side can just be increased by 3 dB;
- the integration of the vorticity is restricted to the non-linear region of the boundary layer above the viscous sublayer, so bound vorticity on the hydrofoil is

ignored; and

- high Reynolds number, the contribution of tangential shear stresses is ignored.

Using the Green's function for a rounded leading edge, Howe approximates the farfield acoustic pressure as

$$p(x, \omega) = \frac{\rho \omega \sqrt{ik_o} \sin^{1/2} \psi \sin\left(\frac{\theta}{2}\right) e^{ik_o|x|}}{\pi \sqrt{2\pi} |x|} \oint_S \Phi^*(y) v_{ln}(y, \omega) dS(y), \quad |x| \rightarrow \infty \quad (2.23)$$

where

θ, ψ define the observer orientation direction $\mathbf{x} / |\mathbf{x}|$

$\Phi^*(y)$ is the velocity potential describing the flow of unit speed in a clockwise sense over the profile S of the hydrofoil

v_{ln} is the normal component of the upwash velocity.

When a conformal mapping is done for the hydrofoil surface, equation (2.23) is approximated as:

$$\Phi(x, \omega) \approx 0.35 \frac{U_c/c_o}{\pi^4} \left(\frac{hL}{|x|^2} \right) \left(\frac{1+\alpha\beta^2}{1+\alpha} \right) \sin \psi \sin^2\left(\frac{\theta}{2}\right) |F(\omega, k_c)|^2, \quad |x| \rightarrow \infty \quad (2.24)$$

where

$$F(\omega, k_c) = \int_{\zeta_0}^{\infty} \sqrt{\Phi_{pp}(s, \omega)} [1 + e^{-|k_c| h'(s)}] e^{ik_c s} d\zeta, \quad s=s(\zeta), \quad s_o=s(\zeta_o) \quad (2.25)$$

α, β define the nose shape in the conformal mapping of the profile S onto the real ζ axis;

h is the constant thickness of the hydrofoil;

L is the span of the hydrofoil; and

$\Phi_{pp}(s, \omega)$ is the point pressure spectrum of TBL wall pressure fluctuations
(To account for the transition zone, $\Phi_{pp}(s, \omega)$ includes a weighting with $\gamma(s)$.)

Equation (2.24) represents the far field sound due to turbulent hydrodynamic fluctuations on the upper surface of the hydrofoil.

2.6.2 Bodies of Revolution

We know that transition in an adverse pressure gradient will result in higher radiated and structural excitation levels due to the possibility of separation and re-attachment of the flow. The Haddle and Skudrzyk (1969) data and Perraud (1989) data are representative of the case of separation-induced transition on the nose of a body of revolution. These are presented in section 2.7.1.

The rms pressure level measured under the transition region on a 1.5 caliber ogive nose was reported by Arakeri (1975) to be some 2 to 2.5 times higher than the rms

pressure measured further back under the fully developed TBL. The hemispherical nose shape does promote laminar separation and the rms pressure levels measured in and around the separation reattachment point are 10 times higher than the TBL rms pressure levels. The separation-induced wall pressure fluctuations are 4 to 5 times higher than those induced by transition. Similar measurements were performed by Huang and Shen (1989). Several axisymmetric headforms were tested in the Anechoic Flow Facility at David Taylor Model Basin where wall pressure fluctuations induced by either natural transition or laminar separation were determined. They arrived at the same conclusions as Arakeri regarding the magnitude of the pressure fluctuations.

Arakeri, et al. (1991) found a scaling equation for the flow noise received at the stagnation point of axisymmetric bodies of the form:

$$S_p(f) = S_m(f) + 50 \log\left(\frac{U_{\infty p}}{U_{\infty m}}\right) + 20 \log\left(\frac{D_p}{D_m}\right) + \Delta S_d + \Delta S_T \quad (2.26)$$

where m, p refer to model and prototype conditions,

D is body diameter,

ΔS_d refers to losses due to surface diffraction, and

ΔS_T refers to a reduction in levels due to transducer configuration and directivity.

However, the measured data, shown here as Figure 2.4, appear to yield a $U_{\infty}^{7.5}$ dependence. This agrees with the theoretical prediction of Lauchle (1989). This also results in better agreement with the Haddle and Skudrzyk data presented as Figure 11 in

Arakeri et al. (1991), reproduced with additions as Figure 2.5. Therefore, it is suggested that equation (2.26) be modified as (see also Lauchle, 1992):

$$S_p(f) = S_m(f) + 75 \log\left(\frac{U_{\infty p}}{U_{\infty m}}\right) + 20 \log\left(\frac{D_p}{D_m}\right) + \Delta S_d + \Delta S_T . \quad (2.27)$$

The models described in this dissertation all suggest that higher radiated pressure levels will result from (1) a shorter streamwise extent of the transition zone, (2) an increase in the normal velocity due to an increase in $\Delta\delta^*/\Delta t$, or (3) a decrease in t_i . Each of these situations can be associated with the noses of axisymmetric bodies and adverse pressure gradients. An example of the effect of a change in Δx is shown in Figure 2.6. It compares predicted radiated noise using Equation (2.13) for $\Delta x=0.061$ m as appropriate for the hemispherical nose, and $\Delta x=0.15$ m as would be calculated by Equation (1.1) for a flat plate at the same Reynolds number. A shorter transition zone results in a slight increase in the peak amplitude of the power spectrum and shifts the peak to a higher frequency.

Howe (1999a) has also extended his model to axisymmetric bodies with similar assumptions as described in section 2.6.1.

2.6.3 Airfoils and Hydrofoils

Just as trailing edge flows are critical to the direct radiation, excitation, re-radiation and scattering of noise for airfoil trailing edges (see Brooks and Hodgson, 1981, Gershfeld, 1997, Howe, 1998b, 1999b,c), so may transition near the leading edge of

an airfoil act as a noise source. Of course, the characteristics of the transition location and extent is quite dependent upon the chordwise distribution of thickness for the airfoil. This is well discussed in the papers by Halstead et al. (1995a,b,c,d) and Lou and Hourmouziadis (1999). These investigations encompassed operation with periodic flows due to upstream blade wakes in the former and a downstream rotating flapper valve in the latter reference. Transition as well as laminar separation and turbulent reattachment were observed. However, in that case, the growth of the instability did not match that for natural transition on a flat plate. It was suggested by Wilde and Rose (1997) that transition noise may be most important in cases where the surface area covered by transitioning flow is comparable to fully turbulent flow area. This is potentially the case with airfoils used in turbines which encounter bypass and separation-induced transition due to inflow wakes (Addison and Hodson, 1991 and Halstead et al., 1995a,b,c,d). The applicability of any of the reviewed models for transitional flow on blades would most likely be the substitution of the appropriate leading edge Green's function into the fluctuating displacement thickness model following the work of Howe (1998, 1999a).

2.7 Need for Refining the Fluctuating Boundary Layer Displacement Thickness Model in a Natural Transition Region

It is now possible to make some refinements to the Lauchle (1981) model with the availability of the empirically derived Josserand space-time correlation function (Josserand and Lauchle, 1990). It should be noted that a similar treatment can also be incorporated into the two-fluids model.

Audet et al. (1989b) point out that a significant difference between their prediction from Equation (2.21) and Lauchle's (2.13) is that they leave the factor $1/|\mathbf{r}-\mathbf{r}_0|^2$ inside the integral. This is important when calculating the directly radiating near-field contribution to measured wall pressure fluctuations whereas Lauchle made a far-field (and compact source) approximation of $1/|\mathbf{r}-\mathbf{r}_0|^2 \rightarrow 1/r^2$ which becomes a constant. Therefore, this term should be brought back inside the integral for making predictions from a transition zone which may not appear compact or necessarily in the far-field to a transducer. This is often the case for buoyant vehicle and sonar self-noise tests.

Using the chosen intermittency space-time correlation function in Lauchle's Equation (2.12) provides a refined equation for the radiated pressure power spectrum:

$$G(r,f) = \frac{\rho^2 (\Delta\delta^*)^2 \omega^4}{4 \pi^2 [1+(\omega t_i)^2]} \int_{-\infty}^{\infty} \int_0^{\Delta x} \int_{W/2}^{W/2} \int_{-\eta_x}^{1-\eta_x} \int_{-1.5\eta_x \tan \alpha}^{1.5\eta_x \tan \alpha} \frac{1}{|\mathbf{x}-\mathbf{y}|} \frac{1}{|\mathbf{x}-(\mathbf{y}+\boldsymbol{\xi})|} \cdot R_f(\eta_x, \xi_x, \xi_z, t) e^{i\omega\tau} d\xi_z d\xi_x d\eta_z d\eta_x d\tau \quad (2.28)$$

The limits of integration for $d\xi_z$ have been decreased from infinity to a correlation length limit approximated by the spot transverse extent. Chen and Thyson (1971) found this to be $\pm 1.5 \eta_x \tan \alpha$ where α is the spot boundary angle to the flow axis ($\alpha \approx 10$ degrees). Also, assuming homogeneity in the η_z direction, Equation (2.25) becomes a quadruple integral with a transition zone width factor, W , in the numerator of the leading coefficient.

The approach taken by Lauchle using a Liepmann analogy has the advantage of

being able to incorporate both the gross piston like fluctuation of the boundary layer displacement thickness and the acoustic sources associated with the growth of the spot domain involving the horseshoe vortex. The gross piston fluctuation is described by $\Delta\delta^*$, Δx , u_c , t_i and N . The spot size limitation is accounted for by $1.5 \eta_x \tan \alpha$. Whatever spot dynamics (and resulting unsteady pressure sources) haven't been accounted for properly in an empirically derived space-time correlation at the wall will become the necessary future refinements.

In trying to identify these, some useful information has been found on spot statistics in Wygnanski et al. (1976). Experimental evidence was cited to establish that two artificially generated spots displaced laterally did not affect each others' growth rate. They also provide detailed descriptions of spot dynamics as shown in Figures 2.7 and 2.8. The spot shape as a function of normalized surface point passage time in Figure 2.7 shows the variation of the extent of the spot with height off the surface. This variation is important when trying to model the spatial distribution of normal velocity to define the motion of an equivalent "piston". The variation of v_n with normalized time at two elevations (Figure 2.8) shows how difficult it is to define $v_n(\eta_x, \eta_z, t)$. The celerity of the spot's leading and trailing edges vary with y . Gutmark and Blackwelder (1987) reported measuring leading and trailing edge celerities which increased with y from $0.88U_\infty$ and $0.58U_\infty$ at $y=0.1\delta_{lam}$ to $0.93U_\infty$ and $0.60U_\infty$ at $y=\delta_{lam}$. Similar results were found from data of other investigators.

2.7.1 Example Applications of Fluctuating Displacement Thickness Model

Measurements of wall pressures and an apparent upstream acoustic propagation of transition zone emissions have been made on an axisymmetric 0.32 m diameter body in the CEPRA 19 anechoic wind tunnel by Perraud (1989). Comparisons are made to pressure spectra measured using large flush-mounted transducers. In this experiment, $r = 0.3$ m, $\Delta x = 0.20$ m, $u_c/U_\infty = 0.8$, and $\Delta\delta^*$ was estimated to be 0.25 mm. The spectral shape and amplitude were predicted reasonably well with $0.05 \leq u_c t / \Delta x \leq 0.15$.

Computational results are compared to the measured data in Figure 2.9. Low-frequency energy appears centered around the most unstable Tollmein-Schlichting wave frequencies; this contribution is not predicted by the current theoretical model.

A comparison is also made of predicted radiated noise to the buoyant body data of Haddle and Skudrzyk (1969). While there are also contributions from the fully developed TBL and noise from the stabilizing fins, which were found (Lauchle and Brungart 1988), using TBL noise estimates from Blake (1986) and Lauchle (1977), and fin trailing edge noise estimates from Brooks and Hodgson (1981), to be much lower than the measured noise. Results for a typical operational condition of $U_\infty = 15.44$ m/s, $\Delta x = 0.061$ m, $r = 1.0$ m, $u_c/U_\infty = 0.8$, body diameter of 0.48 m and $\Delta\delta^*$ estimated as 0.43 mm have been made. These are all shown in Figure 2.10. The predicted spectral levels for the directly radiated noise from the fully-developed TBL seems inconsistently low relative to the predicted transition noise when compared with the airflow measurements described in Chapter 6. It is believed that several factors may contribute to this. The low wavenumber data used to estimate the TBL noise may have been underestimated by the wavevector

filtering used in the experiment. The scaling relationship used by Blake assumes a rigid flat wall and also neglects the effect of proximity of the source to a nose of the body as examined by Howe (1999a). There could also have been some separation and reattachment of flow near the noise due to slight variation in angle of attack as the buoyant body ascended.

Neither application of the model is particularly satisfying. Likewise, each of the examples presented by Lauchle (1981) seem to have the best fit of predicted versus measured data for non-dimensional rise time, $0.45 < U_c t / \Delta x < 1.0$. However, this tends to describe only the shape of the higher frequency portion of the spectrum. Clearly, improvements to the model are in order.

It is important to point out that in underwater flow situations, the common presence of inhomogeneities, particularly bubbles, can account for a considerable increase in radiated noise. For example, Crighton (1975) shows that air bubble concentrations with a void fraction of less than 1% in turbulent flow can increase the radiated noise power by up to 50 dB due to excitation by passage of the bubbles through high pressure gradient flows.

2.7.2 Study Objectives: General Approach Towards Characterizing the Acoustic Emissions from Isolated Transition Flow Structures and a Natural Transition Zone

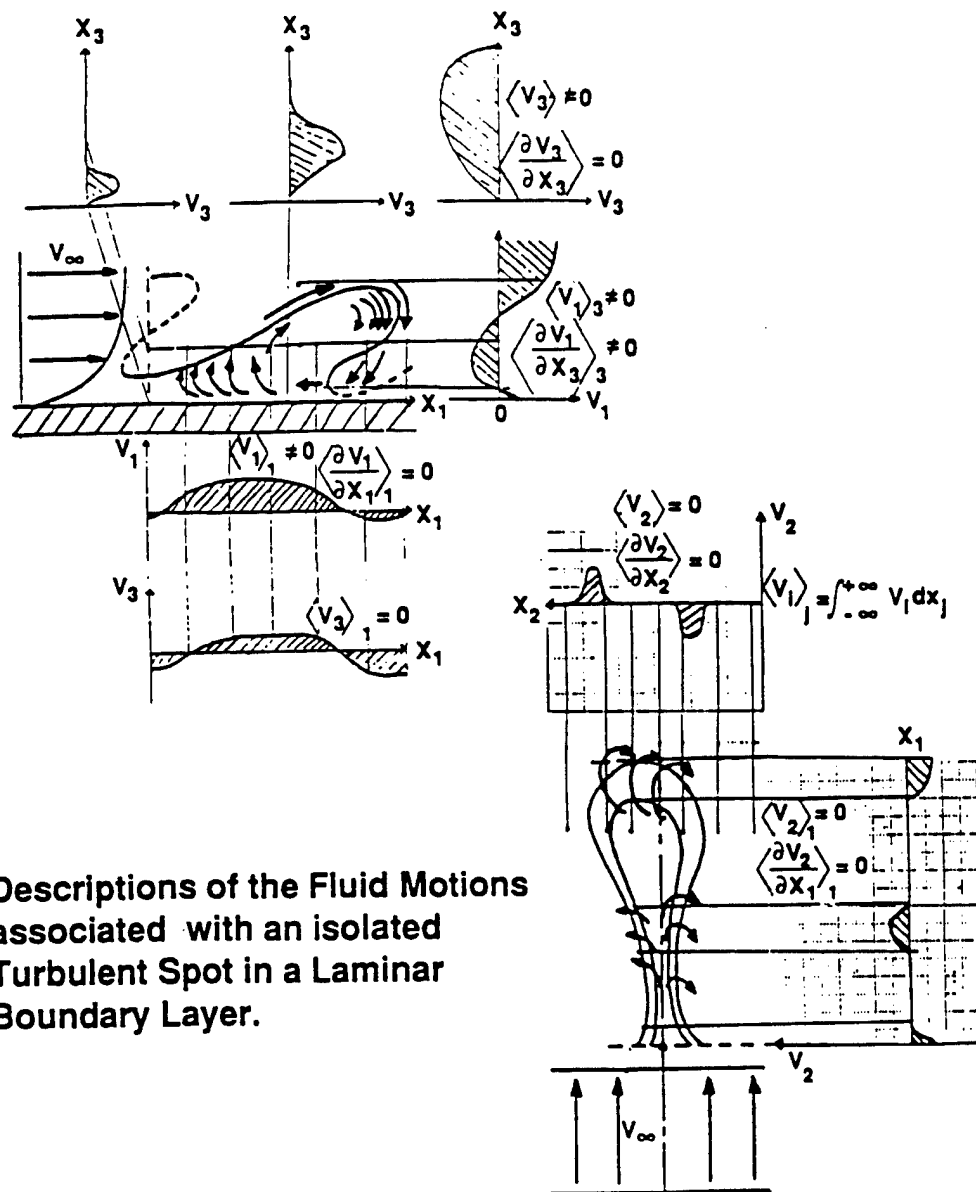
Given the possibility of high radiating energy from the transition zone, understanding the boundary layer transition process is perhaps as important from the point of view as a structural excitation mechanism as it is as a direct radiator. It is beyond

the scope of this dissertation to pursue all of the fluid-structure coupling implications and local excitation of bubbles which must be dealt with to truly predict the transition related signature in an underwater situation. However, this may be the role in which transition is most important for problems of practical concern. It certainly does not appear that direct radiation from such a small area as the transition region (and probably only half of it in terms of spot growth) is significant when compared to fully developed TBL noise over the surface area of the rest of the body or plane in zero or variable pressure gradients. Nevertheless, we are interested in pursuing improvements in both aerodynamic and hydrodynamic modeling of boundary layer transition noise mechanisms and validation through quality experiments because it is reasoned that transition flow structures form the basic building blocks of all subsequent downstream flow behavior and its acoustics.

The problem then is that two basic modeling approaches exist for the direct radiation from a naturally transitioning boundary layer. While the two-fluids model may be the more inclusive, it is also the more difficult to apply in practice. The phenomenological Liepmann approach is the most amenable to incorporation of recent experimental descriptions of the normal velocity fluctuations. This study has concentrated on Liepmann model modifications and further qualitative assessments. A series of experiments have been performed for evaluation of the models.

At this point, the value of direct numerical simulation may be to provide insight on the necessary modeling of substructure dynamics that influence the spatial definition of the normal velocity used in the fluctuating displacement thickness model, and hence contribute, in their own right, to the acoustic pressure, particularly that in the nearfield.

This bridges the gap, to some extent, between the two-fluids model using the Lighthill analogy, and the Liepmann approach used for the fluctuating displacement thickness model.



Descriptions of the Fluid Motions associated with an isolated Turbulent Spot in a Laminar Boundary Layer.

Figure 2.1 Vortex view of a turbulent Spot [from Audet et al. 1989a].

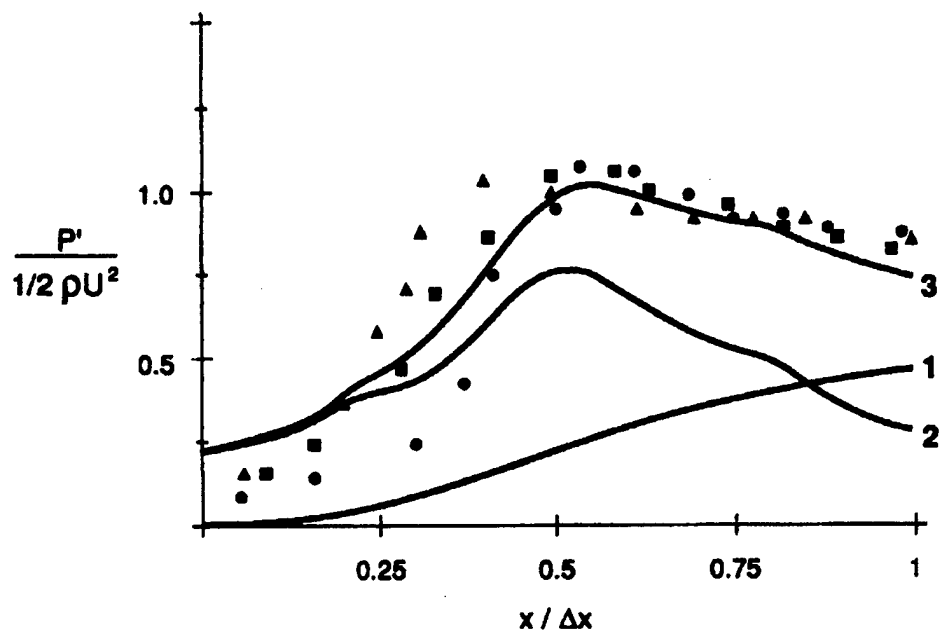


Figure 2.2 The normalized rms wall pressure fluctuations in the transitional boundary layer measured and predicted for a flat plate. The curves are predictions which account for spatial and frequency filtering of the sensors. Curve 1 is γp_T , Curve 2 is the radiated acoustic source term, and Curve 3 is their sum. The symbols are measured data for 3 velocities. [from Audet et al. 1989a,b].

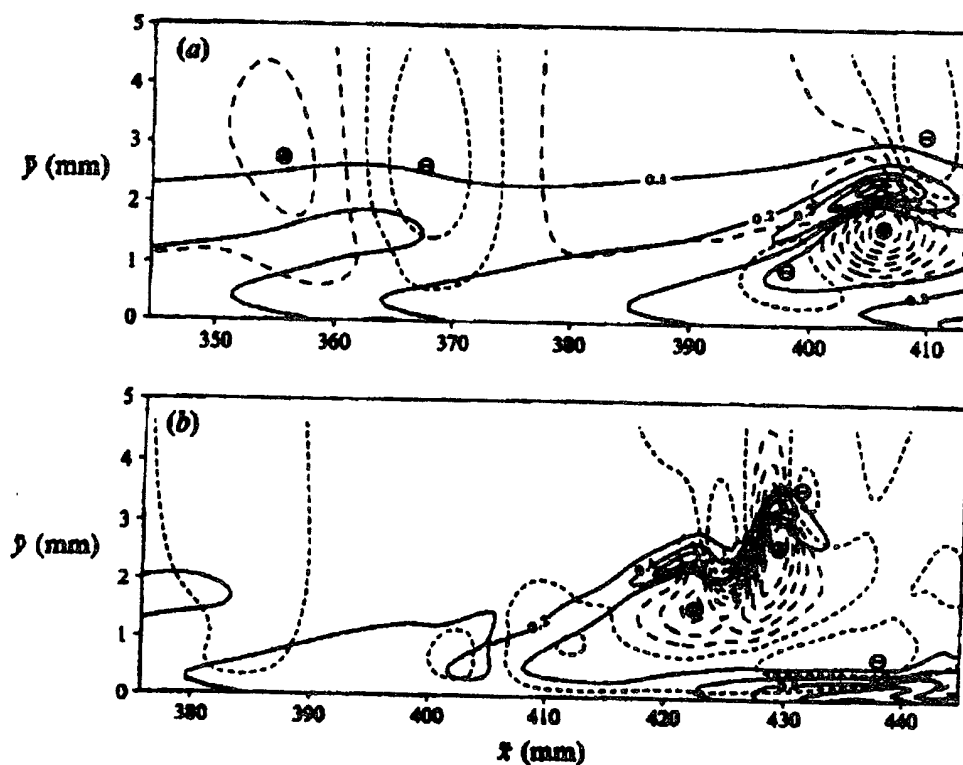


Figure 2.3 Comparison of instantaneous isolines of spanwise vorticity (solid lines) and normal velocity component (dashed lines) at $z=0$: (a) $t=10T$; (b) $t=10.4T$. Local maxima and minima of normal velocity are indicated. [from Rist and Fasel 1995]

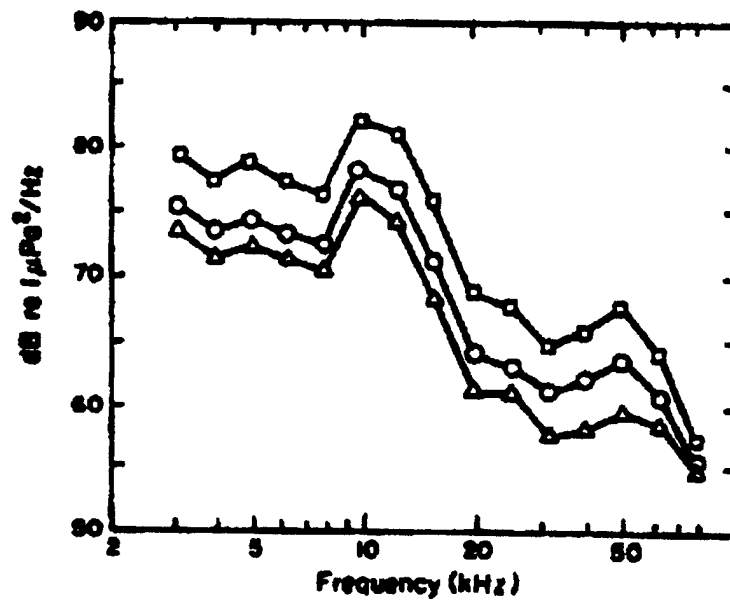


Figure 2.4 Measured flow noise levels on modified ellipsoidal nose. Δ , $U_\infty=10.0$ m/s; \circ , $U_\infty=10.9$ m/s; \square , $U_\infty=12.2$ m/s [from Arakeri et al. 1991]

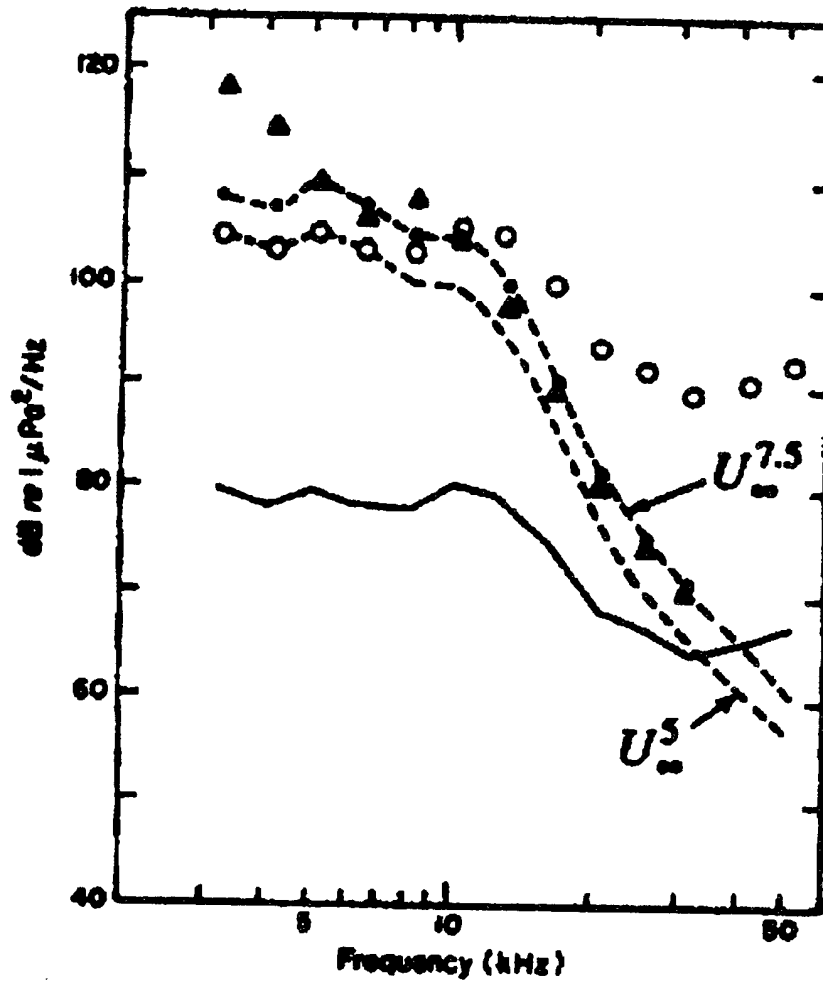


Figure 2.5 Verification of the proposed scaling law with the Haddle and Skudrzyk (1969) results. —, IISc model results with $U_{\infty}=12.2$ m/s and diameter $D=0.075$ m; o, model results extrapolated to Haddle and Skudrzyk conditions of $U_{\infty}=18.5$ m/s and $D=0.42$ m without corrections; - - -, extrapolated results corrected for diffraction loss scaled on two different power laws; Δ , the Haddle and Skudrzyk experimental results [the 5th power law is from Arakeri et al. 1991; the 7.5 power law is from Lauchle 1992].

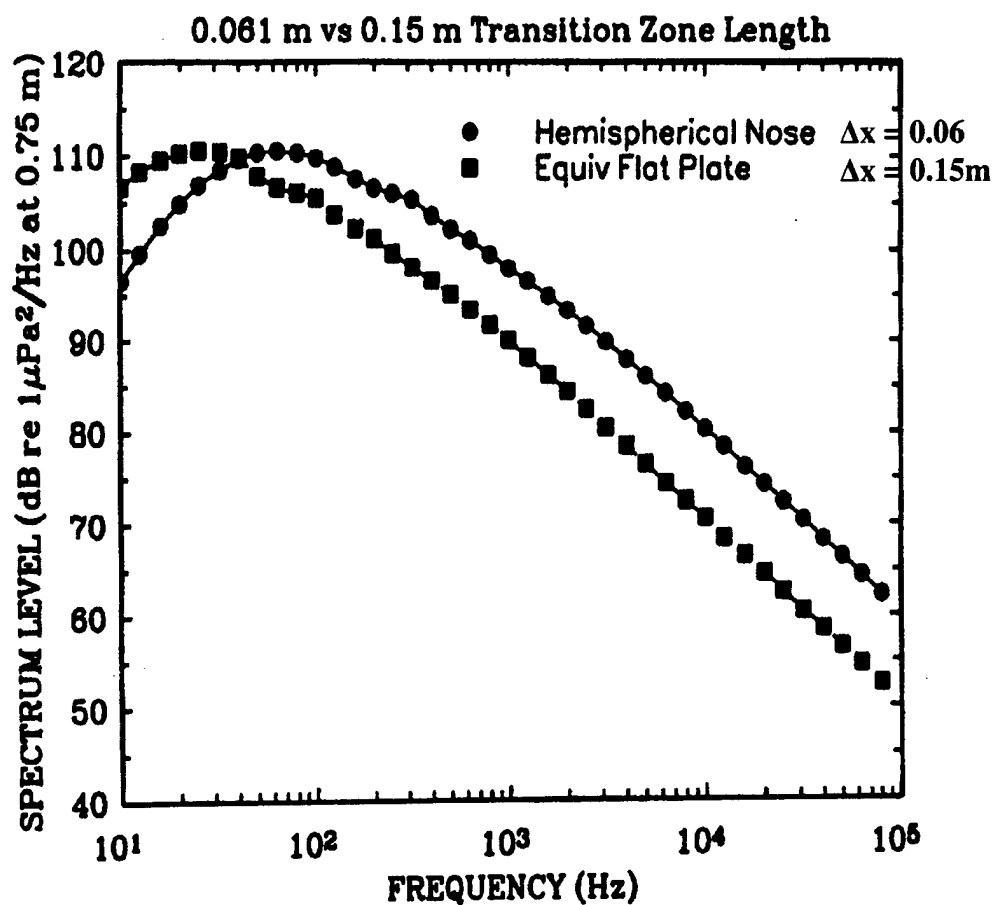


Figure 2.6 Comparison of radiated 1/3 octave levels predicted by Equation (2.13) for the Haddle and Skudrzyk (1969) test conditions using a flat plate (0.15 m) and a hemispherical noise prediction (0.061 m) for transition zone length Δx .

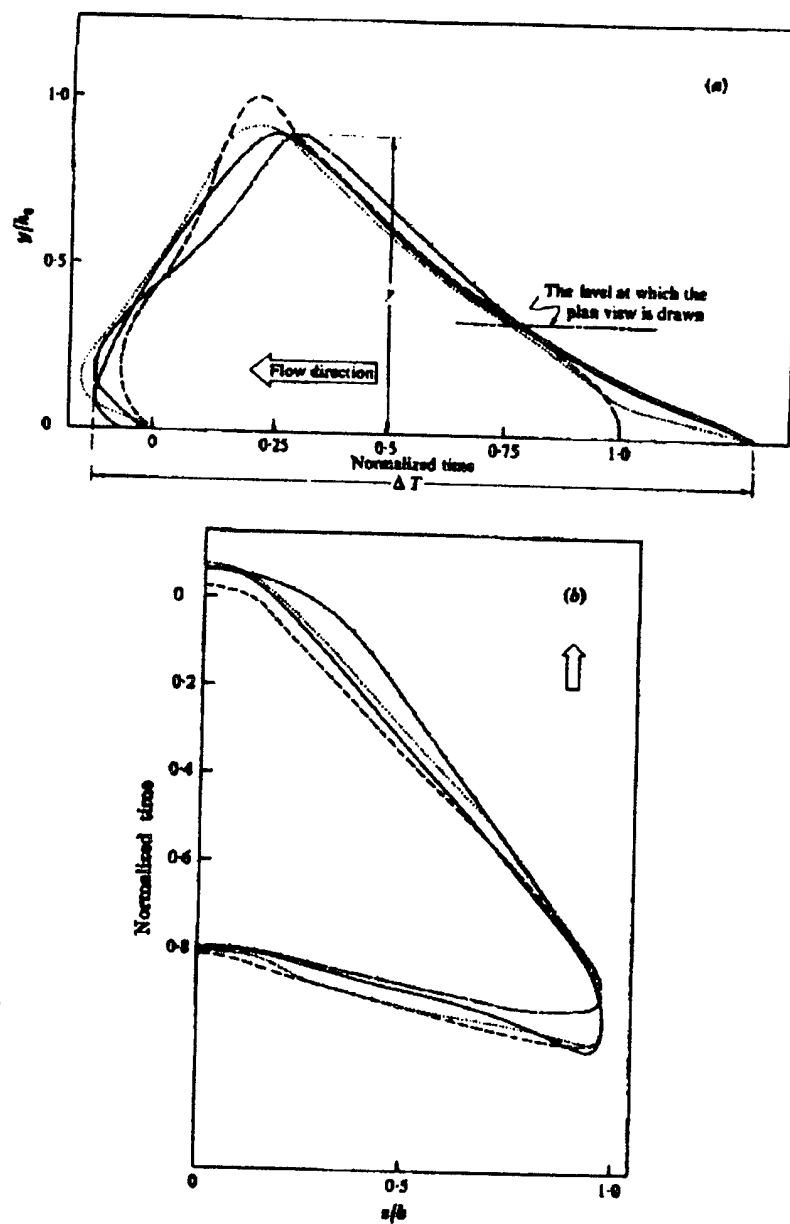


Figure 2.7 Two cross-sections through a spot: a comparison of criteria, $U_\infty=9.4$ m/s, (a) elevation, (b) plan. -x-, Coles and Barker (1974); ---, Wygnanski et al. (1976). Shape based on 2% elevation in U : ●●●●, LE ensemble average; ----, TE ensemble averaged [from Wygnanski et al. 1976].

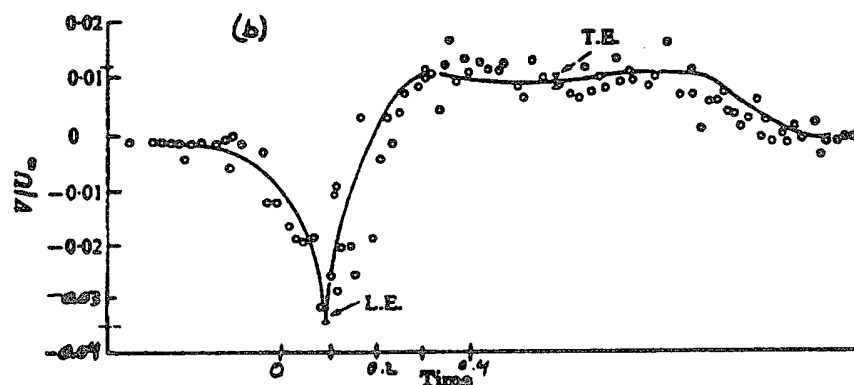
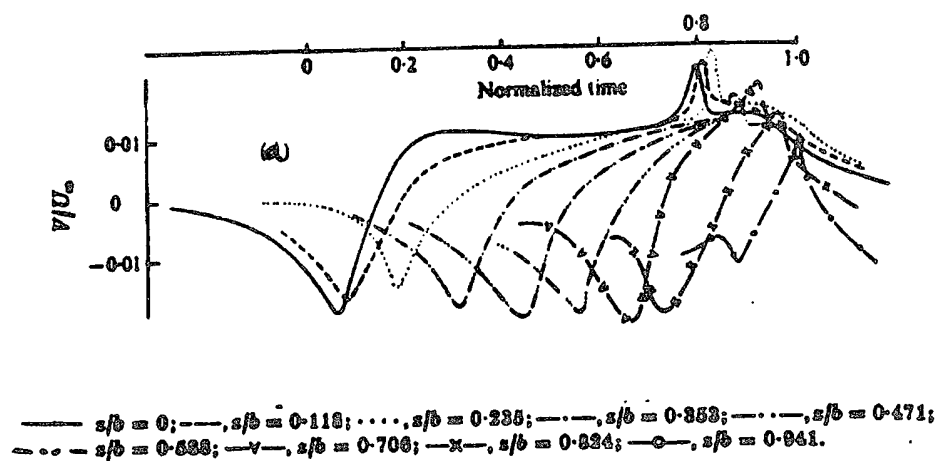


Figure 2.8 Spanwise variation for normal velocity for $x_s U_\infty / \nu = 1.93 \times 10^5$:
 (a) $y/h_o = 0.325$, $0.0 \leq z/\text{span} \leq 0.941$; (b) $y/h_o = 0.54$, $z/\text{span} = 0.0$ [from
 Wagnanski et al. 1976].

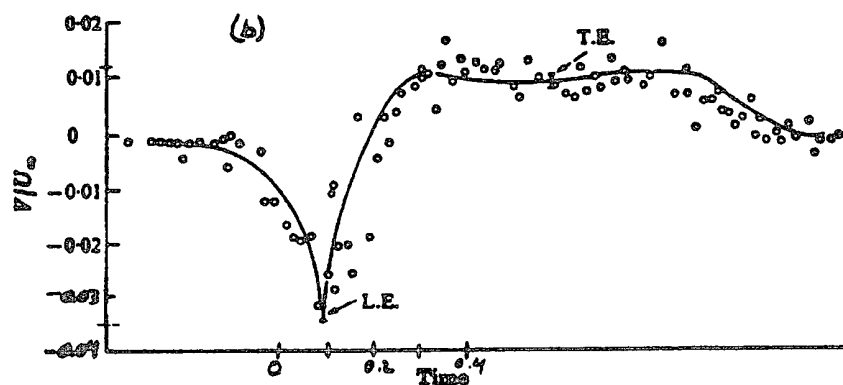
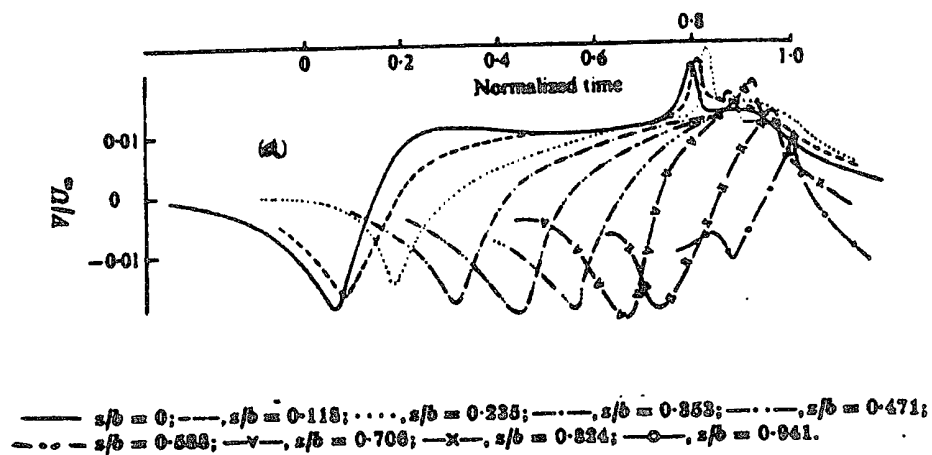
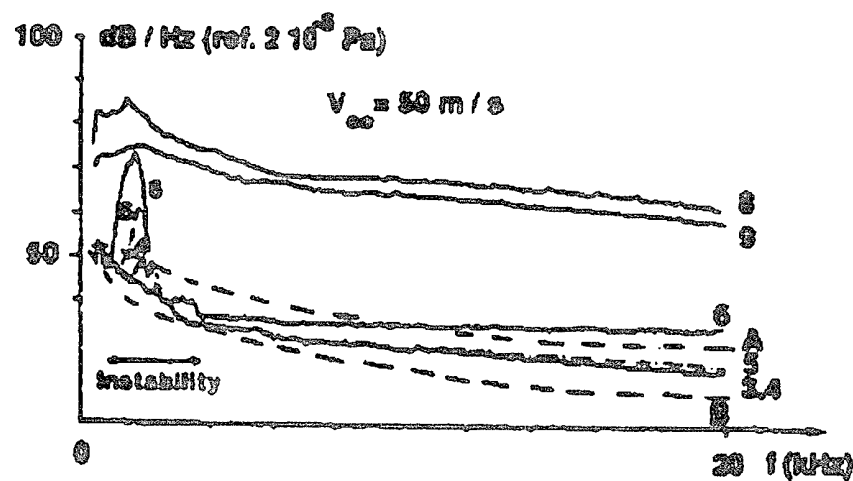


Figure 2.8 Spanwise variation for normal velocity for $x_s U_\infty / \nu = 1.93 \times 10^5$:
 (a) $y/h_o = 0.325$, $0.0 \leq z/\text{span} \leq 0.941$; (b) $y/h_o = 0.54$, $z/\text{span} = 0.0$ [from
 Wygnanski et al. 1976].



Evolution of pressure spectral densities at stations 3 to 9 in
a 20 kHz frequency band
Comparison with Leuchle's model (curves A, B) of levels
measured under the laminar boundary layer (microphone 3)

$$A: \frac{U_c \Gamma_l}{\Delta x} = 0.06$$

$$r = 0.3 \text{ m}$$

$$\Delta x = 0.2 \text{ m}$$

$$\Delta y = 0.25 \cdot 10^{-3} \text{ m}$$

$$U_c = 0.8 U_{\infty}$$

$$B: \frac{U_c \Gamma_l}{\Delta x} = 0.15$$

Figure 2.9 Pressure spectral densities measured under the laminar boundary layer on an axisymmetric body in the CEPRA 19 wind tunnel and comparison with computational model results [from Perraud 1989].

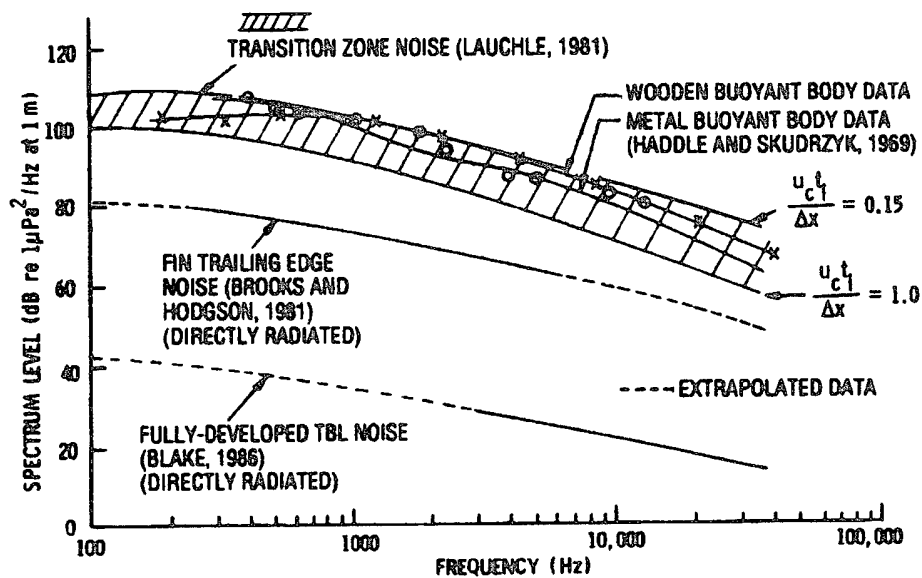


Figure 2.10 Measured and predicted radiated noise spectra for the Haddle and Skudrzyk (1969) buoyant bodies operating at 15.44 m/s [from Lauchle and Brungart, 1988].

CHAPTER 3

MODEL REFINEMENTS

A major objective of this research program is to continue to develop refinements to the radiated noise models for transition noise. These theoretical extensions proposed are necessary to complete the area of investigation of transition zone acoustics in a zero pressure gradient. As discussed previously, there are two major approaches which can be summarized in Figure 3.1. Lauchle began with a Lighthill acoustic analogy and moved to a Liepmann analogy while Sornette and Lagier pursued a more rigorous Lighthill approach. These are indicated by the top and bottom boxes in the figure. The right hand box represents the use of the theoretical space-time correlation function whose form was estimated using phenomenological assumptions. Lauchle (1981), Lagier and Sornette (1986), and Audet, et al. (1989) used this form to make estimates of radiated noise spectra. Similarly, the left hand box represents the semi-empirical form developed by Josserand and Lauchle (1990). The dashed line between the two correlation functions indicates an attempt to derive the constants of the theoretical function from the empirical function. The lines and dates linking the models to the correlation function form boxes indicating when certain modifications were made to the models as they were carried toward validation with measured spectra. The following sections describe some of the further refinements and analysis that are being performed. In order to satisfy the input requirements for both models, it has been necessary to review previous fluid dynamic

experiments which have identified structures within turbulent spots and developed empirical descriptions for spot growth.

3.1 Fluctuating Boundary Layer Displacement Thickness Using a Liepmann Analogy - Theoretical Space-Time Correlation Function

For turbulent spot substructures, one can describe the resultant normal velocity distribution with two terms, using the substantial derivative:

$$v_n(\vec{x}, t) = \frac{D\delta^*}{Dt} \quad (3.1)$$

$$v_n(\vec{x}, t) = U_\infty \frac{\partial \delta^*}{\partial x} + \frac{\partial \delta^*}{\partial t}$$

The first component describes the growth of a spot in a fixed frame of reference. It should have strong statistical descriptors including spatial correlations. It has been found by Krane (1992) that the normal velocity, described by the first component, is directed toward the wall at the spot leading interface and outward over the rest of the spot which requires a higher normal velocity for the potential flow. A streamwise dependence was measured by Krane (1992). A spanwise dependence has not been measured. The adjacent inward and outward velocities produce a weak dipole at low Mach number. The second term is due to the growth of the spot from the creation of internal vorticity. An instantaneous vorticity field was measured by Sankaran et al. (1988, 1991). This is shown in Figures 3.2 and 3.3. The vortex axes are observed to be inclined to the plane wall. As sources of sound, these vortices are likely to be quadrupole in nature. It has been

argued by Sornette and Lagier (1984a) that weak monopoles are created due to: (1) entropy production via viscous dissipation, and (2) kinetic energy dissipation. Spatial growth may occur due to the streamwise increase in the number of vortical substructures. However, when Equation (3.1) is handled with retarded time variables, spatial derivatives become time derivatives according to:

$$\frac{\partial}{\partial x} \Rightarrow -\frac{1}{c} \frac{\partial}{\partial t} \quad (3.2)$$

Then, it reduces to:

$$\begin{aligned} v_n(\vec{x}, t) &= -\frac{U_\infty}{c} \frac{\partial \delta^*}{\partial t} + \frac{\partial \delta^*}{\partial t} \\ &= (1 - M_\infty) \frac{\partial \delta^*}{\partial t} \\ &\approx \frac{\partial \delta^*}{\partial t} \quad \text{for } M_\infty \ll 1 \end{aligned} \quad (3.3)$$

So we really want to concentrate on those sources which describe the temporal fluctuations of the displacement thickness, which are obviously due to the creation and interactions of substructure vortices.

3.1.1 Computational Model Refinements

Several refinements have been performed for the computer program GLPROG81 which implements Equation (2.13). These are described in the rest of this section.

Similar refinements were also made, where appropriate, to GLPROG80 which implements Equation (2.6) for the fluctuating shear stress model.. Examples of all of these Mathcad files are provided in Appendix A.

3.1.1.1 Conversion of Software Environment

The entire program was converted from FORTRAN with its many specific software package mathematical and graphical function calls to the Mathcad 2000 Professional ® (Mathsoft, Inc.) software package. This has several advantages. First, it is a Microsoft Windows supported personal computer product rather than written for use on a Digital Vaxstation computer. Second, the math is presented in true mathematical symbolic form rather than a FORTRAN breakdown into variable names and code lines. This makes the presentation much easier to follow and understand.

3.1.1.2 Intermittency Function Models

Josserand derived a new intermittency factor from his experimental data:

$$\gamma(\eta_x) = 1 - e^{-(1+3.4Z)Z^2} \quad \text{where} \quad Z = \frac{\eta_x}{\Delta x} \quad (3.4)$$

instead of

$$\gamma(\eta_x) = 1 - e^{-4.185Z^2} \quad (3.5)$$

which was developed by Farabee, et al. (1974). The first function follows from a

formulation developed by Gedney (1979) (and Gedney and Leehey, 1989) for a combined Dirac line source and constant source hypothesis. The comparison of these two relations is shown in Figure 3.4. The Farabee relation is seen to have its highest slope earlier in the transition zone. This carries through to modest increases in the predicted amplitudes as well. The Josserand model predicts intermittencies that agree with experimental data better than the Farabee model..

3.1.1.3 Burst Frequency Models

A new spot burst frequency description was also derived by Josserand (1986) based on the Gedney (1979) hypothesis mentioned in Section 3.1.1.2:

$$N(Z_x) = 2.38 \left(\frac{u_o}{\Delta x} \right) \sqrt{[1 - \gamma(Z_x)] \ln \left[\frac{1}{1 - \gamma(Z_x)} \right]} \quad (3.6)$$

instead of

$$N(Z_x) = 1.272 \left(\frac{u_o}{\Delta x} \right) Z_x e^{-4.185(Z_x)^2} \quad (3.7)$$

due to Farabee, et al. (1974). Josserand modified the constant in Equation (3.6) to yield a better match with his experimental data. Note that Equation (3.6) can be evaluated with the intermittency function described by either Equation (3.4) or (3.5). A comparison of these three formulations is shown as a normalized burst rate, $B(Z)$ (where $N(Z_x)$ is multiplied by $u_o/\Delta x$), in Figure 3.5. It can be seen that the magnitudes of the peak burst

rate for the Josserand function variants are about 4 time larger than that for the Farabee model. The non-zero values of $B(Z)$ predicted by Equation (3.6) beyond the end of the transition zone seem physically unrealistic.

Of course, our real interest is in how the use of these different relations will affect the calculation of the radiated noise. The results of these combinations of substitutions of intermittency and burst rate are shown for one case in Figure 3.6. The measured data come from a pressure sensor flush mounted in the laminar flow region on a body of revolution in the CEPRA 19 wind tunnel (Perraud 1989). The parameters for that test affecting the computational model inputs for GLPROG81 are listed in the caption. The normalized rise time of 0.15 was suggested by Perraud. This new spot burst frequency description results in a 6 to 8 dB increase in predicted radiated noise over much of the frequency range of interest. The impact of a change of the intermittency model is negligible compared to that of the burst rate. The Farabee form (Equation 3.7) of the burst frequency function results in a slightly lower peak frequency as well and a larger sound pressure magnitude below 50 Hz.

However, because Josserand (1986) reported a variance of 20% on his calculated burst rate, which makes his empirical fit somewhat questionable, it seems likely that a portion of the predicted high levels of sound are due to this over-prediction of the burst rate.

3.1.1.4 Application of Strip Analysis

Multiplication of the result of Equation (2.13) by the transverse width of the

transition zone, W , yields the total radiated spectral pressure from the transition zone.

This assumes limited spanwise spot interaction which leads to homogeneity.

3.1.2 Incorporation of Measured Normal Velocity Fluctuations

Lauchle's assumed monopole description of the normal velocity in GLPROG81 has a provision for substitution of the normal velocity resulting from the water channel measurements of Krane (1992). He measured the normal velocity using a mass flux deficit to describe the displacement thickness (Figure 3.7). The velocity profile measurement technique was developed by Bruneau and Pauley (1992, 1995). This technique tends to average out the time dependent fluctuations of $\partial\delta^*$, but it does reveal a negative mass flow deficit combined with the previously assumed (by Lauchle, 1981) positive one. Krane identified the streamwise dependence with a weak dipole which results from the negative normal velocity near the leading edge (overhang) of the turbulent spot and a positive velocity associated with the passing of the rest of the spot. The multipole source distribution proposed by Krane is shown in Figure 3.8.

Krane and Pauley (1993) also found that the interaction of two turbulent spots had a minimal effect on the mass flux deficit (displacement thickness) and, therefore, the normal velocity descriptor. This would imply that their normal velocity model should apply to even a natural transition case. For both the single and the interacting spots, a dependence on Z_x was measured. A function was fit to this data,

$$TK(Z_x) = 0.30 - \exp[-1.45 - 3(Z_x)^2] \quad . \quad (3.8)$$

This function is shown compared to Krane's measurements in Figure 3.9.

The dipole source shown in Krane (1992, Figure 5.1) was used to replace the monopole source in GLPROG81. The proposed quadrupole sources were not included because of their reduced radiation efficiency compared to the dipole and they do not appear prominent for all velocities shown by Krane. However, the amplitude of the normal velocity appears to be equal for the positive and negative events and was assumed to be the same as the positive event modeled by Lauchle. Therefore, the dipole was modeled (as shown in Pierce (1981, pp.170) as modifying the monopole pressure by the factor of $2 \sin[(k d \cos\theta)/2]$ where d is the separation distance of the two sources that make up the dipole and the observation distance, $r \gg d$. This can be further simplified for $kd \ll 1$, to $k d \cos\theta$. This would be appropriate for the low frequencies for which transition noise seems important. The limitation in using this in the model is that it would result in an amplitude independent of frequency at higher frequencies.

The separation distance can be modeled as $2 u_c t_i$ which is then equivalent to $d(Z) = 2 \Delta x TK(Z) \approx d = 0.4 \Delta x$. So GLPROG81 could be modified by multiplying the previous result by $4 \sin^2[(0.2 k \Delta x \cos\theta)]$. However, if the separation distance between the two dipole sources is taken to be a random variable, then the mean value of the pressure spectrum is given by

$$G(f) = \overline{f(d)} G_{monopole} = E[f(d')] G_{monopole} \quad (3.9)$$

where $G_{monopole}$ is given by Equation 2.13 with the assumption of spanwise homogeneity.

$$G(r,\omega) = \frac{W\rho^2 (\Delta\delta^*)^2 u_o u_c^2}{8 \pi^2 r^2} F^*(k_c\Delta x, \alpha^*\Delta x, \frac{u_c t_i}{\Delta x}, \frac{u_c}{u_o}) \quad (3.10)$$

The expected value is calculated for the following dipole source multiplier

$$f(d') = 4 \sin^2(\frac{1}{2}k d' \cos\theta) \quad (3.11)$$

This expected value is determined with the assumption of a uniform probability distribution of d' and limits of $0.1\Delta x < d' < 0.2\Delta x$.

$$E[f(d')] = \int p(d') f(d') dd' = \frac{1}{0.1\Delta x} \int f(d') dd' \quad (3.12)$$

This then becomes

$$E[f(d')] = 2 + \left[\frac{2 \sin(0.1 k \Delta x \cos\theta)}{0.1 k \Delta x \cos\theta} \right] [1 - 2 \cos(0.1 k \Delta x \cos\theta)] \quad (3.13)$$

3.2 Fluctuating Boundary Layer Displacement Thickness Using a Liepmann Analogy - Empirical Space-Time Correlation Function

3.2.1 Integration of Josserand-Lauchle Correlation Function

As discussed previously, the substitution of the semi-empirical space-time correlation function developed by Josserand (1986) into Equation (2.12) was coded for integration. The function, from Josserand and Lauchle (1990), is repeated here:

$$R_f(\eta_x, \xi_x, \xi_z, \tau) = \gamma_u \gamma_d + \gamma_u (1 - \gamma_d) \exp \left\{ -5 \left(4 + 200 \left| \tau - \frac{\xi_x}{u_c} \right| \right) \left| \tau - \frac{\xi_x}{u_c} \right| \right\} \cdot \exp \left(\frac{20 |\Lambda_x|}{0.014 + |\Lambda_x|} \left| \tau - \frac{\xi_x}{u_c} \right| \right) \\ \cdot \exp \left(- \left| 15.75 \Delta x - \frac{1260 \left| \tau - \frac{\xi_x}{u_c} \right|}{1 + 71 |\Lambda_z|} \right| \frac{|\Lambda_z|}{1 + 14.2 |\Lambda_x|} \right) \cdot \exp \left[- \frac{A |\Lambda_x|}{0.0014 + |\Lambda_x|} \frac{1}{1 + 1300 \left| \tau - \frac{\xi_x}{u_c} \right|^2} \right] \quad (3.14)$$

where $A = -\ln[1 - \exp(-4.27/\Delta x)]$, (units of Δx are in meters),

$$\Lambda_i = \xi_i / \Delta x \quad ,$$

$\gamma_u = \gamma(\eta_x)$ and $\gamma_d = \gamma(\eta_x + \xi_x)$ when the reference location is upstream of the second location,

$\gamma_u = \gamma(\eta_x + \xi_x)$ and $\gamma_d = \gamma(\eta_x)$ when the reference location is downstream of the second location.

Integration of this function has proven difficult for the Mathcad package. The built-in integration was bypassed with a trapezoidal integration. The use of a high number of integration points smooths this to a large degree. Several approaches have been tried to ease computational burden. One is to set physically reasonable limits of integration. This resulted in limits for ξ_x from $-\eta_x$ to $1 - \eta_x$ and ξ_z from $-1.5 \eta_x \tan \alpha$ to $1.5 \eta_x \tan \alpha$. In an attempt to get better use of the computational dynamic range, the mean was removed from the cross-correlation as indicated in equation (3.15) and the last term of the following equation was ignored.

$$S_{xy}(\omega) = \int R_{xy}(\tau) e^{-i\omega\tau} d\tau = \int [R_{xy}(\tau) - \mu_x \mu_y] e^{-i\omega\tau} d\tau + \mu_x \mu_y \delta(\omega) \quad (3.15)$$

Because of the difficulty in integrating the Josserand (1986) form of the space-time correlation function, an effort was made to look for simplification of the function to make integration easier. However, it does not appear that this function has a form that is direction separable for x and z.

3.2.2 Chase Statistical Modification

Chase (1989) has suggested that the first exponent term in Equation (3.14) can be replaced by a more general term based on the probability of state transition to turbulence of form:

$$\exp \left\{ - \frac{N_d}{\gamma_d (1-\gamma_d)} \left| \tau - \frac{\xi_x}{u_c} \right| \right\} . \quad (3.16)$$

However, Josserand found that both terms predict the measured correlation values well for $0.3 \leq \gamma \leq 0.7$; but, that outside of these limits, the Chase theoretical term tended to over-predict the correlation. Both terms are available as options in the computational software. Limit evaluation has determined that the Chase modification to the Josserand-Lauchle correlation function does not improve the results in comparison to measured data for natural transition. A comparison of the Josserand and the Chase modified correlation surfaces over the transition zone is shown in Figure 3.10. The differences are subtle with the Chase term having deeper troughs in the amplitude surface.

3.3 Two Fluids Model with Refined Normal Velocity

In tying together all the approaches, the Audet and Sornette-Lagier approaches did not provide any advances because of simplifying assumptions to allow integration and heavy dependence on Lauchle's (1981) functions. The refined normal velocity description could be substituted into the two fluids model but it would not provide an advantage over the refined fluctuating displacement thickness model. Knowledge gained of the radiated noise component magnitude can be used to further refine the two-fluids model of Audet, et al. (1989b) for wall pressure fluctuations as input to the fluid-structure interaction problems of interest.

Their predictions used simplifying assumptions for their more general equation. The retarded time in the equation does not take into account the separation distance in the 2 point correlation. It accounts only for the reference point. Global stationarity is assumed. No spot interaction is assumed. All values are taken for $\eta_z=0$. Spatial dependence is separated from temporal dependence.

The good comparison of the Lauchle (1981) model with CEPRA wind tunnel data when using normalized rise times of 0.05 to 0.15 must be viewed with reserve since the authors indicated that some data were contaminated by corner vortex growth overlapping the sensor locations.

3.4 Accounting for Vortical Motions

Another objective of this study is to investigate the feasibility of incorporation of effects due to vorticity into either of Lauchle's models. This will mainly draw upon the

prior work of Powell (1995), Hardin (1991), Lund (1989), and the many papers of Kambe and Obermeier. Williams, Fasel, and Hama (1984) also made a great experimental contribution with their mapping of the three-dimensional vorticity field in boundary layer transition. It is anticipated that this would form a second source term in the fluctuating displacement thickness model in a manner similar to the S and S_0 functions of Lagier and Sornette (1986). Lagier and Sornette concluded that the contribution of a shear interface at the edge of a turbulent spot (due in large measure to the presence of these vortices) was insignificant compared to the overall growth of the spot.

Sankaran, Sokolov, and Antonia. (1988) and Sankaran, Antonia, Bisset, and Sokolov (1991) used instantaneous velocity field measurements to identify a superposition of vortex sources within a turbulent spot. The existence of vorticity formations may help explain the $U_\infty^{7.5}$ noise dependence by looking at the sources as primarily quadrupoles with some monopole like bursting. The measurements indicate that the spatial growth of the spot is directly related to a streamwise increase in the number of substructures. Substructures are generally created near the trailing edge of a spot, and all convect at the same velocity $0.8 U_\infty$. This means that the cumulative contribution from these substructures will be greatest near the midpoint of the transition zone because the number of spots is greatest there. Would incorporation of a distribution of these vortices help account for the highly spatially dependent normal velocity component due to $\partial\delta^*/\partial t$? Many would argue that the hydrodynamic fluctuations due to these substructures is statistically the same as what would be found with a fully turbulent

boundary layer however, the spatial and temporal extent is limited by the axial dependence of intermittency and the burst rate. Hence, the vortical contribution is captured in the use of TBL statistics in models such as Howe's. Therefore, no additional changes are made to any of the models since they either utilize the modified TBL statistics or not.

3.5 Incorporation of Green's Function for Transition Zone Near Half-Plane Leading Edge

Howe's model as described in section 2.6.1 has been implemented in a Mathcad worksheet, MSHTRANS99, that is provided in Appendix A.4.

The trick on the integration of Equation (2.25) is to apply a window function that varies with frequency. A longer window is required for low frequencies and a short window is required for high frequencies. Also, to avoid aliasing, a much higher sampling rate is necessary for high frequencies than for the low frequencies. Trapezoidal integration is also used rather than the Mathcad built-in function.

Howe's original formulation uses the intermittency function shown in Equation (3.5). An alternative Mathcad worksheet uses the Josserand intermittency function (Equation 3.4). The impact is about a 4 dB decrease in the radiated pressure levels with the Josserand intermittency function.

An alternative use of the formulation provided by Howe would be to substitute the pressure spectrum for the wall pressures as determined by Josserand (1986) rather than intermittency modified Chase (1980) description of TBL wall pressures for the section of

the finite thickness half-plane (hydrofoil) surface S covering the transition zone. This has not yet been pursued.

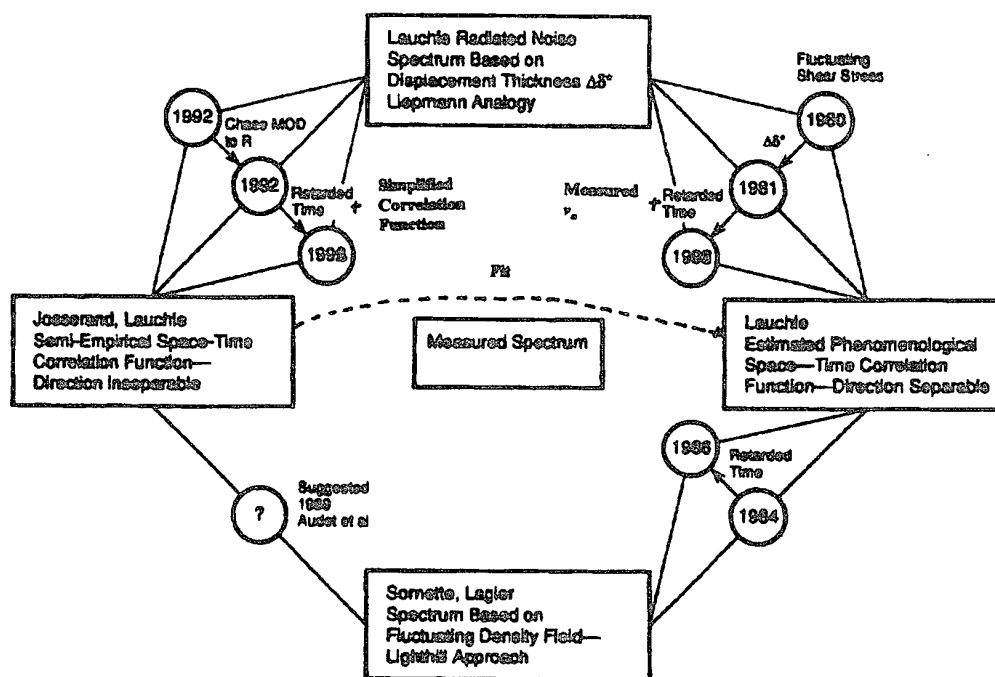


Figure 3.1 Theoretical model refinements for directly radiated noise from a transitioning boundary layer.

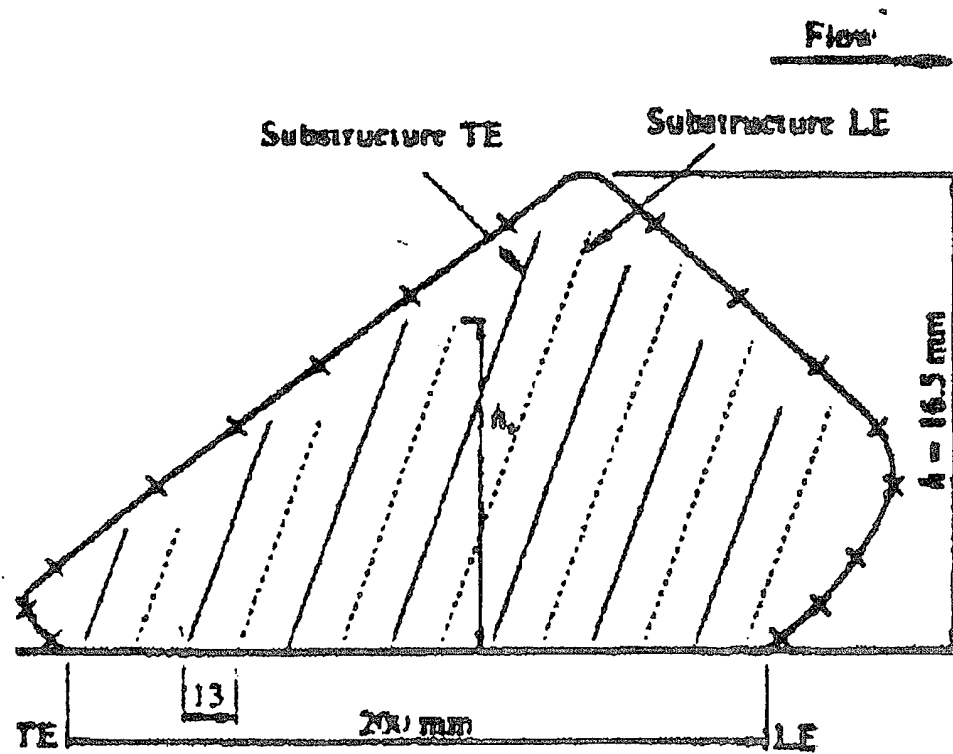


Figure 3.2 Turbulent spot with substructure vortices [from Sankaran et al.1988].

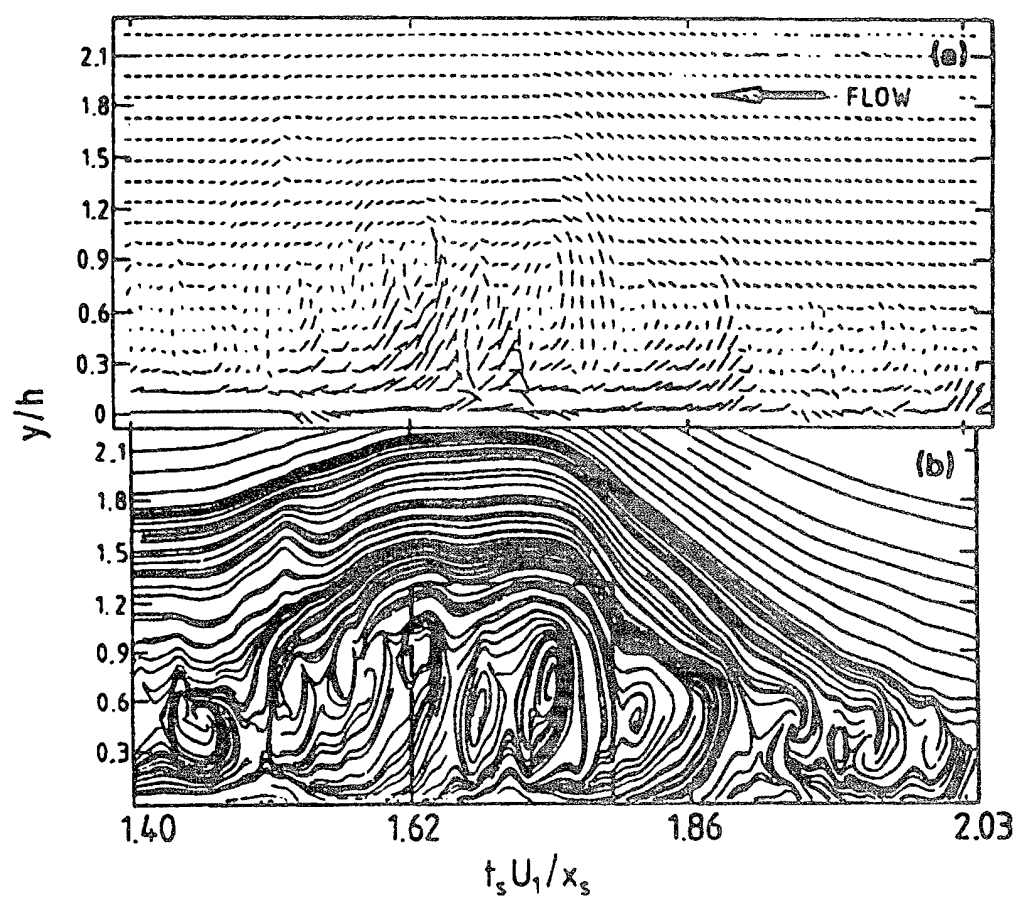
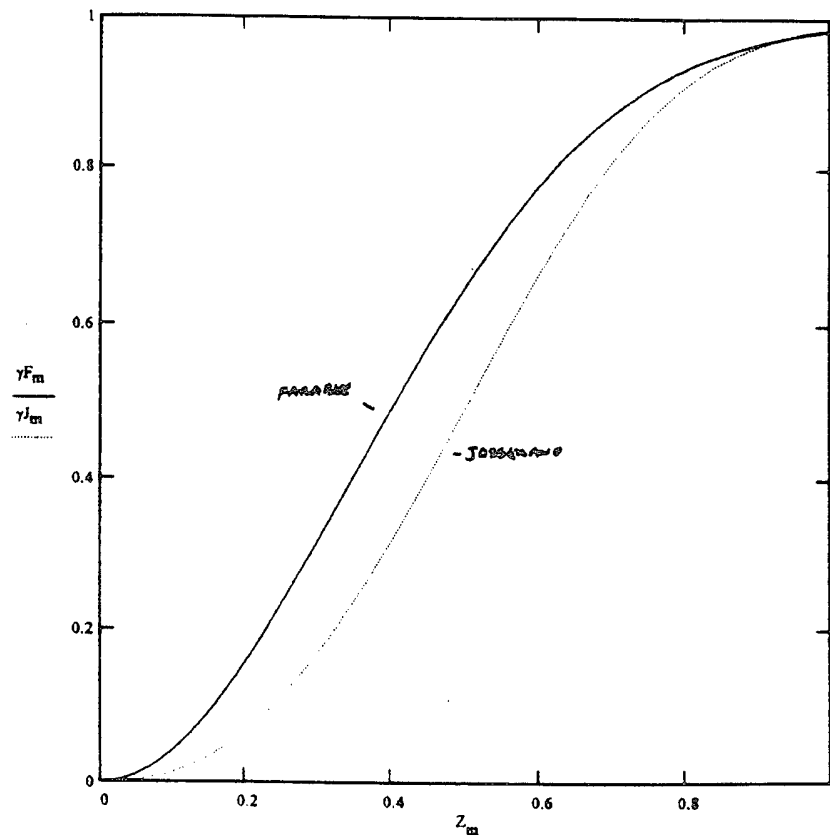


Figure 3.3 Instantaneous velocity vectors and sectional streamlines [from Sankaran et al. 1991].



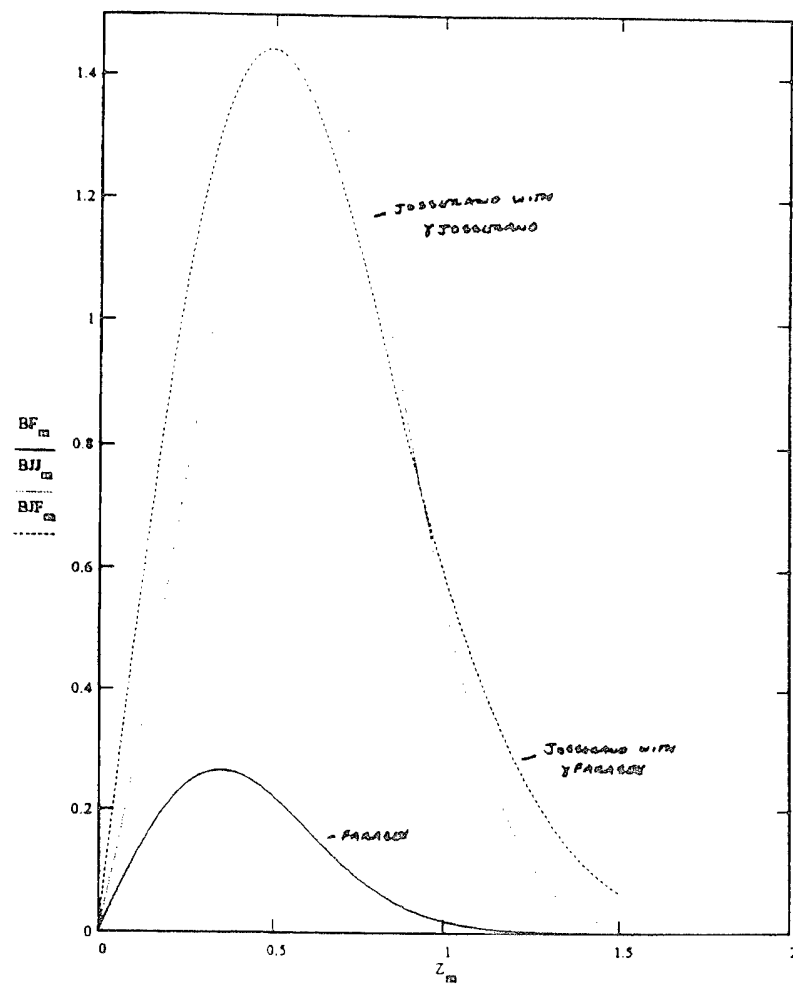
$$\gamma_{\text{Farabee}}(Z) := 1 - \exp(-4.185 \cdot Z^2)$$

Empirical relations from Farabee, et al. (1974).

$$\gamma_{\text{JL}}(Z) := 1 - \exp[-(1 + 3.4 \cdot Z) \cdot Z^2]$$

Empirical relations from Josserand and Lauchle (1986) which was based on the work of Gedney (1979) assessing both a Dirac line source hypothesis and a constant source hypothesis for intermittency.

Figure 3.4 Comparison of empirically derived intermittency functions.



$$BFarabee(Z) := 1.272 \cdot Z \cdot \exp(-4.185 \cdot Z^2)$$

$$BJJ(Z) := 2.38 \cdot \sqrt{\left[(1 - \gamma J_L(Z)) \cdot \ln \left[\frac{1}{(1 - \gamma J_L(Z))} \right] \right]}$$

$$BJF(Z) := 2.38 \cdot \sqrt{\left[(1 - \gamma Farabee(Z)) \cdot \ln \left[\frac{1}{(1 - \gamma Farabee(Z))} \right] \right]}$$

Figure 3.5 Comparison of empirically derived normalized burst rate functions.

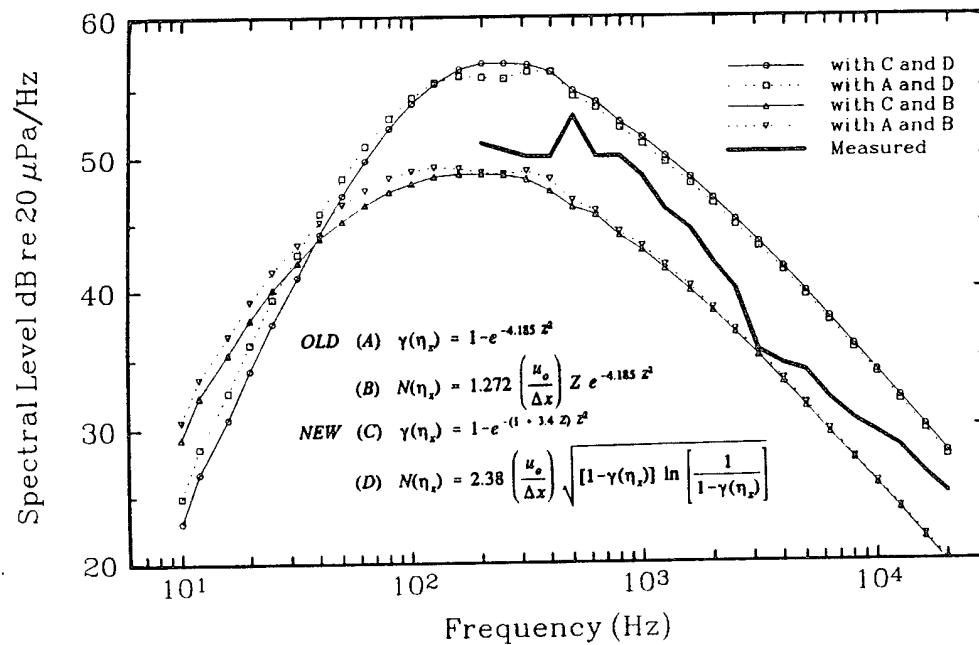


Figure 3.6 Effect of substitution of refined empirically derived equations for the intermittency function, $\gamma(\eta_x)$, and turbulent spot burst frequency, $N(\eta_x)$, for CEPRA 19 axisymmetric body in air, $U_\infty=50$ m/s, $u_{ct}/\Delta x=0.15$, $\Delta\delta^*=0.25$ mm and $\Delta x=0.2$ m (data from Perraud 1989)..

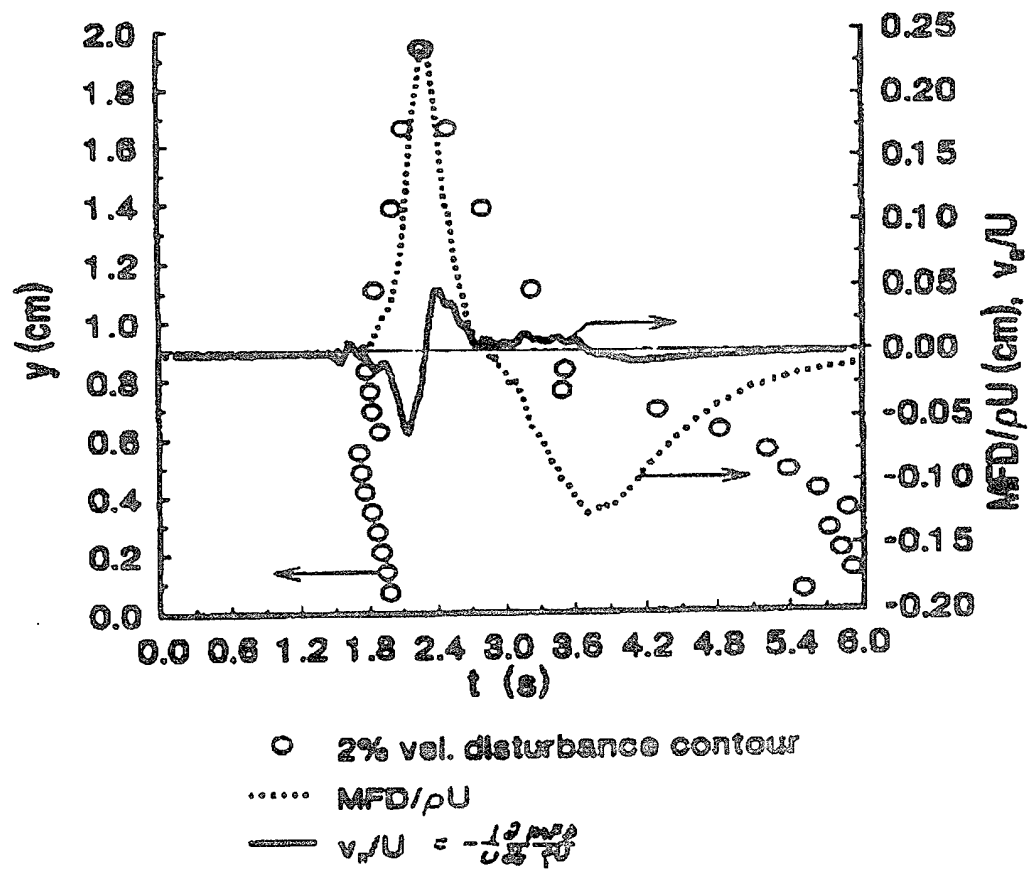


Figure 3.7 Mass flux deficit and derived normal velocity fluctuations at $x=1.13\text{m}$, $z=0$, and $U_\infty=40.6\text{ cm/s}$ in water with spot edge denoted by 2% velocity disturbance contour [from Krane 1992].

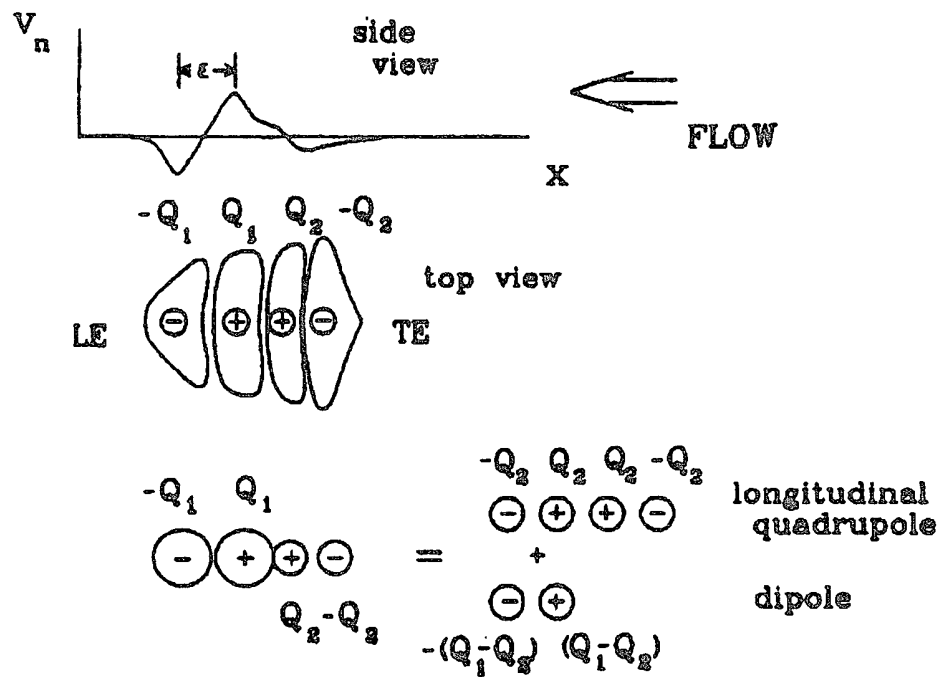


Figure 3.8 Proposed multipole source distribution for the measured normal velocity distribution above a passing turbulent spot, $v_n(\eta_x)$ [from Krane 1992].

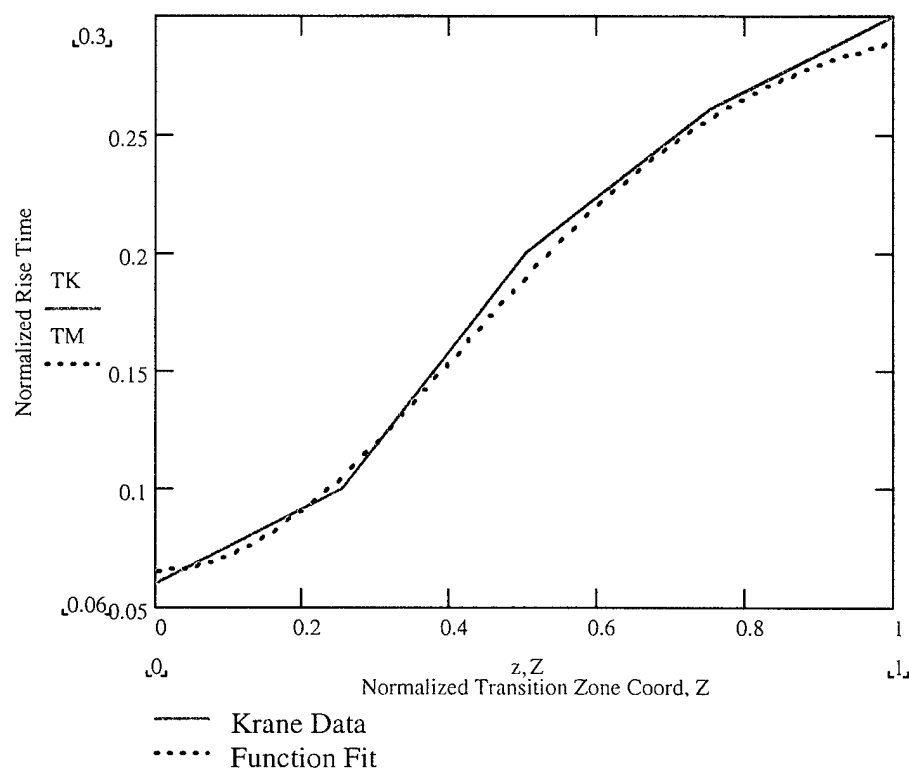
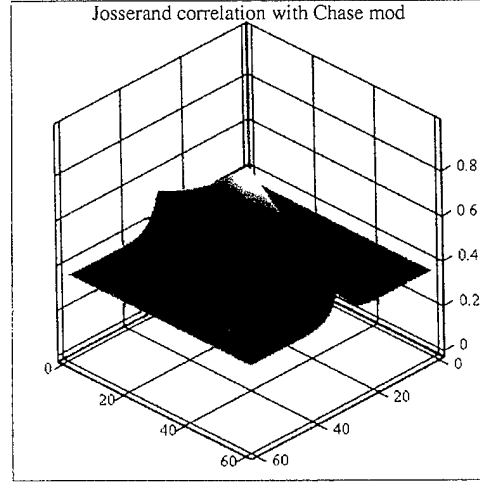
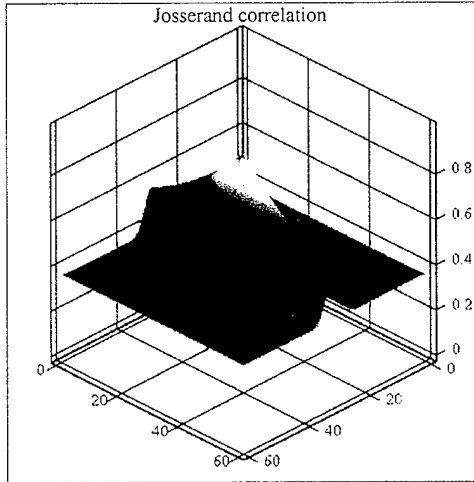


Figure 3.9 Comparison of Krane (1992) measured non-dimensional rise time, $u_c t_i / \Delta x$, and function $TK(Z_x)$ fit to the data.

Variation with τ and ξ_z with $\xi_x=1.0$.



Variation with ξ_x and ξ_z with $\tau=0$.

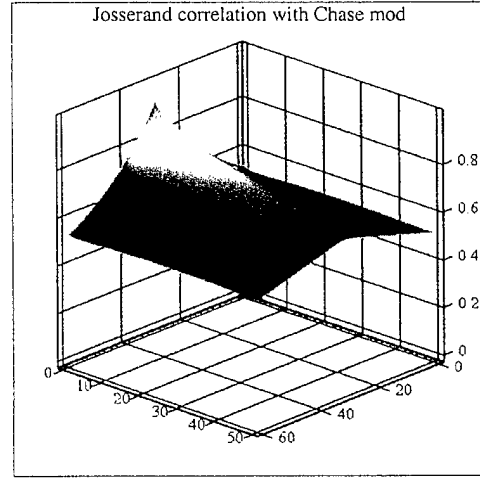
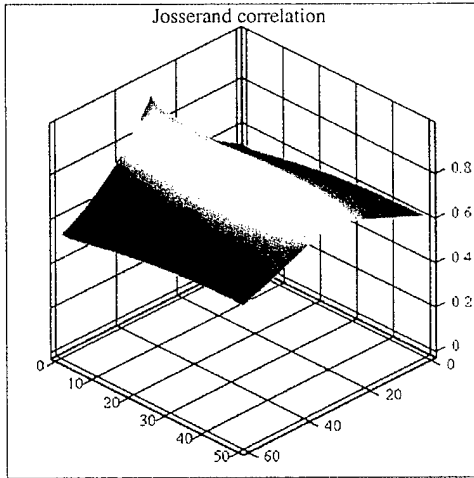


Figure 3.10 Comparison of correlation surface, $R_l(\eta_x, \xi_x, 0, t)$, for empirical space-time correlation function for original Josserand form and Chasefirst exponential term statistical modification for $U=11.8$ m/s, $\Delta x=1.83$ m, with $\eta_x/\Delta x=0.50$.

CHAPTER 4

RADIATED SOUND POWER PREDICTIONS

4.1 Model Comparisons

The three transition noise models based on Lauchle's theoretical space-time correlation function were each exercised to predict far field radiated noise from natural transition a flat plate with zero pressure gradient with seven velocities for air flows and seven velocities for water flows in appropriate ranges. The model which required the integration of the Josserand empirical space-time correlation function was run for selected conditions for comparison to the other models. The higher frequency results for that model are not considered to be appropriate yet. The Mathcad worksheets for these models are all provided in Appendix A:

GLPROG80.MCD (implementing Equation 2.6, Appendix A.1),

(G. Lauchle PROGram 1980)

GLPROG81.MCD (implementing Equation 2.13, Appendix A.2),

(G. Lauchle PROGram 1981)

KMTRANS00.MCD (implementing section 3.1.2, Appendix A.3),

(Krane, Marboe TRAnsition NoiSe 2000)

JLTRANS99.MCD (implementing Equations 2.12 with 2.15, Appendix A.4), and

(Josserand, Lauchle TRAnsition NoiSe 1999)

MSHTRANS99.MCD (implementing Equation 2.24, Appendix A.5)

(M. S. Howe TRAnsition NoiSe 1999).

The models have been run using either or both of the Farabee (Equations 3.5 and 3.7) or the Josserand (Equations 3.4 and 3.6) intermittency and spot burst frequency functions.

The common constants for all runs in air and water respectively are provided in Table 4.1. The necessary model inputs which are freestream velocity dependent were calculated using TRANSITION AIR.MCD (Appendix A.6) and TRANSITION WATER.MCD (Appendix A.7). These are listed in Table 4.2.

Table 4.1 Common Constants for Model Exercising

Variable	Air	Dimension	Fresh Water
Uc/Uo	0.7		0.7
W	0.305	m	0.305
r	1	m	1
ρ	1.2	kg/m ³	999
co	343	m/s	1525
ν	1.51×10^{-5}	m ² /s	1.01×10^{-6}
θ	0	degree	0
Ret	1500000		1500000
Pref	20×10^{-6}	Pa	1×10^{-6}

Table 4.2 Calculated Model Inputs

Air			Fresh Water		
U _o	Δx	$\Delta \delta^*$	U _o	Δx	$\Delta \delta^*$
m/s	cm	cm	m/s	cm	cm
9	86.57	0.649	3	19.74	0.148
12	64.93	0.487	6	9.87	0.074
15	51.94	0.389	9	6.58	0.049
18	43.28	0.325	12	4.93	0.037
21	37.10	0.278	15	3.95	0.030
24	32.46	0.243	18	3.29	0.025
27	28.86	0.216	21	2.82	0.021

4.1.1 Comparisons of Models for Air Flows

Comparisons of radiated noise from the shear stress dipole, Liepmann analogy monopole, and dipole models over a range of freestream velocities from 9 to 27 m/sec are provided in Figures 4.1, 4.2, and 4.3 respectively. The model with the Josserand empirical correlation function was only run for 24 m/sec (Figure 4.4). The Howe model for enhancement of a natural transition near the leading edge of a half-plane was also run for the 24 m/sec case as a comparative case to demonstrate the effect in the change to the Green's function (Figure 4.5). All of the models are compared in Figure 4.6 for the 24 m/sec case.

It is apparent that the shear stress dipole predictions are much too low by 30 dB. The Josserand functions tend to raise the levels by 12 dB compared to the Farabee functions. The peak frequency in the spectra (around 100 Hz) increases with velocity as expected. The Krane dipole results in lower levels for frequencies below 100 Hz but 3 dB higher levels than the monopole model at higher frequencies. This is because of the assumption that the source amplitude (proportional to normal velocity) of each dipole

source is the same as for the monopole, compactness, and an assumed uniform distribution of dipole separation distances [$d = 2 u_c t = 2 \Delta x (u_c t / \Delta x)$]. This tends to smooth out the nulls associated with the sine function.

4.1.2 Comparisons of Models for Water Flows

Comparisons of radiated noise from the shear stress dipole, Liepmann analogy monopole, and dipole models over a range of freestream velocities from 9 to 27 m/sec are provided in Figures 4.7, 4.8, and 4.9 respectively. The model with the Josserand empirical correlation function was only run for 24 m/sec (Figure 4.10). The Howe model for enhancement of a natural transition near the leading edge of a half-plane was also run for the 24 m/sec case as a comparative case to demonstrate the effect in the change to the Green's function (Figure 4.11). All of the models are compared in Figure 4.12 for the 24 m/sec case.

The comparative results are similar to those seen in for the airflow cases but are 45 to 55 dB higher (after accounting for 26 dB difference in reference pressures) for the same freestream velocity.

4.2 Role of Rise Time, t_i

With a factor of $1/t_i^2$ in the amplitude coefficient of the power spectrum, the nondimensional rise time, $u_c t_i / \Delta x$, (where t_i is defined in Figure 1.5) has usually been an independent parameter whose value is chosen to get the model results to match the experimental data. It has taken on many values from 0.05 to the physically implausible

1.36. This parameter is difficult to measure and would seem to be quite dependent on the pressure gradient. However, it is useful to look at some values which have been extracted from various experimental investigations in order to make a reasonable first estimate for use in the computational code. A delta wing generated vortex as seen in Emmons spots produced by Littell and Eaton (1991) yielded a nondimensional rise time of 0.05. Use of data from Huang and Shen (1989) gave $u_c t / \Delta x = 0.187$. Other recent investigations on a flat plate showed a value of 0.30. As mentioned previously, Perraud (1989) found best agreement for $0.05 < u_c t / \Delta x < 0.15$. Audet et al. (1989) used a value of 1.36 which indicates normal velocity fluctuations continues even after the flow is fully turbulent. Lauchle (1981) found that 0.45 provided the best agreement with the Haddle and Skudrzyk (1969) data. It appears that a band of values for $u_c t / \Delta x$ around 0.20 will provide a reasonable first estimate. Data from the experiments performed by Krane (1992) in the fluid mechanics portion of the ONR project indicate that for an isolated turbulent spot the rise time is $0.06 < u_c t_{i, rise} / \Delta x < 0.30$ and non-dimensional fall time is $0.13 < u_c t_{i, fall} / \Delta x < 0.74$. Therefore, $u_c t / \Delta x = 0.20$, was used for each of the models for the comparison shown in Figure 4.13 for the airflow condition measured in the experiment described in Chapters 5 and 6.

4.3 Effects of Pressure Gradient

It has become evident that transition zone noise production is quite dependent upon the pressure gradient over the transition surface. Narasimha et al. (1984) and Mautner (1985) found that a positive pressure gradient results in wall pressure fluctuation

spectral shape and amplitude very close to those for a zero pressure gradient case. Mautner found that for an adverse pressure gradient that the nondimensional wall pressure power spectrum stayed constant to a nondimensional frequency of $f\delta^*/U_\infty=1$ rather than rolling off as $1/f^2$ after $f\delta^*/U_\infty=0.1$. Mautner concluded that this broader frequency forcing function would result in a greater wall pressure field coupling with both the structure and the acoustic field to produce more intense near and far field noise levels.

Huang and Shen (1989) found wall pressure levels 2 to 3 times higher for transition in adverse pressure gradients compared to TBL wall pressure levels. Mautner and Van Atta (1982) found rms wall pressures for individual turbulent spots to be 0.010-0.015 of dynamic pressure ($\frac{1}{2} \rho U_o^2$) for zero and favorable pressure gradients and 0.015-0.030 of dynamic pressure in adverse gradients. More importantly, in the adverse gradient, the wall pressure spectrum was nearly constant magnitude with increasing frequency rather than the typical decreasing slope. This is enhanced further if transition is induced by laminar boundary layer separation and re-attachment. In particular, Huang and Shen found that wall pressures in reattachment zones for laminar separation were 10 to 15 times higher.

The models all have a sensitivity to the length of the transition zone and the consequent decrease in the rise and fall time of the intermittency indicator function. Favorable pressure gradients demonstrate similar or slower transition than a zero pressure gradient. An adverse gradient will tend to accelerate transition and shorten the transition zone and spot growth. Transition in an adverse pressure gradient will result in higher

radiated and structural excitation levels in comparison to transition in a zero pressure gradient. It is also important to note that for adverse pressure gradients, it is very possible that some amount of flow separation and re-attachment is contributing to the radiated noise.

4.4 Effects of Scattering by a Plane Leading Edge

Howe's model shows the impact of the transition zone to be only at very low frequencies (below about 200 Hz). The quadrupole noise normally associated with the fully turbulent boundary dominates for higher frequencies in this model since it is not restricted to the transition zone alone. The effect of using the Josserand intermittency function is to decrease the radiated noise by about 4 dB (as shown in Appendix A.5). This is because the intermittency is used to multiply the point pressure spectrum and the Josserand levels are slightly lower for a given Z_x than the Farabee derived function. In the other models, it is the Josserand burst rate that accounts for the increased levels calculated when the Josserand functions are used.

4.5 General Assessment of Models

The general applicability of the models described or treated in this dissertation are assessed as follows:

Fluctuating Shear Stress Using a Lighthill Analogy (GLPROG80) - Predicted noise levels are much too low (35 dB below other models). Even the use of the Josserand intermittency and burst frequency functions only increases the results by 12 dB.

Fluctuating Displacement Thickness Using a Liepmann Analogy. Theoretical Space-Time Correlation Function (GLPROG81) - The premise for the model assumes the growth of a turbulent spot from a laminar displacement thickness height to a turbulent height over a convection time in the transition zone. Based on the highest measured burst rates of spots being between 25 % and 60% of the transition zone (Josserand 1986 and Farabee et al., 1974), predictions have appeared to be best using a normalized rise time, $u_{ct}/\Delta x$, of 0.5 to 1.0. Audet et al. claim a best fit with their measurements using normalized rise time of 1.35 which is physically implausible. This is because the monopole model of the sound source is not correct and a higher radiation efficiency is modeled than appropriate. Thus, slower growth times must be used to compensate. This is where the substitution of the dipole description of $v_n(t)$ yields a better model in that, at low frequencies, it is $kd \cos \theta$ lower than the levels calculated in GLPROG81. The lower efficiency dipole is necessary to allow the use of normalized rise times of 0.20 (or the variation from 0.15 to 0.30 over the transition region) for individual spots measured by Krane (1992) in an open water channel. This dipole is implemented in a variation of GLPROG81 called KMTRANS00. For $kd > 1$, the sound pressure level amplitudes predicted by GLPROG81 and KMTRANS00 are within a few dB of each other because of what appears to be two sources with constructive and destructive interference and a smearing due to the range of d for the dipole description of all the spots in the transition zone. The prediction by KMTRANS00 matched the measured spectral shape better for frequencies greater than 200 Hz. The uncertainty in the angle of the dipole axis also has a great effect on the amplitude of the prediction. The uncertainty in the measurement for

lower frequencies does not allow a meaningful comparison.

Fluctuating Displacement Thickness Using a Liepmann Analogy. Empirical Space-Time Correlation Function (JLTRANS89) - This produces prediction levels slightly higher in low frequencies than GLPROG81 but still does not compute well in Mathcad. While it might provide a better empirical basis for modeling, it does not appear to provide enough of an advantage over the simpler models for design.

Two-Fluids Model - Lagier and Sornette Formulation - This model has two source terms. The first is modification of TBL source levels by multiplication with the intermittency factor. In effect, this makes it a lesser source at higher frequencies than the nearby (and covering a much greater spatial extent) fully developed turbulent boundary layer. The second term is a radiated pressure from a monopole source based on a Lighthill analogy that is effectively the same as the fluctuating baffled piston-like source due to the Liepmann analogy used by Lauchle. Their formulation provides no real improvement over GLPROG81, and is computationally more complex.

Boundary Layer Transition on Symmetric Hydrofoils - Howe Formulation (MSHTRANS99) - This model highlights the effect of the scattering and diffraction from a nearby leading edge on the low-frequency, flow-induced noise spectrum due to the transition zone. No comparison can be made yet against wind tunnel or water tunnel measurements. The spectrum derived from Josserand's empirical space-time correlation function model (Lauchle and Park, 2000) could be substituted for the Chase spectrum model for the calculations covering the transition zone. The impact of this substitution is not known but is not expected to be large. The low frequency amplitudes may be low due

to only using the intermittency weighted Chase point pressure spectrum and not including the acoustic pressures measured in this study and in wall pressures in a transition zone in air measured by Dufourq (1984).

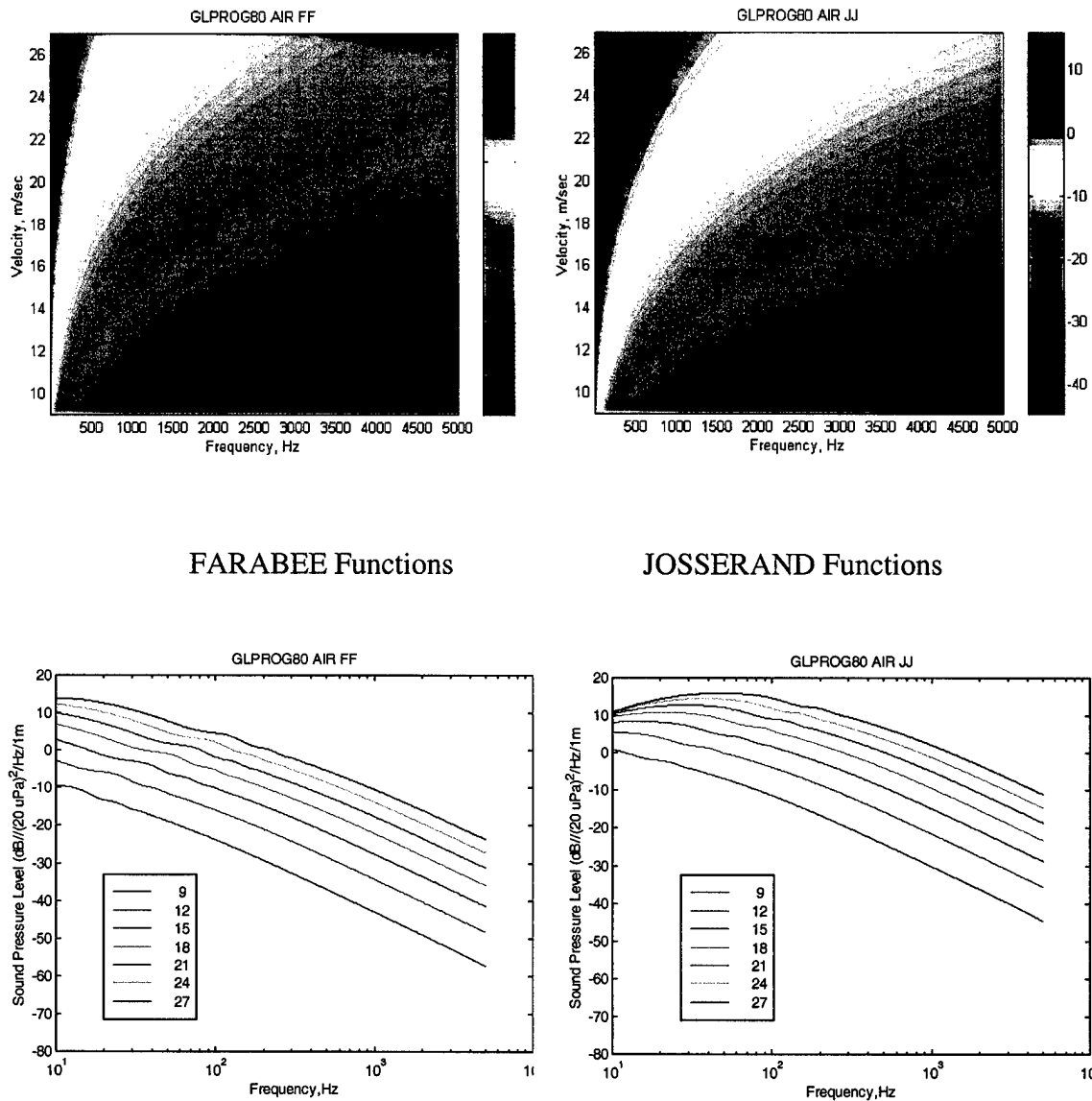
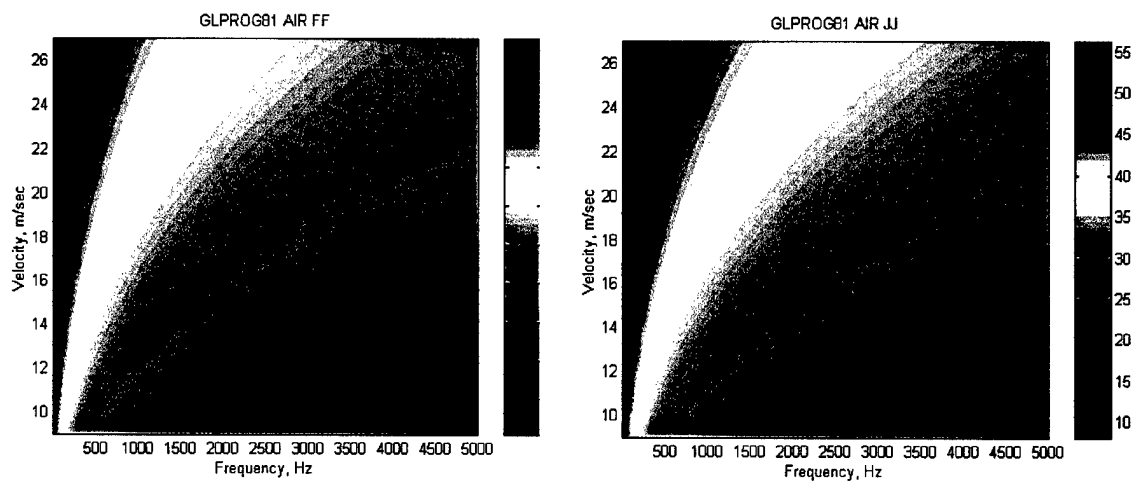


Figure 4.1 GLPROG80 predicted radiated pressure levels for a zero pressure gradient flat plate in air for $9 \text{ m/s} < U_{\infty} < 27 \text{ m/s}$.



FARABEE Functions

($u_c t_i / \Delta x = 0.15$)

JOSSERAND Functions

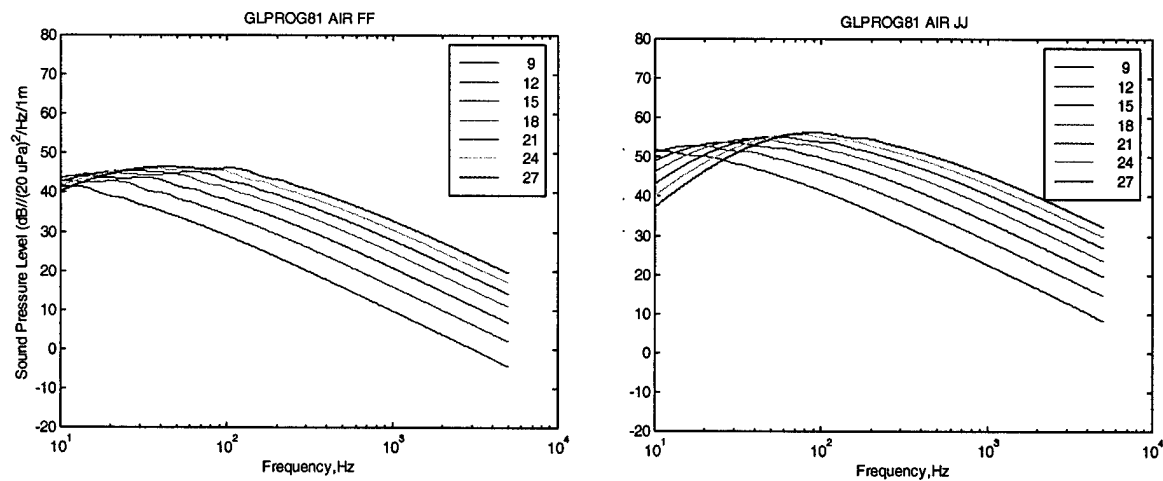
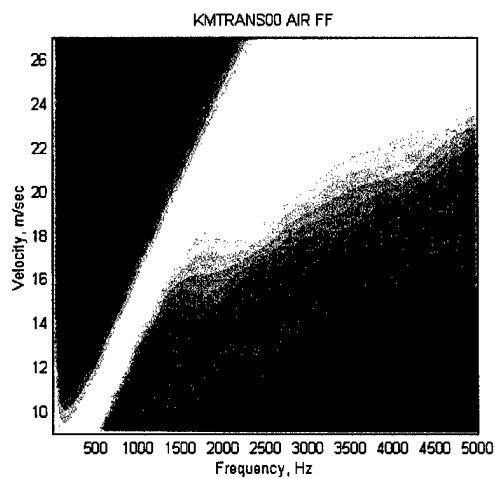
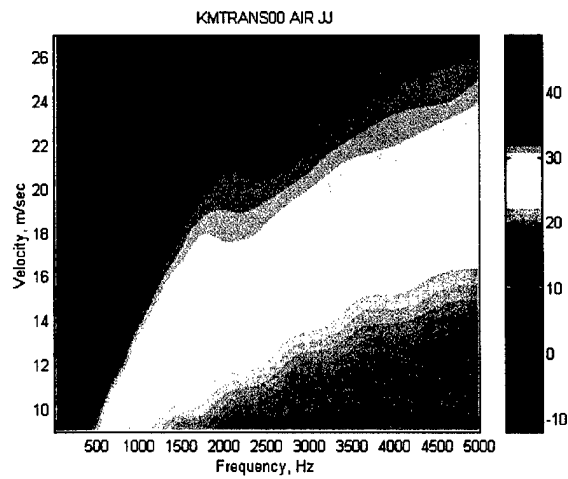


Figure 4.2 GLPROG81 predicted radiated pressure levels for a zero pressure gradient flat plate in air for $9 \text{ m/s} < U_\infty < 27 \text{ m/s}$.



FARABEE Functions



JOSSERAND Functions

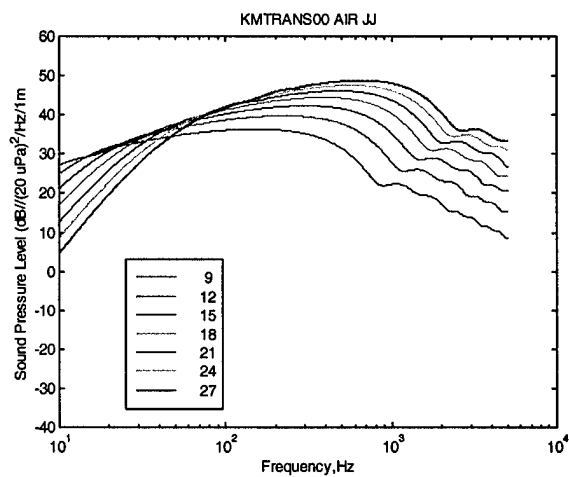
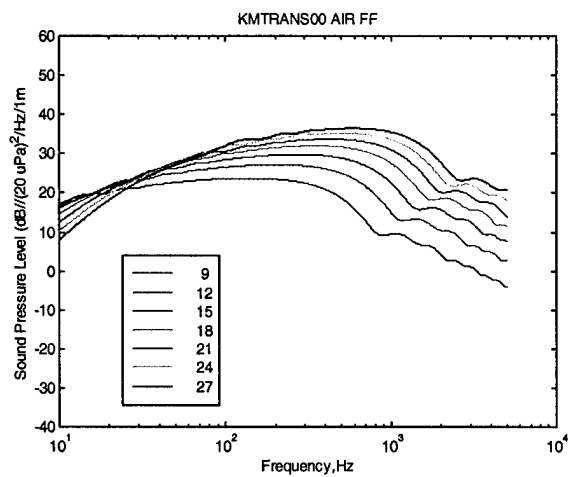


Figure 4.3 KMTRANS00 predicted radiated pressure levels for a zero pressure gradient flat plate in air for $9 \text{ m/s} < U_{\infty} < 27 \text{ m/s}$.

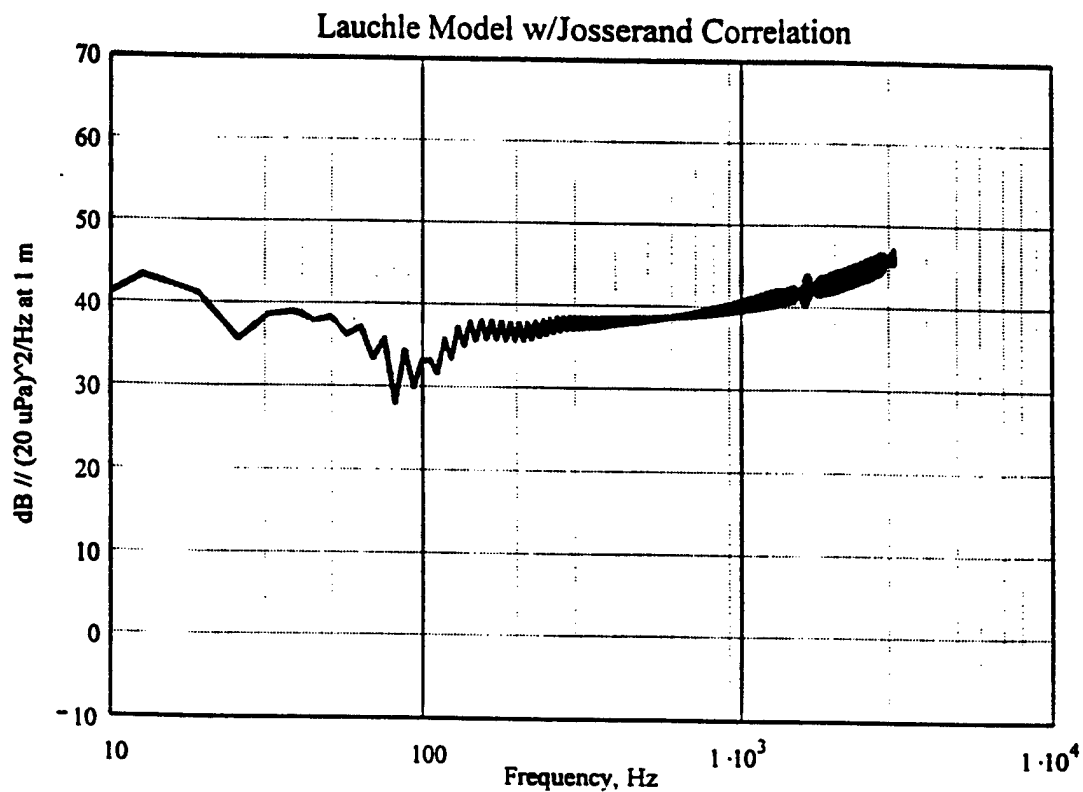


Figure 4.4 JLTRANS99 predicted radiated pressure levels for a zero pressure gradient flat plate in air for $U_{\infty} = 24$ m/sec.

Farabee Intermittency Function

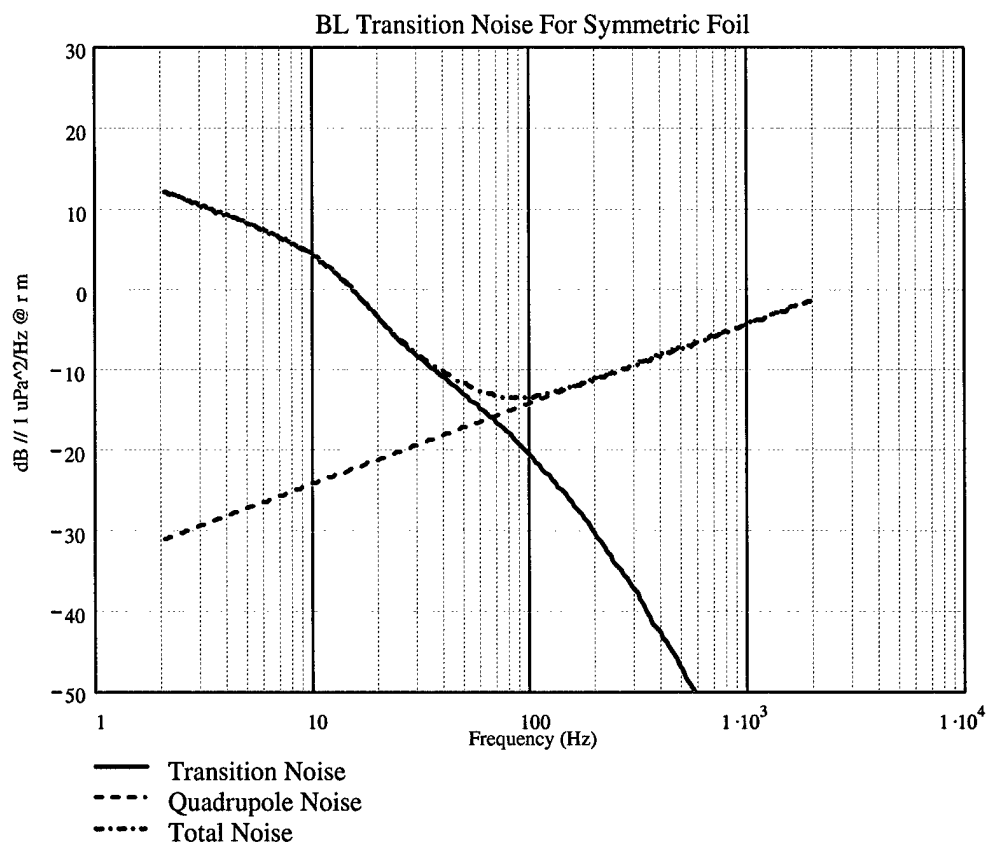


Figure 4.5 MSHTRANS99 predicted radiated pressure levels for a zero pressure gradient flat plate in air for $U_\infty = 24$ m/s.

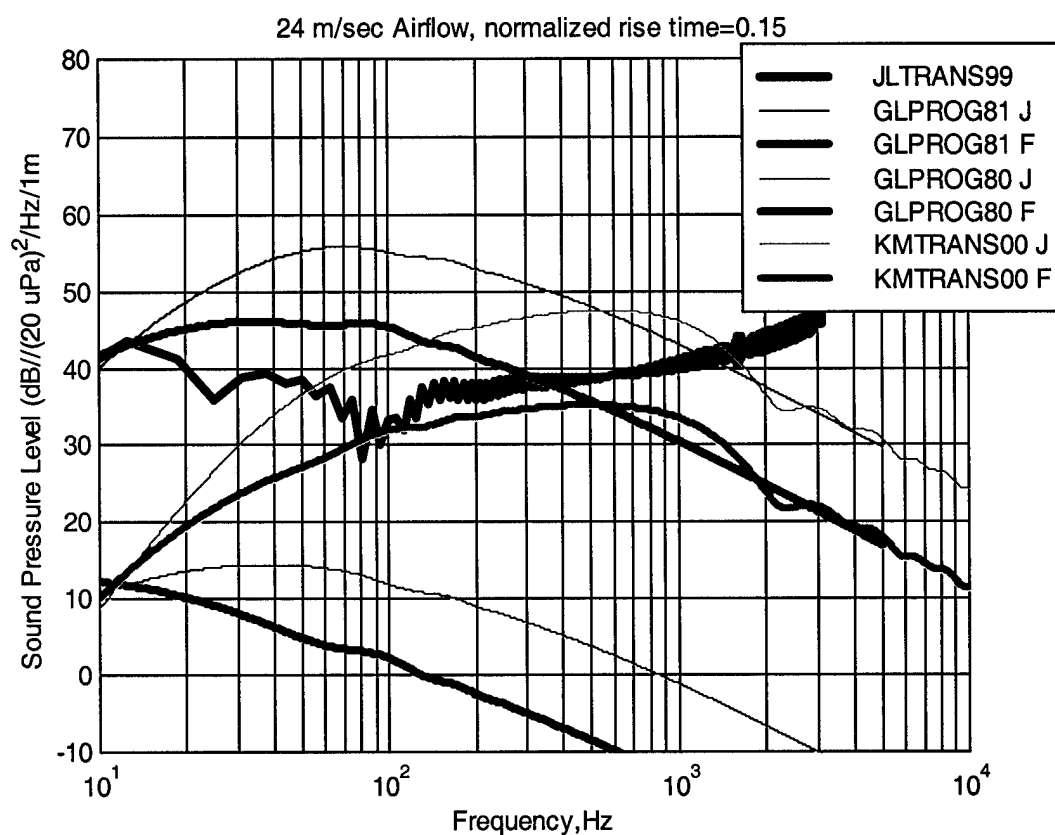
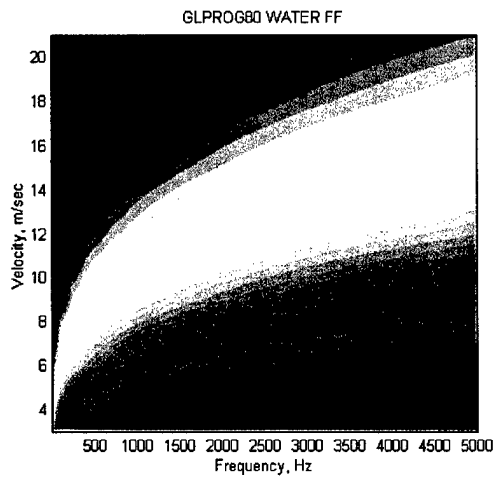
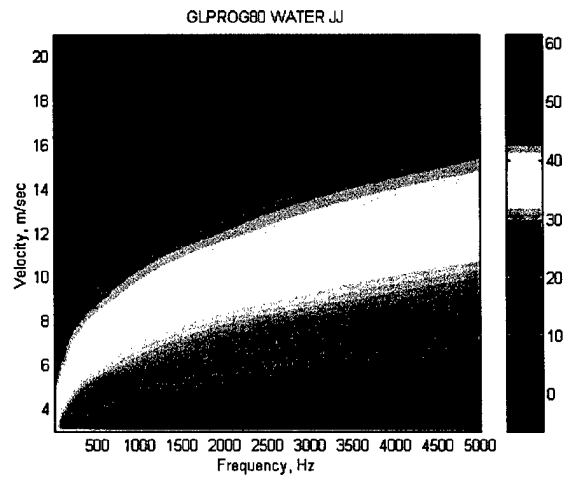


Figure 4.6 Comparison of models for radiated pressure levels for a zero pressure gradient flat plate in airflow, $U_\infty=24$ m/s, $\Delta\delta^*=0.243$ cm, $\Delta x=0.32$ m, $u_c/U_\infty=0.7$, $r=1.0$ m.



FARABEE Functions



JOSSERAND Functions

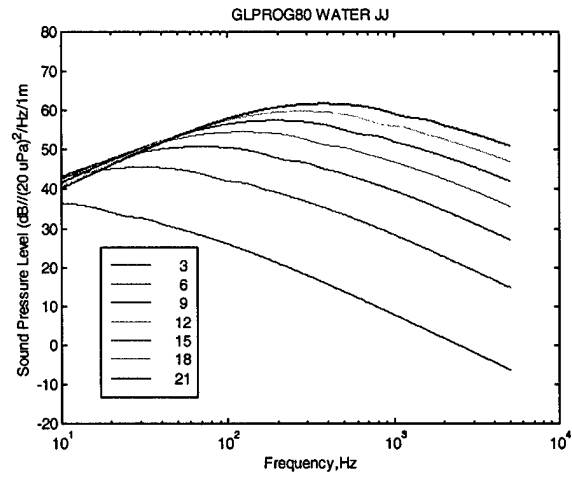
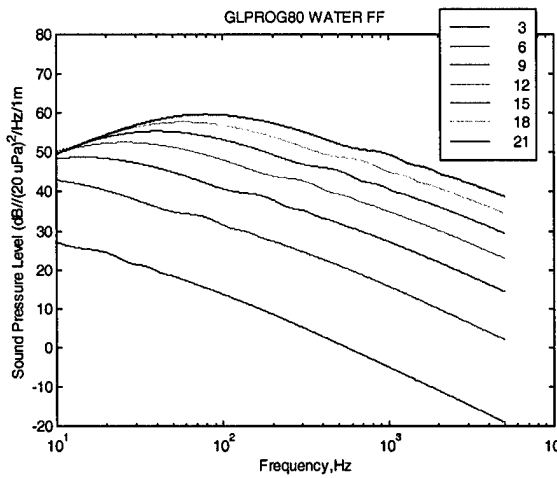
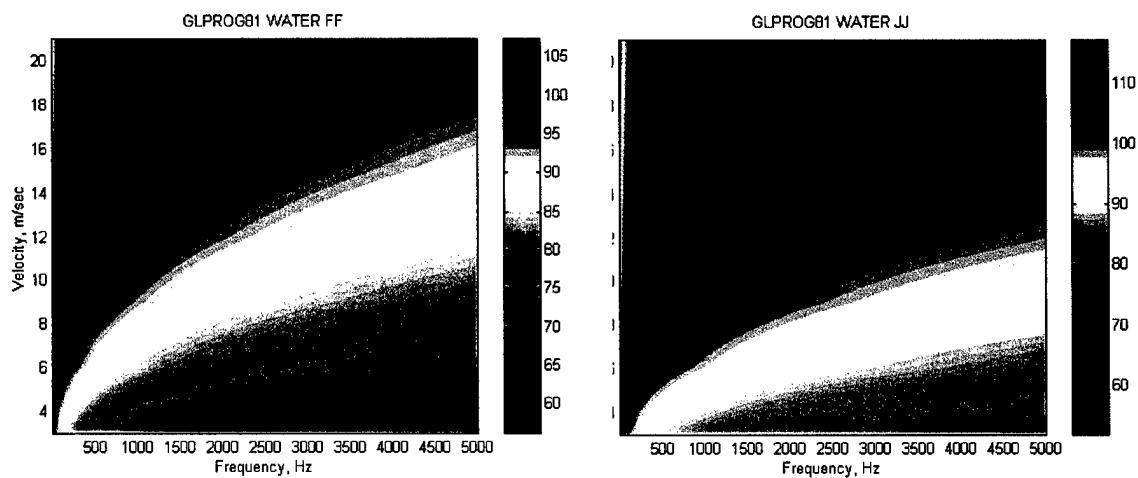


Figure 4.7 GLPROG80 predicted radiated pressure levels for a zero pressure gradient flat plate in water for $3 \text{ m/s} < U_{\infty} < 21 \text{ m/s}$.



FARABEE Functions

($u_c t_i / \Delta x = 0.15$)

JOSSERAND Functions

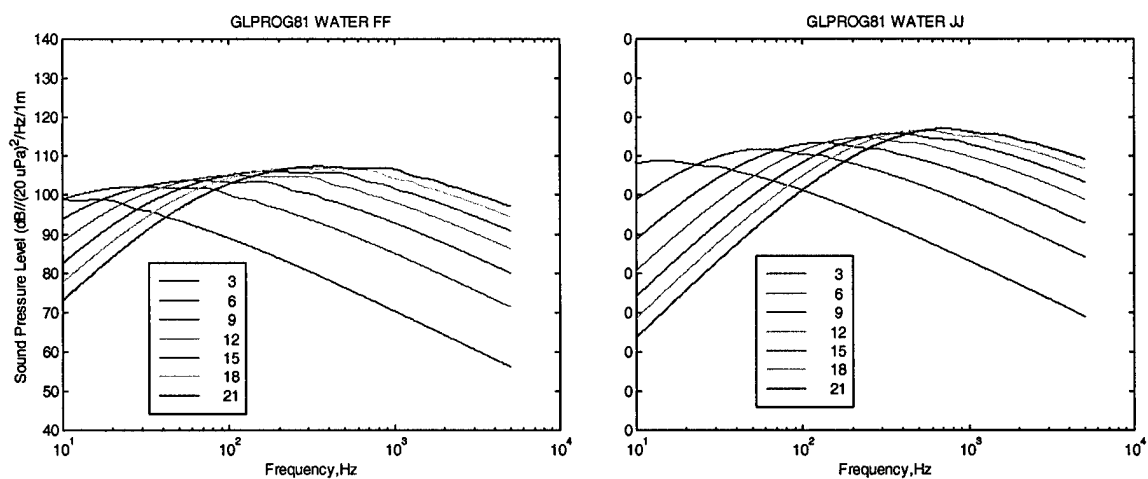
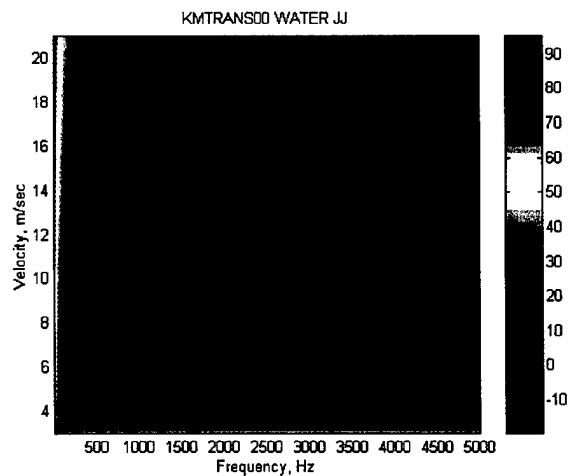
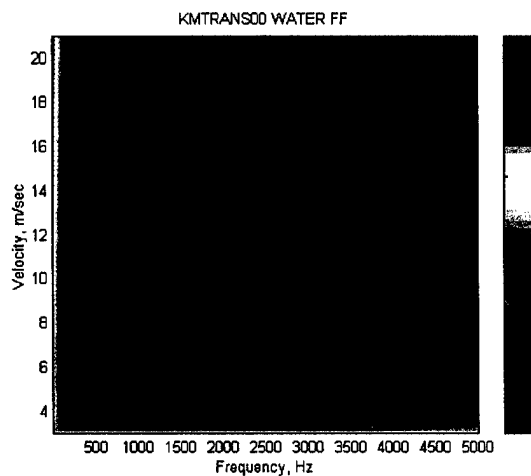


Figure 4.8 GLPROG81 predicted radiated pressure levels for a zero pressure gradient flat plate in water for $3 \text{ m/s} < U_\infty < 21 \text{ m/s}$.



FARABEE Functions

JOSSERAND Functions

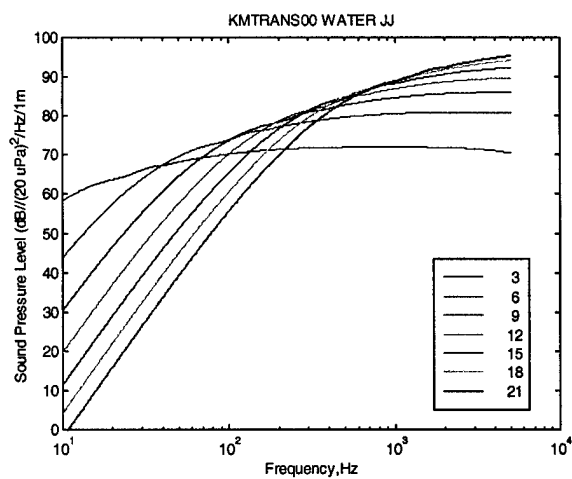
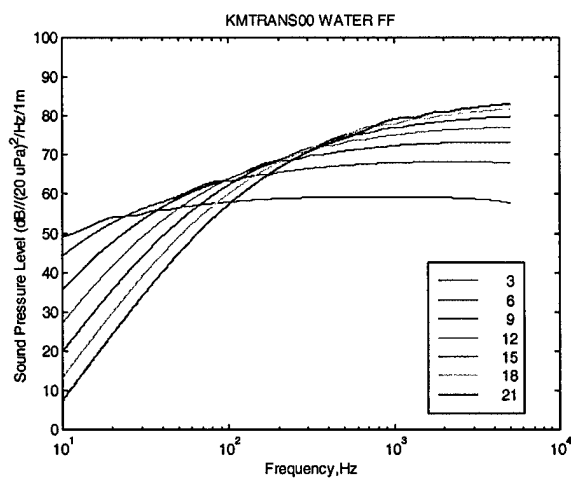


Figure 4.9 KMTRANS00 predicted radiated pressure levels for a zero pressure gradient flat plate in water for $3 \text{ m/s} < U_{\infty} < 21 \text{ m/s}$.

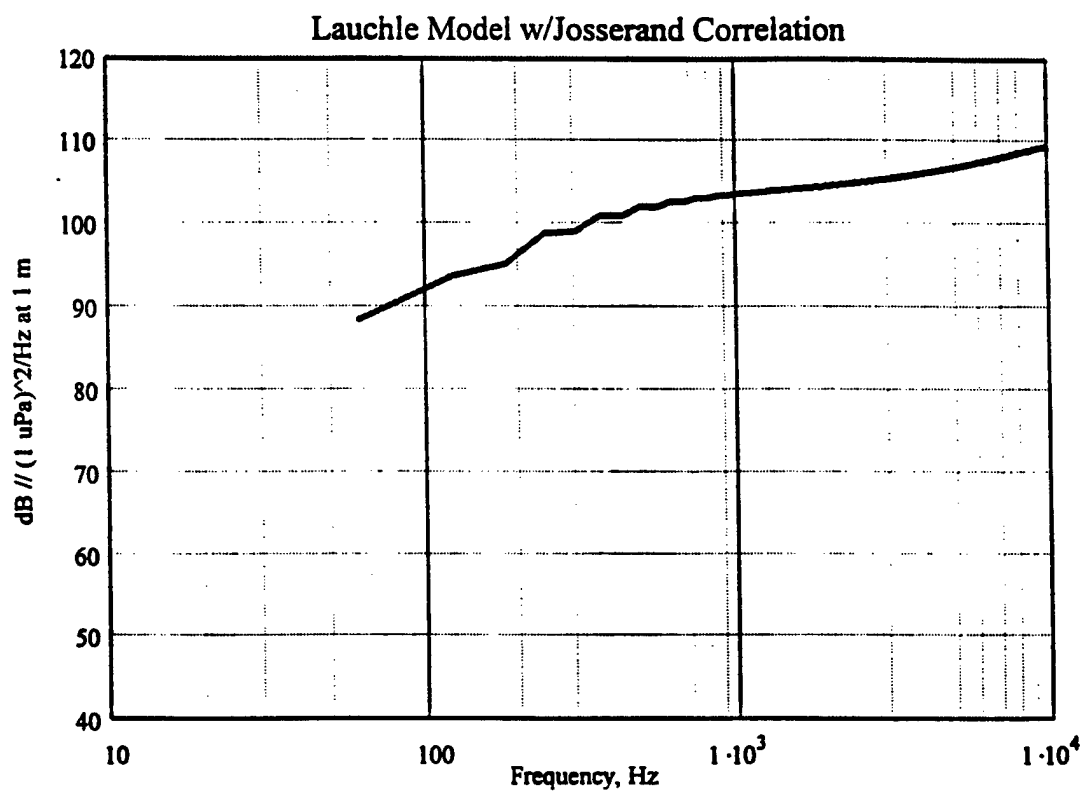


Figure 4.10 JLTRANS99 predicted radiated pressure levels for a zero pressure gradient flat plate in water for $U_{\infty} = 21$ m/sec.

Farabee Intermittency Function

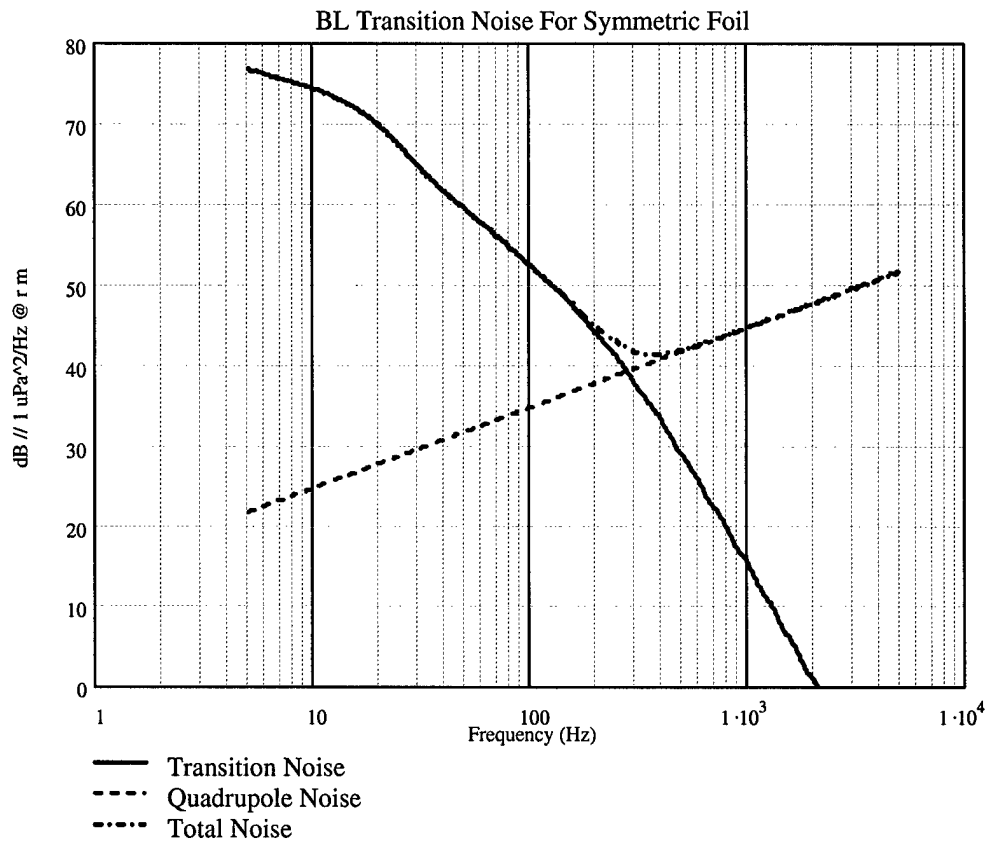


Figure 4.11 MSHTRANS99 predicted radiated pressure levels for a zero pressure gradient flat plate in water for $U_{\infty} = 21$ m/s.

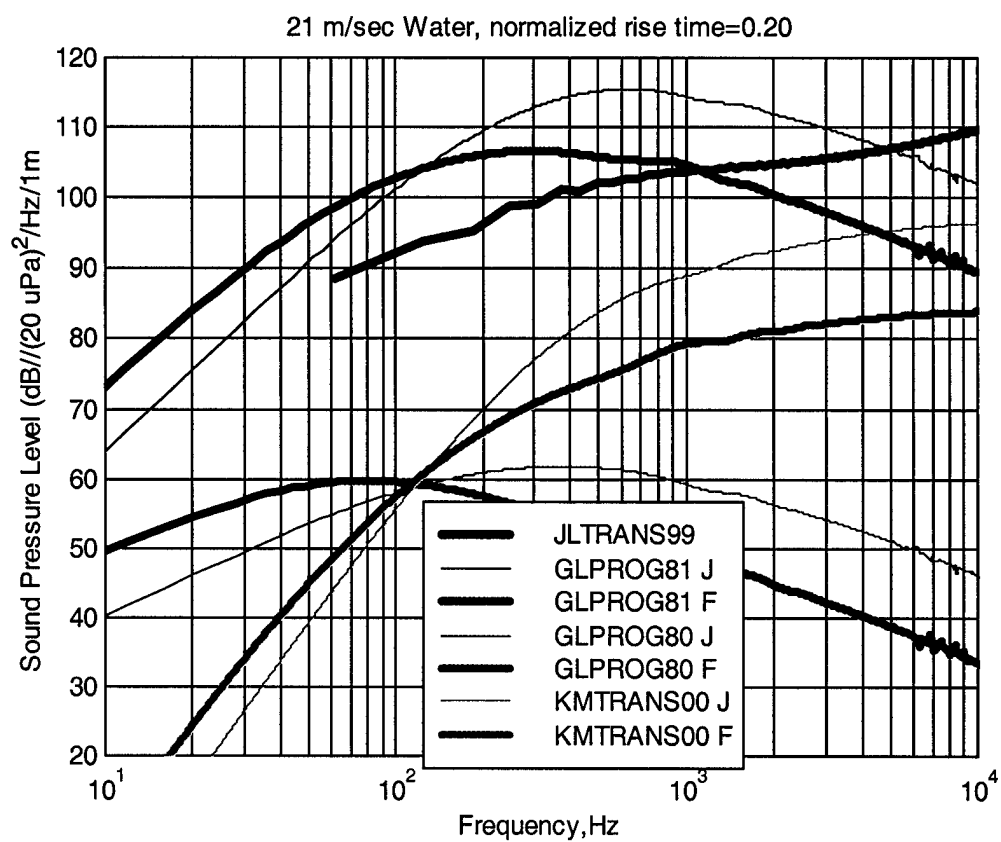


Figure 4.12 Comparison of models for radiated pressure levels for a zero pressure gradient flat plate in water, $U_\infty=21$ m/s, $\Delta\delta^*=0.021$ cm, $\Delta x=0.028$ m, $u_c/U_\infty=0.7$, $r=1.0$ m.

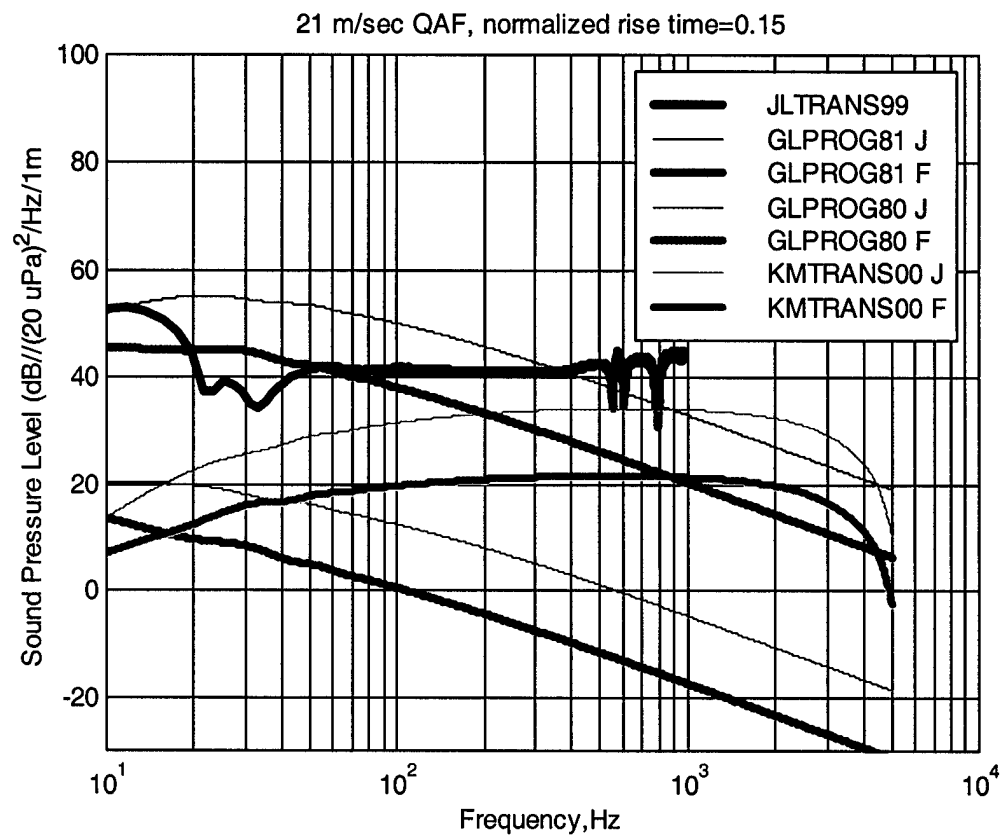


Figure 4.13 Comparison of models for radiated pressure levels for a zero pressure gradient flat plate in airflow, $U_{\infty}=21$ m/s, $\Delta\delta^*=0.278$ cm, $\Delta x=0.9$ m, $u_c/U_{\infty}=0.7$, $r=1.0$ m.

CHAPTER 5

EXPERIMENTAL APPARATUS

A significant effort was made during the ONR initiative phase of this investigation to develop a facility with sufficiently low background noise which maintained laminar flow over at least the first third of a test plate. The components of the entire experimental apparatus and environment include the ARL flow-through anechoic chamber, the quiet flow source, the flow management section, nozzle, diffuser, and the various test plates that have been created. Further information on the facility and original planned research use can be found in Marboe, et al. (1991). Subsequent development of a test section located on the floor of the anechoic chamber by Brungart (1997) utilizing most of the Quiet Airflow Facility components appeared to be much closer to the required background noise levels to conduct the desired measurements. This facility was further enhanced to finally create a quiet enough environment for the measurements. While not all of the Marboe, et al. (1991) apparatus was used in the present measurements, it is relevant to discuss the effort that went into trying to develop a facility quiet enough to make validation measurements. This is described in more detail in Appendix B. The difficulties encountered do emphasize perhaps how insignificant zero pressure gradient boundary layer transition noise is when compared to other potential noise sources.

5.1 Quiet Airflow Facility

This facility is basically a quieted air source connected to a flow management nozzle. The nozzle can form an open jet or a closed entrance into a test section. Several different nozzles exist. One has a semi-circular (15.2 cm radius) orifice situated normal to a planar baffle. A second nozzle has a square orifice 18 inches on a side. The current nozzle has a 15.2 cm x 30.5 cm rectangular orifice. The entire Quiet Airflow Facility as finally configured for this investigation is shown in Figure 5.1.

5.1.1 Flow-Through Anechoic Chamber

A low-frequency acoustic test facility to study the acoustics of air flow and air-moving machinery was constructed in 1986. The ARL Penn State Flow-Through Anechoic Chamber was designed to have a minimum cut-off frequency of 70 Hz (per ISO standard), using fiberglass wedges. To handle the air flow requirements of an experimental Axial Flow Research Fan, the air inlet wall provides 100 square feet of open area to insure quiet flow. The openings are uniformly distributed over the entire wall opposite the test facility location with openings omitted in the wedge blocks adjacent to the side walls (Figure 5.2). Two layers of screen and perforated sheet metal help to insure uniform distribution of flow with minimum turbulence. The exit angle between the wedges on the air inlet wall was designed for non-turbulent flow. This final wall design was established following a scale model study by Quartararo and Lauchle (1985).

The test facility opening to the upper control room is placed symmetrically in the chamber so that flow distortion is at a minimum. Air can either be discharged into the

control room or anechoic chamber with flow return via the ceiling plenum. The floor wedges are removable to gain access to the interior of the test volume which also allows the facility to be used as a hemi-anechoic chamber. A modular wire mesh platform is available for mounting experiments within the volume.

The performance characteristics of the chamber were reported in Prout and Marboe (1990). The chamber meets the requirements of both ISO 3745 and IEC 268 (International Standards 1972, 1977) from 90 Hz to 12.5 kHz. Sound pressure measurements may be made to ISO tolerances within 1.0 to 4.0 meters of the source at frequencies as low as 70 Hz. Figure 5.3 shows sound level meter levels plotted on a set of NCB Balanced Noise Criterion curves (Beranek, 1988). (These are revised from the PNC curves used prior to 1988). The empty shell noise levels were approximately NCB-26. The octave band background noise levels in the anechoic chamber meet a balanced noise criterion of NCB-13 at the highest octave band measured (8000 Hz) and is lower than NCB-10 in frequency bands below that. Accordingly, the chamber would have a rating of NCB-13. An NCB-15 level had been predicted for the chamber when the wedge system had been installed. The A-weighted overall level of the ambient noise inside the chamber is 17 dB.

5.1.2 Air Source

A 20 HP centrifugal blower is acoustically and mechanically isolated from the wall jet apparatus by placing it in a sound and vibration isolation box (Figures 5.4 and 5.5) that is located in the control room adjacent to the chamber. The inlet to the blower is

muffled and the outlet air passes through a treated labyrinth and flexible hose to the settling chamber of the wall jet facility where turbulence management screens are located. It was necessary to design some additional sound absorption into the plenum side of the sound isolation box to minimize the noise traveling down the flex hose. A set of baffles was designed to create four 90 degree turns for the flow so that higher frequency noise would be attenuated by the Soundcoat ® 2.5 cm thick foam-lead-foam material which was used to line the box and the baffles as shown in Figure 5.6. This treatment plus the intake muffler significantly reduces the airborne noise from the blower.

A Buffalo Forge centrifugal blower, size 4 with wheel diameter of 42 cm, is used as the prime air mover (Figure 5.7). It is powered by a 20 HP AC motor driven by an ABB inverter. The motor is water cooled to decrease the build up of heat inside the foam lined box. Pillow block bearings reduce the transmission of motor induced vibrations to the impeller. A rubber bellows attaches the blower discharge to the attenuation plenum. A Conic-Flow Silencer muffler has been attached to the inlet to the blower (Figure 5.5). A capability for suction for flow management in the test section is provided by the blower intaking air from a 10 cm hose attached to the duct between the muffler and the rubber isolation hose into the blower. A throttle can be mounted on the muffler intake to provide the coarse adjustment of the suction strength. However, neither the suction nor the throttle capabilities were used either during the measurements for this investigation.

The air is discharged from the source plenum vertically through a 40 cm diameter flexible vinyl hose and turned with a 120 degree damped sheet-metal elbow. A section of sheet-metal 40 cm diameter tubing passed through the portal into the anechoic chamber

(Figure 5.8) before being turned by another elbow itself into another Conic-Flow Silencer muffler. A piece of flexible hose attached the silencer outlet to a diffuser section for entry in the acoustic settling plenum (Figure 5.9). The diffuser is lined with 2.5 cm thick Soundcoat. The plenum is lined with foam acoustic wedges. The wedges are Illbruck SONEXsuper™ 15.24 cm high foam with 3 wedges in a 30.5 cm by 30.5 cm square. Their sound absorption characteristics are listed in Table 5.1. A square bell mouth was constructed out of split, 8 cm PVC pipe. This provides a smooth inlet into the flow management section.

Table 5.1 Sound Absorption Coefficients of Foam and Wedges Used in QAF

Frequency (Hz)	SONEXsuper Wedges	Soundfoam Embossed
125	0.18	0.15
250	0.86	0.45
500	1.22	0.70
1000	1.24	0.92
2000	1.14	0.97
4000	1.20	0.98

5.1.3 Flow Management

The preceding plenum, diffuser, and settling chamber with flow management screens are shown in Figure 5.10. Ten layers of screens are used to reduce turbulence and create as homogeneous a flow as possible. The entire assembly is mounted on rubber pads for vibration isolation. Care was taken to make all corners within the settling chamber and nozzle as smooth as possible to help maintain laminar irrotational flow.

A new nozzle was designed with a greater contraction than the prior square nozzle. The design of the nozzle followed a procedure described by Morel (1975). The nozzle is shown in Figure 5.11. The design calculation is described in more detail in a Mathcad document in Appendix A. The nozzle pieces were rolled into the correct curvature using templates, welded into four corner sections and then assembled.

5.1.4 Test Section

The test section consists of an aluminum test plate bottom and three plexiglas sides (Figure 5.12). The aluminum plate is 30.5 cm wide and 91.4 cm long. It is a 12.7 mm thick sandwich construction with damping material placed in the middle. A series of 2.5 mm holes were drilled at 25.4 mm intervals along the centerline of the plate for insertion of a hot film probe and turbulent spot trip mechanisms (see Figure 5.13). When the tunnel is operating, the unused holes are filled with wax.

The top of the test section is removable and can be adjusted so that a zero pressure gradient is maintained over the entire test plate. The top is shown removed in Figure 5.14. The opening in the wedge structure for air recirculation in the anechoic chamber is also apparent. The top of the test section has a 61 cm long by 17.8 cm wide window cut into it with the leading edge 14 cm downstream of the leading edge of the test section. A 0.0127 mm (0.5 mils) thick piece of 3M mylar film was stretched over the entire inner side of the top. A spray adhesive, 3M Repositionable 75, was used to secure the mylar. A hair dryer was used to tighten up the shrinkable mylar. One of the sides of the test section has been modified with measurement slots so that hot wire probes, stethoscope

burst probes, and anemometer probes could be inserted. The forward slots were eventually replaced with a 20.3 cm long by 10.2 high window cut into it with the leading edge 5.1 cm downstream of the leading edge of the test section. It was covered in mylar in a manner similar to above. A downstream slot was located at 85.75 cm downstream of the leading edge of the test section. Typically, the inside of the slot would be covered with clear tape and a small hole would be made to accommodate the desired probe.

By surveying over the plate with a capillary total head tube on a stethoscope (Figure 5.15), the bursting typical of transition was found to occur near the trailing edge of the test and working forward as velocity was increased. Side wall turbulent contamination is generally thought to expand at an angle of about 10 degrees from the corner juncture of the walls of the test section (Motohashi and Blackwelder, 1983). This contamination should join across the test section nearly at the end of the test section.

5.1.5 Half-Plane

A half-plane is also available for the test section. The splitter plate is 1.75 cm thick. A nose portion (aluminum) is the leading 12.4 cm of the plate. It is attached to another 71.3 cm long plate (aluminum anodized blue) as shown in Figure 5.16. The leading edge follows design guidance from Narasimha and Prasad (1995) using a nose length of 3 times the plate thickness. The super-elliptic profile is given by:

$$\left(\frac{a-x}{a} \right)^n + \left(\frac{y}{b} \right)^n = 1, \quad 0 \leq x \leq a \quad n > 2 \quad (5.1)$$

where

- a length of the nose
- b half-thickness of the plate
- n was 2.5 for this application.

A diffuser insert can be attached to the trailing edge of the plate for a smooth transition to diffusion.

5.1.6 Diffuser

A new diffuser needed to be designed to work with the rectangular test section. The trick in diffuser design is to diffuse the flow, slowing it down, as quickly as possible without creating flow separation on the diffuser walls. This was especially necessary in the configuration being used in this investigation because of the limited distance from the test section to the wall of the anechoic chamber. As it was, the discharge was purposely pointed toward the air outlet wall and the anechoic wedges were removed in that area. Soundcoat material was placed along the wall of the chamber at a slight angle to reduce direct reflection back into the diffuser.

The diffuser was designed following a method described by Kline, Abbott, and Fox (1959). Details can be found in section B.5. Even though the design methodology was followed, the diffuser walls were still prone to a transitory stall bubble that resulted in unsteady flow discharging from the diffuser. The final configuration created an operating point just on the edge of another stall avoidance criterion later found in Barlow et al. (1999). However, that unsteadiness did not propagate back upstream into the test section based on the hot wire measurements near the trailing edge of the test section.

The diffuser was lined with 2.5 cm thick embossed Soundcoat ® to absorb sound propagating down the diffuser and any reflections back from downstream. The lining is shown in Figure 5.17. The absorption properties of the material are included in Table 5.1.

With the mylar window in the top of the test section, it was necessary to increase the resistance at the end of the diffuser to increase the pressure in the test section so the mylar was not drawn down into the test section. This draw down introduced significant asymmetry in the flow when it first occurred. The test requires that the flow on the top and bottom of the test section be the same so the intermittency measurements could be made along with the acoustic measurements. Four 1.2 cm thick fibrous filters were used to provide this resistance. These are also shown in Figure 5.17. This had the added advantage of eliminating any transitory stall in the diffuser.

5.2 Instrumentation and Signal Processing

5.2.1 Hot Wire Anemometry

5.2.1.1 Probe Positioning

Measurement probes are positioned in the test section with a three dimensional Velmex traversing mechanism, accurate to $25.4\ \mu\text{m}$, through two, 6.35 mm wide slots cut in the plexiglass tunnel sidewall. A Mitutoyo digital caliper, also accurate to $25.4\ \mu\text{m}$, attached to the vertical stage of the mechanism to facilitate the measurement of boundary layer velocity profiles. Additionally, the vertical stage is equipped with a rotation stage, thereby allowing a measurement probe to be rotated relative to the test section axis for added ease of probe positioning. The Velmex traversing mechanism is attached to a

precision leveling table adjacent to the wind tunnel test section.

5.2.1.2 Pitot-Static and Total Head Probe Measurements

The mean flow velocity, U , is determined by manipulating the Bernoulli equation and correcting for fluid density changes due to temperature variations. The relationship for U [m/s] is

$$U = \sqrt{\frac{20.69546(1.00841(V - V_0) - 0.0110667) \left(\frac{5}{9}(T - 32) + 273.16 \right)}{P}} \quad (5.2)$$

where P atmospheric pressure in psi
 T temperature (degrees Fahrenheit)
 V voltage relative to total pressure
 V_0 voltage relative to static pressure

Although a pitot-static probe is unsuitable for unsteady velocity measurements because of the slow response of the fluid-filled tubes leading to the differential pressure sensor, relatively rapid mean pressure/velocity measurements were made with the use of a calibrated Micro Switch differential pressure transducer in conjunction with a DISA integrating voltmeter. The maximum error due to voltmeter uncertainty is estimated to be ± 0.005 V.

When making boundary layer velocity measurements, a total head probe with an inner diameter of 0.0495 cm was used. Additionally, the static pressure is measured for the same fluid velocity and tunnel streamwise location by using the static tap of a pitot-

static probe. Pitot-Static probes may be used for velocity measurements only when at least five probe diameters separate the wall and the probe. This avoids the creation of a venturi passage between the wall and the probe. Otherwise, the flow would be accelerated, thereby lowering the static pressure on one side of the probe, resulting in inaccuracies in static pressure; consequently, imprecise fluid velocities would be obtained. When conditions permitted, a 0.132 cm diameter pitot-static probe was used.

5.2.1.3 Hot Wire Anemometer Measurements

Both mean and fluctuating velocities were measured with a two channel TSI IFA 300 Research Constant Temperature Anemometer. The anemometer is controlled with TSI's ThermalPro software via an RS232 interface with a Gateway 2000 486 DX2 66V personal computer. A high speed A/D converter, mounted internal to the computer, is used to convert the analog data output from the anemometer to digital data for manipulation. Hot-wire data are sampled at a frequency of 10 kHz with a low pass filter set at 5 kHz. Data are acquired for a period of 6.5536 seconds resulting in 64,000 points at each measurement location. Typically, an overheat ratio (the ratio of operating resistance to actual hot wire resistance) of 1.72 was used. The ThermalPro software calculates the velocity statistics up to the fourth order moment (i.e., kurtosis). All data are archived on Zip disks using an Iomega Zip 100 drive connected to the host computer.

The hot-wire probes are visually aligned in the flow field and positioned as required with the Velmex traversing mechanism. A TSI Model 1218E Boundary Layer Probe constructed of a single 5 μ m diameter platinum-coated tungsten wire with a

sensing area length of 1.27 mm was used for streamwise velocity measurements.

Single component wires are calibrated in-situ over a range of velocities from 0.0 m/s to 25.0 m/s with pitot-static probe measurements as the known standard. TSI's ThermalPro software generates a calibration curve for every probe calibration and calculates the mean square error which is usually less than 0.3. Probe velocity calibrations are checked prior to every profile measurement to minimize errors. The experiment temperature is checked throughout each data run so as to correct for deviations from the calibration temperature. Equations (5.3) and (5.4) illustrate how a small change in temperature can cause an erroneous fluid velocity to be determined if the temperature departure is not appropriately accounted for.

$$E = E_b \sqrt{\frac{(T_s - T_c)}{(T_s - T_e)}} \quad (5.3)$$

where E_b wheatstone bridge voltage
 T_s hot-wire sensor operating temperature
 T_c hot-wire sensor calibration temperature
 T_e hot-wire sensor experiment temperature

$$V_{eff} = K + AE + BE^2 + CE^3 + DE^4 \quad (5.4)$$

where V_{eff} = effective velocity (velocity component normal to the hot-wire)
 $K, A, B, C,$ and D are calibration constants

For example, if the experiment temperature were to unaccountably increase, the

effective velocity as determined from Equation (5.4) would be lower than the actual velocity.

Because hot-wire probes are calibrated against pitot-static probes and due to the sensitivity of hot-wire measurements to temperature changes, pitot-static probe mean velocity measurements are considered more accurate than hot-wire measurements.

5.2.1.4 Handheld Anemometry

Velocity measurements were also made in the test section with a TSI Model 8345 VelociCalc handheld anemometer (S/N 00030146). It has an accuracy of 3% of scale (or ± 0.015 m/sec, whichever is greater) although the calibration was less than 1.7%. This anemometer reads from 0 to 30 m/sec with a resolution of 0.01 m/sec. It was used to verify flow conditions and temperature in the test section.

5.2.2 Sound Pressure

The single channel sound pressure measurements used for diagnostics are made with a Brüel & Kjær Type 4135 ½ inch microphone (serial number 1946536) with Type 2670 preamplifier (serial number 2003873). A Brüel & Kjær Type 5935L power supply and amplifier (serial number 2016632) is used with linear weighting set. The amplifier is capable of -5 to +55 dB gain. It is battery powered for low noise. If necessary, a Krohn-Hite 3342 2 channel filter (serial number 216) is used as a high pass filter to remove very low frequency facility noise. This is then input to the DSP Technologies SigLab signal analyzer described in section 5.2.5. The procedures for use of the acoustic intensity

methods are well documented in Fahy (1989).

5.2.3 Acoustic Intensity

The two channel sound intensity measurements are made with a Bruel & Kjaer Type 4178 Intensity $\frac{1}{2}$ inch microphone set consisting of Type 4135 microphone (serial number 1946506) with Type 2670 preamplifier (serial number 2003871) for channel 1 and Type 4135 microphone (serial number 1946464) with Type 2670 preamplifier (serial number 2003873) for channel 2. Otherwise, the signal processing equipment is the same. Table 5.2 provides a full list of equipment used for the time-averaged intensity method.

The microphones are generally placed outside of the mylar windows. The acoustic transparency of this material was established by Kargus and Lauchle (1997). The insertion loss is generally less than 3 dB with deviations less than 1 dB from 300 Hz to 3 KHz.

5.2.3.1 Real-Time Analog Intensity Circuitry

A real-time active acoustic intensity circuit has been developed to provide a signal that can be processed along with a hot film shear stress sensor to yield a coherent output intensity similar to coherent output power processing. Figure 5.19 provides a process diagram.

The electronic circuit was designed and fabricated by Todd Batzel of ARL Penn State. It is described in detail in Appendix C including circuit diagrams. The gains in the circuitry are multiply by 250 at the input filter, multiply by 295 in the integrator,

and divide by 10 in the multiplier. This gives a total gain multiplier of 7375 or 38.7 dB. A high pass filter has been implemented with a cut-off at 30 Hz. The filter is a fourth order Bessel filter with linear phase. This was chosen for this particular application in order to remove some low frequency tunnel noise that otherwise would have used up about 40 dB of dynamic range. A reset button is installed for the integrator to allow re-zeroing in case of a built up bias. The circuit can be powered by two onboard 9V batteries or an AC adapter.

5.2.3.2 Calibration

Two plane wave tubes were fabricated for calibration of the two microphone intensity probe. They cover frequency ranges 800-5270 Hz and 70-950 Hz, respectively. They are PVC pipe with aluminum ends for probe mounting. They are shown in Figure 5.18. Further details are provided in Table 5.3. The individual microphones are also calibrated with a Brüel & Kjær Type 4220 pistonphone (serial number 347321).

Table 5.2 Equipment List for Time-Averaged Acoustic Intensity Measurement.

Component	Channel 1	Channel 2
Microphone	Brüel & Kjær 4178 pair (phase matched 4135 mic) S/N 1946464 3.67 mV/Pa	Brüel & Kjær 4178 pair (phase matched 4135 mic) S/N 1946506 3.55 mV/Pa
Preamplifier	Brüel & Kjær Type 2670 Falcon® Range w/ LEMO connectors S/N 2003871	Brüel & Kjær Type 2670 Falcon® Range w/ LEMO connectors S/N 2003873
Power Supply / Amplifier	Brüel & Kjær Type 5935L 2 channel S/N 2016632	Same
Digital Signal Processor	DSP Technologies SigLab 20-42 S/N 11204	Same
Computer	Dell Latitude LM 133 S/N 6533L Microsoft Windows 95 SigLab 3.24 Matlab 5.3	Same

Table 5.3 Calibration Tube Characteristics.

	Tube 1	Tube 2
Cal Frequency (Hz)	800 - 5,270	70 - 950
Tube Length (m)	0.625	4.88
Tube diameter (cm)	3.8	20.3
Speaker	7.6 cm Mid/Tweeter	20.3 cm Woofer
Speaker response (Hz)	700 - 20,000	40 - 3,000

5.2.4 Coherent Output Intensity

The signal processing diagram for the calculation of coherent output intensity is provided in Figure 5.18. The output of the real-time active intensity processing circuit is input to channel 1 of the SigLab analyzer. The output of the TSI anemometer is input to channel 2 of the SigLab analyzer. The coherence is computed and multiplied along with microphone sensitivity and other constants with channel 1 to yield the desired coherent output intensity. This is all covered in more detail in Appendix C.

5.2.4.1 Hot Film Sensor

The hot film signals are measured with a TSI Incorporated model 1750 constant temperature anemometer (serial number 2318). A TSI probe model 1237-10 (serial number 984071) is inserted flush into holes in the test plate. A 31 ohm control resistor is necessary. The holes were spaced 25.4 mm apart longitudinally along the centerline of the test plate. The other holes were waxed over.

5.2.4.2 Conditioning with a Shear Stress Sensor

It is desired to apply the power of coherent output processing to the acoustic measurements. In this case, it is assumed that shear stress due to passage of a turbulent spot is caused by the same physical phenomenon (i.e. growth of the spot) that results in acoustic radiation. Therefore, there should be coherence between those signals. The noise associated with each sensor is assumed to be independent. Hot films have been shown to be insensitive to acoustic noise. The coherence is calculated using Equation

(5.5) using the shear stress signal and the intensity circuit signal.

$$\gamma_{t_o f_r}(f) = \frac{|G_{t_o f_r}(f)|^2}{G_{t_o t_o}(f) G_{f_r f_r}(f)} \quad (5.5)$$

5.2.5 Other Processing Hardware and Software

The analog signals are processed by a DSP Technologies, Inc. SigLab Model 20-42 dynamic signal analyzer. This has four channels of 0-20 kHz analysis. Each channel contains a fourth order quasi-elliptic filter with liner phase for anti-aliasing. The signal path include sigma delta analog-to-digital converters, an ADSP-2105 decimating digital filter, and a Texas Instruments TMS320C31 digital signal processor. The dynamic range is greater than 90 dB. A SCSI interface connects it to a Dell Latitude LM 133 notebook PC. The SigLab has a hardware performance verification procedure that calibrates channel input and output gain and offsets which are written to the EEPROM.

The SigLab 3.24 software is written in The Mathworks, Inc MATLAB 5.3. Plots can be made on a Hewlett Packard DeskJet 870Cxi inkjet printer. The anemometer and the microphone amplifier are shown in Figure 5.20. The rest of the signal processing instrumentation is shown in Figure 5.21.

Table 5.4 Equipment List for Coherent Output Intensity.

Component	Channel 1	Channel 2
Microphone	Brüel & Kjær 4178 pair (phase matched 4135 mic) S/N 1946464 3.67 mV/Pa	Brüel & Kjær 4178 pair (phase matched 4135 mic) S/N 1946506 3.55 mV/Pa
Preamplifier	Brüel & Kjær Type 2670 Falcon® Range w/ LEMO connectors S/N 2003871	Brüel & Kjær Type 2670 Falcon® Range w/ LEMO connectors S/N 2003873
Power Supply / Amplifier	Brüel & Kjær Type 5935L 2 channel S/N 2016632	Same
Analog Filter and Amplifier	Krohn-Hite 3342 2 channel S/N 216	Same
Real - Time Processor	ARL Penn State 2 channel Real-Time Active Intensity Circuit	Same
Shear Stress Conditioning Signal		TSI Model 1237-10 Hot Film S/N 984071 Model 1151 Probe Holder
Anemometer		TSI Constant Temperature Anemometer Model 1750 S/N 2318
Digital Signal Processor	DSP Technologies SigLab 20-42 S/N 11204	Same
Computer	Dell Latitude LM 133 S/N 6533L Microsoft Windows 95 SigLab 3.24 Matlab 5.3	Same

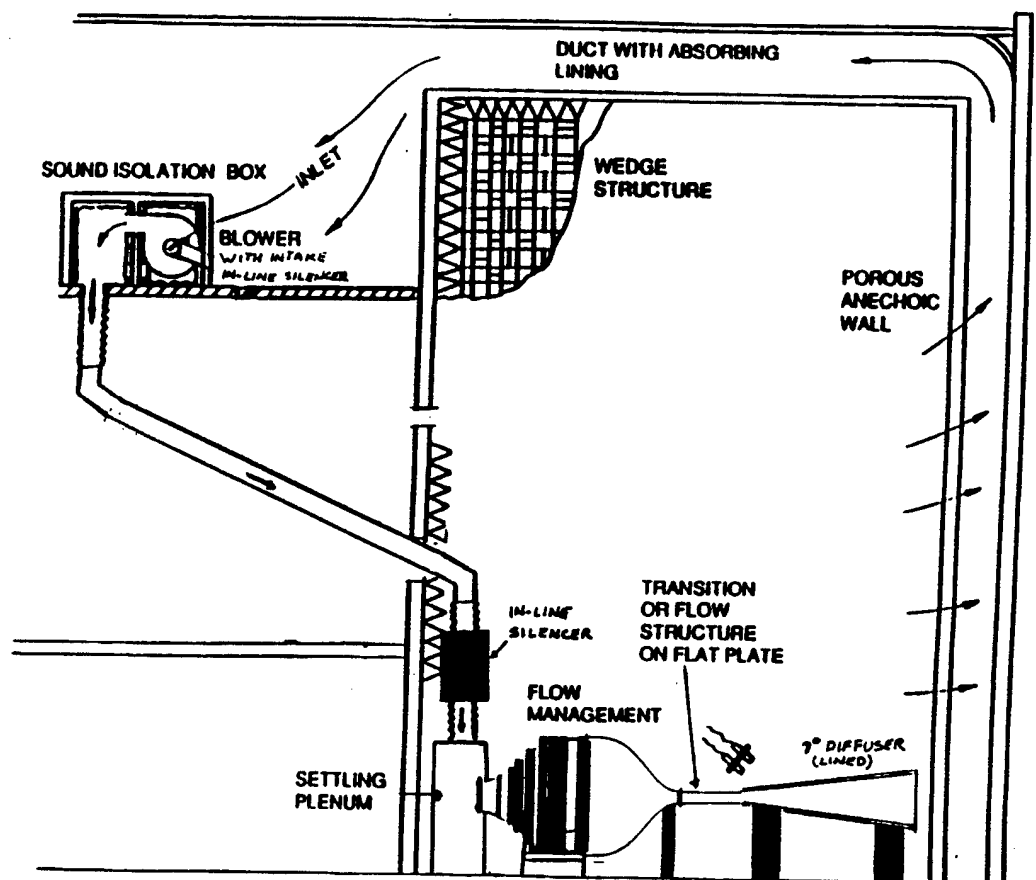


Figure 5.1 Quiet Airflow Facility configuration for present experiment.

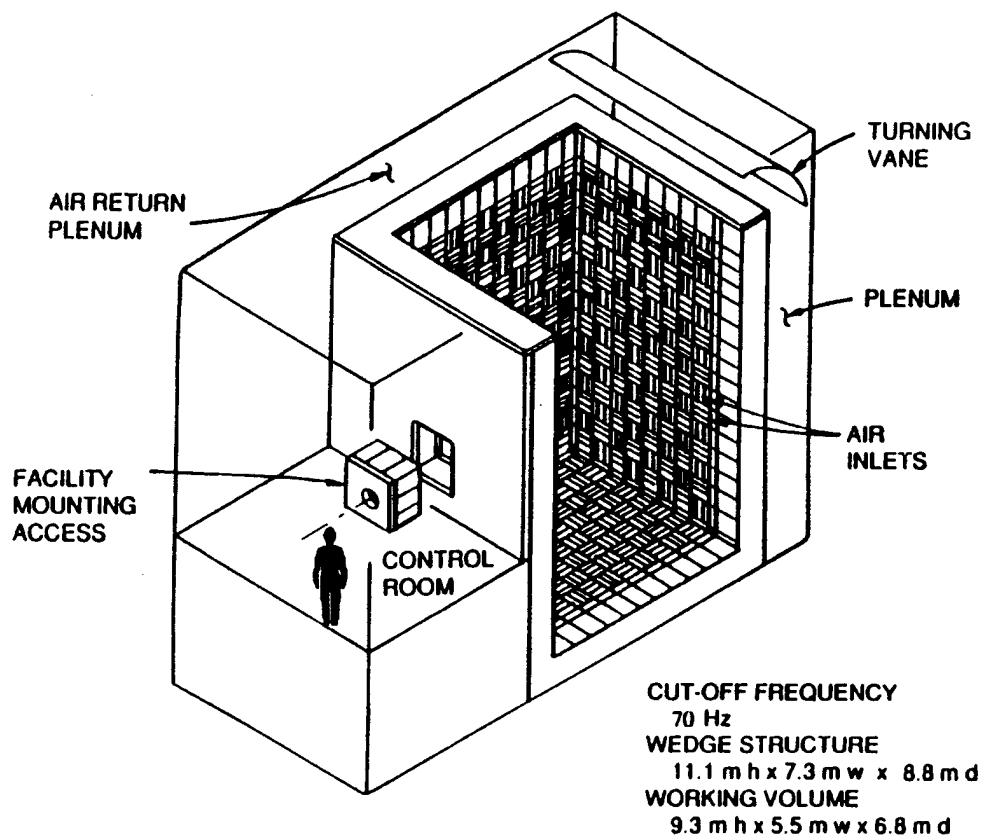
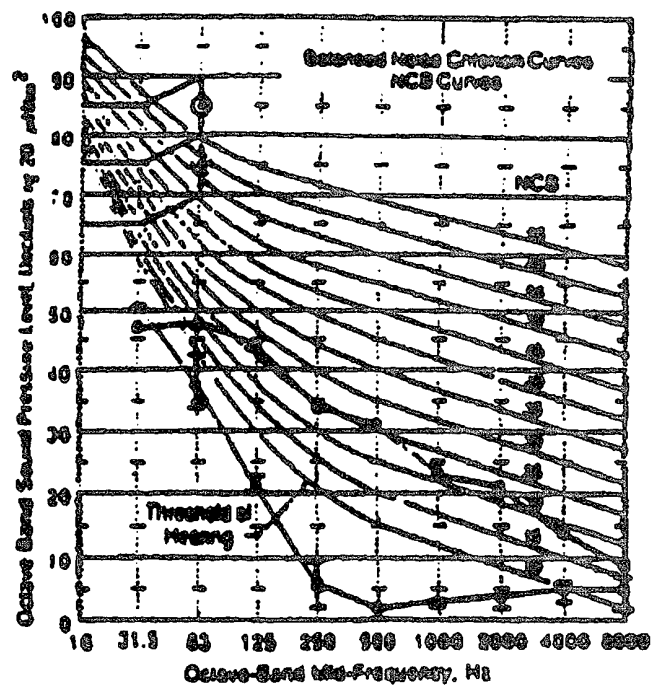


Figure 5.2 Flow-through anechoic chamber.



a Noise spectrum in completed Anechoic Chamber

b Noise spectrum in Chamber shell before installation of wedge structure

Balanced Noise Criterion (NCB) Curves. These curves are revised versions of the NC curves. The NCB curves were derived from measurements made in occupied rooms with all systems operating (after Garach).

Figure 5.3 Anechoic chamber background noise relative to balanced noise criterion (NCB) curves.

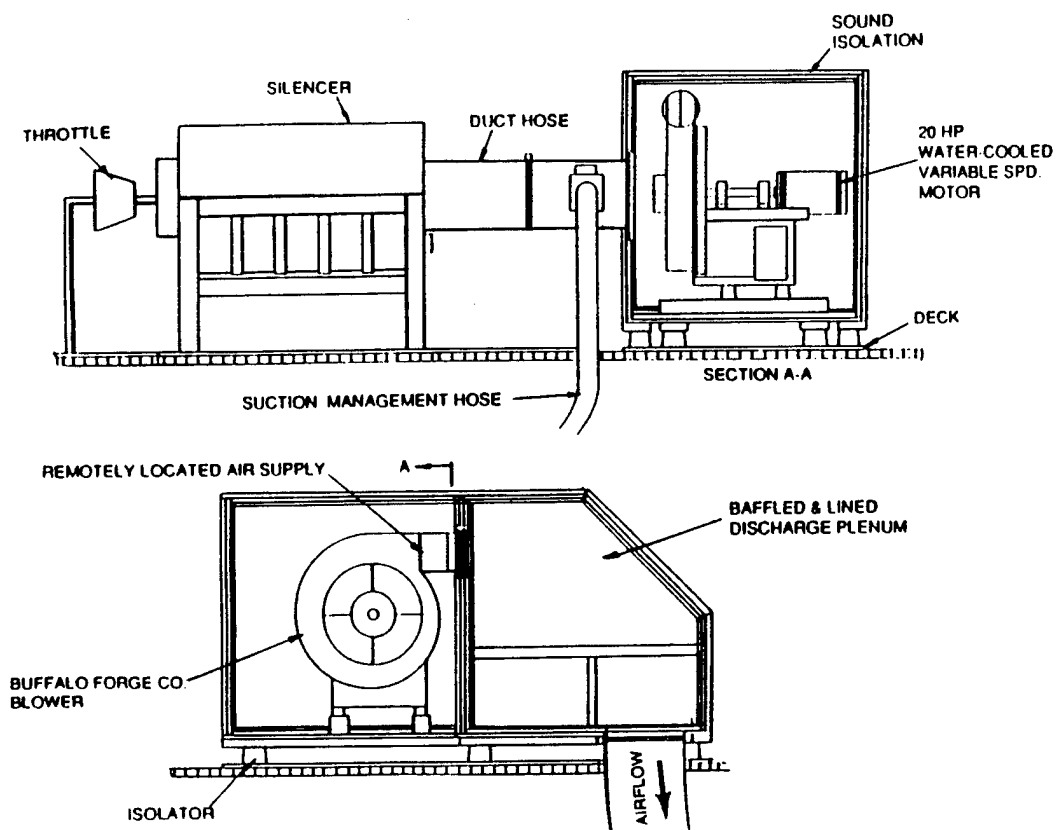


Figure 5.4 Blower and sound/vibration isolation box .

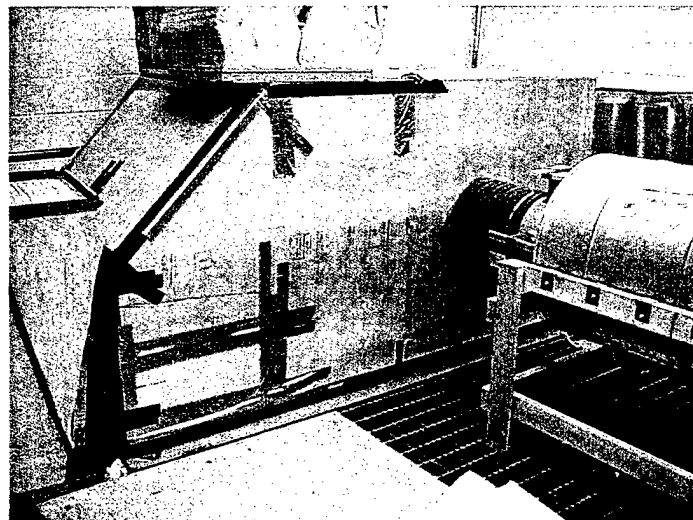
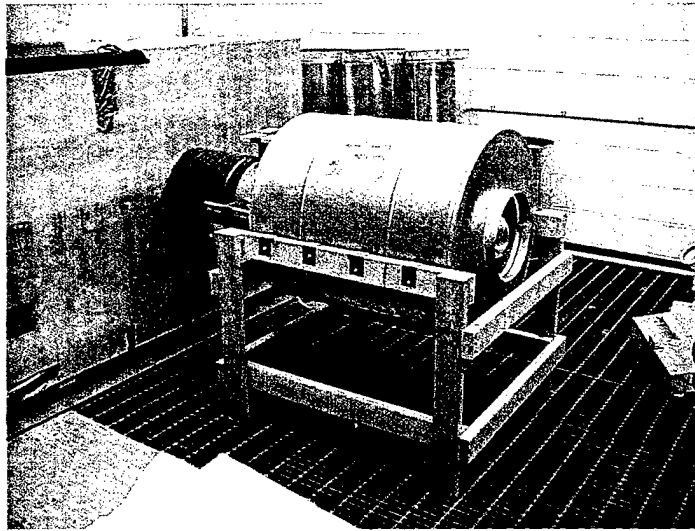


Figure 5.5 Flow source enclosure, plenum, and silencer.

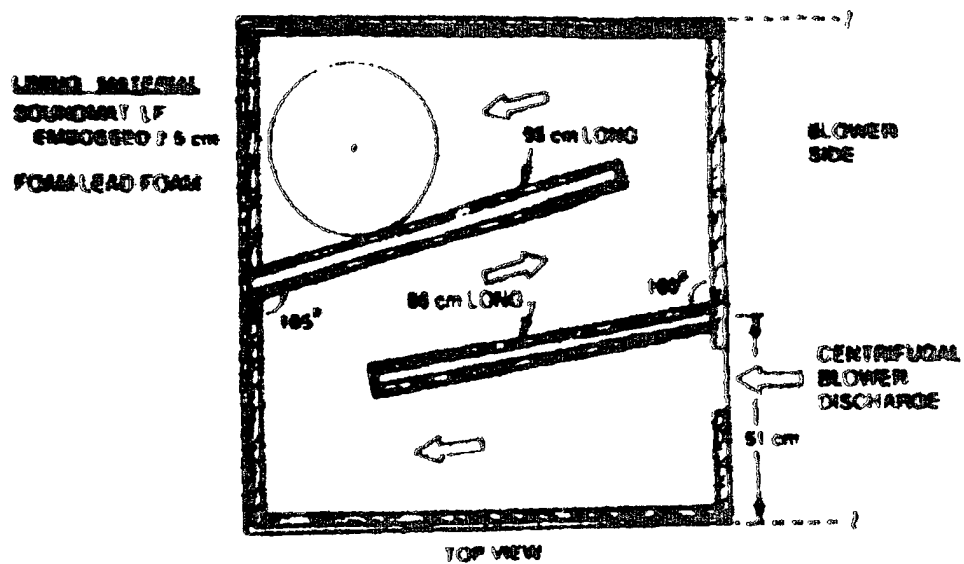


Figure 5.6 Flow source noise attenuation plenum.

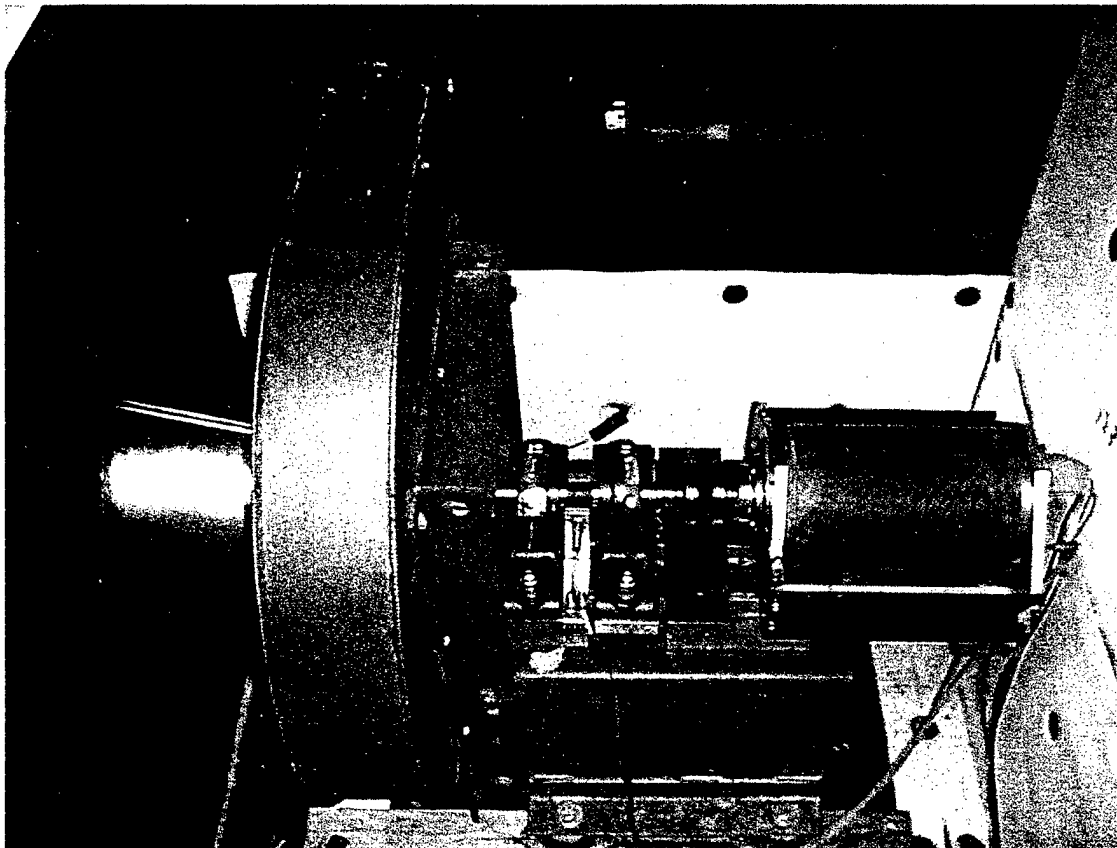


Figure 5.7 Buffalo Forge blower and motor.

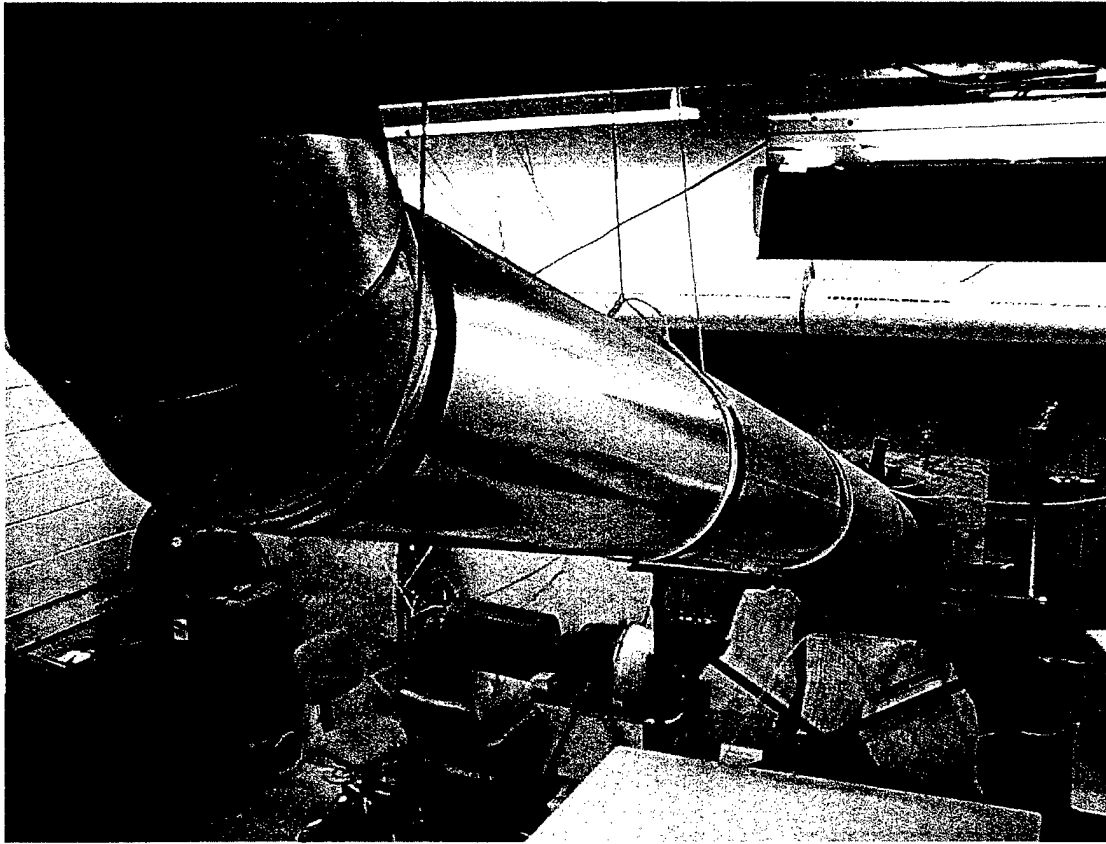


Figure 5.8 Elbow and conduit pipe for flow into anechoic chamber.

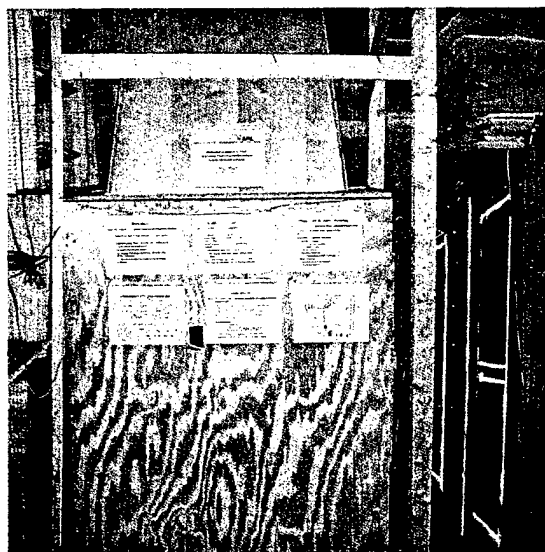
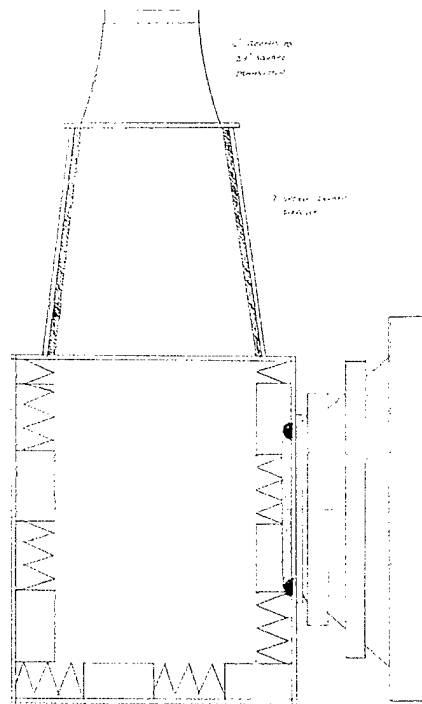
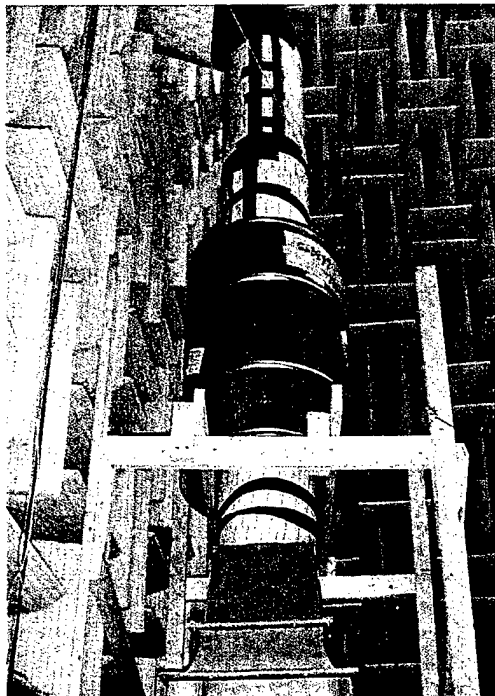


Figure 5.9 In-flow silencer and diffuser into acoustic settling chamber.

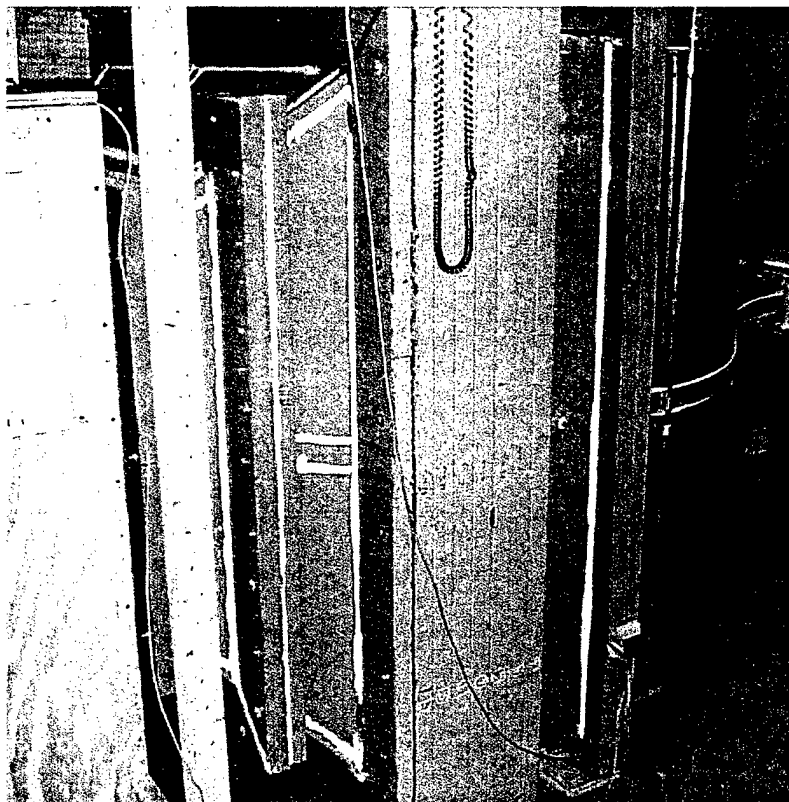


Figure 5.10 Flow management plenum, diffuser, screens, and settling sections prior to nozzle.

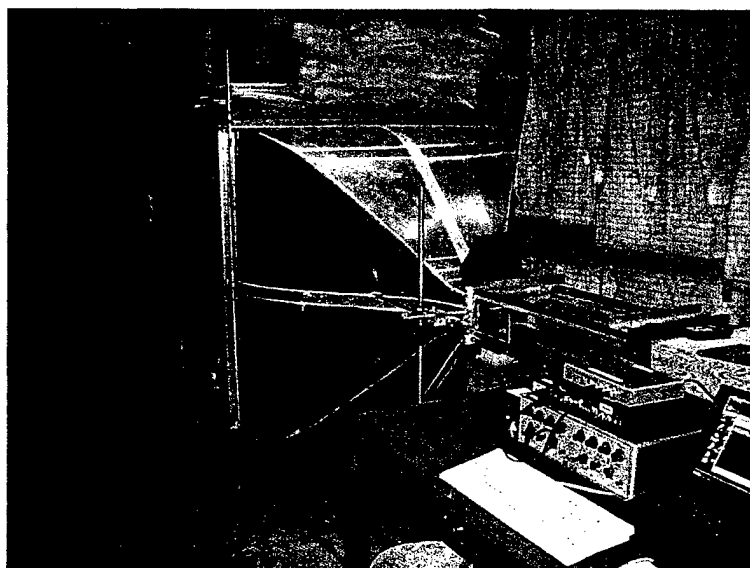
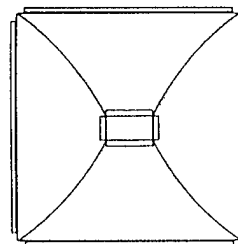
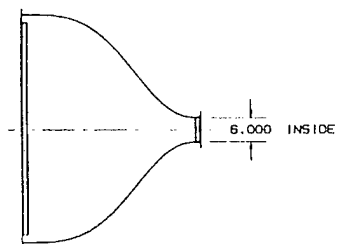
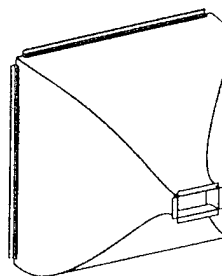
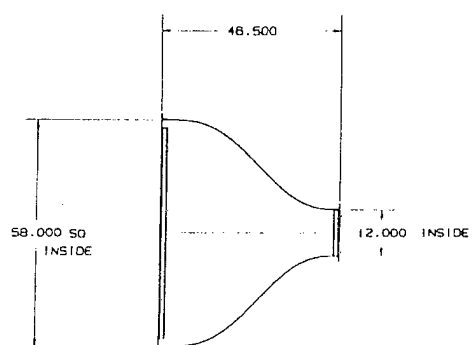


Figure 5.11 New nozzle contracting to 15.2 cm x 30.5 cm.

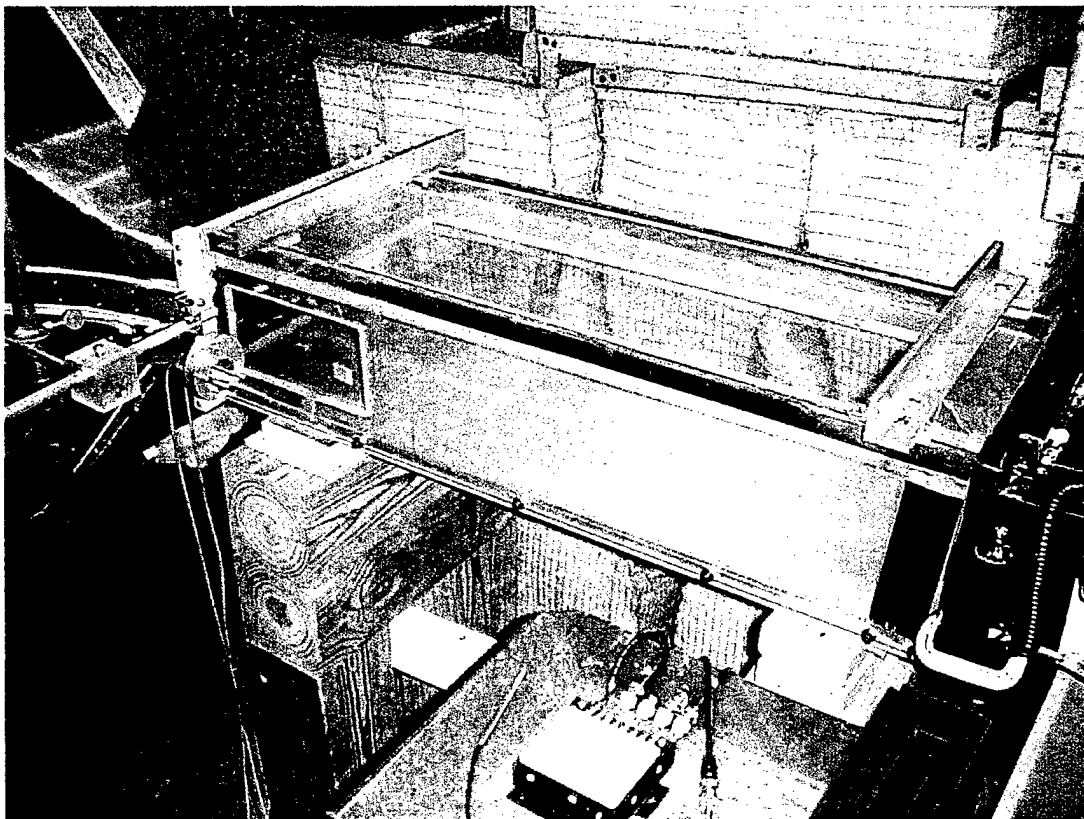


Figure 5.12 View of test section.

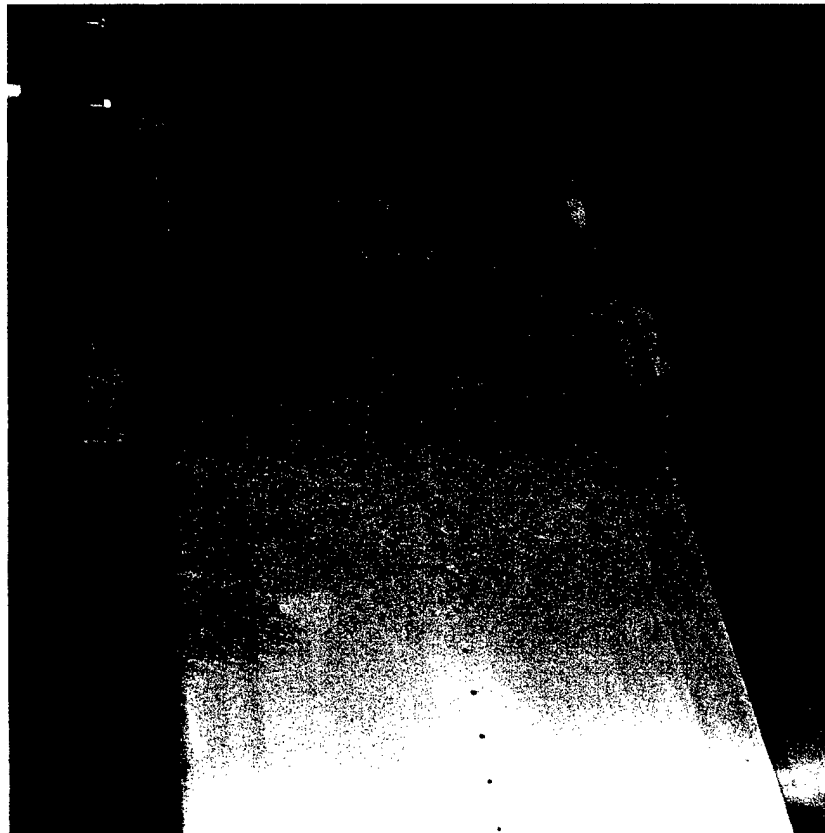


Figure 5.13 Test section view showing drilled holes for hot film probe or spot generation excitation.

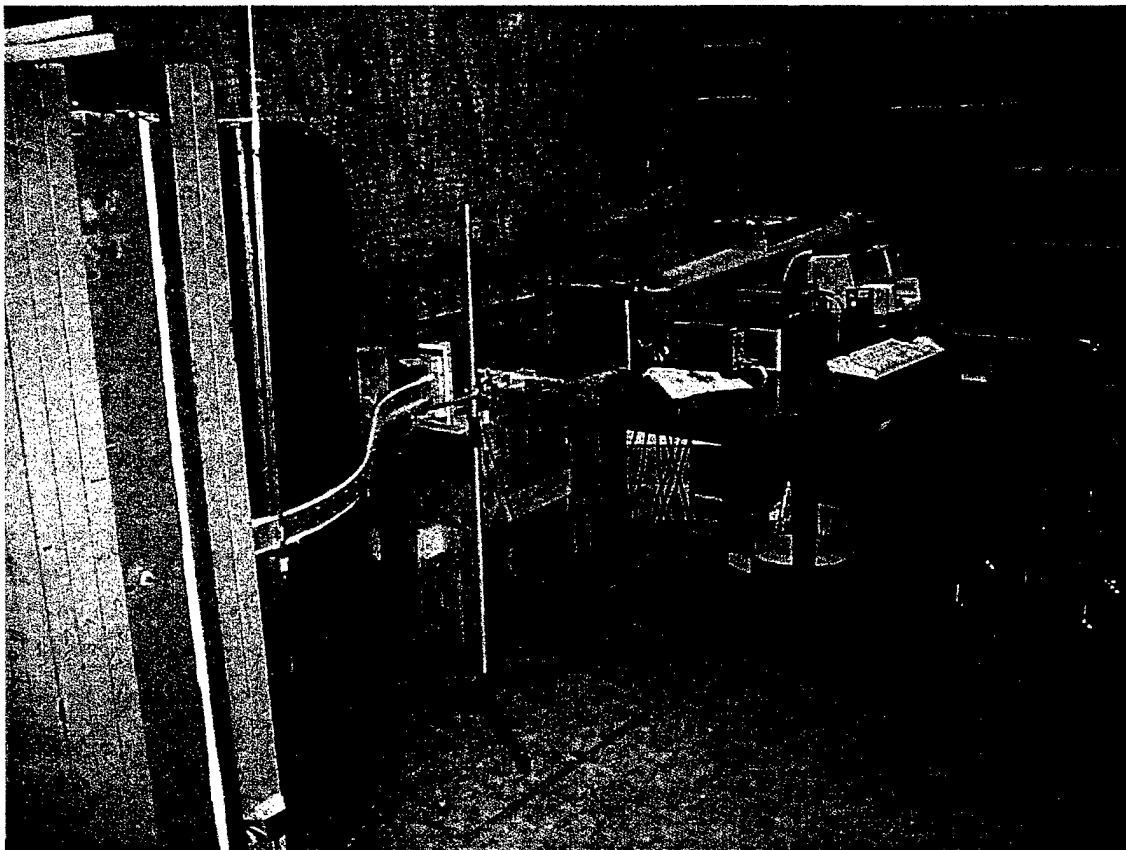


Figure 5.14 View of nozzle, plenum, and diffuser.

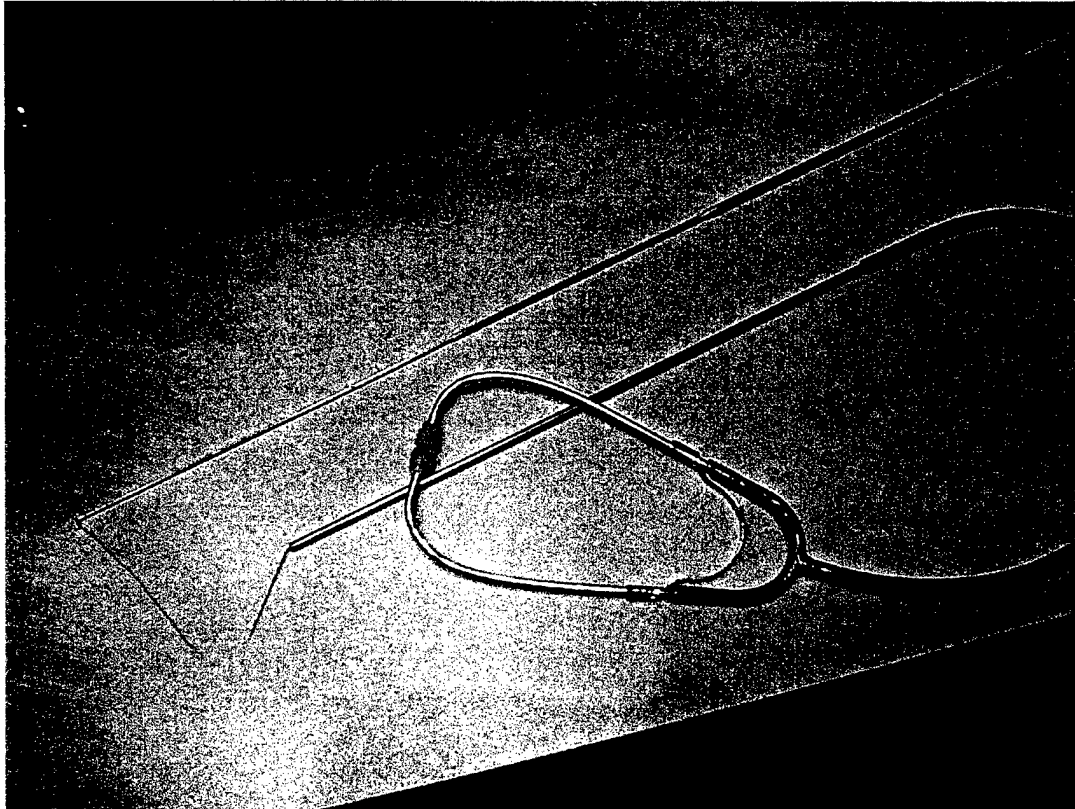


Figure 5.15 Stethoscope burst probe and tuft wand.

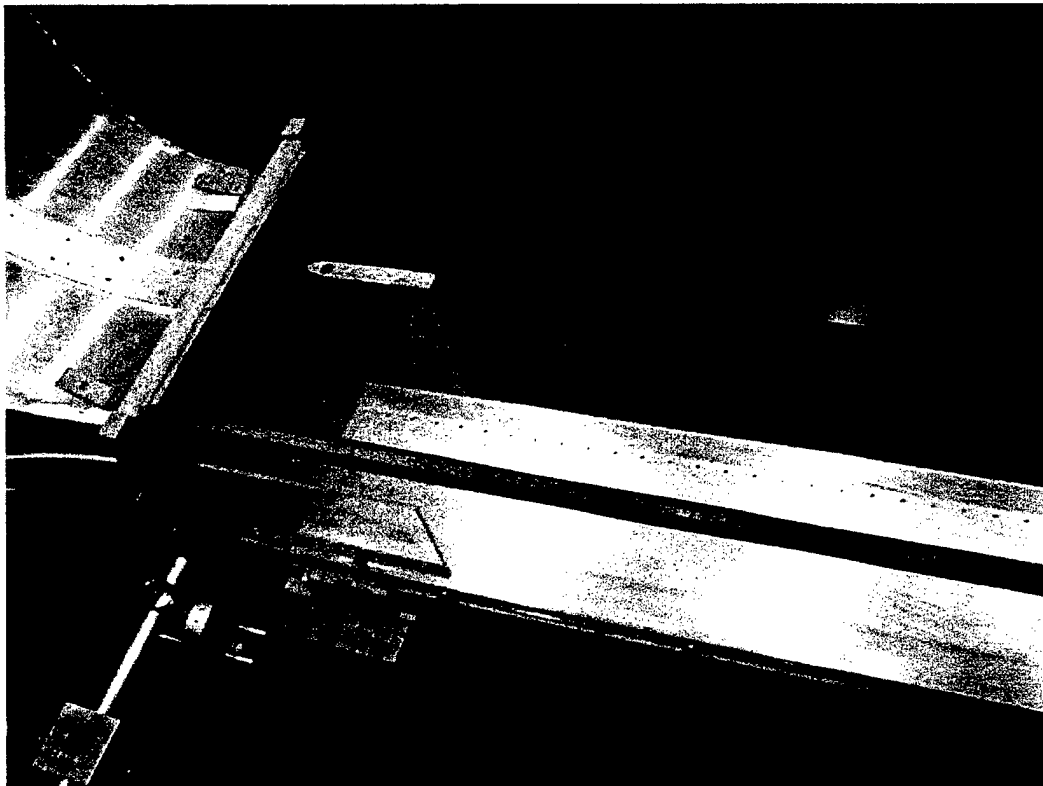
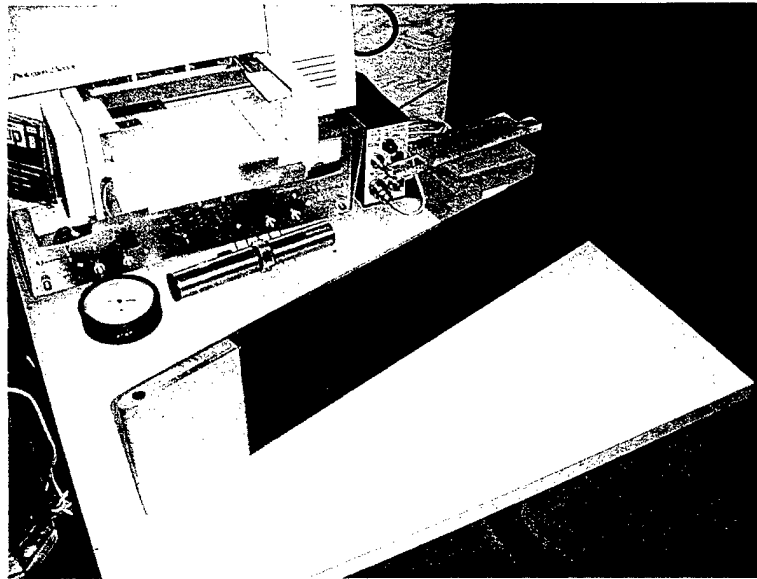


Figure 5.16 Half-plane plate designed for test section.

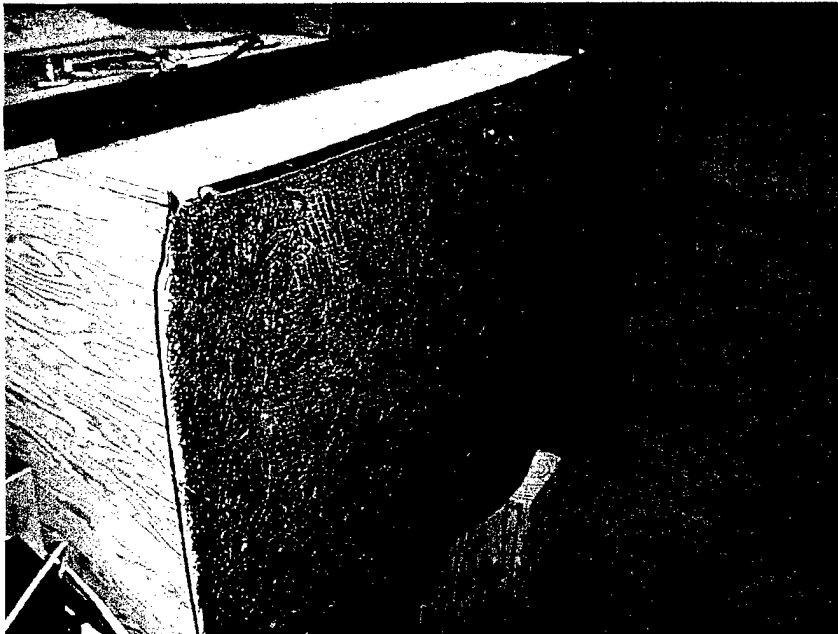
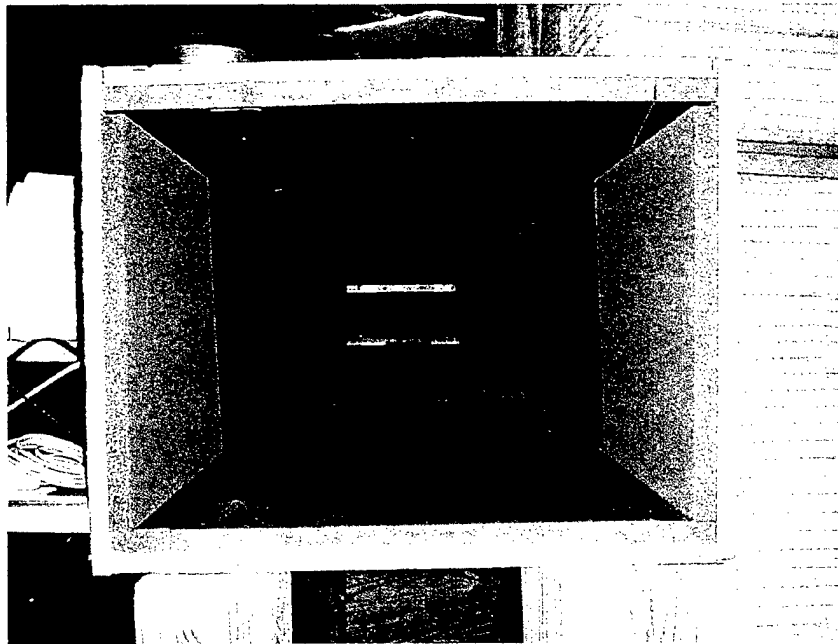
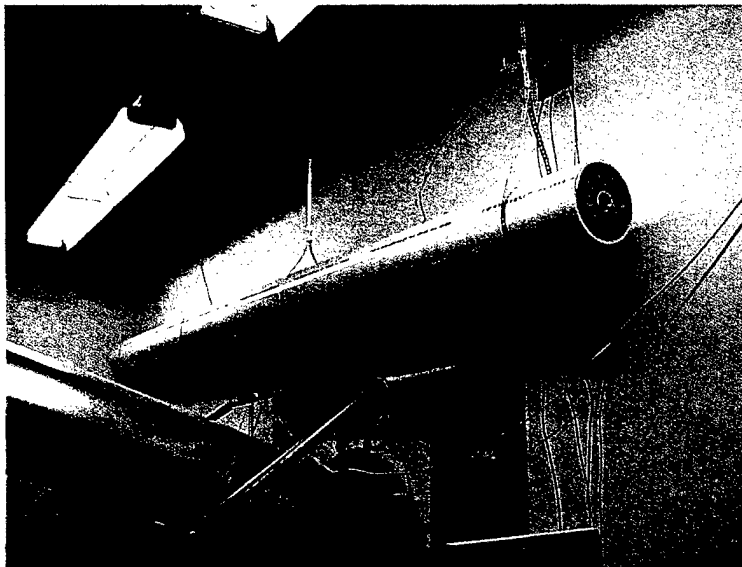


Figure 5.17 Looking upstream through diffuser to the test section and the added diffuser resistance.



(a)



(b)

Figure 5.18 Intensity probe calibration tubes, (a) high frequency and (b) low frequency

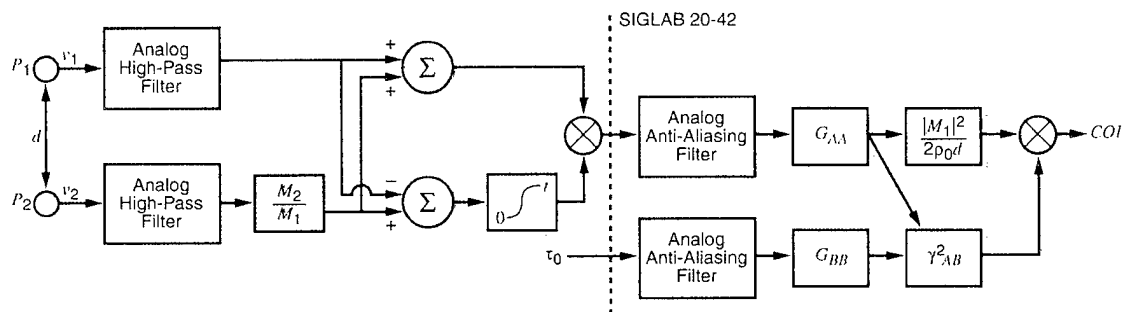


Figure 5.19 Processing diagram for coherent output intensity.

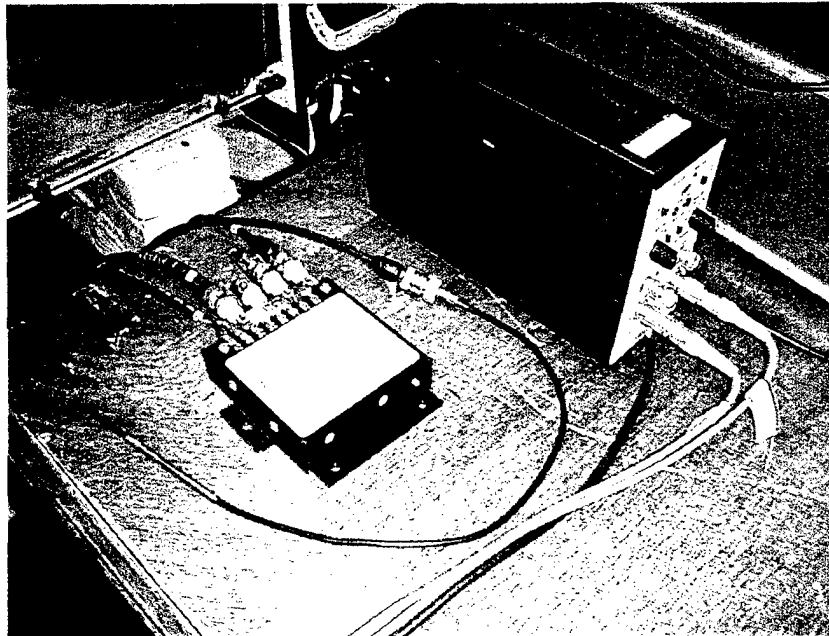


Figure 5.20 Anemometer and microphone amplifier

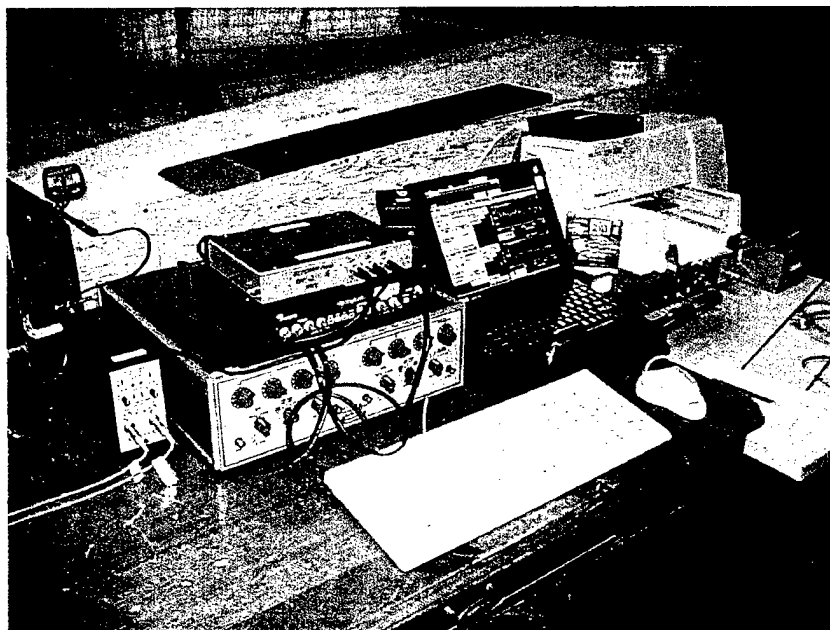


Figure 5.21 Test instrumentation.

CHAPTER 6

MEASUREMENT RESULTS

6.1 Test Section Flow

The test section flow was characterized at two longitudinal locations in the test section using hot wire anemometry. These were $x = 7.6$ cm and 77.5 cm of the test section. The forward measurement was used to establish that there was uniform laminar entering the test section. This is shown in Figure 6.1 for two tunnel velocities and compared to the Blasius boundary layer profile. The uniformity across the test section area is seen in Figure 6.2. The hot wire measurements were made traversing across the test section at heights of 25, 50, and 75% of the vertical dimension of the test section. The variation is less than 1%. It should be noted that these measurement were conducted prior to the addition of the resistance on the end of the diffuser which was done during the acoustic measurements. Thus, the top velocity in the test section is higher than could be achieved for the acoustic measurements.

The downstream measurement location was used to establish a zero pressure gradient flow condition. Spacers were placed under the support arms on the test section top until the proper uniformity of flow was achieved. A similar survey uniformity was completed at this location. Those results are shown in Figure 6.3.

A 15 cm strip of 6.3 mm mesh screen placed near the leading edge of the test section was used to trip the boundary layer in order to check the fully developed turbulent

flow at the end of the test section. Figure 6.4 shows a comparison of the boundary layer profiles and turbulence intensities for this test and similar data taken with a separate nozzle and test section in the Quiet Airflow Facility. The flow behavior appears normal with this nozzle and test section.

6.2 Intensity Measurement Calibration

A calibration sequence was performed with the intensity instrumentation. The configuration for a free-field calibration is shown in Figure 6.5. The SigLab signal generator was used to provide a 2.5 Vrms, 10 kHz bandwidth white noise input to a 25 cm woofer speaker mounted in a wooden baffle. The intensity probe was positioned above the speaker 81 cm. Reflections were minimized by use of 13 cm thick fiberglass pads.

Before the speaker test was done, the microphones were amplitude calibrated using the pistonphone. A magnitude and phase mismatch test was performed in the small calibration tube (Figure 6.6). The microphones were extended into the tube to make sure that the pressure compensation holes on the preamplifiers were exposed. This is the reason for the notable spikes around 2 kHz. This corresponds to a quarter wavelength for reflection from the end wall of the tube back to the microphone. The phase error is generally less than 0.4 degrees and the magnitude error is less than 0.5 dB. For this instrumentation phase error, the intensity error is 0 to -1 dB down to 60 Hz. The microphones have a 25.4 mm spacing. This spacing produces an accuracy within 1.0 dB over a range of 320 to 2500 Hz. Above this, the error increases to 5 dB at 5000 Hz.

There are also bias errors associated with the type of source field and the measurement distance (Fahy, 1989). This bias error is shown for point monopole and dipole fields, and a measurement distance of 5 cm in Figure 6.7. The effect is very small below 3 KHz. All of the mentioned biases apply in the same manner to each of the measurements conditions, so relative amplitude differences are still meaningful. The random error was reduced by taking 256 averages for each measurement which yields a ± 0.4 dB random error for the cross-spectrum used in the analysis.

The results of the speaker calibration verification is shown in Figure 6.8. The P-P intensity is compared to the far field intensity determined by $P_1^2/\rho c$. The agreement is very good down to about 150 Hz where the near-field errors increase and produce the amplitude fluctuations seen in the figure. Above 3.5 kHz, the discrepancy is due to finite-difference approximations. The test section top with the mylar window was then placed between the speaker and the intensity probe. The results in Figure 6.8b show generally good agreement with narrowband deviations being more pronounced with the mylar. Figure 6.9 shows the same data processed using 50 Hz constant bandwidth and 1/3 octave bandwidths. This shows agreement within 1 dB over the frequency range of interest from 250 Hz to 3 kHz.

The value of the use of an intensity probe (with its cosine directivity) over a single microphone is shown in Figure 6.10. A 5-12 dB improvement in signal-to-noise ratio is achieved. The equivalent pressure level converted from the intensity level is compared to the pressure level from only microphone 1 of the intensity probe for two measurement locations.

6.3 Flat Plate Natural Transition Zone

Acoustic active intensity measurements were made for a natural transition zone occurring on the top surface of the test section. The tunnel was run at its highest possible velocity condition of 21 m/sec. In this case, the transition began just downstream of the mylar window leading edge. The downstream edge of the mylar window was at about 65% of the transition zone. It is within this range that the predominant portion of the radiated acoustics has been predicted to occur according to Audet et al.(1989a,b) as shown in Figure 2.2. Any further extension of the mylar window would have been unpractical due to a weakening of its structure and higher likelihood of surface dynamics. A longitudinal survey was conducted over the mylar window with the probe orientation normal to the window as shown in Figure 6.11.

Hot film measurements were made by inserting the hot film through predrilled, but waxed over, holes in the bottom of the test section. It is presumed from the uniform flow measured previously that the boundary layer growth and transition on the bottom of the test section matches that on top of the test section. A comparison is made in Figure 6.12 of the locations and amplitudes of the measured intermittency to the Josserand intermittency function.

The intermittency was determined using the circuitry used by Josserand (1986) which turns turbulent spot shear fluctuations into a one or zero volt indicator that is integrated to show an intermittency. The match with the Josserand function for a 90 cm transition zone is very good. The intensity measurement locations are also indicated on the graph. The Josserand intermittency values at those locations were then used for any

subsequent intermittency weighted calculations.

Recall from Figure 6.8 that the intensity probe showed narrowband fluctuations at lower frequencies that were not present in the far field processed output. These fluctuations are due to tunnel modes with their characteristic constructive and destructive interference. Even though sources on the bottom of the test section should be at least 12 dB lower than similar sources on the top of the test section as received at the intensity probe, due to a certain mode, the source could seem to be located near the top. The true spectrum should be smoother as for the far field in Figure 6.8. So further processing was done to smooth the spectra by using 50 Hz constant bandwidth processing. All of the presentations of measurements will therefore be shown in both 1.6 Hz and 50 Hz processing bandwidths. Figure 6.13 shows a comparison of these processing bandwidths to a 1/3 octave processed representative measurement.

The active intensity measured at the 7 longitudinal positions are shown in Figure 6.14. The flow condition at $x=20$ cm is laminar. Selective spectra are shown in Figure 6.15 for the laminar location and the transition locations near what is predicted to be the peak for acoustic pressure.

A second experiment was conducted with a boundary layer trip consisting of a 6 cm long strip of 50 grit sandpaper located at $x = 2$ cm which is upstream of the mylar window (Figure 6.16). The measured active intensity spectra are shown in Figures 6.17 and 6.18. The intent was to demonstrate that there was signal to noise available for measurement of laminar and turbulent signatures and that they were distinctive from the transitional structure radiation.

A third experiment was conducted to try to reduce the length of the transition zone by stimulating the boundary layer to transition earlier. Several variations of sandpaper grits and sizes were tried to get a condition that was determined by stethoscope to be intermittent rather than turbulent. Finally, two, 10 mm long strips of 150 grit sandpaper were located at x 12 and 15 cm. The results are provided in Figures 6.19 and 6.20. Even with the stimulation, the results are not significantly different from those of natural transition.

Comparisons are made for each measurement locations between these three test cases in Figures 6.21 through 6.27. The spectra for natural transition tend to be less than the turbulent spectra in frequencies above 1 kHz by 2-3 dB except for the $Z_x = 0.45$ position where the transition levels exceed the fully turbulent measured levels. This correlates well with the wall pressures measured by Dufourq (1984) shown in Figure 6.28. Recall from Equation 2.17 in the description of the two fluids model that the wall pressure is modeled as an intermittency weighted wall pressure spectrum due to turbulence plus an acoustic pressure due to the spot dynamics in intermittency. The acoustic measurements described here are the first validation of that hypothesis since the active acoustic intensity is the radiating component and not unduly influenced by the near field reactive intensity. At the next Z_x positions, the turbulent and transitional levels are more equivalent similar to the wall pressure measurement. At these locations and beyond, the quadrupole turbulent noise production is dominating the higher order spot related radiation due to coalescence.

The transition intensity measurements were then summed, but weighted by the

longitudinal extent of the area covered by that measurement in order to get one transition intensity spectrum. Thus it still reflects pW/m^2 which can be converted to the pressure spectrum using the far field assumption for comparison to the computational model predictions. All models were exercised for the QAF measurement condition of $U = 21$ m/sec, $\Delta x = 90$ cm, and $\Delta\delta^* = 0.278$ cm. These results are compared to the measured radiated pressure levels in Figure 6.29. As expected, the displacement thickness model with the dipole source and the Farabee intermittency and burst rate functions provides the best estimate to the measured from 300 Hz to 3000 Hz (the range for which bias and random errors are within 2 dB).

Both the transition and tripped, fully turbulent measurements were summed based on an area weighting of power to get a representative zone acoustic power signature. The turbulent spectra were weighted at each measurement location for the local intermittency representative of that area. These spectra are compared in Figure 6.30. For frequencies above 1250 Hz, the turbulent spectra is about 3 dB above the transition levels. This would be expected for the frequencies where turbulent boundary layer noise would tend to dominate. However, for lower frequencies, that are predicted to be dominated by transition flow structure acoustic sources, the transition levels exceed the turbulent levels 3 to 5 dB. This confirms that, locally, the transition zone noise affects low frequency signature and has a source order higher than quadrupole.

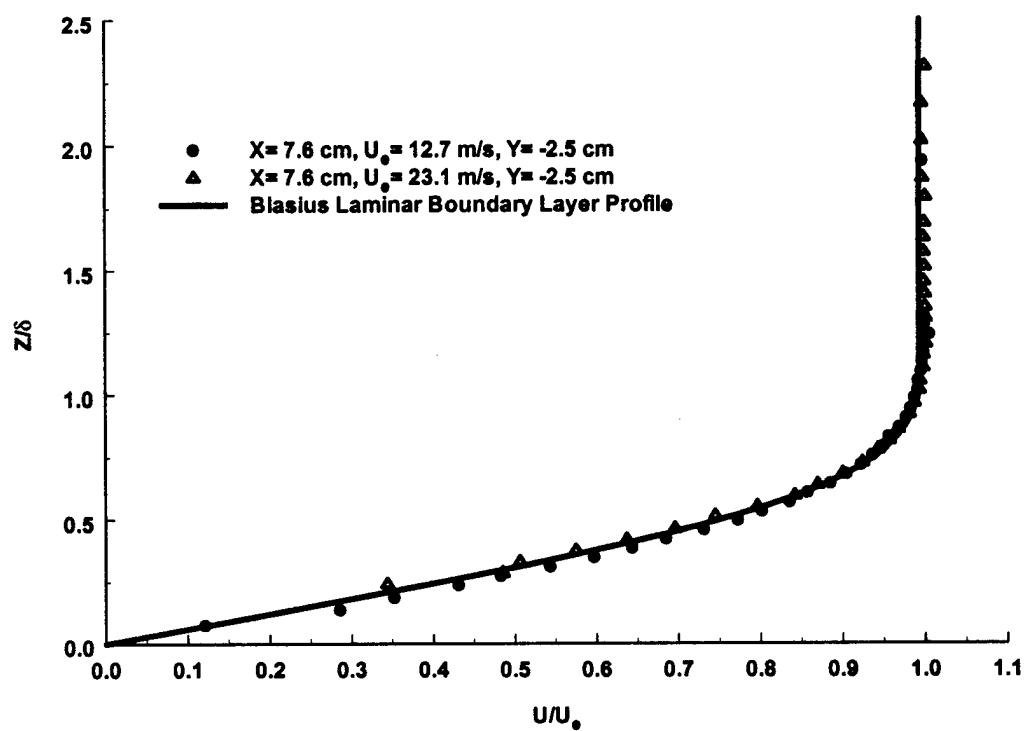


Figure 6.1 Boundary layer profile for $U = 23.1 \text{ m/s}$, $x = 7.6 \text{ cm}$, $y = 2.54 \text{ cm}$ from centerline.

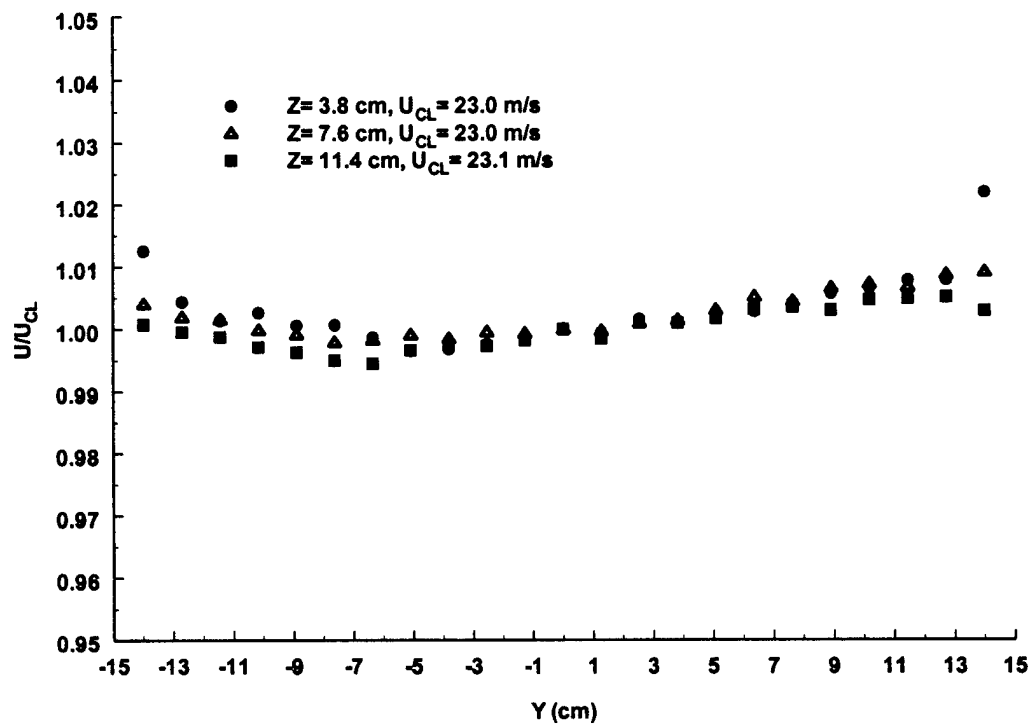


Figure 6.2 Spanwise uniformity of the test section streamwise velocity for $U=23.1 \text{ m/s}$, $x = 7.6 \text{ cm}$, at 25, 50, and 75% of test section height.

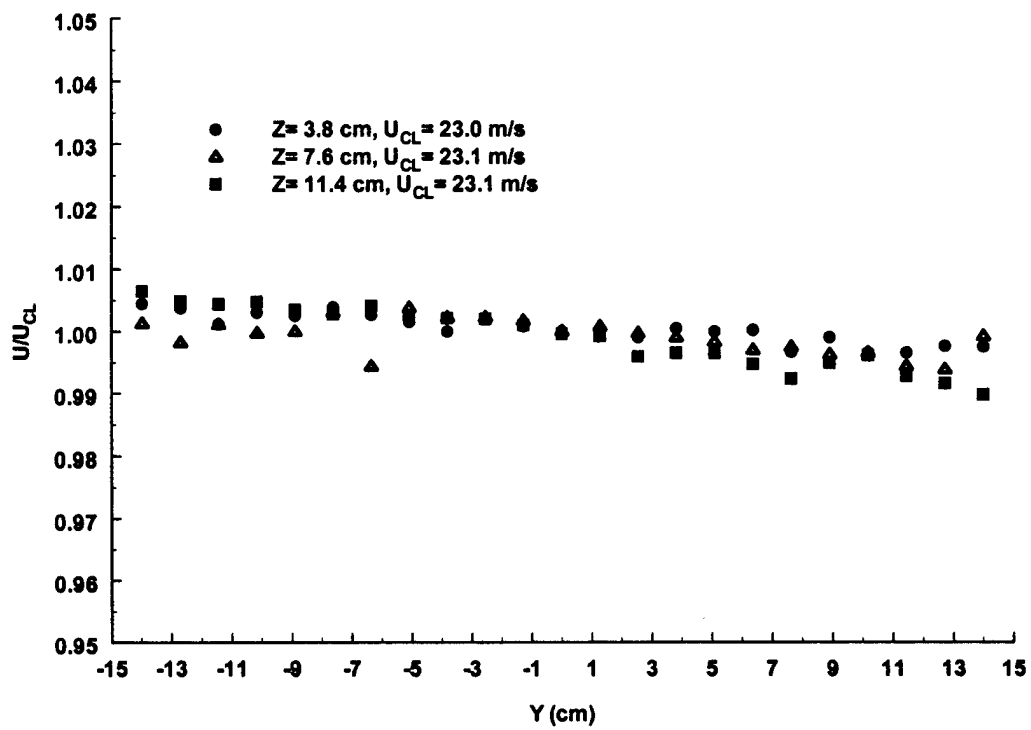


Figure 6.3 Spanwise uniformity of the test section streamwise velocity for $U=23.1 \text{ m/s}$, $x = 77.5 \text{ cm}$, at 25, 50, and 75% of test section height.

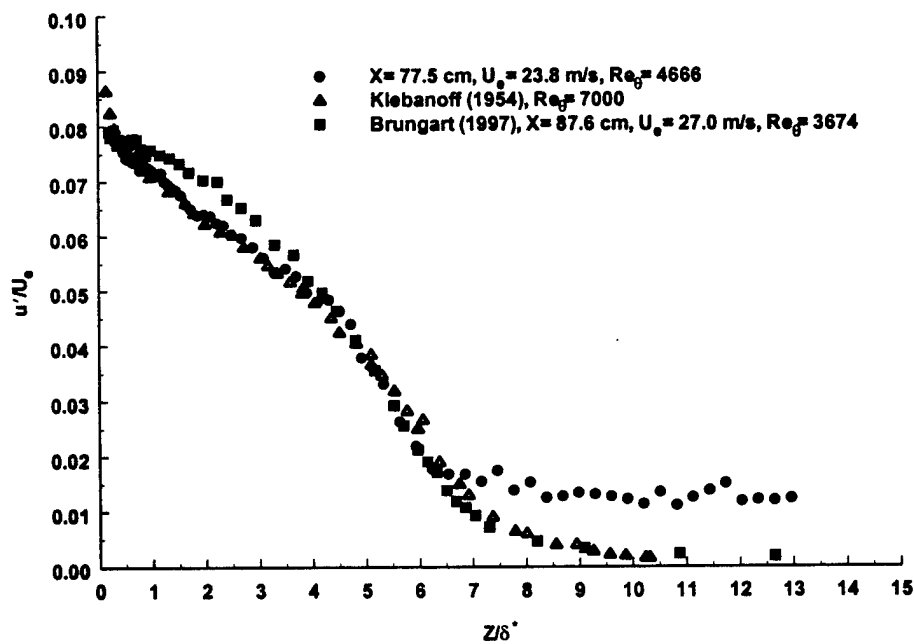
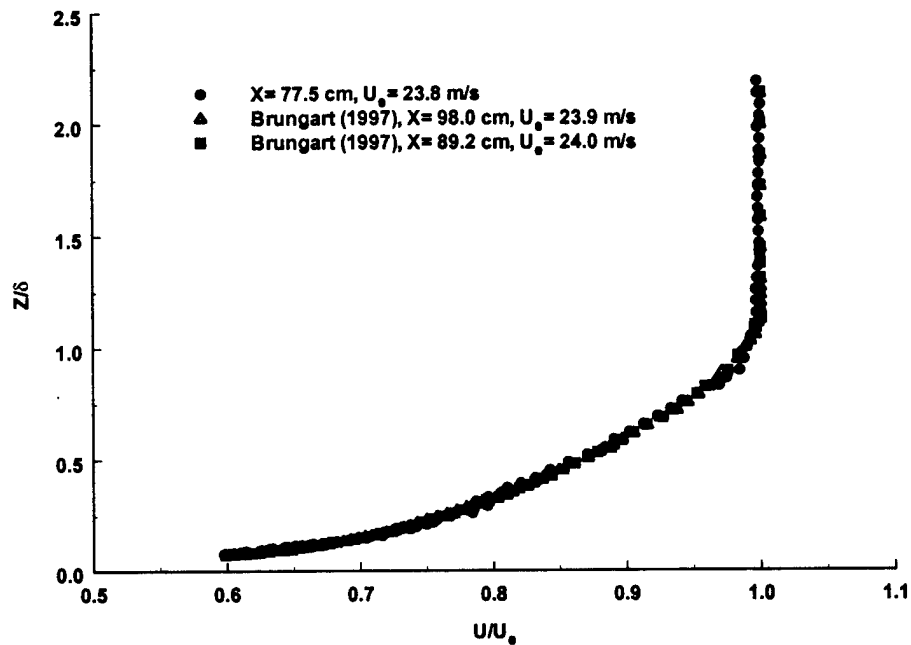


Figure 6.4 Comparison of boundary layer profiles and turbulence intensity profiles tripped, fully turbulent flow for nominal $U = 23.9 \text{ m/s}$ near end of test section.

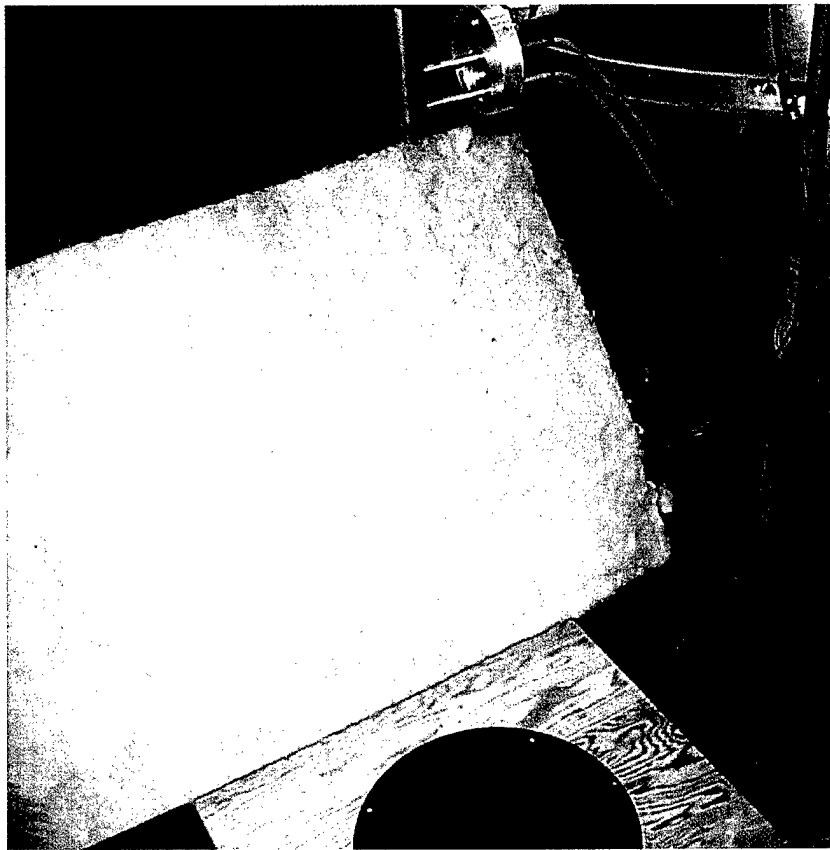


Figure 6.5 Calibration configuration.

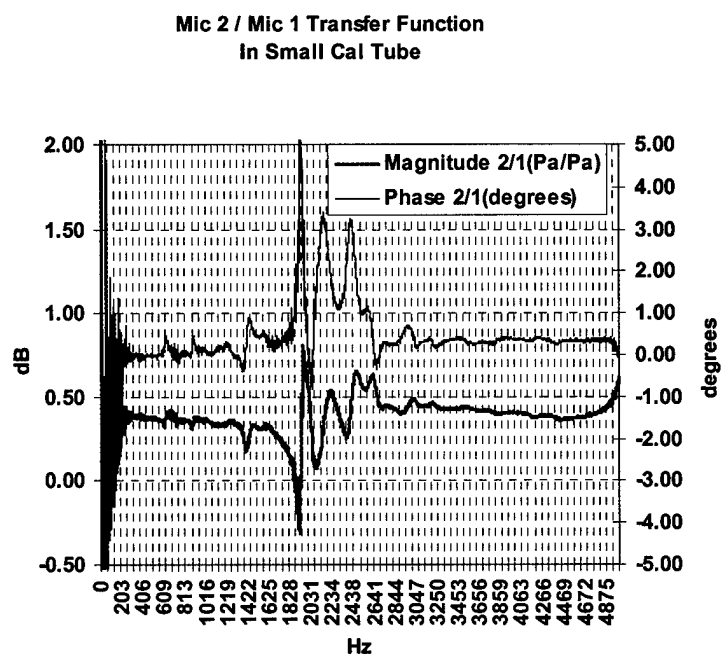


Figure 6.6 Magnitude and phase of microphone mismatch as measured in small calibration tube.

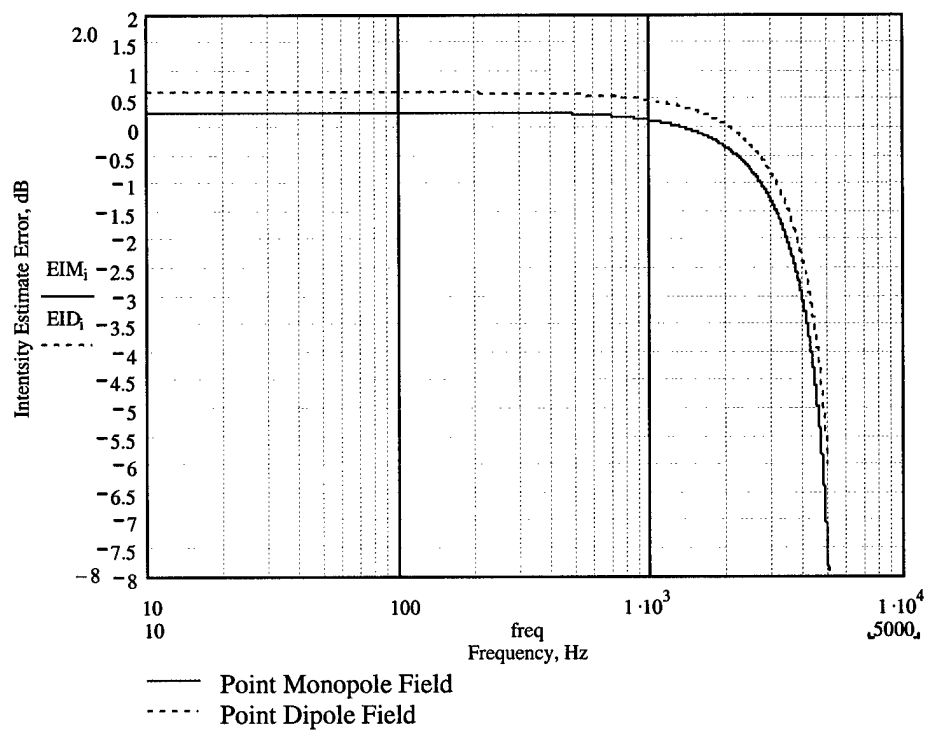


Figure 6.7 Intensity estimate bias errors due to point monopole and dipole source fields for microphone separation of 2.54 cm.

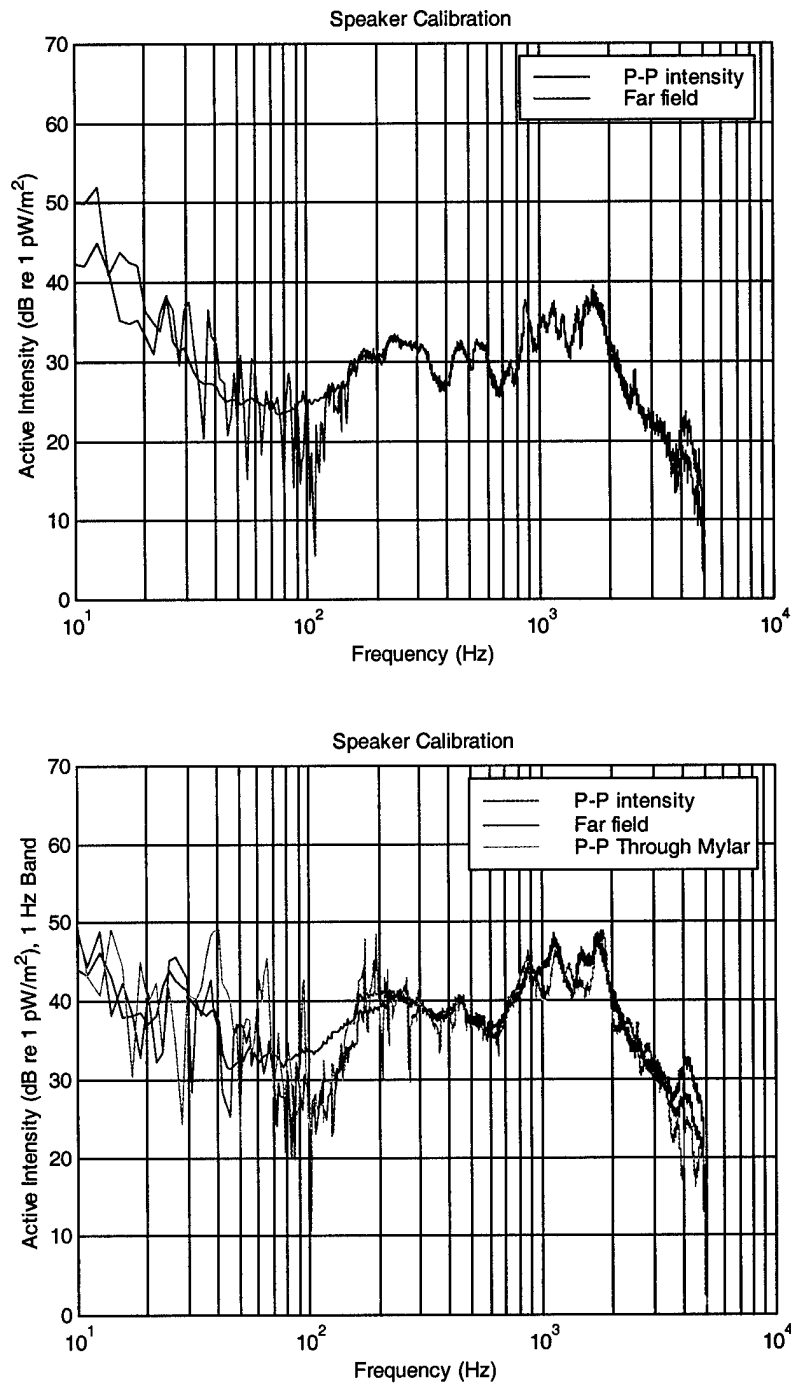


Figure 6.8 Comparison of (a) P-P time-averaged intensity measurement to far field intensity at 0.8m above speaker, and (b) P-P time-averaged intensity measurement with and without mylar to open far field intensity at 0.5m above speaker in 1.6 Hz bands.

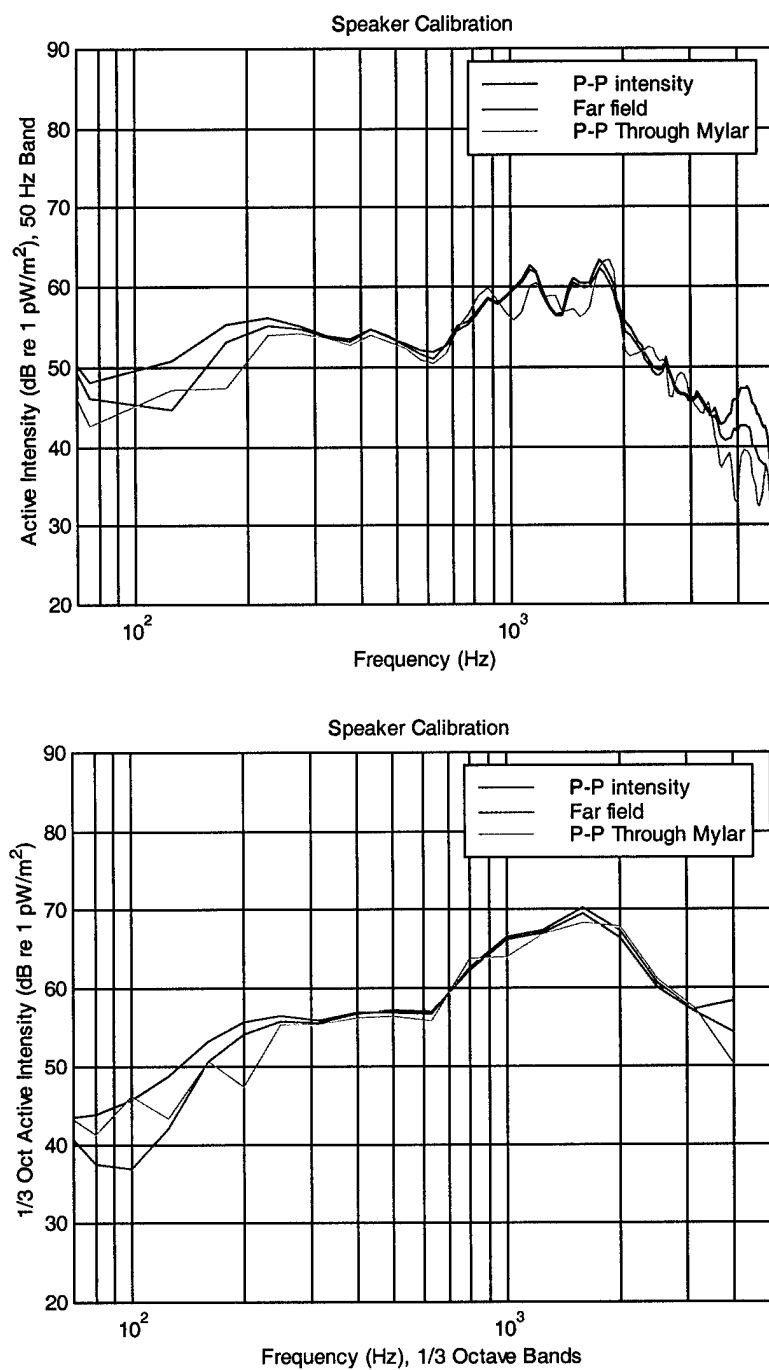


Figure 6.9 Comparison of P-P time-averaged intensity measurement with and without mylar to open far field intensity at 0.5m above speaker in (a) 50 Hz bands and (b) 1/3 octave bands.

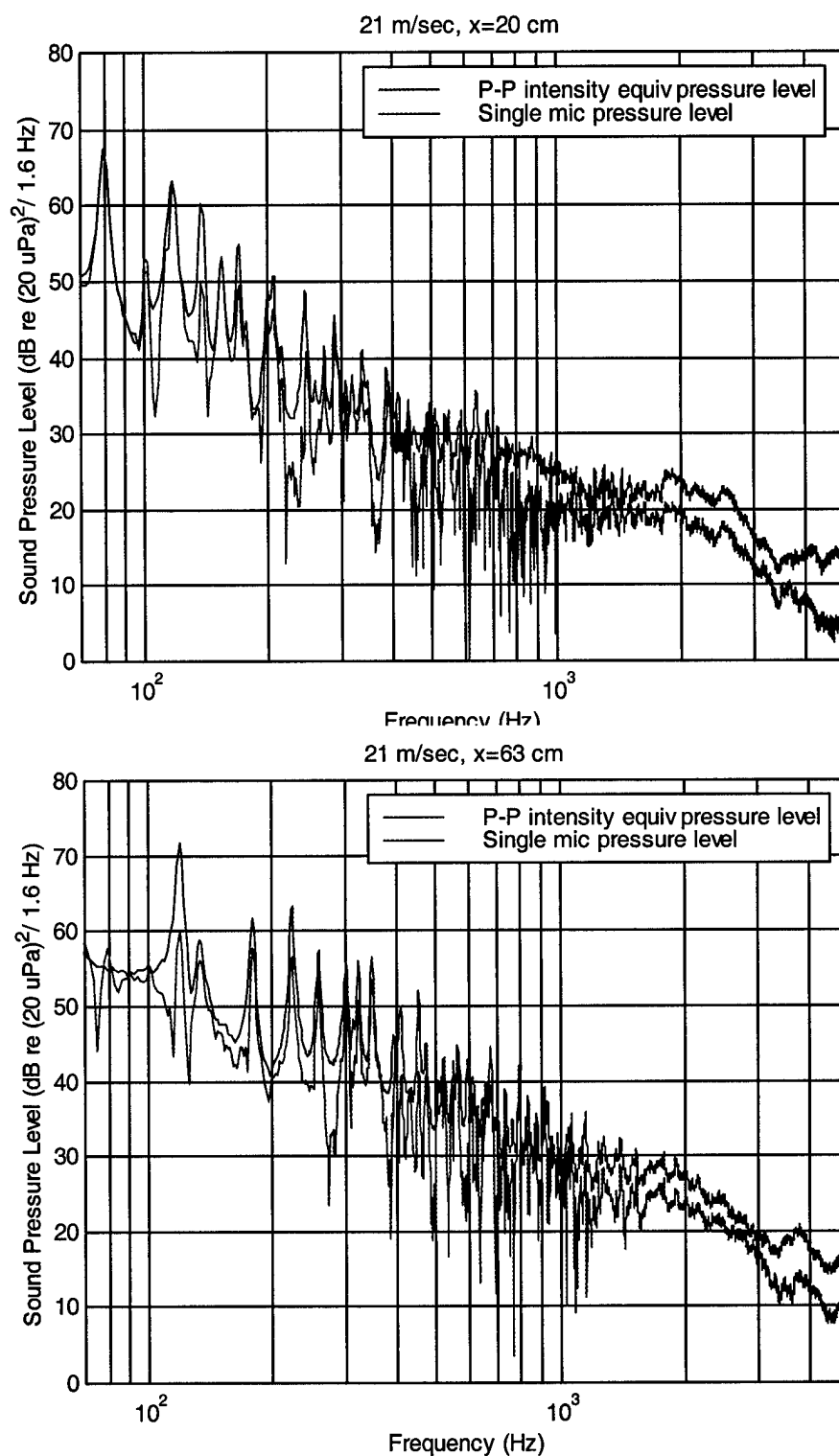


Figure 6.10 Intensity probe gain over a single microphone.

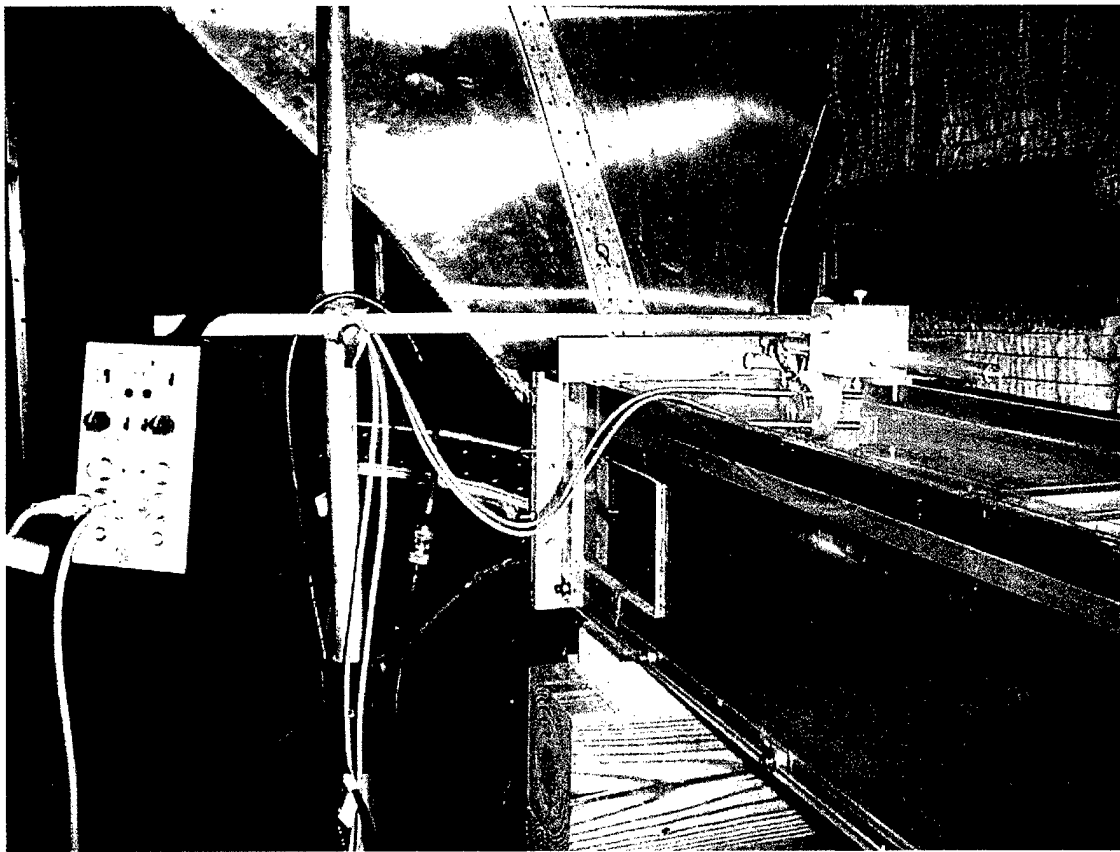


Figure 6.11 Configuration of P-P intensity probe for transition zone measurements.

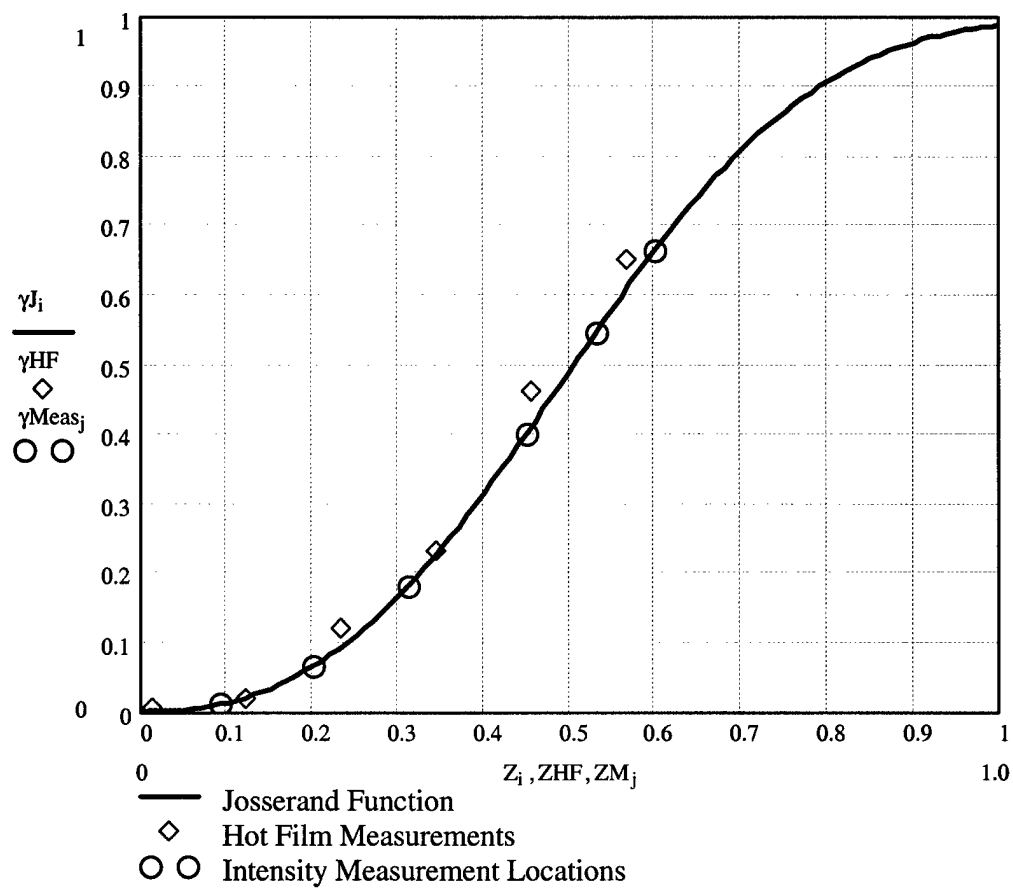


Figure 6.12

Locations and levels of hot film measurements for intermittency compared to Josserand intermittency function and locations of intensity measurements.

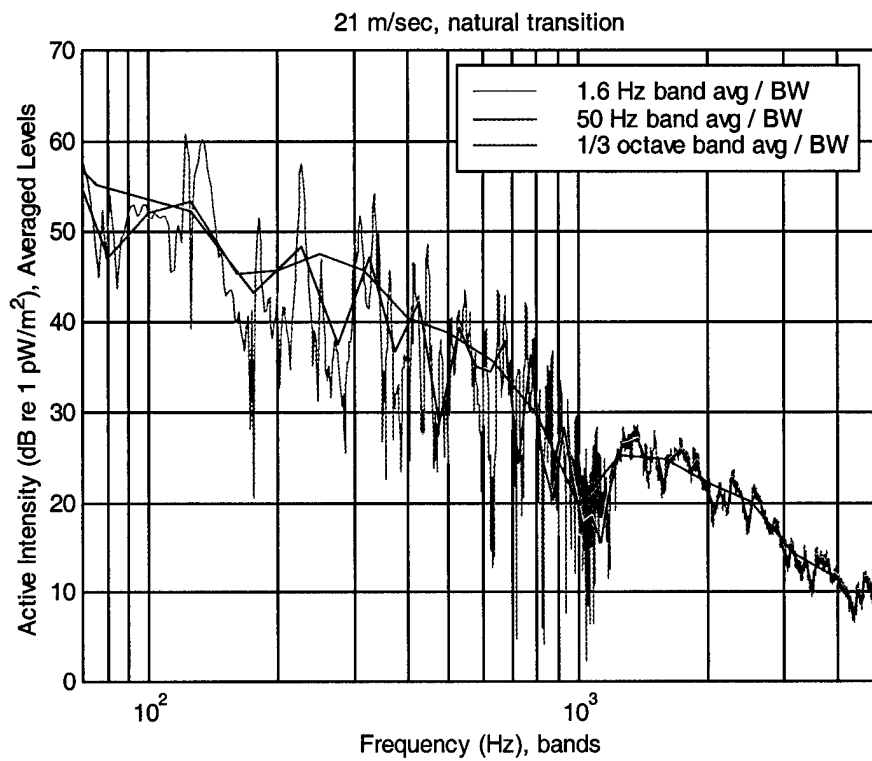


Figure 6.13 Examples of spectrum smoothing achieved through wider band processing.

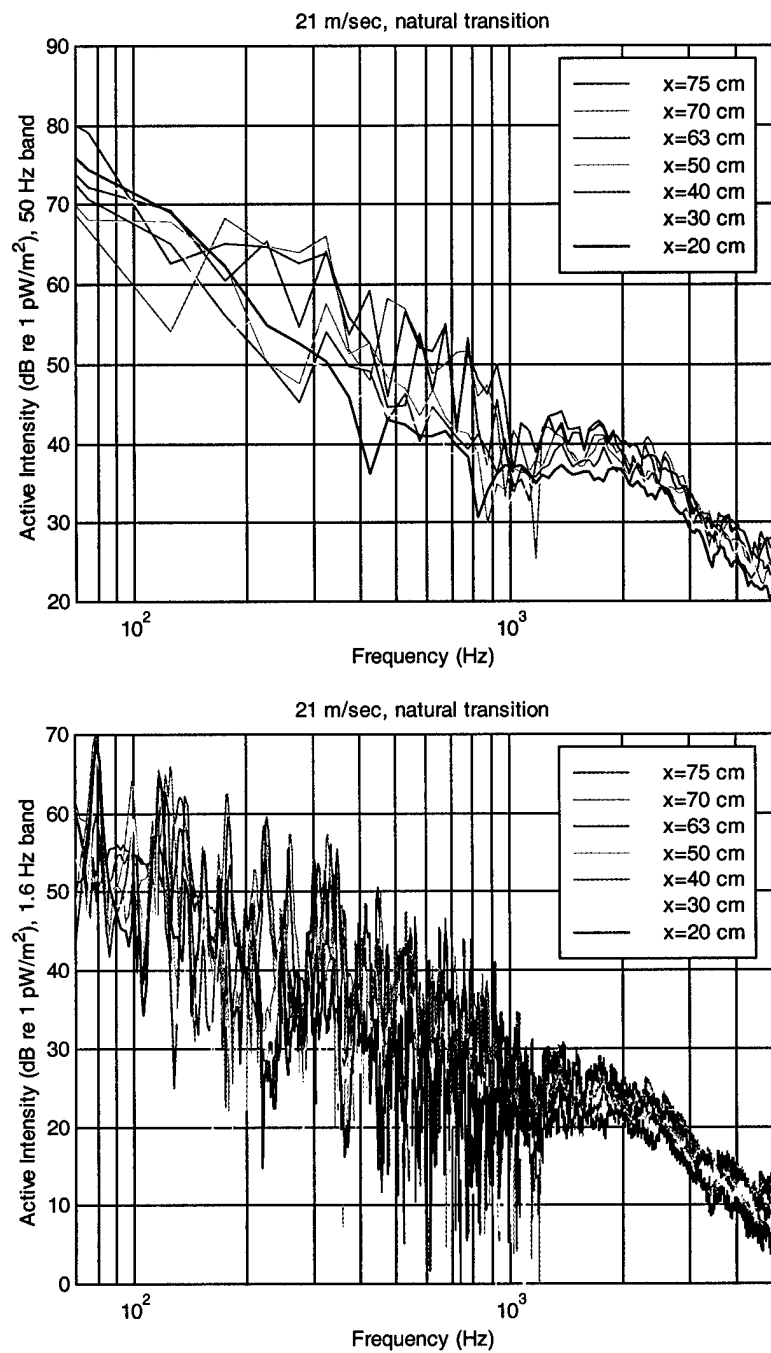


Figure 6.14 Active intensity in 1.6 and 50 Hz processing bands measured for natural transition region of 21 m/s in zero pressure gradient above mylar wall for $-0.03 < Z_x < 0.60$.

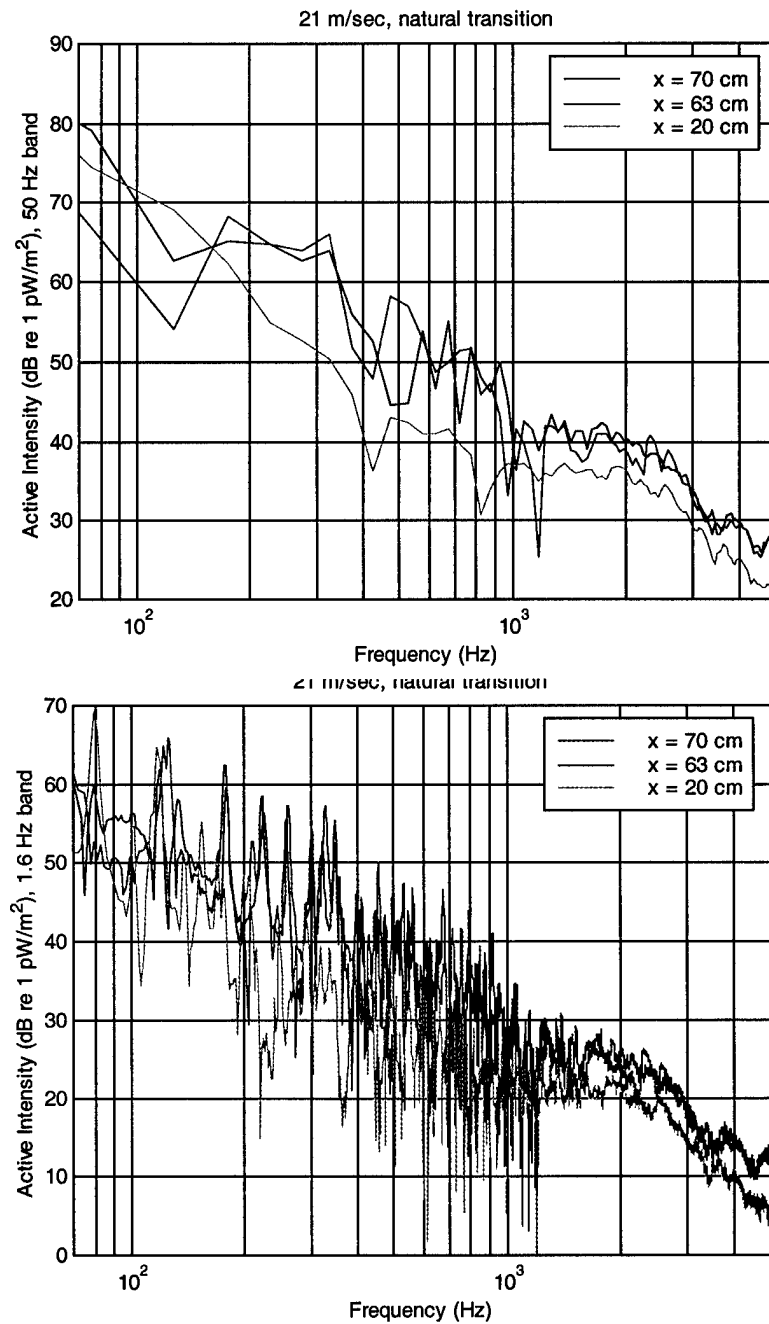


Figure 6.15 Active intensity in 1.6 and 50 Hz processing bands measured for natural transition region of 21 m/s in zero pressure gradient above mylar wall for $Z_x = -0.03, 0.45$ and 0.53 .

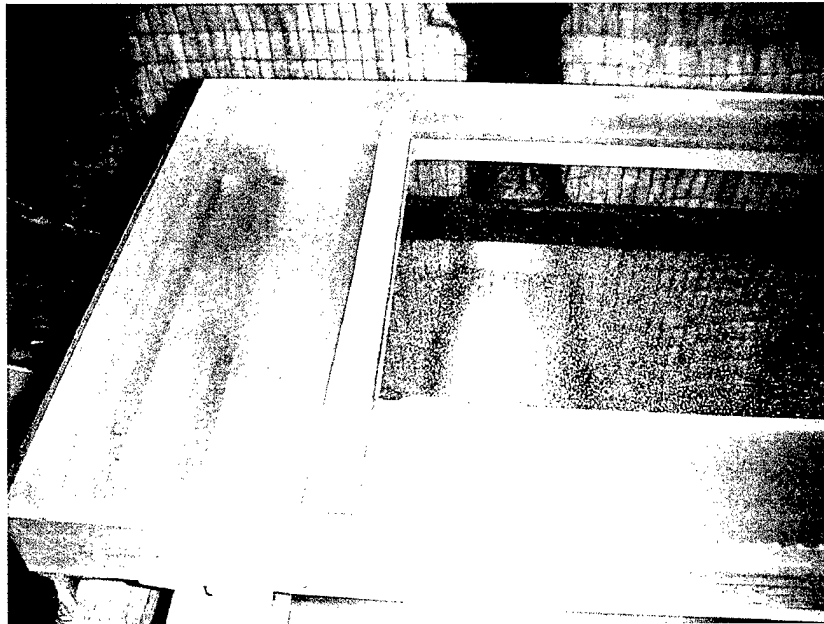
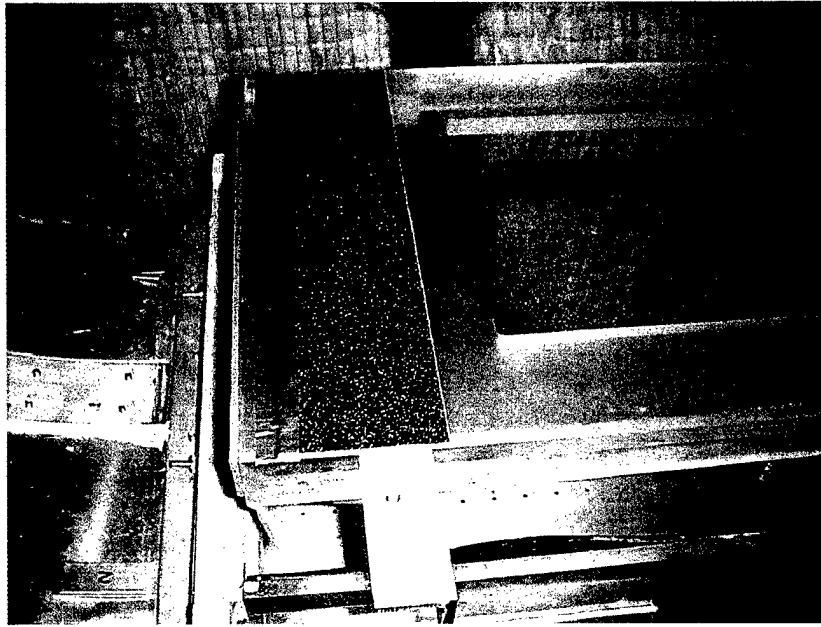


Figure 6.16 Boundary layer trip of 50 grit sandpaper in 6 cm long strip at $x = 20$ cm and boundary layer stimulation of 150 grit sandpaper in two 10mm long strips at $x = 12$ and 15 cm .

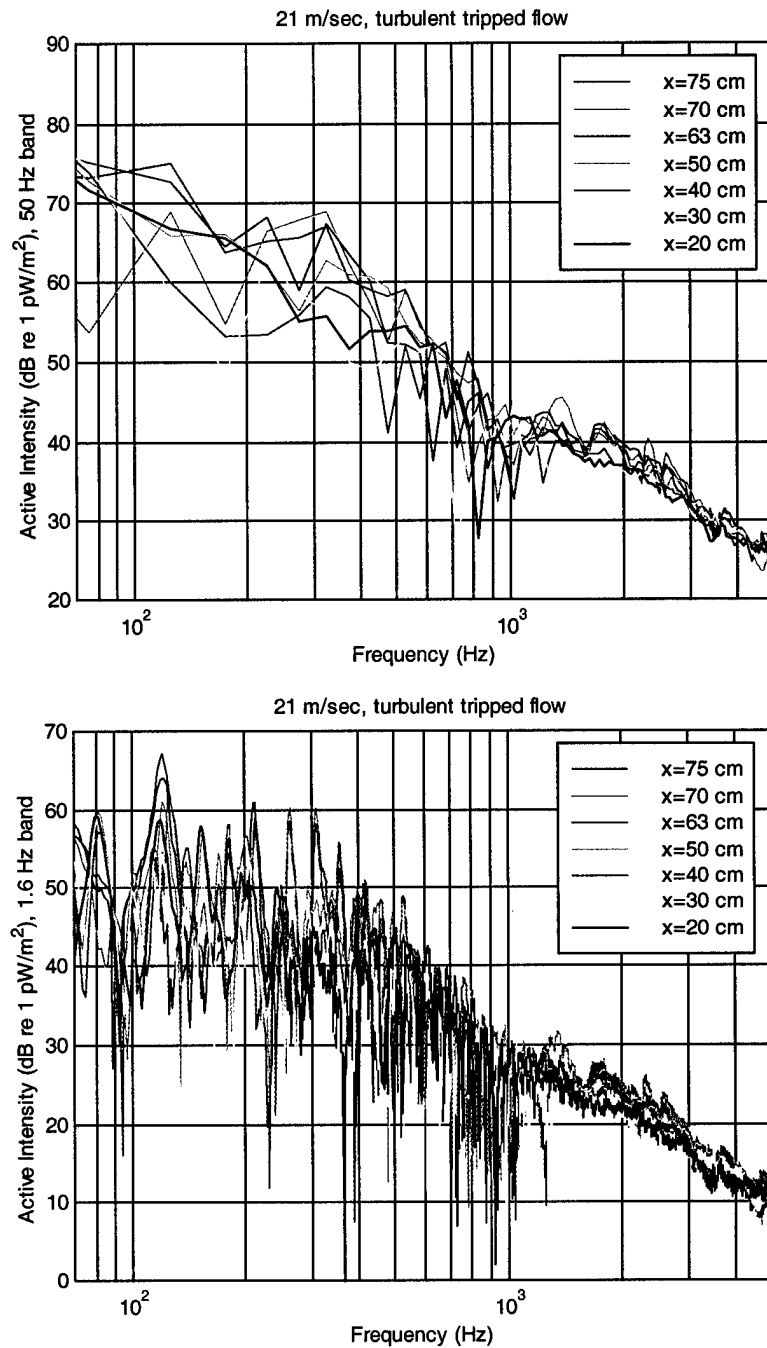


Figure 6.17 Active intensity in 1.6 and 50 Hz processing bands measured for tripped turbulent flow at 21 m/s in zero pressure gradient above mylar wall for $-0.03 < Z_x < 0.60$.

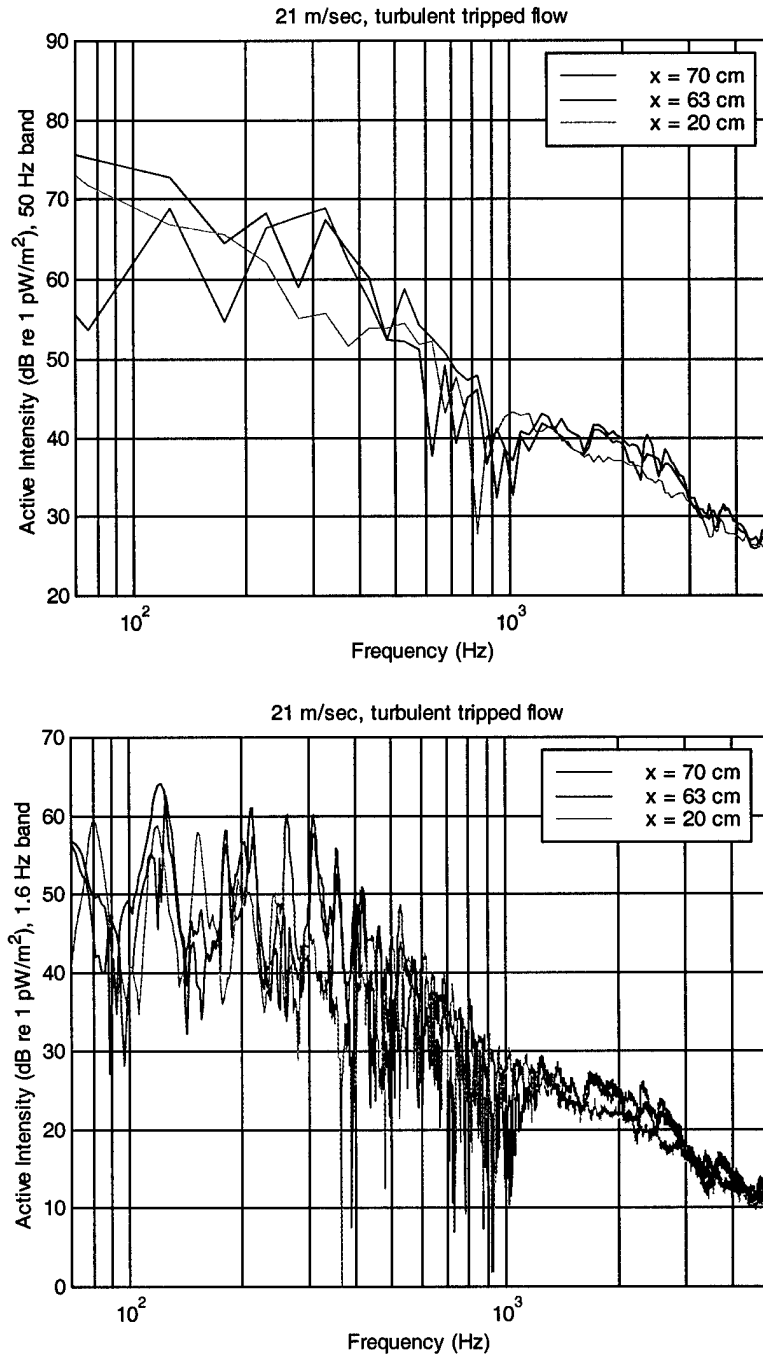


Figure 6.18 Active intensity in 1.6 and 50 Hz processing bands measured for tripped turbulent flow at 21 m/s in zero pressure gradient above mylar wall for $Z_x = -0.03, 0.45$ and 0.53 .

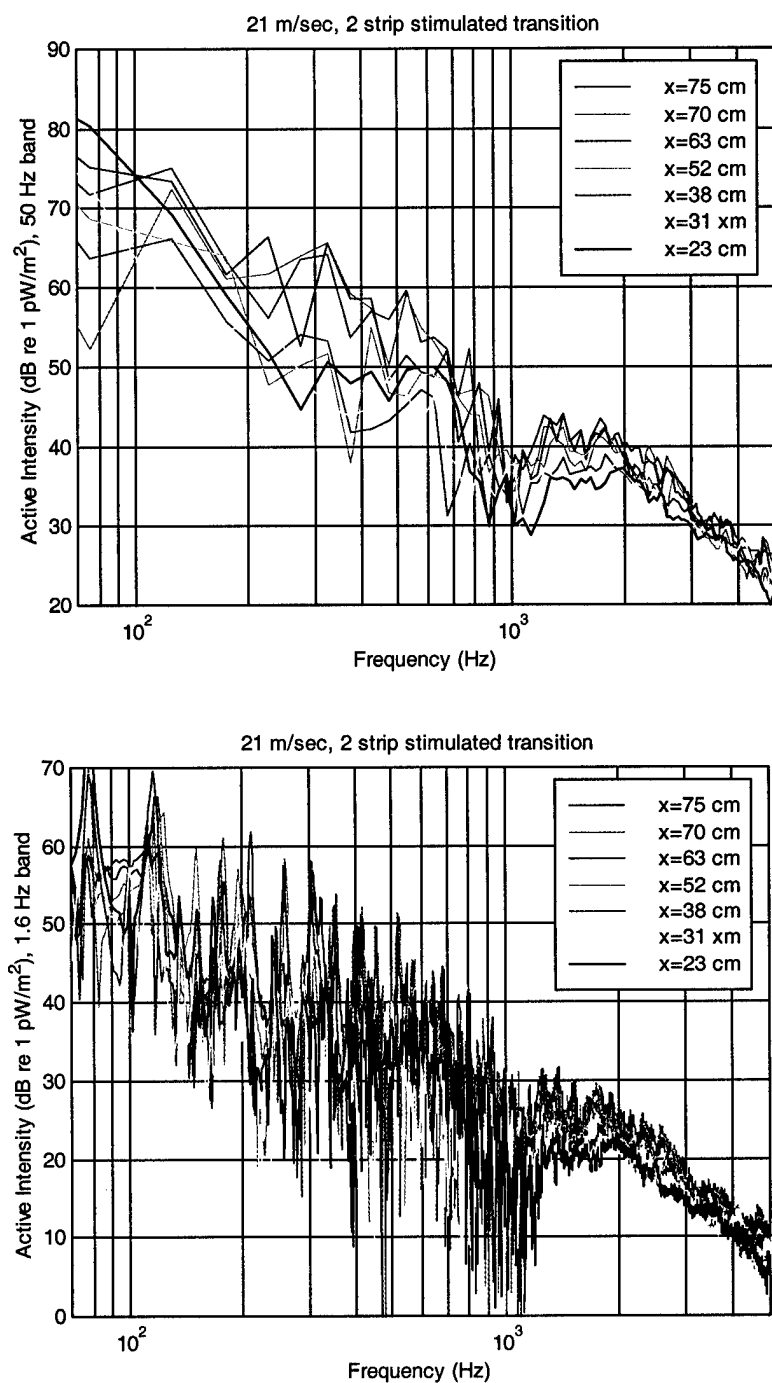


Figure 6.19 Active intensity in 1.6 and 50 Hz processing bands measured for stimulated transition region at 21 m/s in zero pressure gradient above mylar wall for $-0.03 < Z_x < 0.60$.

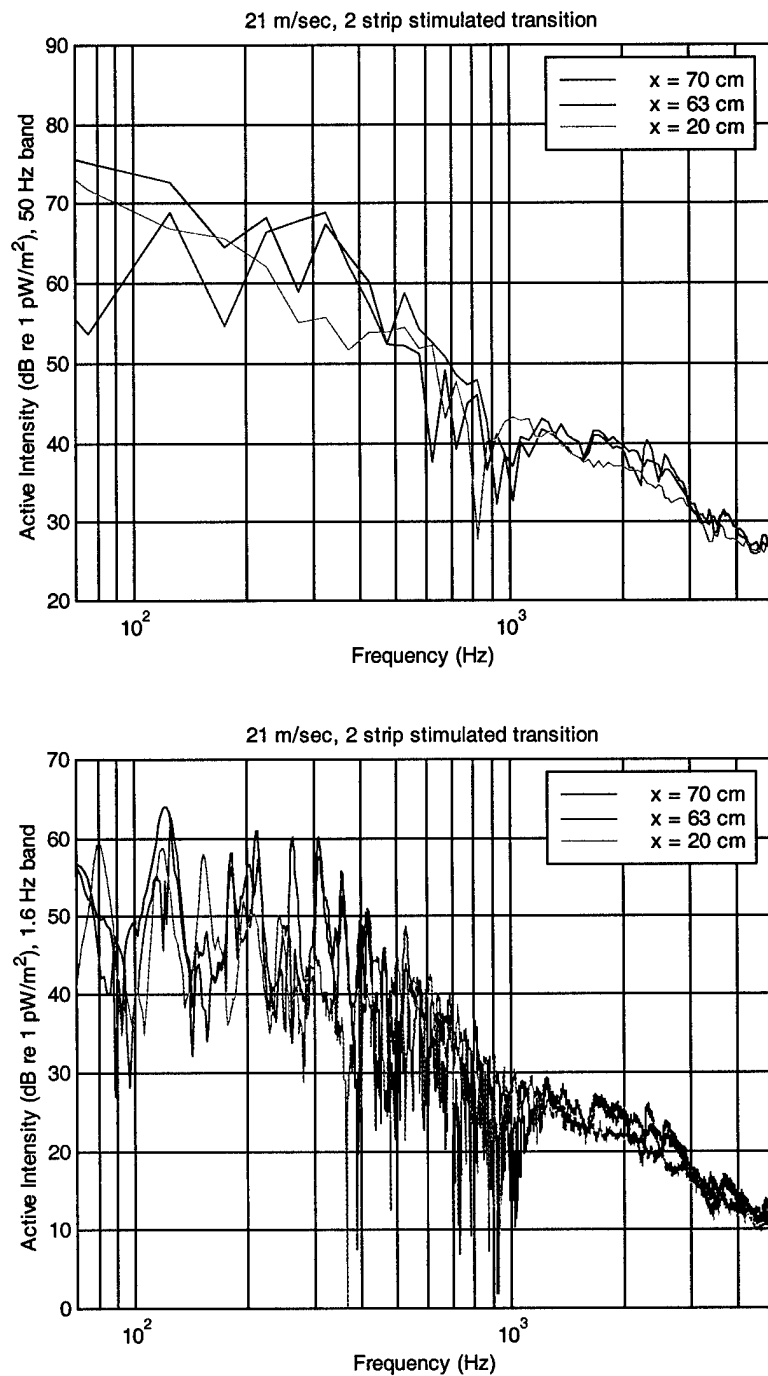


Figure 6.20 Active intensity in 1.6 and 50 Hz processing bands measured for stimulated transition region at 21 m/s in zero pressure gradient above mylar wall for $Z_x = -0.03, 0.45$ and 0.53 .

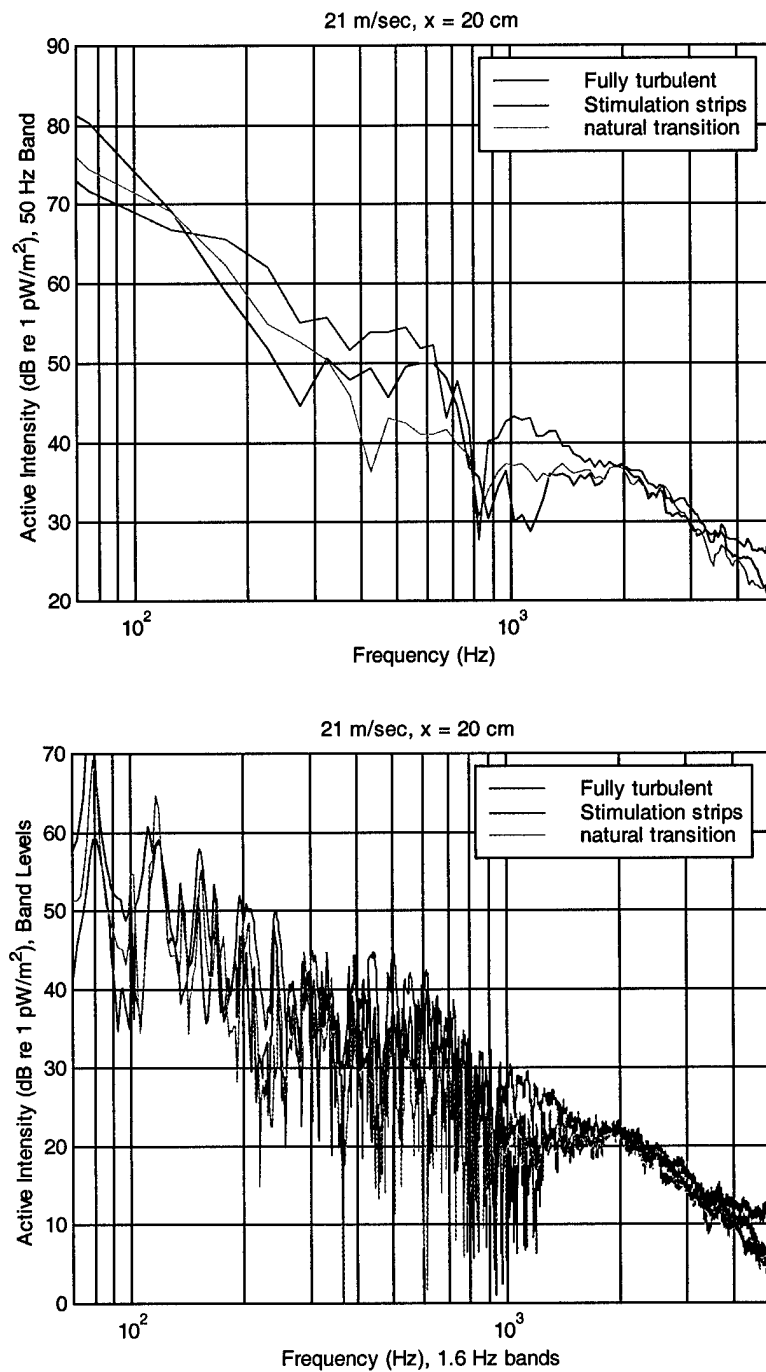


Figure 6.21 Comparison of active intensity in 1.6 and 50 Hz processing bands measured for natural and stimulated transition and tripped turbulent flow at 21 m/s in zero pressure gradient above mylar wall for $Z_x = -0.03$.

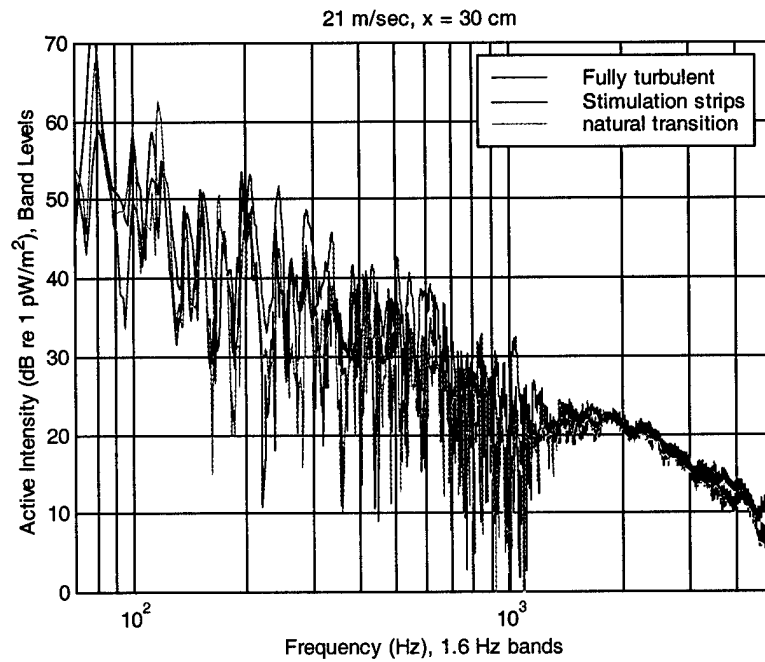
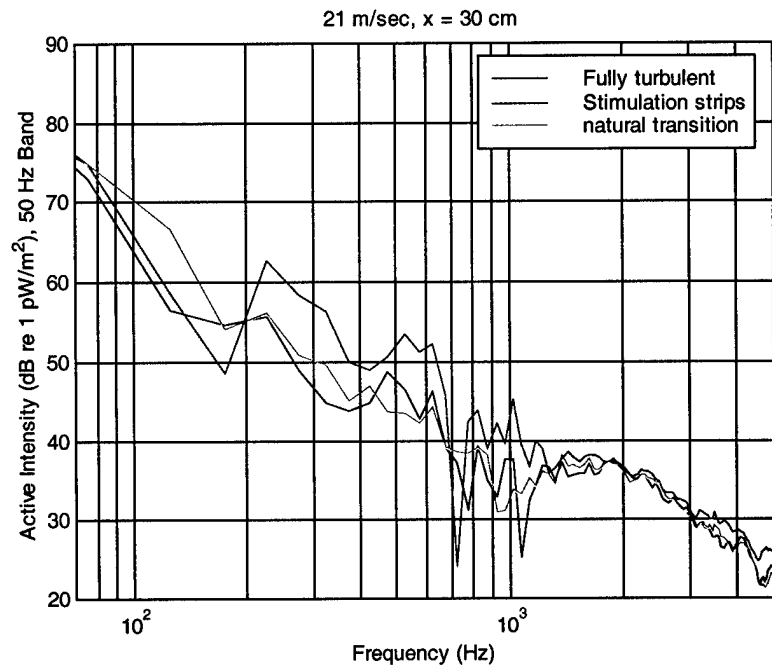


Figure 6.22 Comparison of active intensity in 1.6 and 50 Hz processing bands measured for natural and stimulated transition and tripped turbulent flow at 21 m/s in zero pressure gradient above mylar wall for $Z_x = 0.09$.

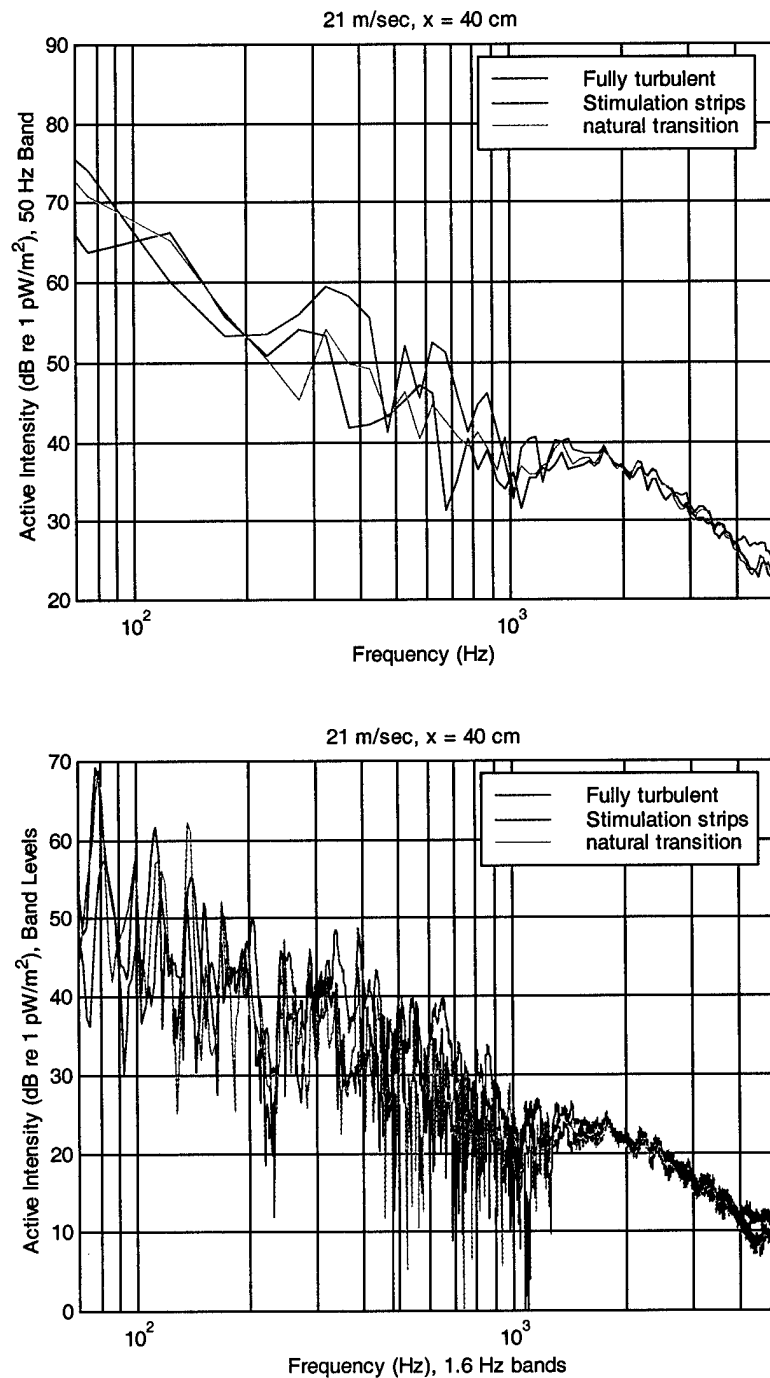


Figure 6.23 Comparison of active intensity in 1.6 and 50 Hz processing bands measured for natural and stimulated transition and tripped turbulent flow at 21 m/s in zero pressure gradient above mylar wall for $Z_x = 0.20$.

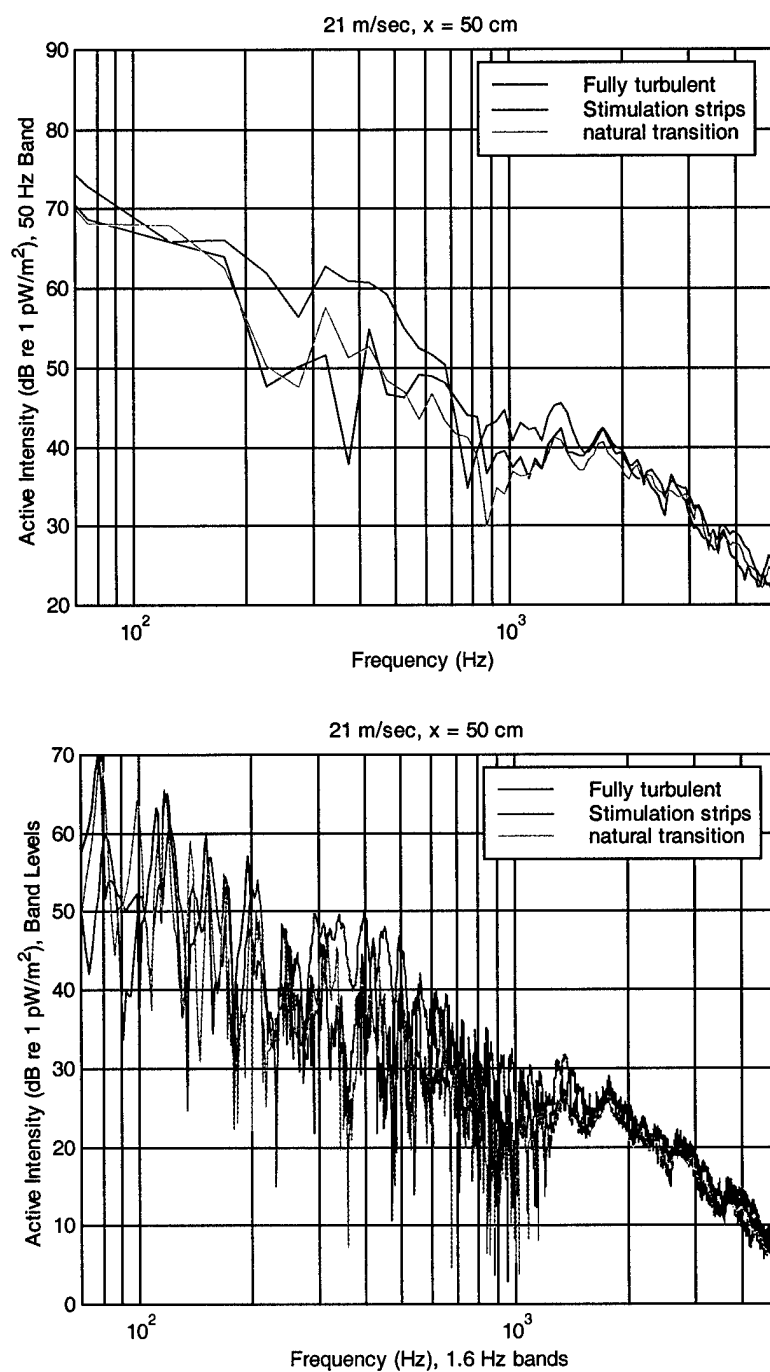


Figure 6.24 Comparison of active intensity in 1.6 and 50 Hz processing bands measured for natural and stimulated transition and tripped turbulent flow at 21 m/s in zero pressure gradient above mylar wall for $Z_x = 0.31$.

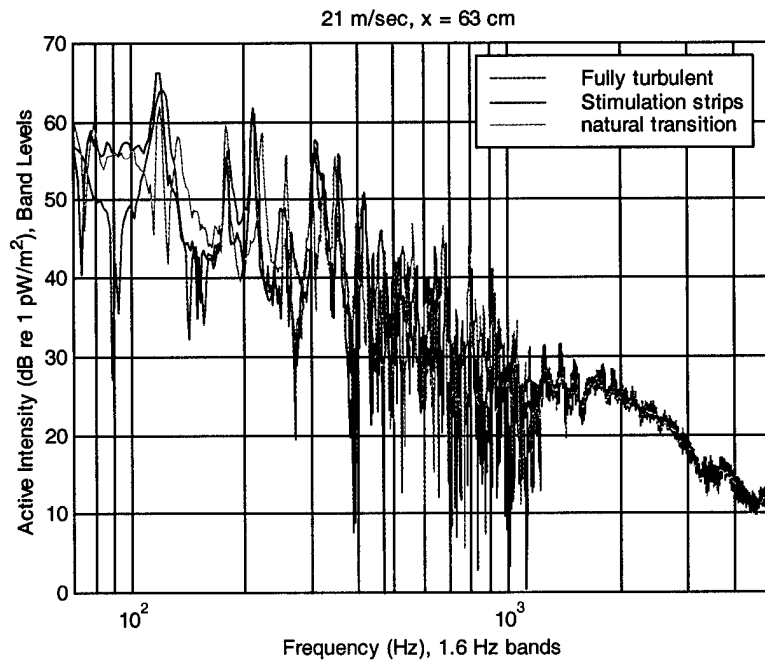
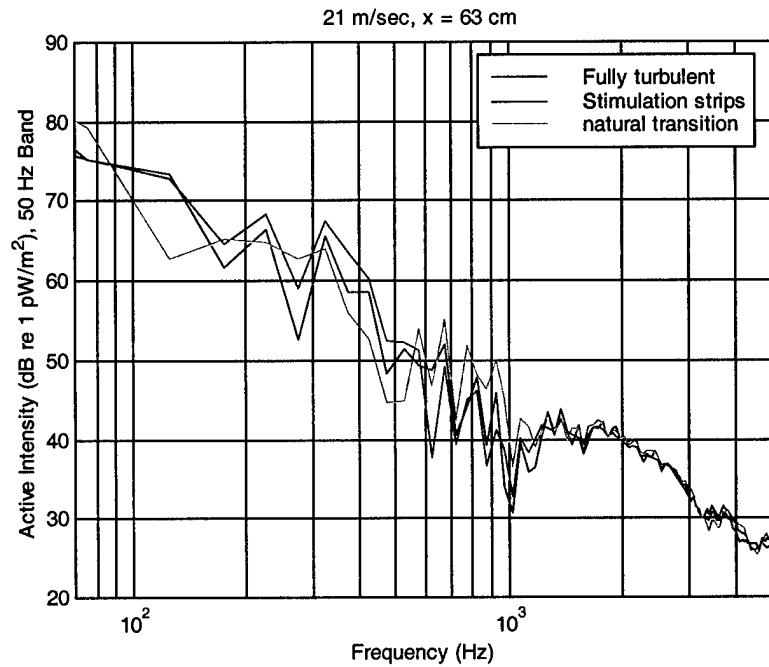


Figure 6.25 Comparison of active intensity in 1.6 and 50 Hz processing bands measured for natural and stimulated transition and tripped turbulent flow at 21 m/s in zero pressure gradient above mylar wall for $Z_x = 0.45$.

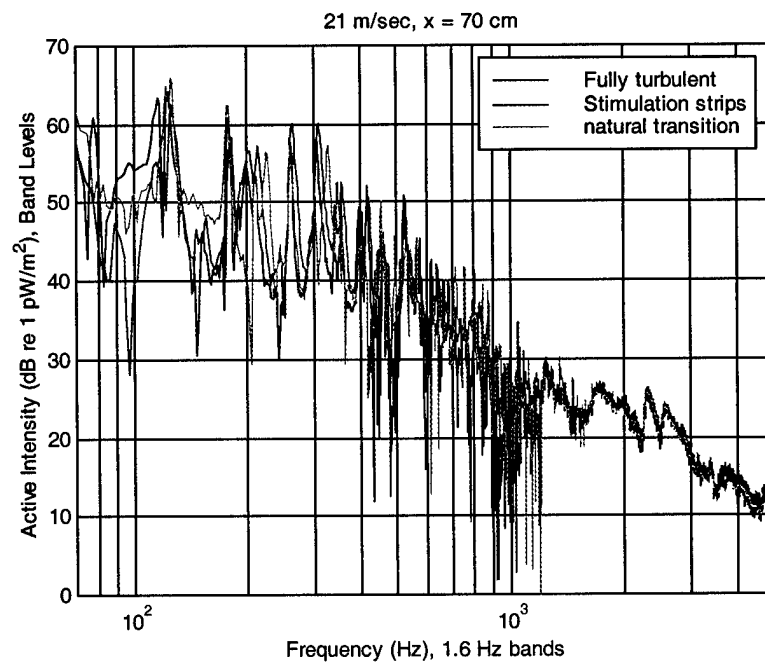
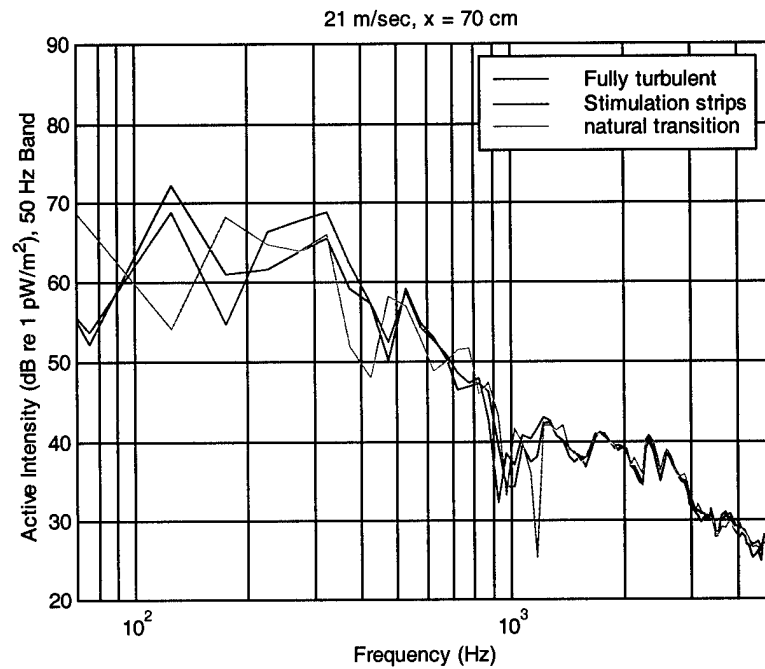


Figure 6.26 Comparison of active intensity in 1.6 and 50 Hz processing bands measured for natural and stimulated transition and tripped turbulent flow at 21 m/s in zero pressure gradient above mylar wall for $Z_x = 0.53$.

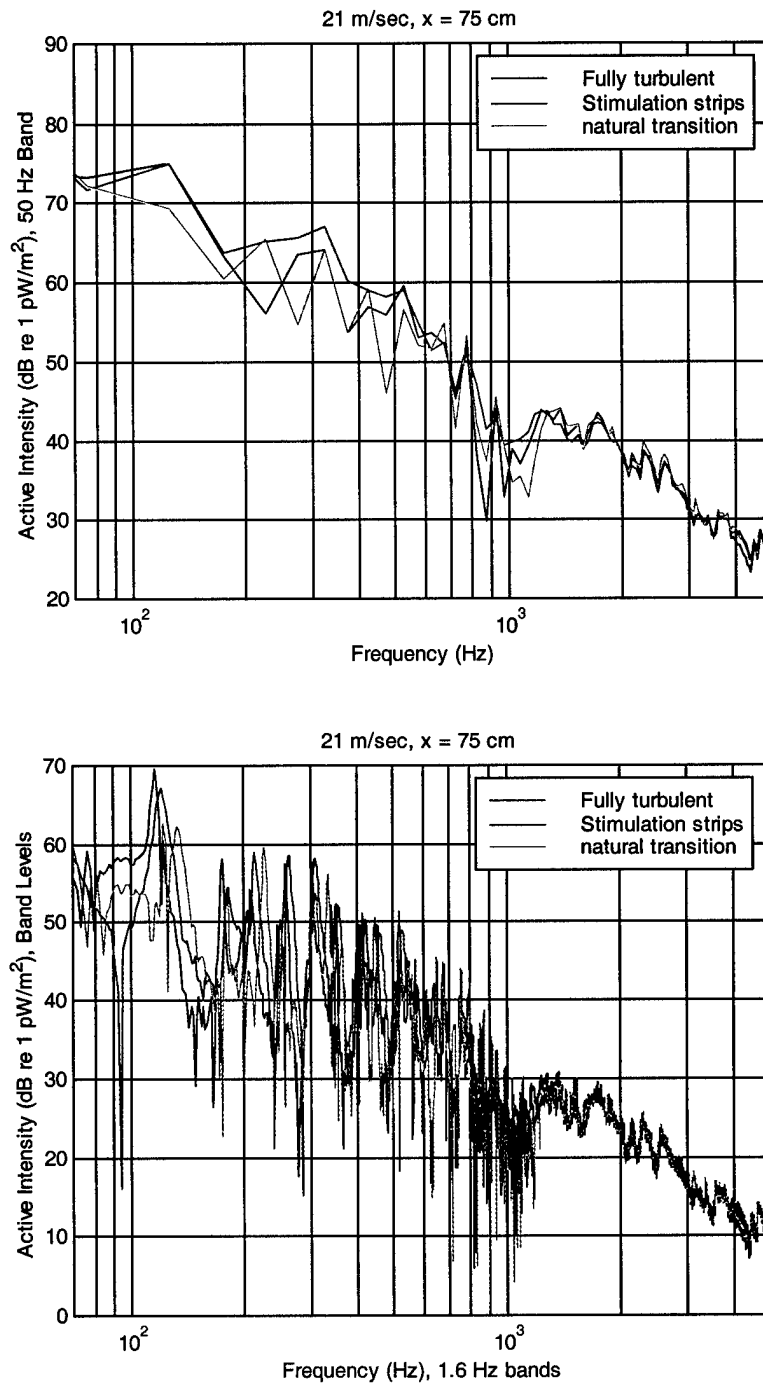


Figure 6.27 Comparison of active intensity in 1.6 and 50 Hz processing bands measured for natural and stimulated transition and tripped turbulent flow at 21 m/s in zero pressure gradient above mylar wall for $Z_x = 0.60$.

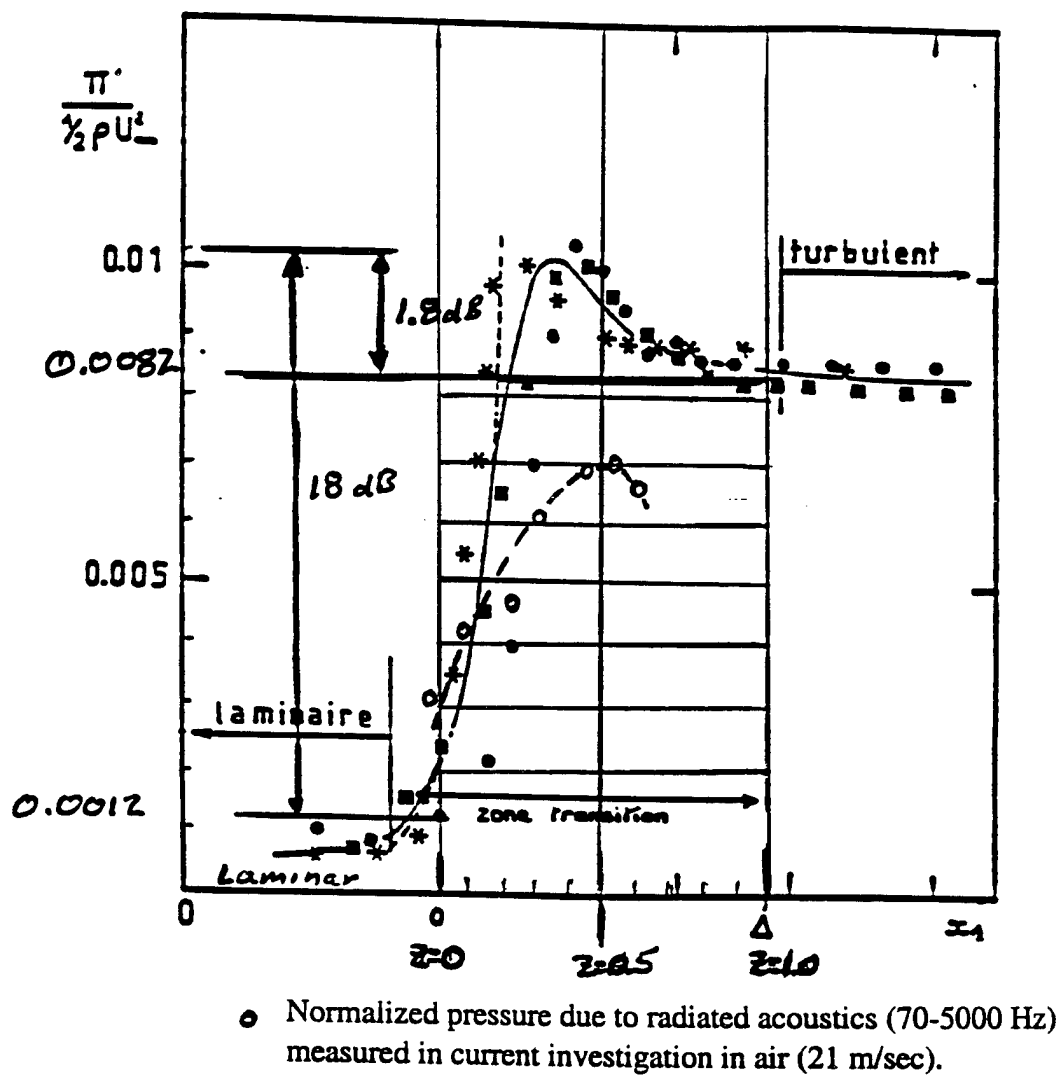
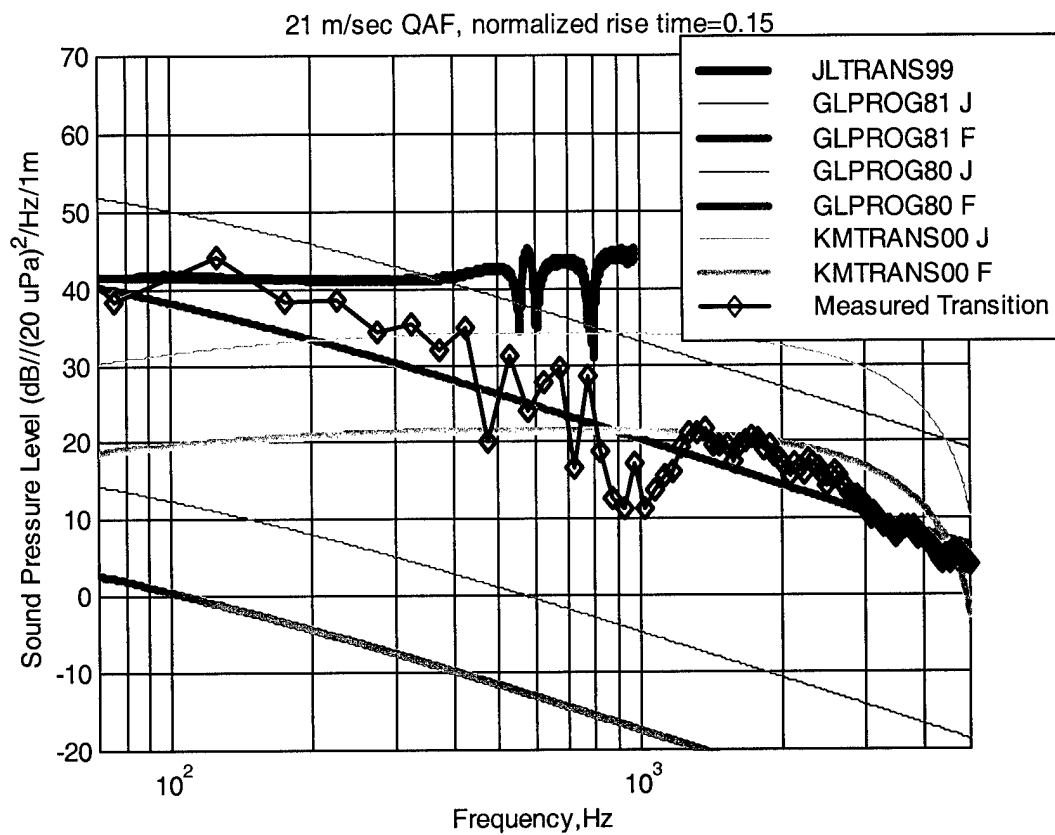


Figure 6.28 Fluctuating wall pressure measurements made in air by Dufourq (1984).



(Measured data presented with 50 Hz processing but corrected to 1 Hz spectral level)

Figure 6.29 Comparison of transition noise model predictions with measured directly radiated sound pressure levels.

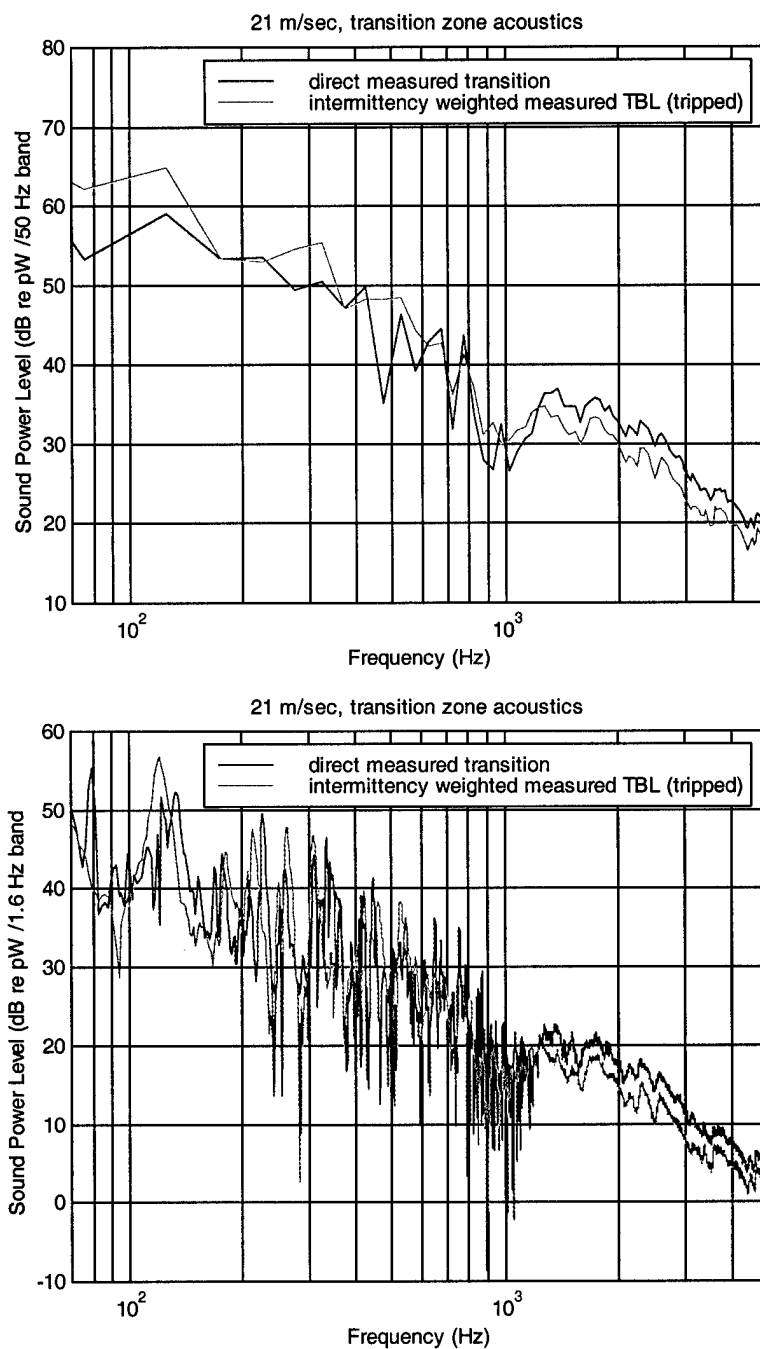


Figure 6.30 Comparison of intermittency weighted measured turbulent boundary layer noise with measured transition zone directly radiated sound pressure levels.

CHAPTER 7

CONCLUSIONS AND FUTURE WORK

7.1 Conclusions

The research described in this dissertation has resulted in the following unique contributions and conclusions.

1. First unambiguous direct measurement of the acoustic radiation from a boundary layer transition zone.
2. Confirmed that the wall pressure peak measured by Dufourq (1984) in the range $0.4 < Z_x < 0.55$ under a transition zone is due to the radiated acoustic pressure.
3. The acoustic theory developed by Lauchle using the Liepmann fluctuating displacement thickness approach, and an infinite flat plate Green's function with monopole source field appears to be incorrect when compared against the measurements. Lauchle's model has been improved by using a dipole source field based on the Krane (1992) water channel data, and on qualitative observations of the flow structures present during transition. The true axis angle of the dipole relative to the wall has yet to be determined. There may even be an occurrence of multiple angles in a natural transition zone.
4. Rather than using a constant dipole axis (source separation distance), which results in unrealistic high-frequency content of the predicted transition noise (extensive sinusoidal null variation in levels), a statistical estimate is constructed by treating the dipole axis as a random variable. This variable is assumed

uniformly distributed over physically predictable limits. This results in a smoothed spectral estimate and better match with the measured data. This prediction model provides the best fit to the measured data for frequencies above 300 Hz. Because of measurement uncertainty, a proper comparison cannot be made below that frequency at this time. In addition, the angle of the dipole may vary depending on the growth dynamics of the turbulent spot. A treatment similar to the one described for dipole source separation distance in section 3.1.2 could also be incorporated for this dipole axis angle.

5. Demonstrated that the intermittency-weighted, fully turbulent boundary layer radiated sound power level is a good approximation to the directly radiated sound power level from the transition zone. The level was found to be about 3 dB below that of the transition zone noise for $f < 1$ kHz and 3 dB high for $f > 1$ kHz.
6. The two-fluids model proposed by Lagier and Sornette offers no real prediction benefit over the Lauchle model once the spatial dependence is brought back inside the integral and given the simplifications that were necessary to make the two fluids model integrable.

7.2 General Observations on Transition Noise

The following are observations that have resulted from the cumulative knowledge gained over the course of this research including the background materials and understanding of the previous works of others.

1. Most of the focus in boundary layer transition acoustics in the last eight years has

been on developing direct numerical simulation (DNS) approaches to modeling using spatial and temporal approaches to solving the complete Navier-Stokes equations. Based on the results of Wang, et al. (1996), there appears to be more “noise” in the calculation than is produced by the actual fluid dynamics. However, the value of DNS may really be to provide insight on the necessary modeling of substructure dynamics that influence the spatial definition of the normal velocity used in the fluctuating displacement thickness model and contribute in their own right to the acoustic pressure particularly influencing the near-field. This bridges the gap to some extent between the two fluids model using the Lighthill analogy and the Liepmann approach used for the fluctuating displacement thickness model.

2. The predicted low frequency contribution of transition noise seems to be significant, particularly for $f < 300$ Hz and higher mean flow velocities. Audet et al. (1989a, Figure 10) show this as a domination of the low polar order growth mechanism of the spot (a la Lauchle) over the quadrupole source due to the TBL statistics in the turbulent spots. Howe’s model (1999) for the effect of a transition zone near the leading edge of a hydrofoil clearly show an enhancement of the same low frequency regime due to the transition zone.
3. Laboratory measurements performed prior to this dissertation indicate that transition zone noise levels may be contaminated by other sources. It is suspected that one contaminating source for early measurements in this investigation (with an early QAF configuration) was trailing edge noise when a jet was discharging

across a flat plate. However, the axisymmetric body tests by Perraud (1989) indicated propagation of acoustic noise from the transition region to sensors in the laminar flow zone. The results reported here qualitatively supports this finding.

4. Transition in an adverse pressure gradient will result in higher radiated and structural excitation levels in comparison to transition in a zero pressure gradient. Huang and Shen (1989) found wall pressure levels 2 to 3 times higher for transition in adverse pressure gradients compared to TBL wall pressure levels. Mautner and Van Atta (1982) found rms wall pressures for individual turbulent spots to be 0.010-0.015 of dynamic pressure ($\frac{1}{2} \rho U_o^2$) for zero and favorable pressure gradients and 0.015-0.030 of dynamic pressure in adverse gradients. More importantly, in the adverse gradient, the wall pressure spectrum was nearly constant magnitude with increasing frequency rather than the typical decreasing slope. This is enhanced further if transition is induced by laminar boundary layer separation and re-attachment. In particular, Huang and Shen found that wall pressures in reattachment zones for laminar separation were 10 to 15 times higher. Hwang and Shang (1989) and Hwang and Maidanik (1990) have worked on approaches for modeling the coupling of these wall pressures within transition zones with the underlying structure.
5. The preceding observation is perhaps what should command our continued interest because of the engineering relevance associated with forebodies of bodies of revolution and for airfoil leading edges where acoustic sources may be located. Just as trailing edge flows are critical to the direct radiation, excitation, re-

radiation and scattering of noise at airfoil trailing edges (see Brooks and Hodgson, 1981 and Gershfeld, 1997), so may transition near the leading edge of an airfoil act as a noise source. Of course, this is quite dependent upon the chordwise distribution of thickness for the airfoil and the local radii of curvature (Howe, 1981).

7.3 Recommended Future Work

The recommendations for future work are as follows.

- CFD Validation - More experimental data will be needed at increasing Reynolds numbers to validate the computational fluid dynamics solution approaches using Reynolds Averaged Navier-Stokes (RANS) or Large Eddy Simulation (LES)
- Transition Noise in Adverse Pressure Gradients - Radiated noise and fluid mechanics measurements need to be made for a systematic variation of adverse pressure gradient. Pursuit of further modeling or measurement of zero pressure gradient flows does not seem warranted based on the small contribution to the overall flow-induced radiated noise for a flat plate. However, the indications are that adverse pressure gradients should shorten the transition zone and, thus, result in a higher radiated noise component.
- Transition on Blades - Radiated noise due to boundary layer transition on air- and hydrofoils is a topic of continued interest. The usefulness of the models described in this thesis when coupled with the proper Green's function should be evaluated against measurements. But, it is noted that the mechanism for transition on blades

is often a bypass phenomenon or a result of separation.

- Experimental Validation - Continue to utilize the current Quiet Airflow Facility to measure the radiation from the leading edge of the existing a half-plane foil in the presence of various pressure gradients, particularly adverse. Also, perform similar experiments on axisymmetric headforms.
- Coherent Output Intensity - This procedure should continue to be pursued with a better implementation of the real-time intensity circuitry. The concept of using a sensor unaffected by the acoustic field to condition the intensity measurement is very powerful.

BIBLIOGRAPHY

- Abraham, B. M. and Keith, W. L., 1997, "Wavenumber Spectra of High Magnitude Wall Pressure Events in a Numerically Simulated Turbulent Boundary Layer," *Trans. ASME, J. Fluids Eng.* **119**, pp. 281-288.
- Addison, J. S. and Hodson, H. P., 1991, "Modelling of Unsteady Transitional Boundary Layers," Paper 91-GT-282, ASME International Gas Turbine and Aeroengine Congress and Exhibition, Orlando, FL, June 1991.
- Arakeri, V. H., 1975, "A Note on the Transition Observations on an Axisymmetric Body and Some Related Fluctuating Wall Pressure Measurements," *Trans. ASME, J. Fluids Eng.* **97**, pp. 82-86.
- Arakeri, V. H., Satyanarayana, S. G., Mani, K. and Sharma, S. D., 1991, "Studies on Scaling of Flow Noise Received at the Stagnation Point of an Axisymmetric Body," *J. Sound Vib.* **146**, pp. 449-462.
- Assessment of Experimental Uncertainty with Application to Wind Tunnel Testing*, 1999, American Institute of Aeronautics and Astronautics (AIAA) Standard S-071A-1999, Reston, VA.
- Audet, J., Dufourcq, Ph. and Lagier, M., 1989a, "Pression parietale sous une couche limite Lors de la transition vers la turbulence," *J. Acoustique* **2**: pp. 369-378. (Translation available: Marboe, R. C., Applied Research Laboratory / Penn State University Tech. Memo. 91-81, 5 April 1991.)
- Audet, J., Dufourcq, Ph., Lagier, M. and Sornette, D., 1989b, "Wall Pressure Fluctuations in the Intermittent Regime of a Transition Boundary Layer: Comparison Between Theory and Experiment," *Symposium on Flow- Induced Noise due to Laminar-Turbulence Transition Process*, (Farabee, T. M., Hansen, R. J. and Keltie, R. F., eds.), ASME NCA-Vol. 5, pp. 25-30.
- Bandyopadhyay, P. R. and Ahmed, A., 1993, "Turbulent Boundary Layers Subjected to Multiple Curvatures and Pressure Gradients," *J. Fluid Mech.* **246**, pp. 503-527.
- Barenblatt, G. I., 1990, "On a Model of Laminar-Turbulent Transition," *J. Fluid Mech.* **212**, pp. 487-496.

- Barker, S. J., 1974, "Measurements of Radiated Noise in the CALTECH High-Speed Water Tunnel, Part 1: Radiated Noise from Turbulent Boundary Layers," Graduate Aeronautical Laboratories Report, California Institute of Technology, Pasadena, CA, 30 August 1974.
- Barlow, J. B., Rae, W. H., Jr., and Pope, A., 1999, *Low-Speed Wind Tunnel Testing*, 3rd Ed., John Wiley and Sons, New York.
- Barrow, J., Barnes, F. H., Ross, M. A. S., and Hayes, S. T., 1984, "The Structure of a Turbulent Spot in Blasius Flow," *J. Fluid Mech.* **149**, pp. 319-337.
- Bendat, J. S. and Piersol, A. G., 1993, *Engineering Applications of Correlation and Spectral Analysis*, Second Edition, John Wiley & Sons, New York, Chapter 4.
- Beranek, L. L., 1988, *Noise and Vibration Control*, Revised Edition, Institute of Noise Control Engineering, Washington, DC, pp. 575.
- Bergeron, R. F., 1973, "Aerodynamic Sound and Low Wavenumber Wall-Pressure Spectrum of Nearly Incompressible Boundary Layer Turbulence," *J. Acoust. Soc. Am.* **54**, pp. 123-133.
- Bershadskii, A. and Tsinober, A., 1994, "On the Near Field Pressure Radiation and Localized Structures in Turbulence," *J. Sound Vib.* **173**, pp. 699-701.
- Blair, M. F., 1992a, "Boundary-Layer Transition in Accelerating Flows With Intense Freestream Turbulence: Part 1 - Disturbance Upstream of Transition Onset," *Trans. ASME, J. Fluids Eng.* **114**, pp. 313-321.
- Blair, M. F., 1992b, "Boundary-Layer Transition in Accelerating Flows With Intense Freestream Turbulence: Part 2 - The Zone of Intermittent Turbulence," *Trans. ASME, J. Fluids Eng.* **114**, pp. 322-332.
- Blake, W. K., 1986, *Mechanics of Flow-Induced Sound and Vibration, Volumes I and II*, Academic Press, Orlando, Chapters 2, 9, and 11.
- Bowles, R. G. A. and Smith, F. T., 1995, "Short-Scale Effects on Model Boundary-Layer Spots," *J. Fluid Mech.* **295**, pp. 395-407.
- Brooks, T. F. and Hodgson, T. H., 1981, "Trailing Edge Noise Prediction from Measured Surface Pressures," *J. Sound Vib.* **78**, pp. 69-117.

- Bruneau, S. D. and Pauley, W. R., 1992, "Digital Image Processing of Hydrogen Bubble Lines for Instantaneous Velocity Profiles," Applied Research Laboratory / Penn State University Tech. Report 92-10, November 1992.
- Bruneau, S. D. and Pauley, W. R., 1995, "Measuring Unsteady Velocity Profiles and Integral Parameters Using Digital Image Processing of Hydrogen Bubble Timelines," *Trans. ASME, J. Fluids Eng.* **117**, pp. 331-340.
- Brungart, T. A., 1997, "Boundary Condition Effects on Turbulent Boundary Layer Wall Pressure Fluctuations," Ph.D. Thesis in Acoustics, The Pennsylvania State University, December 1997.
- Capone, D. E. and Lauchle, G. C., 1995, "Calculation of Turbulent Boundary Layer Wall Pressure Spectra," *J. Acoust. Soc. Am.* **98**: pp. 2226-2234.
- Chase, D. M., 1980, "Modeling the Wavevector-Frequency Spectrum of Turbulent Boundary Layer Wall Pressure," *J. Sound Vib.* **70**, pp. 29-47.
- Chase, D. M., 1987, "The Character of the Turbulent Wall Pressure Spectrum at Subconvective Wavenumbers and a Suggested Comprehensive Model," *J. Sound Vib.* **112**, pp. 125-142.
- Chase, D. M., 1989, *private communication*.
- Chase, D. M., 1991, "The Wave-Vector-Frequency Spectrum of Pressure on a Smooth Plane in Turbulent Boundary-Layer Flow at Low Mach Number," *J. Acoust. Soc. Am.* **90**, pp. 1032-1040.
- Chen, K. K. and Thyson, N. A., 1971, "Extension of Emmons' Spot Theory to Flows on Blunt Bodies," *AIAA J.* **9**, pp. 821-825.
- Chernys, M. and Pauley, W. R., 1994, "The Effect of Interaction Strength on the Development and Acoustic Signature of Aligned Turbulent Spot Pairs," *Symposium on Boundary Layer and Free Shear Flows*, (Donovan, J. F. and Dutton, J. C., eds.), ASME FED-Vol. 184, pp. 21-35.
- Ching, C. Y. and LaGraft, J. E., 1995, "Measurement of Turbulent Spot Convection Rates in a Transitional Boundary Layer," *Exper. Thermal and Fluid Sci.*, **11**, pp. 52-60.
- Clark, J. P., Jones, T. V., and LaGraft, J. E., 1996, "Turbulent Spot Propagation in a Decelerating, Compressible Flow," *Trans. ASME, J. Fluids Eng.* **118**, pp. 612-614.

- Coleman, H. W. and Steele, W. G., 1999, *Experimentation and Uncertainty Analysis for Engineers*, 2nd Ed., John Wiley and Sons, New York.
- Coles, D. and Savas, O., 1979, "Interactions for Regular Patterns of Turbulent Spots in a Laminar Boundary Layer," In Proc. IUTAM Symposium Laminar-Turbulent Transition, Stuttgart, Germany, September 16-22, 1979, Springer-Verlag, Berlin, pp. 277-287.
- Corcos, G. M., 1963, "Resolution of Pressure in Turbulence," *J. Acoust. Soc. Am.* **35**, pp. 192-199.
- Crighton, D. G., 1975, "Basic Principles of Aerodynamic Noise Generation," *Prog. Aerosp. Sci.*, **16**, pp. 31-39.
- Curle, N., 1955, "The Influence of Solid Boundaries Upon Aerodynamic Sound," *Proc. Royal Soc. London A*, **231**, pp. 505-514.
- DeMetz, F. C. and Casarella, M. J., 1973, "An Experimental Study of the Intermittent Properties of the Boundary Layer Pressure Field During Transition on a Flat Plate," David W. Taylor Naval Ship Research and Development Center Report AD-775-299, November 1973.
- Dey, J. and Narasimha, R., 1991, "Effect of Favorable Pressure Gradient on Transitional Spot Formation Rate," *Exper. Thermal and Fluid Sci.* **4**, pp. 192-197.
- Dhawan, S. and Narasimha, R., 1958, "Some Properties of Boundary Layer Flow During The Transition from Laminar to Turbulent Motion," *J. Fluid Mech.* **3**, pp. 318-436.
- Ducros, F., Comte, P., and Lesieur, M., 1996, "Large-Eddy Simulation of Transition to Turbulence in a Boundary Layer Developing Spatially Over a Flat Plate," *J. Fluid Mech.* **326**, pp. 1-36.
- Dufourq, Ph., 1984, "Influence d'un Écoulement de Type Couche Limite sur la Localisation de Sources Sonores Placées en Paroi," Doctoral Thesis, Ecole Centrale de Lyon.
- Emmons, H. W., 1951, "The Laminar-Turbulent Transition in a Boundary-Layer, Part I," *J. Aeron. Sci.* **18**, pp. 490-498.
- Fahy, F. J., 1989, *Sound Intensity*, Elsevier Applied Science, New York
- Farabee, T. M., Casarella, M. J., and DeMetz, F. C., 1974, "Source Distribution of Turbulent Bursts During Natural Transition," David W. Taylor Naval Ship Research and Development Center Report SAD-89E-1942, August 1974.

- Ffowcs Williams, J. E., 1967, "Flow Noise," *Underwater Acoustics, Vol. II*, Albers, V. M. (ed), Plenum Press.
- Ffowcs Williams, J. E., 1969, "Hydrodynamic Noise," *Ann. Rev. Fluid Mech.* **1**, pp. 197-221.
- Ffowcs Williams, J. E., 1977, "Aeroacoustics," *Ann. Rev. Fluid Mech.* **9**, pp. 447-468.
- Ffowcs Williams, J. E., 1982, "Noise Source Mechanisms in Unsteady Flow," *Acustica* **50**, pp. 167.
- Gad-el-Hak, M., 1989, "Flow Control," *Appl. Mech. Rev.* **42**, pp. 261.
- Gad-el-Hak, M., Blackwelder, R. F. and Riley, J. J., 1981, "On the Growth of Turbulent Regions in Laminar Boundary Layers," *J. Fluid Mech.* **110**, pp. 73-95.
- Gad-el-Hak, M. and Fazole Hussain, A. K. M., 1986, "Coherent Structures in a Turbulent Boundary Layer, Part 1: Generation of 'Artificial' Bursts," *Phys. Fluids* **29**, pp. 2124-2138.
- Gedney, C. J., 1979, "Wall Pressure Fluctuations During Transition on a Flat Plate," Mass. Institute of Tech. Report 84618-1.
- Gedney, C.J. and Leehey, P., 1989, "Wall Pressure Fluctuations During Transition on a Flat Plate," *Symposium on Flow-Induced Noise Due to Laminar-Turbulence Transition Process*, (Farabee, T. M., Hansen, R. J. and Keltie, R. F., eds.), ASME NCA-Vol. 5, pp. 1-10.
- Gershfeld, J. L., 1997, "Sound Generation from Spatially Inhomogeneous Wall Pressure Fields (Polyvinylidene Fluoride)," Ph.D. Thesis, The Catholic University of America, August 1997.
- Gogineni, S. and Shih, C., 1997, "Experimental Investigation of the Unsteady Structure of a Transitional Plane Wall Jet," *Exper. in Fluids* **23**, pp. 121-129.
- Goldstein, M. E., Leib, S. J. and Cowley, S. J., 1992, "Distortion of a Flat-Plate Boundary Layer by Free-Stream Vorticity Normal to the Plate," *J. Fluid Mech.* **237**, pp. 231-260.
- Goldstein, M. E. and Leib, S. J., 1993, "Three-Dimensional Boundary-Layer Instability and Separation Induced by Small-Amplitude Streamwise Vorticity in the Upstream Flow," *J. Fluid Mech.* **246**, pp. 21-41.

- Graham, W. R., 1997, "A Comparison of Models for the Wavenumber-Frequency Spectrum of Turbulent Boundary Layer Pressures," *J. Sound Vib.* **206**, pp. 541-565.
- Gutmark, E. and Blackwelder, R. F., 1987, "On the Structure of a Turbulent Spot in a Heated Laminar Boundary Layer," *Exper. in Fluids* **5**, pp. 217-229.
- Haddle, G. P. and Skudrzyk, E. J., 1969, "The Physics of Flow Noise," *J. Acoust. Soc. Amer.* **46**, pp. 130-157.
- Haidari, A. H. and Smith, C. R., 1994, "The Generation and Regeneration of Single Hairpin Vortices," *J. Fluid Mech.* **277**, pp. 135-162.
- Halstead, D. E., Wisler, D. C., Okiishi, T. H., Walker, G. J., Hodson, H. P. and Shin, H. W., 1995a, "Boundary Layer Development in Axial Compressors and Turbines, Part 1 of 4: Composite Picture," Paper 95-GT-461, ASME International Gas Turbine and Aeroengine Congress and Exhibition, Houston, TX, June 1995.
- Halstead, D. E., Wisler, D. C., Okiishi, T. H., Walker, G. J., Hodson, H. P. and Shin, H. W., 1995b, "Boundary Layer Development in Axial Compressors and Turbines, Part 2 of 4: Compressors," Paper 95-GT-462, ASME International Gas Turbine and Aeroengine Congress and Exhibition, Houston, TX, June 1995.
- Halstead, D. E., Wisler, D. C., Okiishi, T. H., Walker, G. J., Hodson, H. P. and Shin, H. W., 1995c, "Boundary Layer Development in Axial Compressors and Turbines, Part 3 of 4: L. P. Turbines," Paper 95-GT-463, ASME International Gas Turbine and Aeroengine Congress and Exhibition, Houston, TX, June 1995.
- Halstead, D. E., Wisler, D. C., Okiishi, T. H., Walker, G. J., Hodson, H. P. and Shin, H. W., 1995d, "Boundary Layer Development in Axial Compressors and Turbines, Part 4 of 4: Computation and Analyses," Paper 95-GT-464, ASME International Gas Turbine and Aeroengine Congress and Exhibition, Houston, TX, June 1995.
- Hardin, J. C., 1991, "Acoustic Sources in the Low Mach Number Turbulent Boundary Layer," *J. Acoust. Soc. Am.* **90**: pp. 1020-1031.
- Henningson, D. S. and Alfredsson, P. H., 1987, "The Wave Structure of Turbulent Spots in Plane Poiseuille Flow," *J. Fluid Mech.* **178**, pp. 405-421.
- Henningson, D. S. and Kim, J., 1991, "On Turbulent Spots in Plane Poiseuille Flow," *J. Fluid Mech.* **228**, pp. 183-205.

- Honkan, A. and Andreopoulos, Y., 1999, "Vorticity, Strain-Rate and Dissipation Characteristics in the Near-Wall Region of Turbulent Boundary Layers," *J. Fluid Mech.* **350**, pp. 29-96.
- Howe, M. S., 1981, "The Role of Displacement Thickness Fluctuations in Hydroacoustics and the Jet-Drive Mechanism of the Flue Organ Pipe," *Proc. Royal Soc. London A*, **374**, pp. 543-568.
- Howe, M. S., 1991, "Surface Pressures and Sound Produced by Turbulent Flow Over Smooth and Rough Walls," *J. Acoust. Soc. Am.* **90**: pp. 1041-1047.
- Howe, M. S., 1998a, *Acoustics of Fluid-Structure Interactions*, Cambridge University Press, Cambridge, UK.
- Howe, M. S., 1998b, "Reference Manual on the Theory of Lifting Surface Noise at Low Mach Numbers," Boston University, Dept. of Aerospace and Mechanical Engineering Report, AM-98-001, January 1998.
- Howe, M.S., 1999a, "Noise Generated at Low Mach Numbers by Boundary Layer Transition on Symmetric Hydrofoils and Axisymmetric Headforms," Applied Research Laboratory / Penn State University Technical Memorandum, 99-017, February 1999.
- Howe, M. S., 1999b, "Trailing Edge Noise Evaluated at Very Low Mach Number from Incompressible Flow Simulations," Boston University, Dept. of Aerospace and Mechanical Engineering Report, AM-99-003, March 1999.
- Howe, M. S., 1999c, "Trailing Edge Noise at Low Mach Numbers," *J. Sound and Vib.* **225**, pp. 211-238.
- Huang, T. T. and Shen, Y. T., 1989, "Wall Pressure Fluctuations in Adverse Pressure Gradient Transition Regions," *Symposium on Flow-Induced Noise Due to Laminar-Turbulence Transition Process*, (Farabee, T. M., Hansen, R. J. and Keltie, R. F., eds.), ASME NCA-Vol. 5, pp. 11-16.
- Huerre, P. and Monkewitz, P. A., 1990, "Local and Global Instabilities in Spatially Developing Flows," *Ann. Rev. Fluid Mech.* **22**, pp. 473-537.
- Hwang, Y. F. and Shang, P. C., 1989, "Effects of Laminar-Turbulent Transition on the Coupling of Structural Modes and Fluid Flow," *Symposium on Flow-Induced Noise Due to Laminar-Turbulence Transition Process*, (Farabee, T. M., Hansen, R. J. and Keltie, R. F., eds.), ASME NCA-Vol. 5, pp. 39-48.

- Hwang, Y. F. and Maidanik, G., 1990, "A Wavenumber Analysis of the Coupling of a Structural Mode and Flow Turbulence," *J. Sound Vib.* **142**, pp. 135-152.
- International Standard, 1972, "Sound System Equipment, Part 5: Loudspeakers," International Electrotechnical Commission (IEC) 268-5.
- International Standard, 1977, "Determination of Sound Power Levels of Noise Sources - Precision Methods for Anechoic Rooms," International Standards Organization (ISO) 3745, (E), Annex. A.
- Jahanmari, M., Prabhu, A., and Narasimha, R., 1996, "Experimental Studies of a Distorted Turbulent Spot in a Three-Dimensional Flow," *J. Fluid Mech.* **329**, pp. 1-24.
- Jeon, W. P. and Kang, S. H., 1995, "Measurement of Transitional Boundary Layer on a Flat Plate Using a Computational Preston Tube Method," *Exper. in Fluids* **20**, pp. 29-37.
- Joslin, R. D., 1991, "The Effect of Compliant Walls on Three-Dimensional Primary and Secondary Instabilities in Boundary Layer Transition," Applied Research Laboratory / Penn State University Tech. Report 91-003, April 1991.)
- Josserand, M. A., 1986, "Wavevector-Frequency Spectrum of Transition Zone Wall Pressure Fluctuations," Ph.D. Thesis in Acoustics, The Pennsylvania State University, (see also Josserand, M. A. and Lauchle, G. C., Applied Research Laboratory / Penn State University Tech. Report 86-008, December 1986.)
- Josserand, M. A. and Lauchle, G. C., 1989, "Cross-Spectral Density of the Wall Pressure Fluctuations Under a Turbulent Boundary Layer," *J. Sound Vib.* **128**, pp. 519-522.
- Josserand, M. A. and Lauchle, G. C., 1990, "Modeling the Wavevector-Frequency Spectrum of Boundary Layer Wall Pressure During Transition on a Flat Plate," *Trans. ASME. J. Vib. and Acoustics* **112**, pp. 523-534.
- Kambe, T., 1984, "Influence of Viscosity on the Aerodynamic Sound Emission in Free Space," *J. Sound Vib.* **95**, pp. 351-360.
- Kambe, T., 1986, "Acoustic Emissions by Vortex Motions," *J. Fluid Mech.* **173**, pp. 643-666.
- Kambe, T. and Minota, T., 1981, "Sound Radiation from Vortex Systems," *J. Sound Vib.* **74**, pp. 61.

- Kambe, T. and Minota, T., 1983, "Acoustic Wave Radiated by Head-on Collision of Two Vortex Rings," *Proc. R. Soc. London A* **386**, pp. 277-308.
- Kambe, T., Minota, T., and Ikushima, Y., 1985, "Acoustic Wave Emitted by a Vortex Ring Passing Near the Edge of a Half-Plane," *J. Fluid Mech.* **155**, pp. 77-103.
- Kargus, W. A., IV, 1997, "Flow-Induced Sound From Turbulent Boundary Layer Separation Over a Rearward Facing Step," Ph.D. Thesis in Acoustics, The Pennsylvania State University, (see also Kargus, W. A., IV, and Lauchle, G. C., Applied Research Laboratory / Penn State University Tech. Report 97-007, December 1997.)
- Katz, R. A. , Galib, T. A., and Cembrola, J. M., 1990a, "Classical and Nonlinear Analysis of Transitional and Turbulent Boundary Layer Flow," *Proc. of Second Int. Symp. On Performance Enhancement for Marine Applications*, Newport, RI, 14-16 October 1990, pp. 119-127.
- Katz, Y., Seifert, A., and Wynanski, I., 1990b, "On the Evolution of the Turbulent Spot in a Laminar Boundary Layer with a Favourable Pressure Gradient," *J. Fluid Mech.* **221**, pp. 1-22.
- Keith, W. L. and Abraham, B. M., 1997, "Effects of Convection and Decay of Turbulence on the Wall Pressure Wavenumber-Frequency Spectrum," *Trans. ASME, J. Fluids Eng.*, **119**, pp. 50-55.
- Kinsler, L. E., Frey, A. R., Coppers, A. B., and Sanders, J. V., 1982, *Fundamentals of Acoustics, Third Edition*, Jon Wiley & Sons, New York.
- Klebanoff, P. S., Cleveland, W. G., and Tidstrom, K. D., 1992, "On the Evolution of a Turbulent Boundary Layer Induced by a Three-Dimensional Roughness Element," *J. Fluid Mech.* **237**, pp. 101-187.
- Kline, S. J., 1959, "On the Nature of Stall," *Trans. ASME, J. Basic Eng.* **81(D)**, pp. 305-320.
- Kline S. J., Abbott, D. E., and Fox, R. W., 1959, "Optimum Design of Straight-Walled Diffusers," *Trans. ASME, J. Basic Eng.* **81(D)**, pp. 321-331.
- Kloker, M. , Konzelmann, and Fasel, H., 1993, "Outflow Conditions for Spatial Navier-Stokes Simulations of Transition Boundary Layers," *AIAA J.* **31(4)**, pp. 620-628.
- Koh, Y-M, 1993, "The Pressure Distribution Around Unsteady Boundary Layers," *J. Fluid Mech.* **255**, pp. 437-446.

- Krane, M. H., 1992, "Estimation of the Direct Acoustic Radiation from Turbulent Spots, Using Boundary Layer Velocity Measurements," Ph.D. Thesis in Aerospace Engineering, The Pennsylvania State University, (see also Krane, M. H. and Pauley, W. R., Applied Research Laboratory / Penn State University Tech. Report 92-11, November 1992.)
- Krane, M. H. and Pauley, W. R., 1992, "Measurements of the Unsteady Flux Deficit of a Turbulent Spot: Implications for Boundary Layer Transition Noise," *Int. Symposium on Flow-Induced Vibration and Noise: Volume 3 - Flow-Structure and Flow-Sound Interactions*, (Farabee, T. M. and Paidoussis, M. P., eds.), ASME NCA-Vol. 13, pp. 133-146.
- Krane, M. H. and Pauley, 1993, "The Effects of Weak Interaction and Reynolds Number on Boundary Layer Scalars with Tandem Turbulent Spots," *Trans. ASME, J. Fluids Eng.*, **116**, pp. 653-656.
- Krane, M. H. and Pauley, W. R., 1995, "Estimation of the Direct Acoustic Radiation from a Transitional Boundary Layer Using Velocity Measurements," *J. Sound Vib* **181**(5), pp. 737-763.
- Krogstad, P-A. and Antonia, R. A., 1994, "Structure of Turbulent Boundary Layers on Smooth and Rough Walls," *J. Fluid Mech.* **277**, pp. 1-21.
- Lagier, M. and Sornette, D., 1986, "A Two Fluids Model of the Acoustic Noise Radiated By Intermittent Flow," *Acustica* **61**: pp. 116-123.
- Lauchle, G. C., 1977, "Noise Generated by Axisymmetric Turbulent Boundary-Layer Flow," *J. Acoust. Soc. Amer.* **61**, pp. 694-702.
- Lauchle, G. C., 1980, "On the Radiated Noise Due to Boundary-Layer Transition," *J. Acoust. Soc. Amer.* **67**, pp. 158-168.
- Lauchle, G. C., 1981, "Transition Noise - The Role of Fluctuating Displacement Thickness," *J. Acoust. Soc. Am.* **69**: pp. 665-671.
- Lauchle, G. C., 1989, "Transition as a Source of Radiated Noise and Vibration," *Symposium on Flow-Induced Noise Due to Laminar-Turbulence Transition Process*, (Farabee, T. M., Hansen, R. J. and Keltie, R. F., eds.), ASME NCA-Vol. 5, pp. 31-38.
- Lauchle, G. C., 1991, "Hydroacoustics of Transitional Boundary-Layer Flow," *Appl. Mech. Rev.* **44**, pp. 517-531.

- Lauchle, G. C., 1992, "Flow Noise Scaling at the Stagnation Point of an Axisymmetric Body," *J. Sound Vib.* **154**, pp. 568-572.
- Lauchle, G. C. and Brungart, T. A., 1988, "Boundary Layer Flow Noise - The Direct Radiation," Applied Research Laboratory / Penn State University Tech. Memo. 88-270.
- Lauchle, G. C. and Park, S., 2000, "Low-Wavenumber Wall Pressure Fluctuations Due to Boundary Layer Transition," Applied Research Laboratory / Penn State University Tech. Memo. 00-100.
- Lauffer, J., Ffows Williams, J. E. and Childress, S., 1964, "Mechanism of Noise Generation in Turbulent Boundary Layers," *AGARDograph 90, Chapter 7*, pp. 39-50.
- Lieb, S. J., Wundrow, D. W. and Goldstein, M. E., 1999, "Effect of Free-Stream Turbulence and Other Vortical Disturbances on a Laminar Boundary Layer," *J. Fluid Mech.* **380**, pp. 169-203.
- Liepmann, H. W. , 1954, "On the Acoustic Radiation from Boundary Layers and Jets," Guggenheim Aeronautics Laboratory, California Institute of Technology, Pasadena, CA.
- Lighthill, M. J., 1952, "On Sound Generated Aerodynamically, Part I: General Theory," *Proc. Royal Soc. London A*, **211**, pp. 564-587.
- Lighthill, M. J., 1954, "On Sound Generated Aerodynamically, Part II: Turbulence as a Source of Sound," *Proc. Royal Soc. London A*, **222**, pp. 1-31.
- Lighthill, M. J., 1958, "On Displacement Thickness," *J. Fluid Mech.* **4**, pp. 383-392.
- Littell, H. S. and Eaton, J. K., 1991, "Unsteady Flowfield Behind a Vortex Generator Rapidly pitched to Angle of Attack," *AIAA J.* **29**, pp. 577-584.
- Lou, W. and Hourmouziadis, 1999, "Experimental Investigation of Periodic-Unsteady Flat Plate Boundary Layers with Pressure Gradients," *Proceedings of the 3rd ASME/JSME Fluids Engineering Conference*, Paper FEDSM99-7190, San Francisco, CA, 18-23 July 1999.
- Lund, F., 1989, "Response of a Filamentary Vortex to Sound," *Phys. Fluids A* **1**, pp. 1521-1531.

- Marboe, R. C. and Lauchle, G. C., 1992, "Acoustic Emissions from Unsteady Transitional Boundary Layer Flow Structures: Theoretical Model Refinements," *Int. Symposium on Flow-Induced Vibration and Noise: Volume 3 – Flow-Structure and Flow-Sound Interactions*, (Farabee, T. M. and Paidoussis, M. P., eds.), ASME NCA-Vol. 13, pp. 181-194.
- Marboe, R. C. and Lauchle, G. C., 1994, "Empirical Refinements to Boundary Layer Transition Noise Models," *Proceedings of NOISE-CON 94*, pp. 209-214.
- Marboe, R. C., Lauchle, G. C. and Kargus IV, W. A., 1991, "Quiet Wall Jet Facility for Basic Aero/Hydroacoustics Research," *Symposium on Hydroacoustic Facilities, Instrumentation, and Experimental Techniques*, (Farabee, T. M. and Arndt, R. E. A., eds.), ASME NCA-Vol. 10, pp. 69-73.
- Mathcad 2000 User's Guide*, 1999, Mathsoft, Inc., Cambridge, MA.
- Mathcad 2000 Reference Manual*, 1999, Mathsoft, Inc., Cambridge, MA.
- Mautner, T. S., 1982, "An Experimental Study of the Wall-Pressure Field Associated with a Turbulent Spot in a Laminar Boundary Layer," *J. Fluid Mech.* **118**, pp. 59-77.
- Mautner, T. S., 1985, "Comparison of the Wall Pressure Fluctuations in Artificially Generated Turbulent Spots, Natural Transition and Turbulent Boundary Layers," NOSC Report 1053, 1985, and also Paper AIAA-88-0409, AIAA 26th Aerospace Science Meeting, Reno, Nevada, January 1988.
- Mohring, W., 1978, "On Vortex Sound at Low Mach Number," *J. Fluid Mech.* **85**, pp. 685-691.
- Mohring, W., Muller, E. A., and Obermeier, F., 1983, "Problems in Flow Acoustics," *Rev. Mod. Phys.* **55**, pp. 707-724.
- Morel, T., 1975, "Comprehensive Design of Axisymmetric Wind Tunnel Contractions," *Trans. ASME, J. Fluids Eng.* **97**, pp. 225 - 233.
- Motohashi, T. and Blackwelder, R. F., 1983, Decreasing the Side Wall Contamination in Wind Tunnels," *Trans. ASME, J. Fluids Eng.* **105**, pp. 435-438.
- Narasimha, R., 1957, "On the Distribution of Intermittency in the Transition Region of a Boundary Layer," *J. Aero. Sci.* **24**, pp. 711-712.

- Narasimha, R., Devasia, K. J., Gururani, G. and Badri Narayanan, M. A., 1984, "Transitional Intermittency in Boundary Layers Subjected to Pressure Gradient," *Exper. in Fluids* **2**, pp. 171-176.
- Narasimha, R. and Prasad, S. N., 1995, "Leading Edge Shape for Flat Plate Boundary Layer Studies," *Exper. in Fluids* **19**, pp. 358-360.
- Obermeier, F., 1977, "The Application of Singular Perturbation Methods to Aerodynamic Sound Generation," *Lecture Notes in Mathematics*, Springer, Berlin, pp. 400-421.
- Obermeier, F., 1979, "On a New Representation of Aeroacoustic Source Distribution, I: General Theory," *Acustica* **42**, pp. 56-61.
- Obermeier, F., 1980, "The Influence of Solid Bodies on Low Mach Number Vortex Sound," *J. Sound Vib.* **72**, pp. 39-49.
- Obermeier, F., 1985, "Aerodynamic Sound Generation Caused by Viscous Processes," *J. Sound Vib.* **99**, pp. 111-120.
- Ochsenknecht, R. I., 1996, "Estimates of the Wavenumber-Frequency Spectra for the Non-Homogeneous Streamwise Transition Flow Pressure Field," M.S. Thesis in Acoustics, The Pennsylvania State University, May 1996.
- Panton, R. L., 1984, *Incompressible Flow*, John Wiley and Sons, New York, pp. 673-703.
- Perraud, J. C., 1989, "Studies of Laminar-Turbulent Transition in Air and in Water Wall Pressure Fluctuations and Acoustic Emission from the Turbulent Intermittency," *Symposium on Flow-Induced Noise due to Laminar-Turbulence Transition Process*, (Farabee, T. M., Hansen, R. J. and Keltie, R. F., eds.), ASME NCA-Vol. 5, pp. 17-24.
- Pierce, A. D., 1981, *Acoustics - An Introduction to its Physical Principles and Applications*, McGraw-Hill, New York.
- Powell. A., 1960, "Aerodynamic Noise and the Plane Boundary," *J. Acoust. Soc. Am.* **32**, pp. 982-990.
- Powell. A., 1964, "Theory of Vortex Sound," *J. Acoust. Soc. Am.* **36**, pp. 177-195.
- Powell. A., 1995, "A Basically Monopole Source Formulation for Vortex-Generated Sound," *J. Acoust. Soc. Am.* **97**, pp. 2144-2146.

- Prout, J. H. and Marboe, R. C., 1990, "Applied Research Laboratory / Penn State University Flow-Through Anechoic Chamber," Applied Research Laboratory / Penn State University Tech. Memo. 89-65, 22 February 1990.
- Quartararo, L. R. and Lauchle, G. C., 1985, "Inlet Wall Design for High-Volume Flow Subsonic Anechoic Chambers," *Noise Control Engineering Journal*, pp. 86-96.
- Rai, M. M. and Moin, P., 1993, "Direct Numerical Simulation of Transition and Turbulence in a Spatially Evolving Boundary Layer," *J. Comput. Phys.* **109**, pp. 169-192.
- Ramesh, O. N., Dey, J., and Prabhu, A., 1996, "Transitional Intermittency Distribution in a Three-Dimensional Constant Pressure Diverging Flow," *Exper. in Fluids* **21**, pp. 259-263.
- Rempfer, D. and Fasel, H. F., 1994, "Evolution of Three-Dimensional Coherent Structures in a Flat-Plate Boundary Layer," *J. Fluid Mech.* **260**, pp. 351-375.
- Rist, U. and Fasel, H., 1995, "Direct Numerical Simulation of Controlled Transition in a Flat-Plate Boundary Layer," *J. Fluid Mech.* **298**, pp. 211-248.
- Sankaran, R., Sokolov, M. and Antonia, R. A., 1988, "Substructures in a Turbulent Spot," *J. Fluid Mech.*, **197**, pp. 389-414.
- Sankaran, R., Antonia, R. A., Bisset, D. K., and Sokolov, M., 1991, "Flow Patterns and Organization Within a Turbulent Spot," *Phys. Fluids A* **3**, pp. 1560-1571.
- Schlichting, H., 1979, *Boundary-Layer Theory*, McGraw-Hill, New York, 7th ed.
- Schneider, S. P., 1995, "Improved Methods for Measuring Laminar-Turbulent Intermittency in Boundary Layers," *Exper. in Fluids* **18**, pp. 370-375.
- Seifert, A. and Wygnanski, I. J., 1995, "On Turbulent Spots in a Laminar Boundary Layer Subjected to a Self-Similar Adverse Pressure Gradient," *J. Fluid Mech.* **296**, pp. 185-209.
- Shivitz, W. F., 1975, "An Experimental Investigation of Artificially Induced Transition to Turbulence on a Body of Revolution," Applied Research Laboratory / Penn State University Technical Memorandum TM 75-178, 19 June 1975.
- SigLab User Guide, Version 3.0*, 1998, DSP Technology, Inc., Fremont, CA.
- SigLab Programming Guide, Version 3.0*, 1998, DSP Technology, Inc., Fremont, CA.

- Singer, B. A., 1997, "Turbulent Wall-Pressure Fluctuations: A New Model for Off-Axis Cross-Spectral Density," *Trans. ASME, J. Fluids Eng.* **119**, pp. 277-280.
- Skudrzyk, E., 1968, *Simple and Complex Vibratory Systems*, The Pennsylvania State University Press, University Park, PA.
- Sornette, D. and Lagier, M., 1984a, "Nature Monopolaire du Rayonnement Acoustique Engendré par les Écoulements Instables," *Acustica* **55**, pp. 255-267. (Translation available: Marboe, R. C., Applied Research Laboratory / Penn State University Tech. Memo. 92-029, 31 January 1992.)
- Sornette, D. and Lagier, M., 1984b, "Acoustic Noise Radiated by Transient Flows," *Acoust. Ltrs.*, Vol. 7, pp. 104-108.
- Stewart, P. A. and Smith, F. T., 1992, "Three-Dimensional Nonlinear Blow-up From a Nearly Planar Initial Disturbance, in Boundary-Layer Transition: Theory and Experimental Comparisons," *J. Fluid Mech.* **244**, pp. 79-100.
- Stratonovich, R. L., 1963, *Topics in the Theory of Random Noise, Volume I*, Gordon Breach Science, New York, pp. 157.
- Tam, C. K. W., 1975, "Intensity, Spectrum and Directivity of Turbulent Boundary Layer Noise," *J. Acoust. Soc. Am.* **57**, pp. 25-34.
- Tani, I., 1969, "Boundary Layer Transition," *Ann. Rev. Fluid Mech.* **1**, pp. 169.
- Van Atta, C. W., Sokolov, M., Antonia, R. A., and Chambers, A. J., 1982, "Potential Flow Signature of a Turbulent Spot," *Phys. Fluids* **25**, pp. 424-428.
- Walker, G. J. and Gostelow, J. P., 1990, "Effects of Adverse Pressure Gradients on the Nature and Length of Boundary Layer Transition," *Trans. ASME, J. Turbomachinery* **112**, pp. 196-205.
- Wang, M., Lele, S. K., and Moin, P., 1996a, "Sound Radiation During Local Laminar Breakdown in a Low Mach Number Boundary Layer," *J. Fluid Mech.* **319**, pp. 197-218, (see also Wang, M., Lele, S. K., and Moin, P., 1994, "Sound Radiation During Local Laminar Breakdown in a Low Mach Number Boundary Layer," Center for Turbulence Research, Stanford University, CTR Manuscript 153, December 1994.)
- Wang, M., Lele, S. K., and Moin, P., 1996b, "Computation of Quadrupole Noise Using Acoustic Analogy," *AIAA J.* **34**, pp. 2247-2254.

- White, F. M., 1974, *Viscous Fluid Flow*, McGraw-Hill, New York.
- Wilde, A. and Rose, M., 1997, "Sound Generation in a Low Mach Number Transitional Boundary Layer," *Proc. of 3rd AIAA/CEAS Aeroacoustics Conference*, pp.362-371.
- Williams, D. R., Fasel, H., and Hama, F. R., 1984, "Experimental Determination of the Three-Dimensional Vorticity Field in the Boundary-Layer Transition Process," *J. Fluid Mech.* **149**, pp. 179-203.
- Wynanski, I., Sokolov, M. and Friedman, D., 1976, "On a Turbulent 'Spot' in a Laminar Boundary Layer," *J. Fluid Mech.* **78**, pp. 785-819.
- Yang, K-S, Spalart, P. R., and Ferziger, J. H., 1992, "Numerical Studies of Natural Transition in a Decelerating Boundary Layer," *J. Fluid Mech.* **240**, pp. 433-468.
- Zhang, D. H., Chew, Y. T., and Winoto, S. H., 1995, "A Proposed Intermittency Measurement Method for Transitional Boundary Layer Flows," *Exper. in Fluids* **19**, pp. 426-428.

APPENDIX A

MATHCAD MODEL FILES

This appendix contains the worksheets for several of the boundary layer transition noise models and experiment diagnostic routines as developed in the Mathcad 2000 Professional computer environment. Mathcad ® is a product of Mathsoft, Inc. of Cambridge, MA. This product is documented in a user's guide and reference manual (1999).

A.1 Fluctuating Shear Stress Using a Lighthill Analogy

Mathcad file: GLPROG80.MCD

RADIATED NOISE DUE TO FLUCTUATING SHEAR STRESS FROM BOUNDARY LAYER TRANSITION

[GLPROG80.MCD, Mathcad 2000 Professional]

This program is the implementation of a boundary layer transition noise model described in:

Lauchle, G. C., 1980, 'On the radiated noise due to boundary-layer transition,' *J. Acous. Soc. of Amer.*, **67**, pp.158-168.

ASSUMPTIONS

- zero pressure gradient flow and natural transition flow structures, i.e. no separation).
- flow is over an infinite, planar, rigid surface
- based on very low Mach number - use only dipole components due to fluctuating shear stress
- flow is statistically homogeneous in spanwise direction, x_3 , non-homogeneous in streamwise direction, x_1 , stationary but Poisson distributed in time so we can use a classical correlation function for a random sequence of bursts, $\exp(-2N|t|)$
- neglect quadrupoles and octupoles due to fluctuating Reynolds stresses due to lower radiation efficiencies - however, their amplitudes relative to shear stresses may overcome this lower efficiency.
- the space-time correlation function for the indicator function $\langle \Pi' \rangle$ is direction separable
- the lateral term integration derived from this separation is equal to $2L_3(\eta_1) = 2(1.5 \eta_1 \tan \alpha)$ which is about $\eta_1/4$ for $\alpha=9.6$ degrees (angle of spreading for turbulent spot)
- U_c/U_o is independent of frequency

DEFINITIONS

Δx is the length of the transition zone in feet or meters

$\Delta\delta^*$ is the change of the boundary layer displacement thickness from laminar to turbulent states in feet or meters ($\Delta\delta^* = \delta^*_{\text{turbulent}} - \delta^*_{\text{laminar}}$) ($\Delta\delta^*$ star in worksheet)

U_o is the freestream velocity in feet/sec or meters/sec

U_c is the convection velocity in feet/sec or meters/sec (nominally $U_c = 0.7*U_o$)

α^* is the flare parameter that accounts for moving axis decorrelation

c is the speed of sound in feet/sec or meters/sec

Re_t is the transition Reynolds number based on Δx

Re_x is the Reynolds number based on the distance to the start of the transition zone

W is the spanwise width of the transition zone in feet or meters

ν is the kinematic viscosity in feet²/sec

ρ is the fluid density in slugs/feet³

r is the far-field observation distance in feet or meters

θ is the angle from the plane of the wall to the observation point

σ is the estimate of the fluctuating wall shear stress

SPECIFY VALUES FOR FLOW AND GEOMETRY VARIABLES

$$\text{Fr} := \begin{pmatrix} 1.0 \\ 1.25 \\ 1.6 \\ 2.0 \\ 2.5 \\ 3.15 \\ 4.0 \\ 5.0 \\ 6.3 \\ 8.0 \end{pmatrix}$$

[Note: Mathcad is operating in SI units mode for all calculations. The user may enter values for variables in any appropriate measurement system so long as the units are specified. The program will automatically make the conversion to SI units during calculation.]

Define 1/3 Octave band center frequencies

$$a := 0..9$$

$$\text{Freq}_a := \text{Fr}_a \cdot 1.0 \cdot \text{Hz}$$

$$b := 10..19$$

$$\text{Freq}_b := \text{Fr}_{(b-10)} \cdot 10.0 \cdot \text{Hz}$$

$$d := 20..29$$

$$\text{Freq}_d := \text{Fr}_{(d-20)} \cdot 100.0 \cdot \text{Hz}$$

$$e := 30..39$$

$$\text{Freq}_e := \text{Fr}_{(e-30)} \cdot 1000.0 \cdot \text{Hz}$$

$$e := 40..49$$

$$\text{Freq}_e := \text{Fr}_{(e-40)} \cdot 10000.0 \cdot \text{Hz}$$

	Constant	Air	Fresh Water	Salt Water
Constants for user	c (m/s)	343	1525	1487
reference.	v (m ² /s)	1.51 x 10 ⁻⁵	1.01 x 10 ⁻⁶	1.01 x 10 ⁻⁶
	ρ (kg/m ³)	1.21	999	1027
	Pref (μPa)	20	1	1

$$\Delta x := 90.0 \cdot \text{cm}$$

$$W := .305 \cdot \text{m}$$

$$c := 343 \cdot \frac{\text{m}}{\text{sec}}$$

$$\Delta \delta_{\text{star}} := 0.278 \cdot \text{cm}$$

$$r := 1 \cdot \text{m}$$

$$v := 1.51 \cdot 10^{-5} \cdot \frac{\text{m}^2}{\text{sec}}$$

$$U_o := 21 \cdot \frac{\text{m}}{\text{sec}}$$

$$\theta := 0 \cdot \text{deg}$$

$$U_c := 0.7 \cdot U_o$$

$$\rho := 1.21 \cdot \frac{\text{kg}}{\text{m}^3}$$

$$\text{Ret} := 0.8 \cdot 10^6$$

$$\text{Pref} := 20 \cdot 10^{-6} \cdot \text{Pa}$$

POWER SPECTRAL DENSITY

This section will calculate some factors which will be used in the leading terms for the final spectrum calculation.

$$X_o := v \cdot \frac{Re_t}{U_o} \quad \text{calculated transition point}$$

$$Rex_o(X_o) := U_o \cdot \frac{X_o}{v} \quad \text{transition point Reynolds number}$$

$$\sigma(X_o) := 0.0288 \cdot \rho \cdot U_o^2 \cdot Rex_o(X_o)^{\frac{-1}{5}} \cdot \left(1 - 11.53 \cdot Rex_o(X_o)^{\frac{-3}{10}} \right) \quad \text{fluctuating wall shear stress}$$

This section will define the intermittency function, $\gamma(Z)$, and the turbulent spot burst rate, $N(Z)$, where $Z = \eta_x / \Delta x$. To lessen computational burden later, the integrations will use another function $B(Z) = N(Z)(\Delta x / U_o)$. Obviously, this just removes the factor $(U_o / \Delta x)$ from the definition of $N(Z)$ but this factor is common to both models of interest and is accounted for in the overall equation..

INTERMITTENCY FACTOR

This is the time-averaged value of the indicator function and represents the percentage of time that the flow is in a turbulent state. Either of two models for this factor can be chosen by the user for the computation of the spectrum. The empirical relation from Farabee, et al. (1974) was used in Lauchle (1980).

$$\gamma_{Farabee}(Z) := 1 - \exp(-4.185 \cdot Z^2) \quad \text{Empirical relations from Farabee, et al. (1974).}$$

$$\gamma_{JL}(Z) := 1 - \exp[-(1 + 3.4 \cdot Z) \cdot Z^2] \quad \text{Empirical relations from Josserand and Lauchle (1986) which was based on the work of Gedney (1979) assessing both a Dirac line source hypothesis and a constant source hypothesis for intermittency.}$$

****CHOOSE INTERMITTENCY FACTOR:** $\gamma(Z) := \gamma_{Farabee}(Z)$

TURBULENT SPOT BURST RATE

This is the time-averaged number of turbulent bursts sensed per second. Either of two models for this factor can be chosen by the user for the computation of the spectrum. The empirical relation from Farabee, et al. (1974) was used in Lauchle (1980).

$$B_{\text{Farabee}}(Z) := 1.272 \cdot Z \cdot \exp(-4.185 \cdot Z^2)$$

$$B_{\text{Marboe}}(Z) := 1.8 \cdot Z^{1.5} \cdot \exp(-4 \cdot Z^2)$$

$$B_{\text{JL}}(Z) := 2.38 \cdot \sqrt{\left[(1 - \gamma(Z)) \cdot \ln \left[\frac{1}{(1 - \gamma(Z))} \right] \right]}$$

****CHOOSE SPOT BURST RATE FUNCTION: $B(Z) := B_{\text{Farabee}}(Z)$**

FLARE PARAMETER

This parameter is used in the longitudinal space-time correlation function to account for moving axis decorrelation due to a burst not remaining perfectly correlated as the distance increases beyond some characteristic scale.

$$\alpha_{\text{star}} \Delta x(Z) := 1 + 83.35 \cdot Z^8$$

Normalized flare parameter used in the longitudinal space-time correlation function developed by Lauchle (1980) using data from Shivitz (1975).

F FUNCTION

This section will define the F function given by Lauchle(1980) equation 37 which is integrated over the transition zone. It is assumed that U_c/U_o is independent of frequency. The spectrum is then calculated for single frequencies which represent 1/3 octave center frequencies from 10 Hz to 80 KHz.

$$T1(KD, Z) := \left[\frac{2 \cdot \alpha_{star} \Delta x(Z)}{(\alpha_{star} \Delta x(Z)^2 + KD^2)^{\frac{1}{2}}} \right]$$

$$T2(KD, Z) := \exp(-\alpha_{star} \Delta x(Z) \cdot Z) \cdot \sin \left(KD \cdot Z - \operatorname{atan} \left(\frac{\alpha_{star} \Delta x(Z)}{KD} \right) \right)$$

$$T3(KD, Z) := \exp[-\alpha_{star} \Delta x(Z) \cdot (1 - Z)] \cdot \sin \left[KD \cdot (1 - Z) - \operatorname{atan} \left(\frac{\alpha_{star} \Delta x(Z)}{KD} \right) \right]$$

$$\text{Func}(KD, \text{VEL}, Z) := \frac{B(Z) \cdot \gamma(Z) \cdot Z \cdot (T1(KD, Z) - T2(KD, Z) + T3(KD, Z))}{\left[\left[4 \cdot (B(Z))^2 \cdot \text{VEL}^{-2} \right] + KD^2 \right] (\alpha_{star} \Delta x(Z)^2 + KD^2)^{\frac{1}{2}}}$$

$$F(A, C) = A^2 \cdot \int_0^1 \text{Func}(A, C, Z) dZ$$

Equation implemented below with trapezoidal integration.

SPECTRAL CALCULATIONS

Define frequency range

ORIGIN := 1

$$f_{\max} := 5000 \cdot \text{Hz} \quad \text{KL} := 1000 \quad k := 1.. \text{KL} \quad f_k := f_{\max} \cdot 10^{3 \cdot \left(\frac{k}{\text{KL}} - 1 \right)}$$

points := 1000

$$nn := 1.. \text{points} + 1 \quad Z_{nn} := \frac{nn - 1}{\text{points}}$$

$$\text{int}_{k, nn} := \text{Func} \left(2 \cdot \pi \cdot f_k \cdot \frac{\Delta x}{U_c}, \frac{U_c}{U_o}, Z_{nn} \right)$$

$$dZ := \frac{1}{\text{points}}$$

$$\text{FF}_k := \sum_{nn=1}^{\text{points}} \frac{(\text{int}_{k, nn+1} + \text{int}_{k, nn})}{2} \cdot dZ$$

Definition of function representing power spectral density:

$$F_k := \left(2 \cdot \pi \cdot f_k \cdot \frac{\Delta x}{U_c} \right)^2 \cdot \text{FF}_k$$

$$G_k := \frac{[W \cdot (\sigma(X_o))^2 \cdot (\cos(\theta))^2 \cdot U_o \cdot (\Delta x)^2] \cdot F_k}{2 \cdot r^2 \cdot \pi^2 \cdot c^2}$$

Calculation of power spectral density:

$$\text{SPEC}G_k := 10 \cdot \log \left[\left[\frac{G_k}{(\text{Pref})^2} \right] \cdot \text{Hz} \right]$$

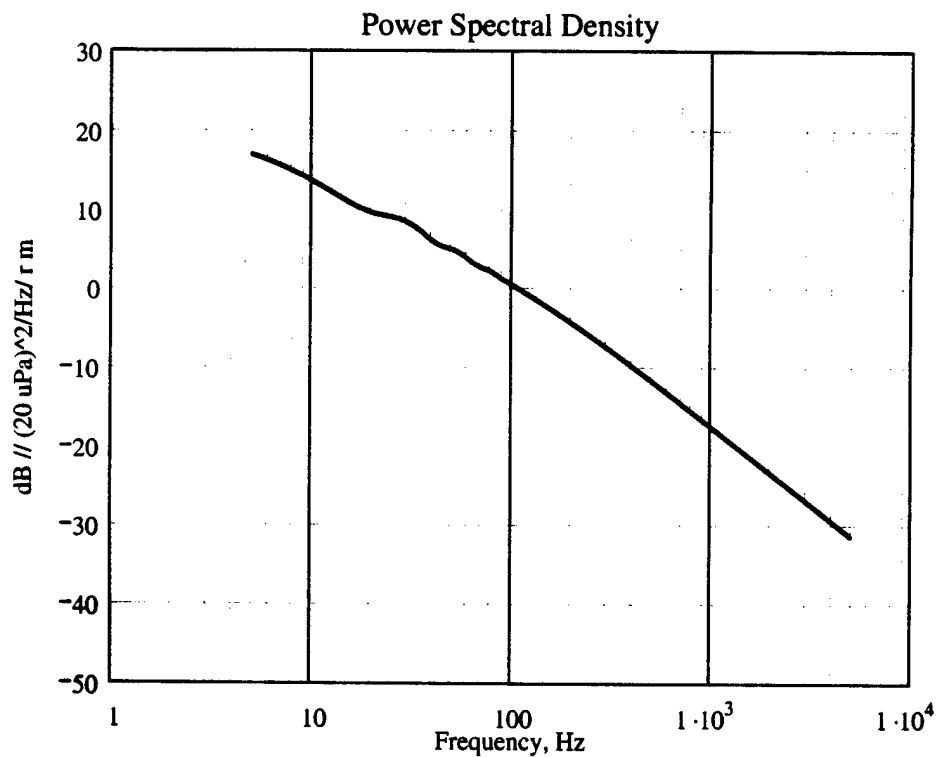
RADIATED NOISE DUE TO SHEAR STRESS FROM BOUNDARY LAYER TRANSITION USING Lighthill ANALOGY

GLPROG80.MCD

$\Delta x = 0.9 \text{ m}$	$W = 0.305 \text{ m}$	$c = 343 \text{ msec}^{-1}$
$\Delta \delta_{\text{star}} = 0.00278 \text{ m}$	$r = 1 \text{ m}$	$\nu = 0.0000151 \text{ m}^2 \text{ sec}^{-1}$
$U_o = 21 \text{ msec}^{-1}$	$\theta = 0$	$\rho = 1.21 \text{ kg m}^{-3}$
$U_c = 14.7 \text{ msec}^{-1}$		
$Re_t = 800000$	$P_{ref} = 0.00002 \text{ kg m}^{-1} \text{ sec}^{-2}$	

$\gamma(Z) = \gamma_{\text{Farabee}}(Z)$ $B(Z) = B_{\text{Farabee}}(Z)$

SPECTRAL PLOTS



REFERENCES

Farabee, T. M., Casarella, M. J., and DeMetz, F. C., 1974, "Source Distribution of Turbulent Bursts During Natural Transition," David W. Taylor Naval Ship Research and Development Center Report SAD-89E-1942, August 1974.

Gedney, C. J., 1979, "Wall Pressure Fluctuations During Transition on a Flat Plate," Massachusetts Institute of Technology Report 84618-1.

Josserand, M. A. and Lauchle, G. C., 1986, "Wavevector-Frequency Spectrum of Transition Zone Wall Pressure Fluctuations," ARL Penn State Technical Report TR 86-008, December 1986.

Shivitz, W. F., 1975, "An Experimental Investigation of Artificially Induced Transition to Turbulence on a Body of Revolution," M.S. Thesis, The Pennsylvania State University.

MODIFICATION HISTORY

Original program	7 May 1998	Conversion of elements of GLPROG VAX
Mod 1	14 May 1998	Addition of choices for intermittency and burst rate functions
Mod 2	4 July 2000	Substitution of trapezoidal integration.

Spectrum⁽¹⁾ := f·sec

Spectrum⁽²⁾ := SPECG


Z:\180 QAF FF 21.TXT

Spectrum

A.2 Fluctuating Boundary Layer Displacement Thickness Using a Liepmann Analogy - Theoretical Space-Time Correlation Function

Mathcad file: GLPROG81.MCD

DEFINITIONS

Δx is the length of the transition zone in feet or meters

$\Delta\delta^*$ is the change of the boundary layer displacement thickness from laminar to turbulent states in feet or meters ($\Delta\delta^* = \delta^*_{\text{turbulent}} - \delta^*_{\text{laminar}}$) ($\Delta\delta^*$ star in worksheet)

U_o is the freestream velocity in feet/sec or meters/sec

U_c is the convection velocity in feet/sec or meters/sec (nominally $U_c = 0.7 \cdot U_o$)

α^* is the flare parameter accounts for moving axis decorrelation

c is the speed of sound in feet/sec or meters/sec

T_i is the time it takes $\delta^*_{\text{laminar}}$ to transition to $d\delta_{\text{turbulent}}$ in sec

rise is the non-dimensional rise time for the $\Delta\delta^*$ (rise = $U_c \cdot T_i / \Delta x$)

Re_t is the transition Reynolds number based on Δx

Re_x is the Reynolds number based on the distance to the start of the transition zone

W is the spanwise width of the transition zone in feet or meters

ν is the kinematic viscosity in feet^2/sec

ρ is the fluid density in $\text{slugs}/\text{feet}^3$

r is the far-field observation distance in feet or meters

θ is the angle from the plane of the wall to the observation point

SPECIFY VALUES FOR FLOW AND GEOMETRY VARIABLES

$$Fr := \begin{pmatrix} 1.0 \\ 1.25 \\ 1.6 \\ 2.0 \\ 2.5 \\ 3.15 \\ 4.0 \\ 5.0 \\ 6.3 \\ 8.0 \end{pmatrix}$$

[Note: Mathcad is operating in SI units mode for all calculations. The user may enter values for variables in any appropriate measurement system so long as the units are specified. The program will automatically make the conversion to SI units during calculation.]

Define 1/3 Octave band center frequencies

$$a := 0..9$$

$$Freq_a := Fr_a \cdot 1.0 \cdot \text{Hz}$$

$$b := 10..19$$

$$Freq_b := Fr_{(b-10)} \cdot 10.0 \cdot \text{Hz}$$

$$d := 20..29$$

$$Freq_d := Fr_{(d-20)} \cdot 100.0 \cdot \text{Hz}$$

$$e := 30..39$$

$$Freq_e := Fr_{(e-30)} \cdot 1000.0 \cdot \text{Hz}$$

$$f := 40..49$$

$$Freq_f := Fr_{(f-40)} \cdot 10000.0 \cdot \text{Hz}$$

Constant- s for user reference.	Constant c (m/s)	Air	Fresh Water	Salt Water
	v (m ² /s)	1.51 x 10 ⁻⁵	1.01 x 10 ⁻⁶	1.01 x 10 ⁻⁶
	ρ (kg/m ³)	1.21	999	1027
	Pref (μPa)	20	1	1
Δx := 2.82·cm		Ti := 0.45·sec		c := 1525· $\frac{\text{m}}{\text{sec}}$
Δδstar := 0.021·cm		rise := 0.15		
Uo := 21.0· $\frac{\text{m}}{\text{sec}}$		W := .305·m		v := 1.01·10 ⁻⁶ · $\frac{\text{m}^2}{\text{sec}}$
Uc := 0.7·Uo		r := 1.0·m		Pref := 1·10 ⁻⁶ ·Pa
Ret := 1.5·10 ⁶		ρ := 999· $\frac{\text{kg}}{\text{m}^3}$		

POWER SPECTRAL DENSITY

This section will define the intermittency function, $\gamma(Z)$, and the turbulent spot burst rate, $N(Z)$, where $Z = \eta_x/\Delta x$. To lessen computational burden later, the integrations will use another function $B(Z) = N(Z)(\Delta x/U_0)$. Obviously, this just removes the factor $(U_0/\Delta x)$ from the definition of $N(Z)$ but this factor is common to both models of interest and is accounted for in the overall equation..

INTERMITTENCY FACTOR

This is the time-averaged value of the indicator function and represents the percentage of time that the flow is in a turbulent state. Either of two models for this factor can be chosen by the user for the computation of the spectrum. The empirical relation from Farabee, et al. (1974) was used in Lauchle (1980).

$$\gamma_{\text{Farabee}}(Z) := 1 - \exp(-4.185 \cdot Z^2) \quad \text{Empirical relations from Farabee, et al. (1974).}$$

$$\gamma_{\text{JL}}(Z) := 1 - \exp[-(1 + 3.4 \cdot Z) \cdot Z^2] \quad \text{Empirical relations from Josserand and Lauchle (1986) which was based on the work of Gedney (1979) assessing both a Dirac line source hypothesis and a constant source hypothesis for intermittency.}$$

****CHOOSE INTERMITTENCY FACTOR:** $\gamma(Z) := \gamma_{\text{Farabee}}(Z)$

TURBULENT SPOT BURST RATE

This is the time-averaged number of turbulent bursts sensed per second. Either of two models for this factor can be chosen by the user for the computation of the spectrum. The empirical relation from Farabee, et al. (1974) was used in Lauchle (1980).

$$B_{\text{Farabee}}(Z) := 1.272 \cdot Z \cdot \exp(-4.185 \cdot Z^2)$$

$$B_{\text{Marboe}}(Z) := 1.8 \cdot Z^{1.5} \cdot \exp(-4 \cdot Z^2)$$

$$B_{\text{JL}}(Z) := 2.38 \cdot \sqrt{\left[(1 - \gamma(Z)) \cdot \ln \left[\frac{1}{(1 - \gamma(Z))} \right] \right]}$$

****CHOOSE SPOT BURST RATE FUNCTION:** $B(Z) := B_{\text{Farabee}}(Z)$

FLARE PARAMETER

This parameter is used in the longitudinal space-time correlation function to account for moving axis decorrelation due to a burst not remaining perfectly correlated as the distance increases beyond some characteristic scale.

$$\alpha_{\text{star}\Delta x}(Z) := 1 + 83.35 \cdot Z^8$$

Normalized flare parameter used in the longitudinal space-time correlation function developed by Lauchle (1980) using data from Shivitz (1975).

F* FUNCTION

This section will define the F function given by Lauchle(1980) equation 37 which is integrated over the transition zone. It is assumed tha U_c/U_o is independent of frequency. The spectrum is then calculated for single frequencies which represent 1/3 octave center frequencies from 10 Hz to 80 KHz.

$$T1(KD, Z) := \left[\frac{2 \cdot \alpha_{star} \Delta x(Z)}{(\alpha_{star} \Delta x(Z)^2 + KD^2)^{\frac{1}{2}}} \right]$$

$$T2(KD, Z) := \exp(-\alpha_{star} \Delta x(Z) \cdot Z) \cdot \sin \left(KD \cdot Z - \operatorname{atan} \left(\frac{\alpha_{star} \Delta x(Z)}{KD} \right) \right)$$

$$T3(KD, Z) := \exp[-\alpha_{star} \Delta x(Z) \cdot (1 - Z)] \cdot \sin \left[KD \cdot (1 - Z) - \operatorname{atan} \left(\frac{\alpha_{star} \Delta x(Z)}{KD} \right) \right]$$

$$\text{Func}(KD, \text{VEL}, Z) := \frac{B(Z) \cdot \gamma(Z) \cdot Z \cdot (T1(KD, Z) - T2(KD, Z) + T3(KD, Z))}{\left[\left[4 \cdot (B(Z))^2 \cdot \text{VEL}^{-2} \right] + KD^2 \right] (\alpha_{star} \Delta x(Z)^2 + KD^2)^{\frac{1}{2}}}$$

$$F(A, C) := A^2 \cdot \int_0^1 \text{Func}(A, C, Z) dZ$$

$$\text{FSTAR}(A, C, T) := \frac{A^2}{(1.0 + A^2 \cdot T^2)} \cdot F(A, C)$$

SPECTRAL CALCULATIONS

Define frequency range

ORIGIN := 1

$$\begin{aligned} f_{\max} &:= 5000 \cdot \text{Hz} & KL &:= 1000 & k &:= 1..KL & f_k &:= f_{\max} \cdot 10^{3 \cdot \left(\frac{k}{KL} - 1\right)} \\ \text{points} &:= 1000 \end{aligned}$$

$$nn := 1.. \text{points} + 1 \quad Z_{nn} := \frac{nn - 1}{\text{points}}$$

$$\text{int}_{k,nn} := \text{Func} \left(2 \cdot \pi \cdot f_k \cdot \frac{\Delta x}{U_c}, \frac{U_c}{U_o}, Z_{nn} \right) \quad dZ := \frac{1}{\text{points}}$$

$$FF_k := \sum_{nn=1}^{\text{points}} \frac{(\text{int}_{k,nn+1} + \text{int}_{k,nn})}{2} \cdot dZ$$

Definition of function representing power spectral density:

$$Fstar_k := \frac{\left(2 \cdot \pi \cdot f_k \cdot \frac{\Delta x}{U_c} \right)^4}{\left[1 + \left(2 \cdot \pi \cdot f_k \cdot \frac{\Delta x}{U_c} \right)^2 \cdot rise^2 \right]} \cdot FF_k$$

$$G_k := \frac{\left[(W \cdot \rho^2 \cdot \Delta \delta star^2) \cdot U_o \cdot U_c^2 \right] \cdot Fstar_k}{8 \cdot r^2 \cdot \pi^2}$$

Calculation of power spectral density:

$$\text{SPEC}G_k := 10 \cdot \log \left[\left[\frac{G_k}{(\text{Pref})^2} \right] \cdot \text{Hz} \right]$$

RADIATED NOISE DUE TO FLUCTUATING DISPLACEMENT THICKNESS FROM BOUNDARY LAYER TRANSITION USING LIEPMANN ANALOGY

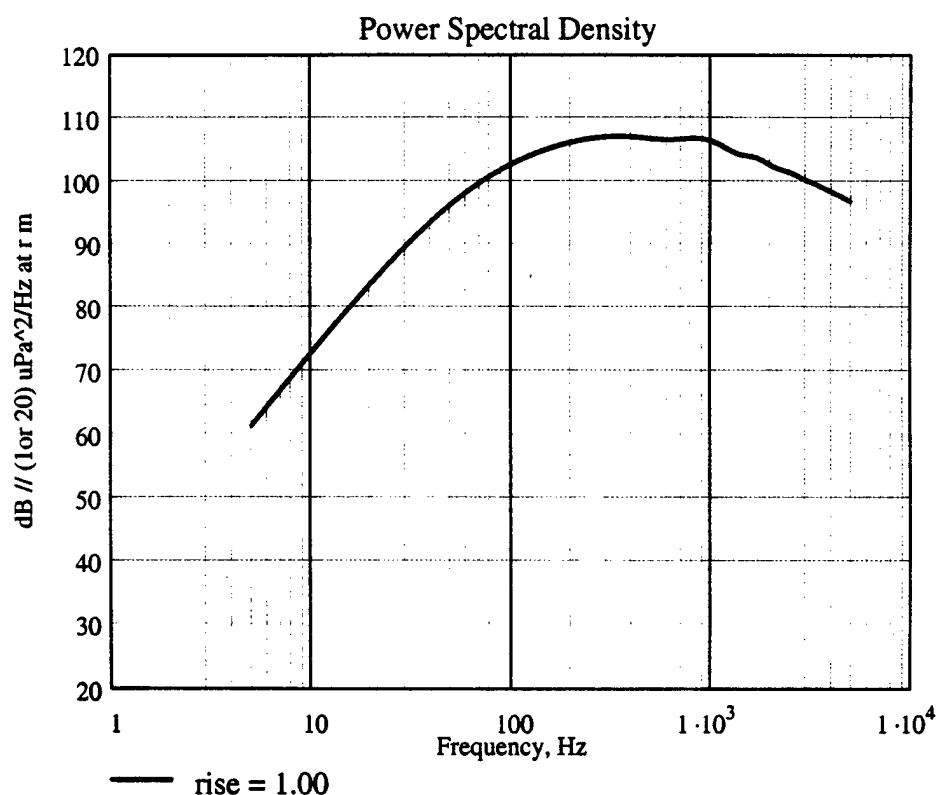
GLPROG81.MCD

$\Delta x = 0.028 \text{ m}$	$W = 0.305 \text{ m}$	$c = 1525 \text{ msec}^{-1}$
$\Delta \delta_{\text{star}} = 0.00021 \text{ m}$	$r = 1 \text{ m}$	$\nu = 0.00000101 \text{ m}^2 \text{ sec}^{-1}$
$U_o = 21 \text{ msec}^{-1}$	$\text{rise} = 0.15$	$\rho = 999 \text{ kg m}^{-3}$
$U_c = 14.7 \text{ msec}^{-1}$	$\text{Pref} = 0.000001 \text{ kg m}^{-1} \text{ sec} \frac{U_c}{U_o} = 0.7$	
$\text{Ret} = 1500000$		

SPECTRAL PLOTS

$\gamma(Z) = \gamma_{\text{Farabee}}(Z)$

$B(Z) = B_{\text{Farabee}}(Z)$



REFERENCES

Farabee, T. M., Casarella, M. J., and DeMetz, F. C., 1974, "Source Distribution of Turbulent Bursts During Natural Transition," David W. Taylor Naval Ship Research and Development Center Report SAD-89E-1942, August 1974.

Gedney, C. J., 1979, "Wall Pressure Fluctuations During Transition on a Flat Plate," Massachusetts Institute of Technology Report 84618-1.

Josserand, M. A. and Lauchle, G. C., 1986, "Wavevector-Frequency Spectrum of Transition Zone Wall Pressure Fluctuations," ARL Penn State Technical Report TR 86-008, December 1986.

Lauchle, G. C., 1980, 'On the radiated noise due to boundary-layer transition,' *J. Acous. Soc. of Amer.*, **67**, pp.158-168.

Shivitz, W. F., 1975, "An Experimental Investigation of Artificially Induced Transition to Turbulence on a Body of Revolution," M.S. Thesis, The Pennsylvania State University.

MODIFICATION HISTORY

Original program	7 June 1998	Conversion of elements of GLPROG VAX
Mod 1	7 June 1998	Addition of choices for intermittency and burst rate functions
Mod 2	4 July 2000	Substituted trapezoidal integration

Spectrum⁽¹⁾ := f·sec

Spectrum⁽²⁾ := SPECG



Z:\181 WATER FF 21.TXT

Spectrum

**A.3 Fluctuating Boundary Layer Displacement Thickness Using a Liepmann
Analogy - Theoretical Space-Time Correlation Function with Krane Dipole
Source Model**

Mathcad file: KMTRANS00.MCD

RADIATED NOISE DUE TO FLUCTUATING DISPLACEMENT THICKNESS FROM BOUNDARY LAYER TRANSITION USING A LIEPMANN ANALOGY WITH KRANE DIPOLE MODEL

[KMTRANS00.MCD, Mathcad 2000 Professional]

This program is the implementation of a boundary layer transition noise model described in:

Lauchle, G. C., 1981, 'Transition noise - The role of fluctuating displacement thickness,' *J. Acous. Soc. of Amer.*, **69**, pp.665-671.

However, the source term has been modified to replace the monopole with a dipole derived from the measurements cited in:

Krane, M. H., 1992, "Estimation of the Direct Acoustic Radiation from Turbulent Spots, Using Boundary Layer Velocity Measurements," Ph.D. Thesis in Aerospace Engineering, The Pennsylvania State University.

ASSUMPTIONS

- builds on fluctuating shear stress model [Lauchle 1981]
- zero pressure gradient flow and natural transition flow structures, i.e. no separation).
- flow is over an infinite, planar, rigid surface
- based on very low Mach number - use only dipole components due to fluctuating displacement thickness
- flow is statistically homogeneous in spanwise direction, x_3 , non-homogeneous in streamwise direction, x_1 , stationary but Poisson distributed in time so we can use a classical correlation function for a random sequence of bursts, $\exp(-2N|t|)$
- neglect quadrupoles and octupoles due to fluctuating Reynolds stresses due to lower radiation efficiencies - however, their amplitudes relative to shear stresses may overcome this lower efficiency.
- the space-time correlation function for the indicator function $\langle \Pi' \rangle$ is direction separable
- the lateral term integration derived from this separation is equal to $2L_3(\eta_1) = 2(1.5 \eta_1 \tan \alpha)$ which is about $\eta_1/4$ for $\alpha=9.6$ degrees (angle of spreading for turbulent spot)
- U_c/U_o is independent of frequency
- the normalized rise time is described as a function of $\eta_1/\Delta x$

DEFINITIONS

Δx is the length of the transition zone in feet or meters

$\Delta\delta^*$ is the change of the boundary layer displacement thickness from laminar to turbulent states in feet or meters ($\Delta\delta^* = \delta^*_{\text{turbulent}} - \delta^*_{\text{laminar}}$) ($\Delta\delta^*$ star in worksheet)

U_o is the freestream velocity in feet/sec or meters/sec

U_c is the convection velocity in feet/sec or meters/sec (nominally $U_c = 0.7 \cdot U_o$)

α^* is the flare parameter accounts for moving axis decorrelation

c is the speed of sound in feet/sec or meters/sec

T_i is the time it takes $\delta^*_{\text{laminar}}$ to transition to $\delta^*_{\text{turbulent}}$ in sec

rise is the non-dimensional rise time for the $\Delta\delta^*$ ($\text{rise} = U_c \cdot T_i / \Delta x$)

Re_t is the transition Reynolds number based on Δx

Re_x is the Reynolds number based on the distance to the start of the transition zone

W is the spanwise width of the transition zone in feet or meters

ν is the kinematic viscosity in feet^2/sec

ρ is the fluid density in slugs/feet^3

r is the far-field observation distance in feet or meters

θ is the angle from the plane of the wall to the observation point

SPECIFY VALUES FOR FLOW AND GEOMETRY VARIABLES

$$\text{Fr} := \begin{pmatrix} 1.0 \\ 1.25 \\ 1.6 \\ 2.0 \\ 2.5 \\ 3.15 \\ 4.0 \\ 5.0 \\ 6.3 \\ 8.0 \end{pmatrix}$$

[Note: Mathcad is operating in SI units mode for all calculations. The user may enter values for variables in any appropriate measurement system so long as the units are specified. The program will automatically make the conversion to SI units during calculation.]

Define 1/3 Octave band center frequencies

$$a := 0..9$$

$$\text{Freq}_a := \text{Fr}_a \cdot 1.0 \cdot \text{Hz}$$

$$b := 10..19$$

$$\text{Freq}_b := \text{Fr}_{(b-10)} \cdot 10.0 \cdot \text{Hz}$$

$$d := 20..29$$

$$\text{Freq}_d := \text{Fr}_{(d-20)} \cdot 100.0 \cdot \text{Hz}$$

$$e := 30..39$$

$$\text{Freq}_e := \text{Fr}_{(e-30)} \cdot 1000.0 \cdot \text{Hz}$$

$$f := 40..49$$

$$\text{Freq}_f := \text{Fr}_{(f-40)} \cdot 10000.0 \cdot \text{Hz}$$

Constant- s for user reference.	Constant c (m/s)	Air 343	Fresh Water 1525	Salt Water 1487
	ν (m ² /s)	1.51×10^{-5}	1.01×10^{-6}	1.01×10^{-6}
	ρ (kg/m ³)	1.21	999	1027
	Pref (μPa)	20	1	1

$$\Delta x := 90 \cdot \text{cm}$$

$$\Delta \delta_{\text{star}} := 0.278 \cdot \text{cm}$$

$$U_o := 21.0 \cdot \frac{\text{m}}{\text{sec}}$$

$$U_c := 0.7 \cdot U_o$$

$$\text{Ret} := 1.5 \cdot 10^6$$

$$\Delta \delta := 1.6 \cdot \text{cm}$$

$$W := .305 \cdot \text{m}$$

$$r := 1.0 \cdot \text{m}$$

$$\theta := 45 \cdot \text{deg}$$

$$c := 343 \cdot \frac{\text{m}}{\text{sec}}$$

$$\nu := 1.51 \cdot 10^5 \cdot \frac{\text{m}^2}{\text{sec}}$$

$$\text{Pref} := 20 \cdot 10^{-6} \cdot \text{Pa}$$

$$\rho := 1.21 \cdot \frac{\text{kg}}{\text{m}^3}$$

POWER SPECTRAL DENSITY

This section will define the intermittency function, $\gamma(Z)$, and the turbulent spot burst rate, $N(Z)$, where $Z = \eta_x/\Delta x$. To lessen computational burden later, the integrations will use another function $B(Z) = N(Z)(\Delta x/U_0)$. Obviously, this just removes the factor $(U_0/\Delta x)$ from the definition of $N(Z)$ but this factor is common to both models of interest and is accounted for in the overall equation..

INTERMITTENCY FACTOR

This is the time-averaged value of the indicator function and represents the percentage of time that the flow is in a turbulent state. Either of two models for this factor can be chosen by the user for the computation of the spectrum. The empirical relation from Farabee, et al. (1974) was used in Lauchle (1980).

$$\gamma_{\text{Farabee}}(Z) := 1 - \exp(-4.185 \cdot Z^2) \quad \text{Empirical relations from Farabee, et al. (1974).}$$

$$\gamma_{\text{JL}}(Z) := 1 - \exp[-(1 + 3.4 \cdot Z) \cdot Z^2] \quad \text{Empirical relations from Josserand and Lauchle (1986) which was based on the work of Gedney (1979) assessing both a Dirac line source hypothesis and a constant source hypothesis for intermittency.}$$

****CHOOSE INTERMITTENCY FACTOR:** $\gamma(Z) := \gamma_{\text{Farabee}}(Z)$

NORMALIZED RISE TIME

This value has previously always been held as a constant throughout the transition zone. It is often used as a parametric variable in the use of GLPROG81. However, Krane measured a variation of this time with longitudinal position in the transition zone. The user may choose to use the Krane function or just set a constant. Parametric values of 0.05, 0.15, 0.45, and 1.0 are common.

$$TK(Z) := 0.30 - \exp(-1.45 - 3 \cdot Z^2) \quad \text{Empirical relation from figures 4.15 and 4.20 in Krane (1992)}$$

****CHOOSE RISE TIME FUNCTION:** $T := 0.15$ Use constant for higher frequency calculations.

TURBULENT SPOT BURST RATE

This is the time-averaged number of turbulent bursts sensed per second. Either of two models for this factor can be chosen by the user for the computation of the spectrum. The empirical relation from Farabee, et al. (1974) was used in Lauchle (1980).

$$B_{\text{Farabee}}(Z) := 1.272 \cdot Z \cdot \exp(-4.185 \cdot Z^2)$$

$$B_{\text{JL}}(Z) := 2.38 \cdot \sqrt{\left[(1 - \gamma(Z)) \cdot \ln \left[\frac{1}{(1 - \gamma(Z))} \right] \right]}$$

****CHOOSE SPOT BURST RATE FUNCTION:** $B(Z) := B_{\text{Farabee}}(Z)$

FLARE PARAMETER

This parameter is used in the longitudinal space-time correlation function to account for moving axis decorrelation due to a burst not remaining perfectly correlated as the distance increases beyond some characteristic scale.

$$\alpha_{\text{star}\Delta x}(Z) := 1 + 83.35 \cdot Z^8$$

Normalized flare parameter used in the longitudinal space-time correlation function developed by Lauchle (1980) using data from Shivitz (1975).

F* FUNCTION

This section will define the F function given by Lauchle(1980) equation 37 which is integrated over the transition zone. It is assumed that U_c/U_o is independent of frequency. The spectrum is then calculated for single frequencies which represent 1/3 octave center frequencies from 10 Hz to 80 KHz.

$$T1(KD, Z) := \left[\frac{2 \cdot \alpha_{star} \Delta x(Z)}{(\alpha_{star} \Delta x(Z)^2 + KD^2)^{\frac{1}{2}}} \right]$$

$$T2(KD, Z) := \exp(-\alpha_{star} \Delta x(Z) \cdot Z) \cdot \sin \left(KD \cdot Z - \operatorname{atan} \left(\frac{\alpha_{star} \Delta x(Z)}{KD} \right) \right)$$

$$T3(KD, Z) := \exp[-\alpha_{star} \Delta x(Z) \cdot (1 - Z)] \cdot \sin \left[KD \cdot (1 - Z) - \operatorname{atan} \left(\frac{\alpha_{star} \Delta x(Z)}{KD} \right) \right]$$

$$\text{Func}(KD, \text{VEL}, Z) := \frac{B(Z) \cdot \gamma(Z) \cdot Z \cdot (T1(KD, Z) - T2(KD, Z) + T3(KD, Z))}{\left[\left[4 \cdot (B(Z))^2 \cdot \text{VEL}^{-2} \right] + KD^2 \right] (\alpha_{star} \Delta x(Z)^2 + KD^2)^{\frac{1}{2}}}$$

$$F(A, C) := A^2 \cdot \int_0^1 \text{Func}(A, C, Z) dZ$$

This is the integration that is performed below using a trapezoidal method.

$$\text{FSTAR}(A, C, T) := \frac{A^2}{(1.0 + A^2 \cdot T^2)} \cdot F(A, C)$$

SPECTRAL CALCULATIONS

Define frequency range

ORIGIN := 1

$$f_{\max} := 5000 \cdot \text{Hz} \quad KL := 1250 \quad k := 1..KL \quad f_k := f_{\max} \cdot 10^{3 \cdot \left(\frac{k}{KL} - 1 \right)}$$

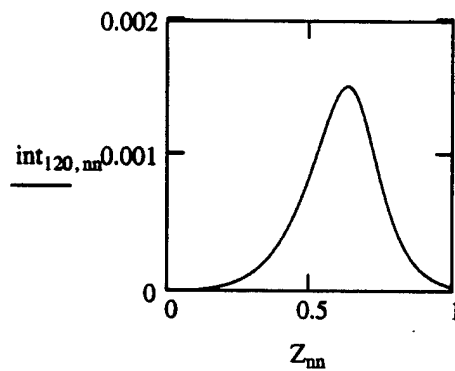
points := 1000

$$nn := 1..points + 1 \quad Z_{nn} := \frac{nn - 1}{points}$$

$$int_{k,nn} := \text{Func} \left(2 \cdot \pi \cdot f_k \cdot \frac{\Delta x}{U_c}, \frac{U_c}{U_o}, Z_{nn} \right)$$

$$dZ := \frac{1}{points}$$

$$FF_k := \sum_{nn=1}^{points} \frac{(int_{k,nn+1} + int_{k,nn})}{2} \cdot dZ$$



Definition of function representing power spectral density:

$$FFSTAR_k := \frac{\left(2 \cdot \pi \cdot f_k \cdot \frac{\Delta x}{Uc}\right)^4}{\left[1.0 + \left(2 \cdot \pi \cdot f_k \cdot \frac{\Delta x}{Uc}\right)^2 \cdot T^2\right]} \cdot FF_k$$

$$Arg_k := 0.1 \cdot \frac{2 \cdot \pi \cdot f_k}{c} \cdot \Delta x \cdot \cos(\theta)$$

From Kinsler & Frey -
constant rise time (and
therefore, d)

$$Dipole_k := 4 \cdot \left[\sin \left[\left(\frac{1}{2} \right) \cdot \left(\frac{2 \cdot \pi \cdot f_k}{c} \cdot \Delta \delta \cdot \cos(\theta) \right) \right] \right]^2$$

$$T50 := 0.1$$

$$Dipole2_k := 4 \cdot \left[\sin \left[\left(\frac{1}{2} \right) \cdot \left[\frac{2 \cdot \pi \cdot f_k}{c} \cdot \left[\Delta \delta^2 + (\Delta x \cdot T50)^2 \right]^{\frac{1}{2}} \cdot \cos(\theta) \right] \right] \right]^2$$

$$DipoleE2_k := 2 + \frac{2 \sin(Arg_k)}{Arg_k} \cdot (1 - 2 \cdot \cos(Arg_k))$$

Modified by calculating the
expected value for a uniform
distribution of the source
separation, d which is a
function of rise time which is
itself a function of Z

$$G_k := \frac{(W \cdot \rho^2 \cdot \Delta \delta \text{star}^2) \cdot Uo \cdot Uc^2 \cdot FFSTAR_k}{8 \cdot r^2 \cdot \pi^2}$$

$$GD_k := Dipole_k \cdot G_k$$

$$GD2_k := Dipole2_k \cdot G_k$$

$$GDE2_k := (DipoleE2_k) \cdot G_k$$

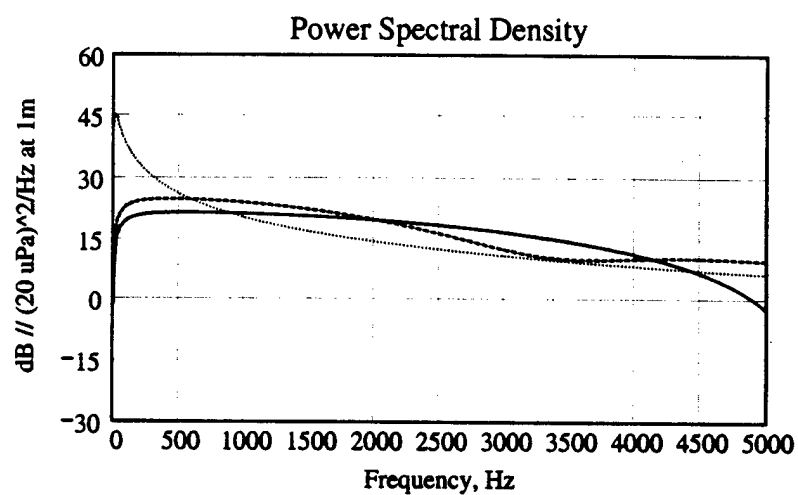
Calculation of power spectral density:

$$SPECG_k := 10 \cdot \log \left[\left[\frac{G_k}{(Pref)^2} \right] \cdot Hz \right]$$

$$SPECGD_k := 10 \cdot \log \left[\left[\frac{GD_k}{(Pref)^2} \right] \cdot Hz \right] \quad SPECGD2_k := 10 \cdot \log \left[\left[\frac{GD2_k}{(Pref)^2} \right] \cdot Hz \right]$$

$$\text{SPECGDE2}_k := 10 \cdot \log \left[\frac{\text{GDE2}_k}{(\text{Pref})^2} \cdot \text{Hz} \right]$$

$$\gamma(Z) = \gamma_{\text{Farabee}}(Z) \quad B(Z) = B_{\text{Farabee}}(Z)$$

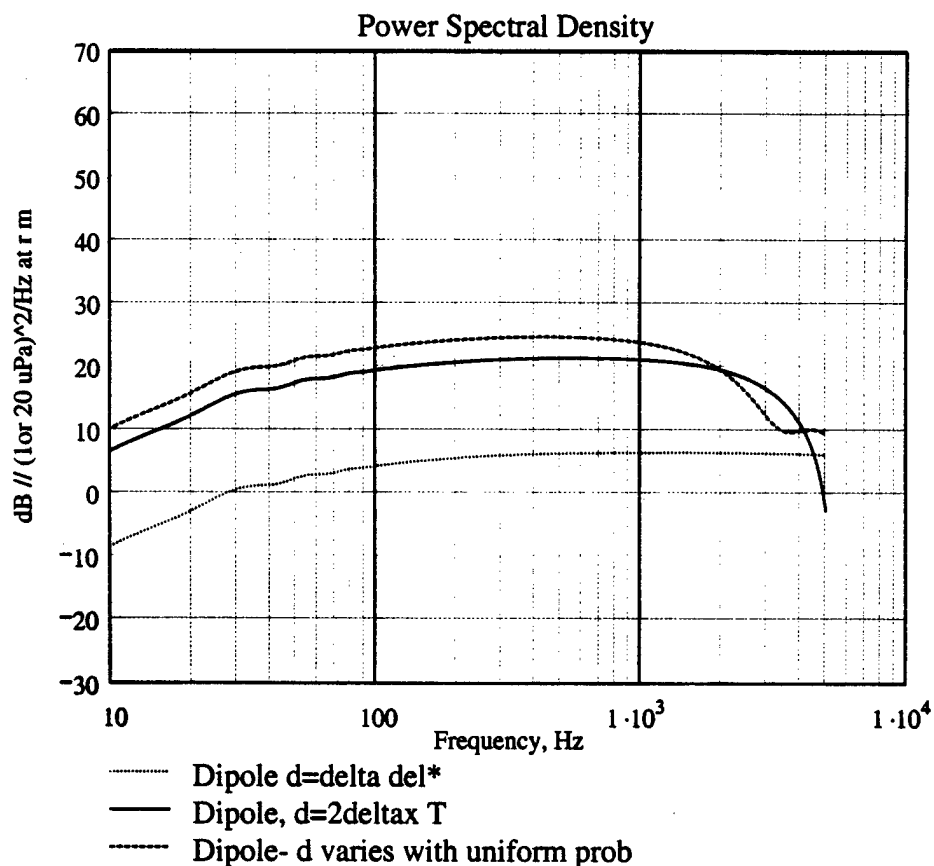


RADIATED NOISE DUE TO FLUCTUATING DISPLACEMENT THICKNESS FROM BOUNDARY LAYER TRANSITION USING LIEPMANN ANALOGY BUT DIPOLE SOURCE FROM KRANE

KMTRANS00.MCD

$\Delta x = 0.9 \text{ m}$	$W = 0.305 \text{ m}$	$c = 343 \text{ msec}^{-1}$
$\Delta \delta_{\text{star}} = 0.00278 \text{ m}$	$\Delta \delta = 0.016 \text{ m}$	$\nu = 151000 \text{ m}^2 \text{ sec}^{-1}$
$U_o = 21 \text{ msec}^{-1}$	$r = 1 \text{ m}$	$\rho = 1.21 \text{ kg m}^{-3}$
$U_c = 14.7 \text{ msec}^{-1}$	$\theta = 45 \text{ deg}$	
$Re_t = 1500000$	$P_{ref} = 0.00002 \text{ kg m}^{-1} \text{ sec}^{-2}$	$\frac{U_c}{U_o} = 0.7$

SPECTRAL PLOTS $\gamma(Z) = \gamma_{Farabee}(Z)$ $B(Z) = B_{Farabee}(Z)$
 $T(Z)=0.15$ Integration points = 1000



REFERENCES

- Farabee, T. M., Casarella, M. J., and DeMetz, F. C., 1974, "Source Distribution of Turbulent Bursts During Natural Transition," David W. Taylor Naval Ship Research and Development Center Report SAD-89E-1942, August 1974.
- Gedney, C. J., 1979, "Wall Pressure Fluctuations During Transition on a Flat Plate," Massachusetts Institute of Technology Report 84618-1.
- Josserand, M. A. and Lauchle, G. C., 1986, "Wavevector-Frequency Spectrum of Transition Zone Wall Pressure Fluctuations," ARL Penn State Technical Report TR 86-008, December 1986.
- Lauchle, G. C., 1980, 'On the radiated noise due to boundary-layer transition,' *J. Acous. Soc. of Amer.*, **67**, pp.158-168.
- Pierce, A. D., 1981, *Acoustics - An Introduction to its Physical Principles and Applications*, McGraw-Hill, New York.
- Shivitz, W. F., 1975, "An Experimental Investigation of Artificially Induced Transition to Turbulence on a Body of Revolution," M.S. Thesis, The Pennsylvania State University.

MODIFICATION HISTORY

Original	8 June 2000	Conversion of GLPROG81 to replace monopole with dipole source and put in normalized rise time
Mod 1	14 June 2000	as a function of Z Upgraded dipole source term to eliminate $kd \ll 1$ low frequency assumption.

$\text{Spectrum}^{(1)} := f \cdot \text{sec}$

$\text{Spectrum}^{(2)} := \text{SPECGD2}$

$\text{Spectrum}^{(3)} := \text{SPECGDE2}$


Z:\KMT\TRANS\QAF\FF21\NEW.TXT

Spectrum

A.4 Fluctuating Boundary Layer Displacement Thickness Using a Liepmann Analogy - Empirical Space-Time Correlation Function

Mathcad file: JLTRANS99.MCD

BOUNDARY LAYER TRANSITION ZONE SOUND RADIATION USING JOSSE RAND'S EMPIRICAL SPACE-TIME CORRELATION

[JLTRANS99.MCD, Mathcad 2000 Professional]

This program is the implementation of a boundary layer transition noise model described in:

Lauchle, G. C., 1981, "Transition noise - The role of fluctuating displacement

thickness," *J. Acous. Soc. of Amer.*, **69**, pp.665-671.

Josserand, M. A. and Lauchle, G. C., 1989, "Cross-Spectral Density of the Wall Pressure Fluctuations Under a Turbulent Boundary Layer," *J. Sound Vib.* **128**, pp. 519-522.

Josserand, M. A. and Lauchle, G. C., 1990, "Modeling the Wavevector-Frequency Spectrum of Boundary Layer Wall Pressure During Transition on a Flat Plate," *Trans. ASME, J. Vib. and Acoustics* **112**, pp. 523-534.

ASSUMPTIONS

- builds on fluctuating displacement thickness model [Lauchle 1981]
- zero pressure gradient flow and natural transition flow structures, i.e. no separation).
- flow is over an infinite, planar, rigid surface
- based on very low Mach number
- uses empirical description for Cross correlation function developed by Josserand
- U_c/U_0 is independent of frequency

DEFINITIONS

Define transition zone length (Δx) and free-stream velocity (U)

$$\Delta x := 0.9 \cdot m \quad U := 21 \cdot \frac{m}{sec}$$

Turbulent spot convection velocity $U_c := 0.8 \cdot U$

Intermittency factor, Josserand & Lauchle (1990) eqn. 11

$$c3 := 1.0 \quad c4 := 3.4$$

$$\gamma(\eta x) := 1 - \exp \left[- \left(c3 + c4 \cdot \frac{\eta x}{\Delta x} \right) \left(\frac{\eta x}{\Delta x} \right)^2 \right]$$

Josserand's space-time correlation function

$$A := -\ln\left(1 - \exp\left(\frac{-4.27 \cdot \text{m}}{\Delta x}\right)\right)$$

$$f1(\xi_x, \tau) := -5 \cdot \text{Hz} \cdot \left(4 + 200 \cdot \text{Hz} \cdot \left|\tau - \frac{\xi_x}{U_c}\right|\right) \cdot \left|\tau - \frac{\xi_x}{U_c}\right|$$

$$f2(\xi_x, \tau) := 20 \cdot \text{Hz} \cdot \frac{\left|\frac{\xi_x}{\Delta x}\right|}{0.014 + \left|\frac{\xi_x}{\Delta x}\right|} \cdot \left|\tau - \frac{\xi_x}{U_c}\right|$$

$$f3(\xi_x, \xi_z, \tau) := -\left|15.75 \cdot \frac{1}{\text{m}} \cdot \Delta x - \frac{1260 \cdot \text{Hz} \cdot \left|\tau - \frac{\xi_x}{U_c}\right|}{1 + 71 \cdot \left|\frac{\xi_z}{\Delta x}\right|}\right| \cdot \frac{\left|\frac{\xi_z}{\Delta x}\right|}{1 + 14.2 \cdot \left|\frac{\xi_x}{\Delta x}\right|}$$

$$f4(\xi_x, \tau) := \frac{-A \cdot \left|\frac{\xi_x}{\Delta x}\right|}{0.0014 + \left|\frac{\xi_x}{\Delta x}\right|} \cdot \frac{1}{1 + 1300 \cdot \text{Hz}^2 \cdot \left(\left|\tau - \frac{\xi_x}{U_c}\right|\right)^2}$$

$$\gamma_u(\eta_x, \xi_x) := \text{if}(\xi_x \geq 0, \gamma(\eta_x), \gamma(\eta_x + \xi_x)) \quad \gamma_d(\eta_x, \xi_x) := \text{if}(\xi_x \geq 0, \gamma(\eta_x + \xi_x), \gamma(\eta_x))$$

$$R(\eta_x, \xi_x, \xi_z, \tau) := \gamma_u(\eta_x, \xi_x) \cdot [\gamma_d(\eta_x, \xi_x) + (1 - \gamma_d(\eta_x, \xi_x)) \cdot e^{f1(\xi_x, \tau)} \cdot e^{f2(\xi_x, \tau)} \cdot e^{f3(\xi_x, \xi_z, \tau)}] \cdot e^{f4(\xi_x, \tau)}$$

Discretize the separation distance range

$$\Delta z(\eta_x) := 3 \cdot \eta_x \cdot \tan(9.4 \cdot \text{deg})$$

$$I_L := 31 \quad i := 0..I_L$$

$$J_L := 15 \quad j := 0..J_L \quad dx_{i,j} := \Delta x \cdot \left(\frac{i}{I_L}\right) \quad dz_{i,j} := \frac{j}{J_L} - \frac{1}{2}$$

$$\xi_x(\eta_x) := dx - \eta_x$$

$$\xi_z(\eta_x) := \Delta z(\eta_x) \cdot dz$$

Discretize the transition zone range and time delay

$$\begin{aligned} KL &:= 31 & N &:= 1000 & T &:= 12 \cdot \frac{\Delta x}{U} \\ k &:= 0..KL & n &:= 0..N-1 \\ \eta x_k &:= \Delta x \cdot \frac{k}{KL} & \tau_n &:= \left(2 \cdot \frac{n}{N} - 1\right) \cdot \frac{T}{2} \end{aligned}$$

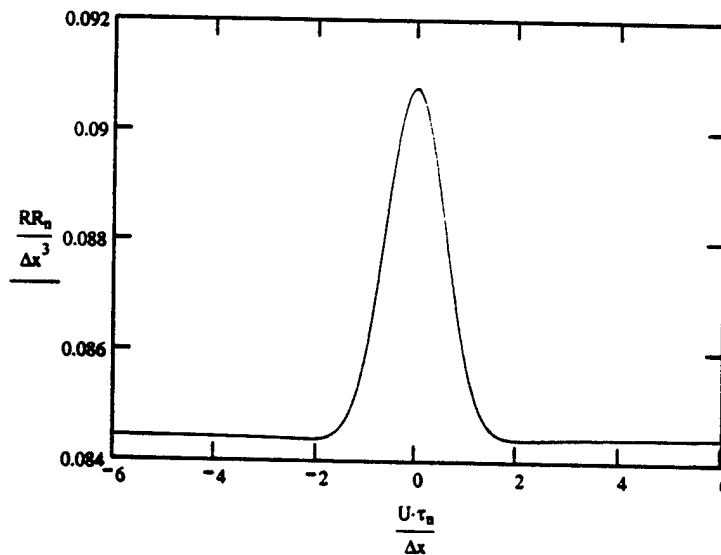
$$ff_{k,n} := \overrightarrow{R(\eta x_k, \xi x(\eta x_k), \xi z(\eta x_k), \tau_n)}$$

Integrate over the separation range

$$int_{k,n} := \frac{\Delta x \cdot \Delta z(\eta x_k)}{4 \cdot IL \cdot JL} \cdot \sum_{i=0}^{IL-1} \sum_{j=0}^{JL-1} \left[(ff_{k,n})_{i,j} + (ff_{k,n})_{i+1,j} + (ff_{k,n})_{i,j+1} + (ff_{k,n})_{i+1,j+1} \right]$$

Integrate over the transition zone

$$RR_n := \frac{\Delta x}{2 \cdot KL} \cdot \sum_{k=0}^{KL-1} (int_{k,n} + int_{k+1,n})$$



Discrete Fourier transform of spatially integrated correlation function

$$f_s := \frac{N}{T}$$

$$G := \frac{N}{f_s} \cdot \text{CFFT}(\text{RR})$$

$$k := 1..0.5 \cdot N$$

$$f_k := \frac{k}{N} \cdot f_s$$

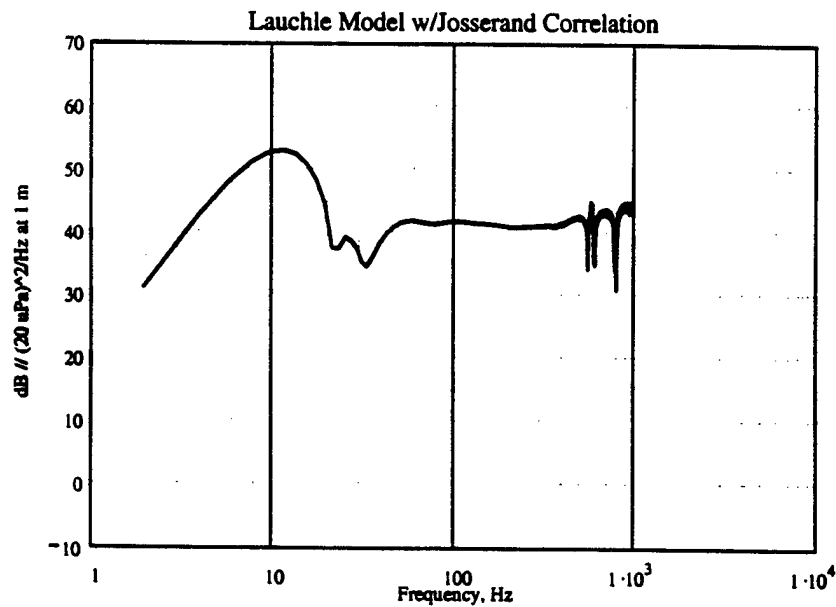
Farfield radiated sound, eqn. 21

$$\rho := 1.21 \cdot \frac{\text{kg}}{\text{m}^3} \quad W := 0.305 \cdot \text{m} \quad \Delta \delta_{\text{star}} := 0.278 \cdot \text{cm} \quad t_i := 0.2 \cdot \frac{\Delta x}{U_c} \quad r := 1 \cdot \text{m}$$

$$\text{pref} := 20 \cdot 10^{-6} \cdot \text{Pa}$$

$$\Phi_k := \frac{\rho^2 \cdot \Delta \delta_{\text{star}}^2 \cdot (2 \cdot \pi \cdot f_k)^4}{4 \cdot \pi^2 \cdot [1 + (2 \cdot \pi \cdot f_k \cdot t_i)^2]} \cdot \frac{1}{r^2} \cdot W \cdot |G_k|$$

$$\text{dB}_k := 10 \cdot \log \left(\frac{\Phi_k \cdot \text{Hz}}{\text{pref}^2} \right)$$



REFERENCES

Farabee, T. M., Casarella, M. J., and DeMetz, F. C., 1974, "Source Distribution of Turbulent Bursts During Natural Transition," David W. Taylor Naval Ship Research and Development Center Report SAD-89E-1942, August 1974.

Gedney, C. J., 1979, "Wall Pressure Fluctuations During Transition on a Flat Plate," Massachusetts Institute of Technology Report 84618-1.

Josserand, M. A. and Lauchle, G. C., 1986, "Wavevector-Frequency Spectrum of Transition Zone Wall Pressure Fluctuations," ARL Penn State Technical Report TR 86-008, December 1986.

Lauchle, G. C., 1980, 'On the radiated noise due to boundary-layer transition,' *J. Acous. Soc. of Amer.*, **67**, pp.158-168.

Shivitz, W. F., 1975, "An Experimental Investigation of Artificially Induced Transition to Turbulence on a Body of Revolution," M.S. Thesis, The Pennsylvania State University.

Spectrum⁽¹⁾ := f·sec

Spectrum⁽²⁾ := dB


Z:\ULTRANS QAF211.TXT

Spectrum

A.5 Noise Generated by Boundary Layer Transition on Symmetric Hydrofoils - Howe Formulation

Mathcad file: MSHTRANS99.MCD

BOUNDARY LAYER TRANSITION NOISE FROM A SYMMETRIC HYDROFOIL

[MSHTRANS99.MCD, Mathcad 2000 Professional]

This program is the implementation of a boundary layer transition noise model described in:

Howe, M. S., 1999, 'Noise Generated at Low Mach Numbers by Boundary Layer Transition on Symmetric Hydrofoils and Axisymmetric Headforms,' Applied Research Laboratory / Penn State University Technical Memorandum, 99-017, February 1999.

ASSUMPTIONS

- very low Mach number. 2D flow;
- symmetric, finite thickness plane (better termed a hydrofoil);
- hydrofoil chord is acoustically non-compact;
- hydrofoil span is much greater than the boundary layer thickness;
- hydrofoil thickness is acoustically compact, and that the leading edge is within the nearfield of the transition zone;
- zero angle of attack and boundary layer fluctuations on opposite sides of the foil are equal and independent so an estimate of one side can just be increased by 3 dB;
- the integration of the vorticity is restricted to the non-linear region of the boundary layer above the viscous sublayer, so bound vorticity on the hydrofoil is ignored; and
- high Reynolds number so the contribution of tangential shear stresses is ignored.

SPECIFY VALUES FOR FLOW AND GEOMETRY VARIABLES

ORIGIN = 1

Physical constants for water at 10°C

$$\rho = 1000 \cdot \frac{\text{kg}}{\text{m}^3} \quad \nu = 1.284 \cdot 10^{-6} \cdot \frac{\text{m}^2}{\text{sec}} \quad c = 1447 \cdot \frac{\text{m}}{\text{sec}} \quad \text{Pref} := 1 \cdot 10^{-6} \cdot \text{Pa}$$

Define hydrofoil parameters

$$\alpha = 0.0013 \quad \beta = 0.02 \quad h = 0.856 \cdot \text{m} \quad \zeta_{\text{trans}} = 1 \quad N_{\text{trans}} = 151$$

Define free-stream velocity, calculate Mach number and Reynolds number

$$U = 15 \cdot \frac{\text{m}}{\text{sec}} \quad \frac{U}{c} = 0.01 \quad \frac{U \cdot h}{\nu} = 1 \times 10^7$$

Define convection velocity using assumption stated on page 12 $U_c := 0.7 \cdot U$

Define frequency range

$$f_{\max} = 2000 \cdot \text{Hz} \quad KL = 200 \quad k := 1..KL \quad f_k := f_{\max} \cdot 10^{3 \left(\frac{k}{KL} - 1 \right)} \quad \omega_k := 2 \cdot \pi \cdot f_k$$

Specify frequency-dependent window length for integration

$$\zeta_{\max k} := 2 \cdot \left(\frac{U_c}{f_k \cdot h} \right)^{0.7} + \zeta_{\text{trans}} \quad N_{\text{window}} := 151$$

Generate hydrofoil profile up to transition point via conformal mapping (eqns. 2.11 and 2.12)

$$n := 1..N_{\text{trans}}$$

$$\zeta_{0n} := \zeta_{\text{trans}} \cdot \frac{n - 1}{N_{\text{trans}} - 1}$$

$$f_c(\zeta) := \frac{1}{\pi} \cdot \left(\zeta \cdot \sqrt{\zeta^2 - 1} - \ln \left(\zeta + \sqrt{\zeta^2 - 1} \right) \right) + \frac{i}{2}$$

$$z_{0n} := h \cdot \frac{f_c(\zeta_{0n}) + \alpha \cdot f_c \left(\frac{\zeta_{0n}}{\beta} \right)}{1 + \alpha} \quad x_{0n} := \text{Re}(z_{0n}) \quad y_{0n} := \text{Im}(z_{0n})$$

Calculate arc length up to transition point

$$n := 1 \dots (N_{\text{trans}} - 1)$$

$$dso_n := \sqrt{(x_{o_{n+1}} - x_{o_n})^2 + (y_{o_{n+1}} - y_{o_n})^2}$$

$$so := \sum_n dso_n$$

Calculate arc length for points beyond transition point (different ζ -range for each frequency)

$$n := 1 \dots N_{\text{window}}$$

$$\zeta_{n,k} := (\zeta_{\text{max}_k} - \zeta_{\text{trans}}) \cdot \frac{n - 1}{N_{\text{window}} - 1} + \zeta_{\text{trans}}$$

$$z_{n,k} := h \cdot \frac{fc(\zeta_{n,k}) + \alpha \cdot fc\left(\frac{\zeta_{n,k}}{\beta}\right)}{1 + \alpha} \quad x_{n,k} := \text{Re}(z_{n,k}) \quad y_{n,k} := \text{Im}(z_{n,k})$$

$$nn := 1 \dots (N_{\text{window}} - 1)$$

$$ds_{nn,k} := \sqrt{(x_{nn+1,k} - x_{nn,k})^2 + (y_{nn+1,k} - y_{nn,k})^2}$$

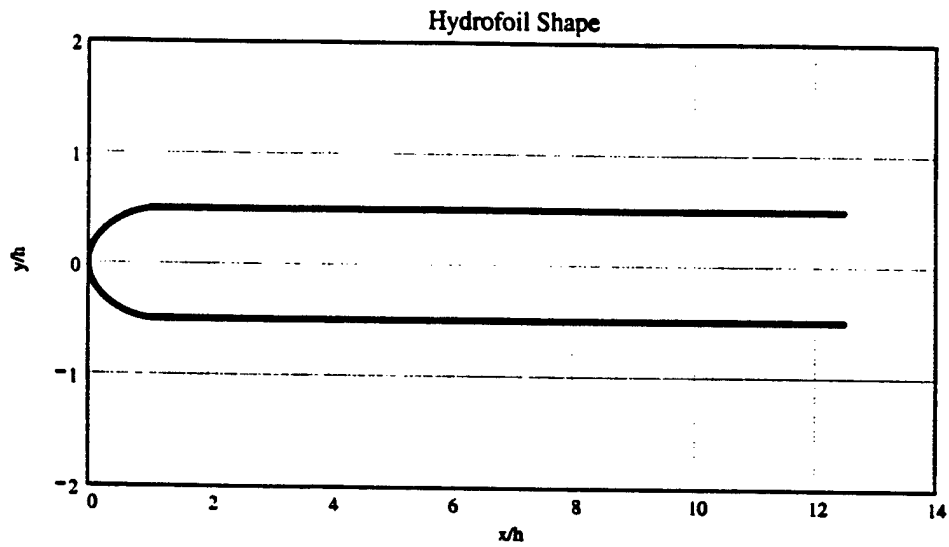
$$s_{1,k} := so$$

$$s_{nn+1,k} := so + \sum_{j=1}^{nn} ds_{j,k}$$

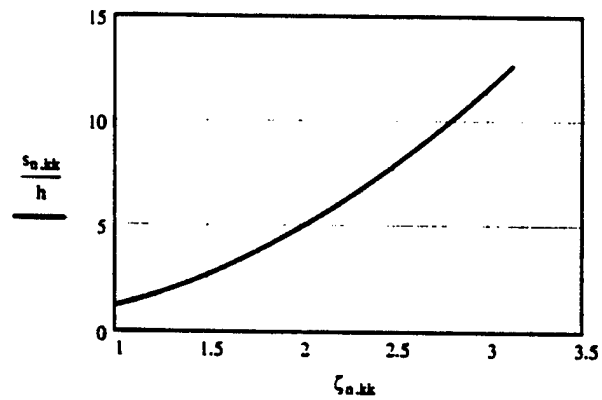
Plot profile up to transition point (red) and windowed integration range (blue)
for a specified frequency

$$kk := 50 \quad \frac{\omega_{kk} \cdot h}{Uc} = 5.761$$

$$n1 := 1 \dots N_{trans} \quad n2 := 1 \dots N_{window}$$



Note that arc length is not a linear function of ζ even beyond the transition point



SPECTRAL CALCULATIONS

Calculate transition zone intermittency function (eqns 3.14 and 3.15)

$$\Delta := 17 \cdot s_o \cdot \left(\frac{U \cdot s_o}{v} \right)^{-0.2} \quad c1 := 4.18 \quad \text{or} \quad \left[1 + 3.4 \left(\frac{s_{n,k} - s_o}{\Delta} \right)^2 \right]$$

$$\gamma_{n,k} := 1 - \exp \left[-c1 \cdot \left(\frac{s_{n,k} - s_o}{\Delta} \right)^2 \right]$$

Calculate boundary layer displacement thickness and friction velocity (eqn. 3.17 and page 14)

$$\delta_{star_{n,k}} := 0.046 \cdot h \cdot \left(\frac{s_{n,k}}{h} \right)^{0.8} \cdot \left(\frac{U \cdot h}{v} \right)^{-0.2}$$

$$v_{star} := 0.035 \cdot U$$

Calculate point pressure spectrum, based on Chase data (eqn. 3.16)

$$\alpha p := 0.12$$

$$\Phi_{pp_{n,k}} := (\rho \cdot v_{star}^2)^2 \cdot \frac{h}{U} \cdot \gamma_{n,k} \cdot \frac{\frac{\delta_{star_{n,k}}}{h} \cdot \left(\omega_k \cdot \frac{\delta_{star_{n,k}}}{U} \right)^2}{\left[\left(\omega_k \cdot \frac{\delta_{star_{n,k}}}{U} \right)^2 + \alpha p^2 \right]^{1.5}}$$

Calculate integrand of eqn. 3.19 $int_{n,k} := \sqrt{\Phi_{pp_{n,k}}} \left[1 + e^{-\left(\frac{\omega_k \cdot h}{Uc} \right)} \right] \cdot e^{i \cdot \frac{\omega_k}{Uc} \cdot s_{n,k}}$

$$nn := 1 \dots (N_{window} - 1)$$

$$d\zeta_{nn,k} := \zeta_{nn+1,k} - \zeta_{nn,k}$$

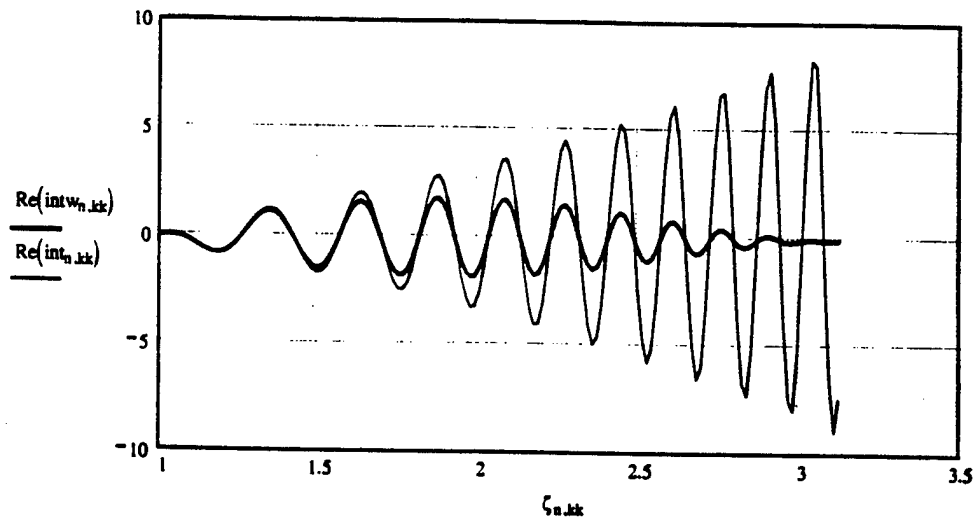
Apply window function

$$w_{n,k} := \cos \left(\frac{\pi}{2} \cdot \frac{\zeta_{n,k} - \zeta_{trans}}{\zeta_{max_k} - \zeta_{trans}} \right)^2$$

$$intw_{n,k} := w_{n,k} \cdot int_{n,k}$$

Plot the integrand for a specified frequency

$$kk := 50 \quad \frac{\omega_{kk} \cdot h}{U_c} = 5.761$$



Evaluate windowed integral using trapezoidal integration

$$nn := 1..(Nwindow - 1)$$

$$F_k := \sum_{nn} \frac{(intw_{nn+1,k} + intw_{nn,k})}{2} \cdot d\zeta_{nn,k}$$

Integral (magnitude squared) for low frequencies, eqn 3.20.

$$F2low_k := 0.146 \cdot \left(\frac{U \cdot h}{v} \right)^{-0.6} \cdot (\rho \cdot vstar^2)^2 \cdot \left(\frac{h}{U} \right) \cdot \left(\frac{1 + \alpha}{1 + \frac{\alpha}{\beta^2}} \right) \cdot \left(\frac{Uc}{U} \right)^2 \cdot \left(\frac{\omega_k \cdot h}{Uc} \right)^{-1.4}$$

Integral (magnitude squared) for high frequencies, eqn 3.21.

$$d\zeta_{dso_k} := \frac{\zeta_{2,k} - \zeta_{1,k}}{s_{2,k} - s_{1,k}}$$

$$F2high_k := c1 \cdot (\rho \cdot vstar^2)^2 \cdot \left(\frac{h}{U} \right) \cdot \left(\frac{h^2}{\Delta} \cdot d\zeta_{dso_k} \right)^2 \cdot \frac{U}{Uc} \cdot \left(\frac{\omega_k \cdot h}{Uc} \right)^{-5}$$

Sound radiation from eqn. 3.19

$$Mc := \frac{Uc}{c} \quad L := 10 \cdot h \quad r := 1 \cdot m \quad \psi := 90\text{-deg} \quad \theta := 90\text{-deg}$$

$$\Phi_k := \frac{0.35 \cdot Mc}{\pi^4} \cdot \left(\frac{h \cdot L}{r^2} \right) \cdot \left(\frac{1 + \frac{\alpha}{\beta^2}}{1 + \alpha} \right) \cdot \sin(\psi) \cdot \sin\left(\frac{\theta}{2}\right)^2 \cdot (|F_k|)^2$$

$$\Phi_{low_k} := \frac{0.35 \cdot Mc}{\pi^4} \cdot \left(\frac{h \cdot L}{r^2} \right) \cdot \left(\frac{1 + \frac{\alpha}{\beta^2}}{1 + \alpha} \right) \cdot \sin(\psi) \cdot \sin\left(\frac{\theta}{2}\right)^2 \cdot F2low_k$$

$$\Phi_{high_k} := \frac{0.35 \cdot Mc}{\pi^4} \cdot \left(\frac{h \cdot L}{r^2} \right) \cdot \left(\frac{1 + \frac{\alpha}{\beta^2}}{1 + \alpha} \right) \cdot \sin(\psi) \cdot \sin\left(\frac{\theta}{2}\right)^2 \cdot F2high_k$$

Calculate and plot dimensional spectrum

$$G_k := 10 \cdot \log \left[\frac{\Phi_k \cdot \text{Hz}}{(\text{Pref})^2} \right] + 11$$

The 11 dB accounts for conversion to $G(f)$, the one sided spectrum.

$$f_k := \frac{\omega_k}{2 \cdot \pi}$$

Calculate and plot Chase spectrum for TBL noise

$$\text{CT} := 0.0046 \quad c2 := \frac{1}{6} \quad b := 0.75 \quad \text{hbar} := 3$$

$$\delta := 8 \cdot \left[0.046 \cdot h \cdot \left[\frac{(s_0 + \Delta)}{h} \right]^{0.8} \cdot \left(\frac{U \cdot h}{v} \right)^{-0.2} \right]$$

$$\Phi_{\text{Chase}_k} := \left[\rho^2 \cdot v_{\text{star}}^3 \cdot \delta \cdot \left(\frac{h \cdot L}{r^2} \right) \right] \cdot \frac{\left[\text{CT} \cdot c2 \cdot b^2 \cdot \frac{(\omega_k \cdot \delta)^4}{c^4} \right]}{\left[\frac{(\omega_k \cdot \delta)}{(\text{hbar} \cdot v_{\text{star}})} \right]^2 \cdot \left(\frac{1}{b^2} \right)^{\frac{3}{2}}}$$

$$G_{\text{Chase}_k} := 10 \cdot \log \left[\frac{\Phi_{\text{Chase}_k} \cdot \text{Hz}}{(\text{Pref})^2} \right] + 11$$

Calculate combined spectrum for transition noise and TBL

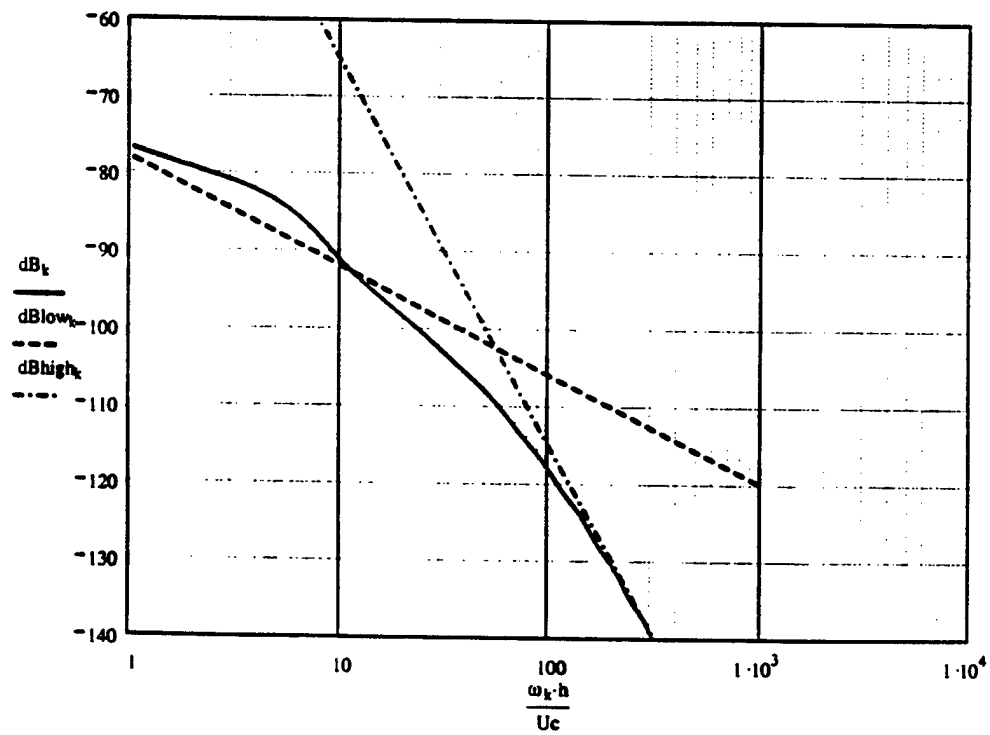
$$G_{\text{total}_k} := 10 \cdot \log \left[\frac{\left[(\Phi_k + \Phi_{\text{Chase}})_k \right] \cdot \text{Hz}}{(\text{Pref})^2} \right] + 11$$

Plot non-dimensional spectrum, compare to Fig. 2

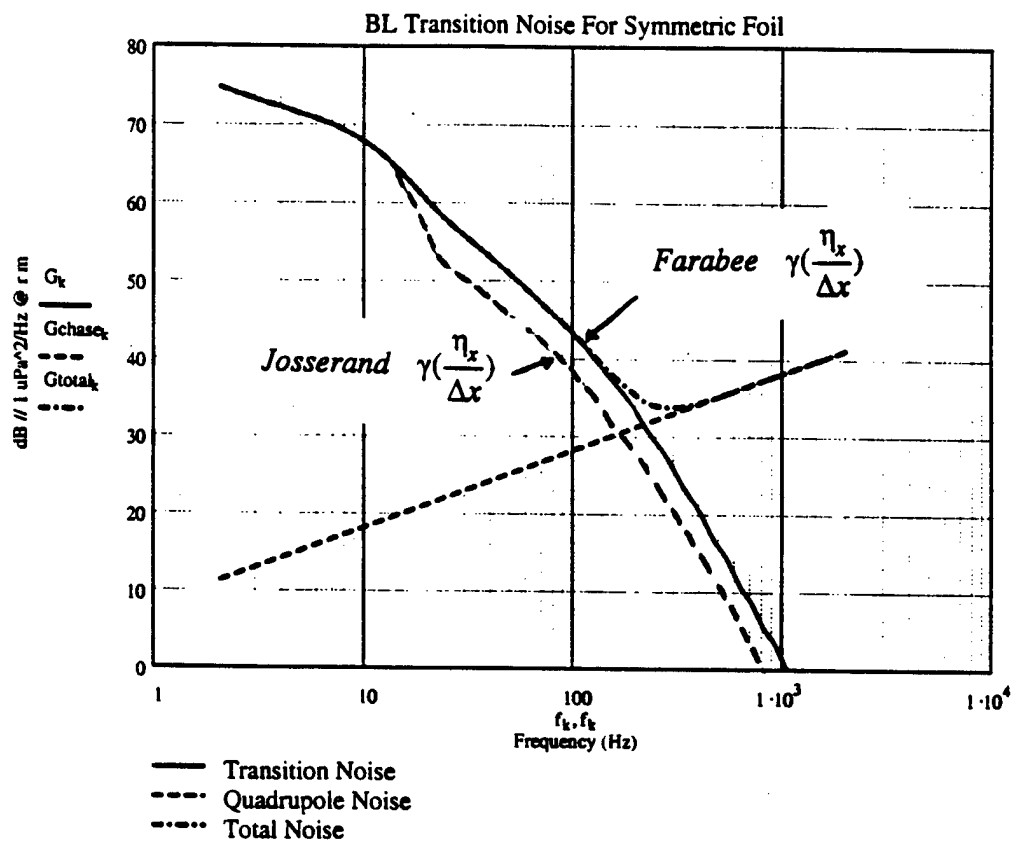
$$dB_k := 10 \cdot \log \left[\frac{U}{h} \cdot \frac{\Phi_k}{(\rho \cdot vstar^2)^2 \cdot \left(\frac{h \cdot L}{r^2} \right) \cdot Mc \cdot \sin(\psi) \cdot \sin\left(\frac{\theta}{2}\right)^2} \right]$$

$$dBlow_k := 10 \cdot \log \left[\frac{U}{h} \cdot \frac{\Phi low_k}{(\rho \cdot vstar^2)^2 \cdot \left(\frac{h \cdot L}{r^2} \right) \cdot Mc \cdot \sin(\psi) \cdot \sin\left(\frac{\theta}{2}\right)^2} \right]$$

$$dBhigh_k := 10 \cdot \log \left[\frac{U}{h} \cdot \frac{\Phi high_k}{(\rho \cdot vstar^2)^2 \cdot \left(\frac{h \cdot L}{r^2} \right) \cdot Mc \cdot \sin(\psi) \cdot \sin\left(\frac{\theta}{2}\right)^2} \right]$$



Farabee $\gamma\left(\frac{\eta_x}{\Delta x}\right)$



MODIFICATION HISTORY

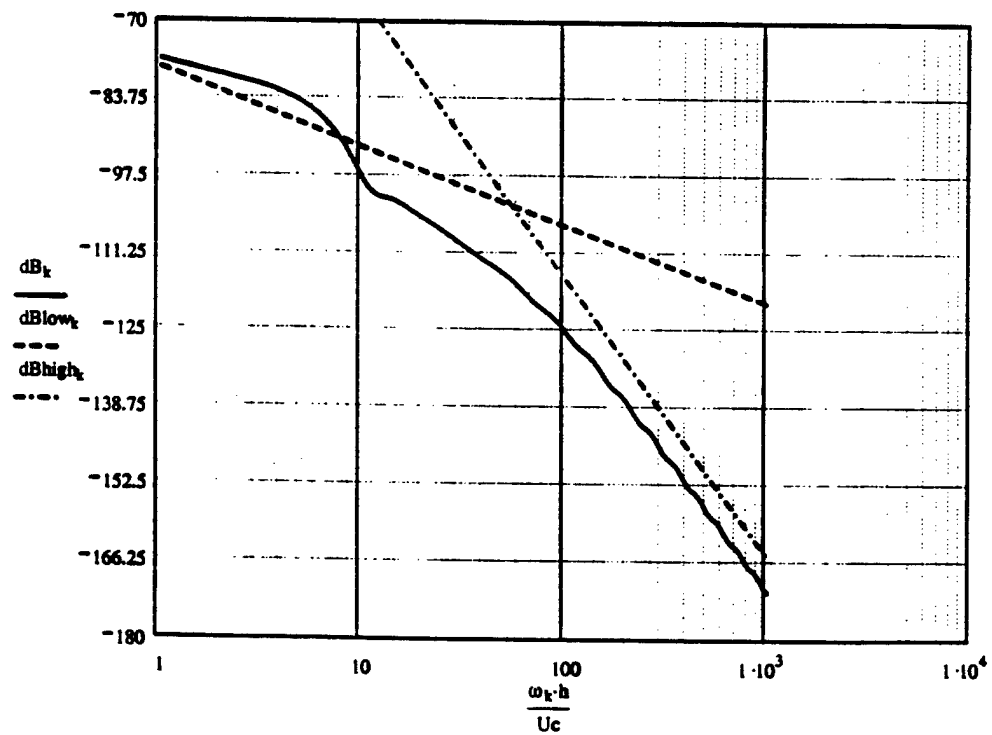
Original	2 June 2000	Full implementation
Mod 1	5 June 2000	Addition of windowing function for integration
Mod 2	6 June 2000	Addition of dimensional spectra and quadrupole spectra

Plot non-dimensional spectrum, compare to Fig. 2

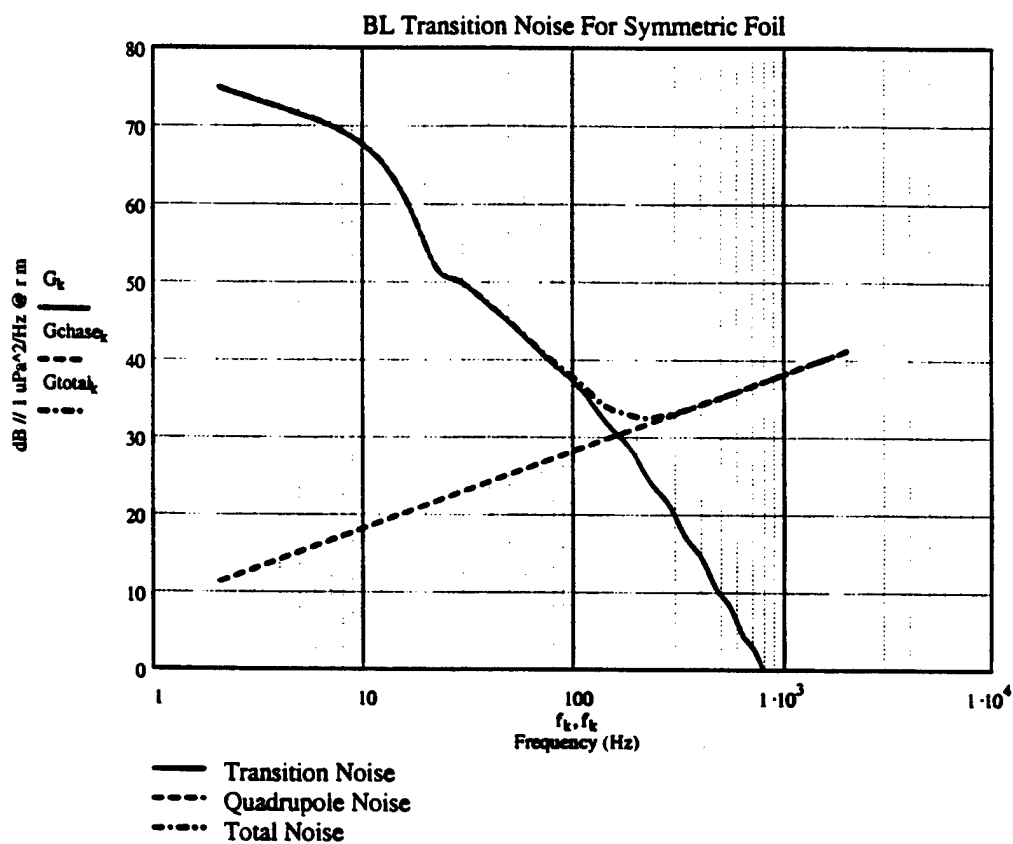
$$dB_k := 10 \cdot \log \left[\frac{U}{h} \cdot \frac{\Phi_k}{(\rho \cdot vstar^2)^2 \cdot \left(\frac{h \cdot L}{r^2} \right) \cdot Mc \cdot \sin(\psi) \cdot \sin\left(\frac{\theta}{2}\right)^2} \right]$$

$$dBlow_k := 10 \cdot \log \left[\frac{U}{h} \cdot \frac{\Phi_{low_k}}{(\rho \cdot vstar^2)^2 \cdot \left(\frac{h \cdot L}{r^2} \right) \cdot Mc \cdot \sin(\psi) \cdot \sin\left(\frac{\theta}{2}\right)^2} \right]$$

$$dBhigh_k := 10 \cdot \log \left[\frac{U}{h} \cdot \frac{\Phi_{high_k}}{(\rho \cdot vstar^2)^2 \cdot \left(\frac{h \cdot L}{r^2} \right) \cdot Mc \cdot \sin(\psi) \cdot \sin\left(\frac{\theta}{2}\right)^2} \right]$$



Josserand $\gamma\left(\frac{\eta_x}{\Delta x}\right)$



MODIFICATION HISTORY

Original	2 June 2000	Full implementation
Mod 1	5 June 2000	Addition of windowing function for integration
Mod 2	6 June 2000	Addition of dimensional spectra and quadrupole spectra and Josserand intermittency function

A.6 Calculation of Boundary Layer Descriptors - AIR

Mathcad file: TRANSITION AIR.MCD

TRANSITIONAL FLOW HYDRODYNAMIC DESCRIPTORS - AIR FLOW

[TRANSITION AIR.MCD, Mathcad 2000 Professional]

This worksheet is to be used to calculate the transition zone length, transition zone Reynolds numbers, convection velocity, and displacement thickness peak amplitude.

From Josserand, I am assuming a initial transition at a Reynolds number of 8×10^5 . The transition Reynolds number (where intermittancy is 50 percent) is equal to 1.5×10^6 . The Reynolds number at the end of the transition zone is an average 2.2×10^6 . These are based on experiments in air for zero pressure gradient flat plate flows.

$$U_o := \begin{pmatrix} 9 \\ 12 \\ 15 \\ 18 \\ 21 \\ 24 \\ 27 \end{pmatrix} \cdot \frac{\text{m}}{\text{sec}}$$

DEFINITIONS

$U_c := U_o \cdot 0.7$	Convection velocity ratio
$x := 0.90 \cdot \text{m}$	Measurement position
$\nu := 1.5 \cdot 10^{-5} \cdot \frac{\text{m}^2}{\text{sec}}$	Kinematic viscosity, air = $1.50 \times 10^{-5} \text{ m}^2/\text{sec}$ water = $1.14 \times 10^{-6} \text{ m}^2/\text{sec}$
$j := 0..6$	
$\text{Re}_{x_j} := U_o_j \cdot \frac{x}{\nu}$	Reynolds number based on measurement position for a flat plate
$\delta_{x\text{lam}_j} := 5.0 \cdot x \cdot (\text{Re}_{x_j})^{\frac{-1}{2}}$	Laminar 99% boundary layer thickness

$$\delta_{xturb_j} := 0.37 \cdot x \cdot (Re_{x_j})^{\frac{-1}{5}}$$

Turbulent boundary layer thickness

$$x_{0_j} := \frac{800000}{U_{0_j}} \cdot \nu$$

Effective leading edge point of transition zone

$$Re_{x_{0_j}} := U_{0_j} \cdot \frac{x_{0_j}}{\nu}$$

Transition LE Reynolds number (by definition)

$$\Delta x_j := \left(\frac{\nu}{U_{0_j}} \right) \cdot 60 \cdot (Re_{x_{0_j}})^{0.667}$$

Length of transition zone
Chen and Thyson use 60,
Josserand found 40

$$\delta_{starlam_j} := 1.743 \cdot \frac{x_{0_j}}{(Re_{x_{0_j}})^{0.5}}$$

Laminar displacement thickness at LE of transition zone

$$x_{t_j} := \frac{2200000}{U_{0_j}} \cdot \nu$$

Effective distance at beginning of fully turbulent region

$$\delta_{starturb_j} := 0.046 \cdot \frac{x_{t_j}}{(2200000)^{\frac{1}{5}}}$$

Displacement thickness at beginning of fully turbulent region

$$\Delta \delta_{star_j} := \delta_{starturb_j} - \delta_{starlam_j}$$

$\Delta \delta^*$ calculation

$$Re \delta_{starturb_j} := 0.018 \cdot (Re_{x_j})^{\frac{6}{7}}$$

CALCULATED TRANSITIONAL FLOW VARIABLES

$$\begin{array}{cccc}
 U_o = \begin{pmatrix} 9 \\ 12 \\ 15 \\ 18 \\ 21 \\ 24 \\ 27 \end{pmatrix} \frac{\text{m}}{\text{sec}} & U_c = \begin{pmatrix} 6.3 \\ 8.4 \\ 10.5 \\ 12.6 \\ 14.7 \\ 16.8 \\ 18.9 \end{pmatrix} \frac{\text{m}}{\text{sec}} & R_{ex} = \begin{pmatrix} 5.4 \times 10^5 \\ 7.2 \times 10^5 \\ 9 \times 10^5 \\ 1.08 \times 10^6 \\ 1.26 \times 10^6 \\ 1.44 \times 10^6 \\ 1.62 \times 10^6 \end{pmatrix} & \Delta x = \begin{pmatrix} 86.569 \\ 64.927 \\ 51.941 \\ 43.284 \\ 37.101 \\ 32.463 \\ 28.856 \end{pmatrix} \text{cm} \\
 \\
 \delta_{xlam} = \begin{pmatrix} 0.612 \\ 0.53 \\ 0.474 \\ 0.433 \\ 0.401 \\ 0.375 \\ 0.354 \end{pmatrix} \text{cm} & \delta_{xturb} = \begin{pmatrix} 2.377 \\ 2.244 \\ 2.146 \\ 2.069 \\ 2.006 \\ 1.953 \\ 1.908 \end{pmatrix} \text{cm} & \delta_{starturb} = \begin{pmatrix} 0.909 \\ 0.682 \\ 0.545 \\ 0.454 \\ 0.39 \\ 0.341 \\ 0.303 \end{pmatrix} \text{cm} & \delta_{starlam} = \begin{pmatrix} 0.26 \\ 0.195 \\ 0.156 \\ 0.13 \\ 0.111 \\ 0.097 \\ 0.087 \end{pmatrix} \text{cm} \\
 \\
 x_o = \begin{pmatrix} 133.333 \\ 100 \\ 80 \\ 66.667 \\ 57.143 \\ 50 \\ 44.444 \end{pmatrix} \text{cm} & Re\delta_{starturb} = \begin{pmatrix} 1.475 \times 10^3 \\ 1.887 \times 10^3 \\ 2.285 \times 10^3 \\ 2.672 \times 10^3 \\ 3.049 \times 10^3 \\ 3.419 \times 10^3 \\ 3.782 \times 10^3 \end{pmatrix} & \Delta\delta_{star} = \begin{pmatrix} 0.649 \\ 0.487 \\ 0.389 \\ 0.325 \\ 0.278 \\ 0.243 \\ 0.216 \end{pmatrix} \text{cm} \\
 \\
 x_t - x_o = \begin{pmatrix} 233.333 \\ 175 \\ 140 \\ 116.667 \\ 100 \\ 87.5 \\ 77.778 \end{pmatrix} \text{cm} & \Delta x = \begin{pmatrix} 86.569 \\ 64.927 \\ 51.941 \\ 43.284 \\ 37.101 \\ 32.463 \\ 28.856 \end{pmatrix} \text{cm}
 \end{array}$$

Non-dimensional boundary layer axial velocity calculation for a laminar boundary layer.

$$\text{unondim} := \begin{pmatrix} 0.0 \\ 0.1 \\ 0.2 \\ 0.3 \\ 0.4 \\ 0.5 \\ 0.6 \\ 0.7 \\ 0.8 \\ 0.9 \\ 0.95 \\ 0.9999 \end{pmatrix} \quad \eta := \begin{pmatrix} 0.0 \\ 0.21 \\ 0.42 \\ 0.64 \\ 0.86 \\ 1.10 \\ 1.33 \\ 1.61 \\ 1.94 \\ 2.4 \\ 2.79 \\ 6.0 \end{pmatrix}$$

$h := 0..11 \quad j := 4$

$$z_h := \eta_h \cdot \left(2 \cdot \nu \cdot \frac{x}{U_{0j}} \right)^{\frac{1}{2}}$$

For $U_{0j} = 21 \text{ msec}^{-1}$

$$\text{unondim} = \begin{pmatrix} 0 \\ 0.1 \\ 0.2 \\ 0.3 \\ 0.4 \\ 0.5 \\ 0.6 \\ 0.7 \\ 0.8 \\ 0.9 \\ 0.95 \\ 1 \end{pmatrix} \quad z = \begin{pmatrix} 0 \\ 0.024 \\ 4.762 \\ 0.073 \\ 0.098 \\ 0.125 \\ 0.151 \\ 0.183 \\ 0.22 \\ 0.272 \\ 0.316 \\ 0.68 \end{pmatrix} \text{ cm}$$

A.7 Calculation of Boundary Layer Descriptors - WATER

Mathcad file: TRANSITION WATER.MCD

$$\delta_{xturb_j} := 0.37 \cdot x \cdot (Re_{x_j})^{\frac{-1}{5}}$$

Turbulent boundary layer thickness

$$x_{0_j} := \frac{800000}{U_{0_j}} \cdot \nu$$

Effective leading edge point of transition zone

$$Re_{x_{0_j}} := U_{0_j} \cdot \frac{x_{0_j}}{\nu}$$

Transition LE Reynolds number (by definition)

$$\Delta x_j := \left(\frac{\nu}{U_{0_j}} \right) \cdot 60 \cdot (Re_{x_{0_j}})^{0.667}$$

Length of transition zone
Chen and Thyson use 60,
Josserand found 40

$$\delta_{starlam_j} := 1.743 \cdot \frac{x_{0_j}}{(Re_{x_{0_j}})^{0.5}}$$

Laminar displacement thickness at LE of transition zone

$$x_{t_j} := \frac{2200000}{U_{0_j}} \cdot \nu$$

Effective distance at beginning of fully turbulent region

$$\delta_{starturb_j} := 0.046 \cdot \frac{x_{t_j}}{(2200000)^{\frac{1}{5}}}$$

Displacement thickness at beginning of fully turbulent region

$$\Delta \delta_{star_j} := \delta_{starturb_j} - \delta_{starlam_j}$$

$\Delta \delta^*$ calculation

$$Re_{\delta_{starturb_j}} := 0.018 \cdot (Re_{x_j})^{\frac{6}{7}}$$

Non-dimensional boundary layer axial velocity calculation for a laminar boundary layer.

$$\text{unondim} := \begin{pmatrix} 0.0 \\ 0.1 \\ 0.2 \\ 0.3 \\ 0.4 \\ 0.5 \\ 0.6 \\ 0.7 \\ 0.8 \\ 0.9 \\ 0.95 \\ 0.9999 \end{pmatrix} \quad \eta := \begin{pmatrix} 0.0 \\ 0.21 \\ 0.42 \\ 0.64 \\ 0.86 \\ 1.10 \\ 1.33 \\ 1.61 \\ 1.94 \\ 2.4 \\ 2.79 \\ 6.0 \end{pmatrix}$$

$h := 0..11 \quad j := 4$

$$z_h := \eta_h \left(2 \cdot \nu \cdot \frac{x}{U_{0j}} \right)^{\frac{1}{2}}$$

For $U_{0j} = 15 \text{ msec}^{-1}$

$$\text{unondim} = \begin{pmatrix} 0 \\ 0.1 \\ 0.2 \\ 0.3 \\ 0.4 \\ 0.5 \\ 0.6 \\ 0.7 \\ 0.8 \\ 0.9 \\ 0.95 \\ 1 \end{pmatrix} \quad z = \begin{pmatrix} 0 \\ 7.767 \times 10^{-3} \\ 1.553 \\ 0.024 \\ 0.032 \\ 0.041 \\ 0.049 \\ 0.06 \\ 0.072 \\ 0.089 \\ 0.103 \\ 0.222 \end{pmatrix} \text{ cm}$$

A.8 Calculation of Nozzle Contour

Mathcad file: NOZZLE CONTOUR.MCD

QAF NOZZLE CONTOUR DESIGN

[NOZZLE CONTOUR.MCD, Mathcad 2000 Professional]

Program to plot shape of a nozzle contour. It uses a seventh order polynomial. The coefficients were found using a Mathematica program by setting the following boundary conditions:

- the inlet and outlet dimensions were set at semi-diameter dimensions of Inlet= 29 inches and outlet=6 and 3 inches depending on side
- the first and second derivatives at $x=0$ and L were set to zero
- the first derivative at $x=L/2$ was set to -1.0
- the coefficient for x^3 was set to zero in order to get a determinate set of equations
- L was chosen to be inlet diameter times 0.80

Coefficients for top and bottom
nozzle contour

$$at := -0.000969861$$

$$bt := 0.00476745$$

$$ct := 0.0166601$$

$$dt := -0.089322$$

$$et := 0.000$$

$$ft := 0.000$$

$$gt := 0.000$$

$$ht := 2.41667$$

Coefficients for sides of
nozzle contour

$$as := 0.00135161$$

$$bs := -0.0214136$$

$$cs := 0.113844$$

$$ds := -0.206753$$

$$es := 0.000$$

$$fs := 0.000$$

$$gs := 0.000$$

$$hs := 2.41667$$

$$y_{top}(x) := at \cdot x^7 + bt \cdot x^6 + ct \cdot x^5 + dt \cdot x^4 + et \cdot x^3 + ft \cdot x^2 + gt \cdot x + ht$$

$$y_{side}(x) := as \cdot x^7 + bs \cdot x^6 + cs \cdot x^5 + ds \cdot x^4 + es \cdot x^3 + fs \cdot x^2 + gs \cdot x + hs$$

dimensions are in feet

$$L = 3.867 \text{ ft}$$

$$m := 0..186$$

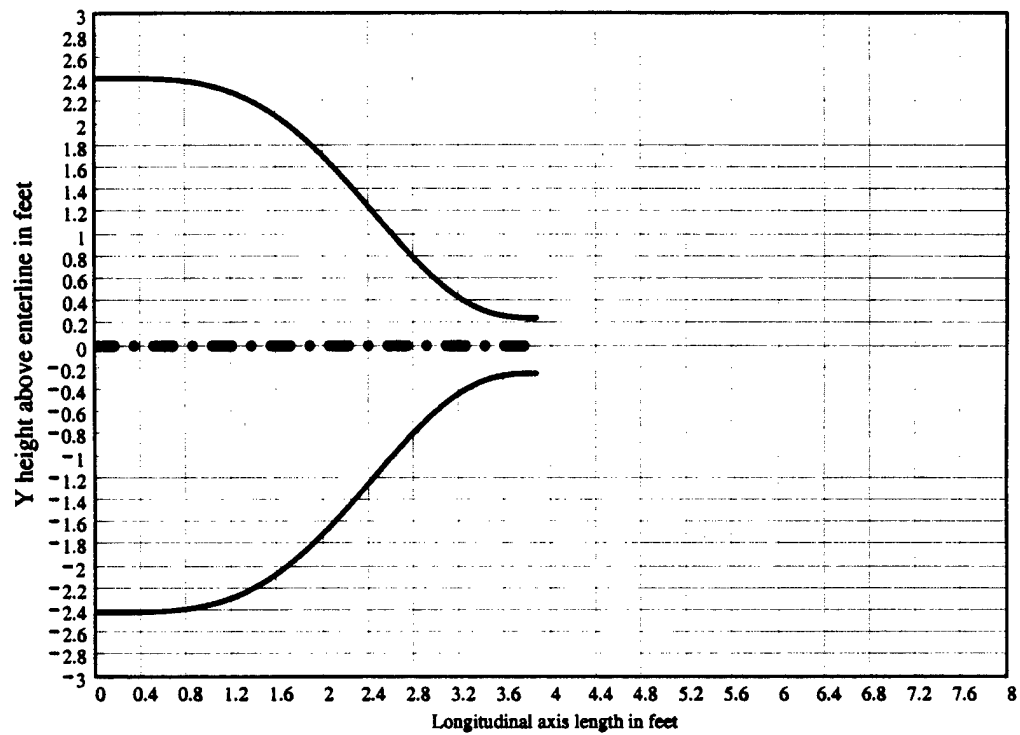
$$dist_m := m \cdot 0.0208333$$

$$ycl_m := 0.00 \cdot dist_m$$

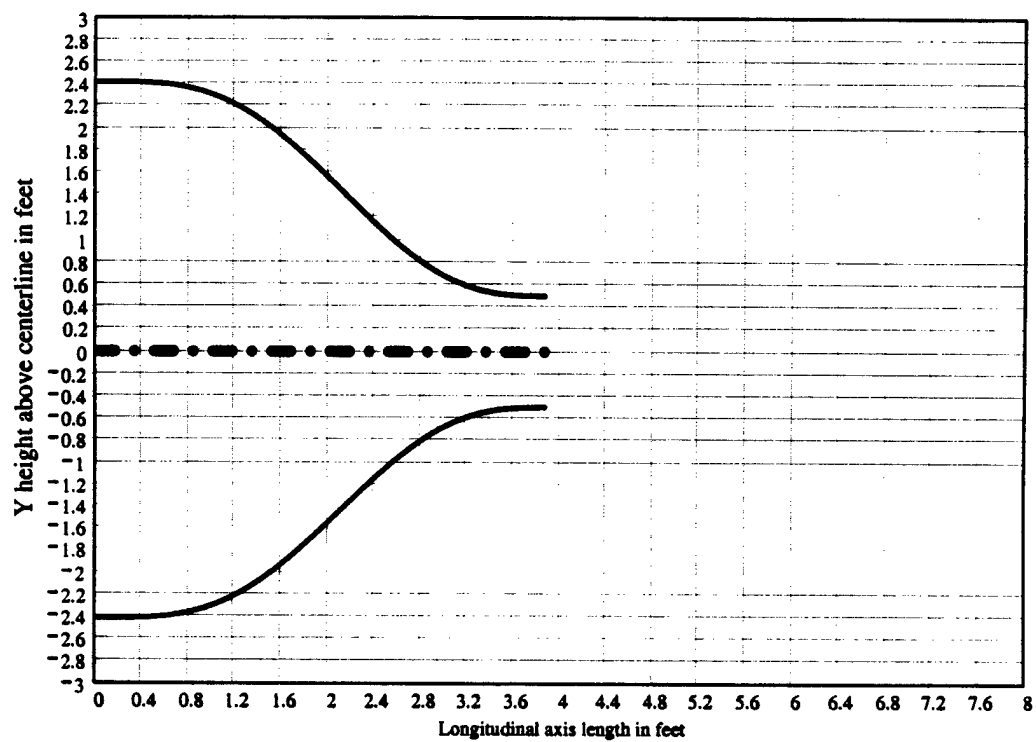
$$yt_m := y_{top}(dist_m)$$

$$ys_m := y_{side}(dist_m)$$

Contour for top and bottom walls of nozzle



Contour for side walls of nozzle



m := 0..33

Longitudinal axis
point in feet from
LE of Nozzle (X)

Distance from Nozzle
centerline in feet for
top and bottom

Distance from Nozzle
centerline in feet for
both sides

dist_m =

0
0.0208
0.0417
0.0625
0.0833
0.1042
0.125
0.1458
0.1667
0.1875
0.2083
0.2292
0.25
0.2708
0.2917
0.3125
0.3333
0.3542
0.375
0.3958
0.4167
0.4375
0.4583
0.4792
0.5
0.5208
0.5417
0.5625
0.5833
0.6042
0.625
0.6458
0.6667
0.6875

yt_m =

2.4167
2.4167
2.4167
2.4167
2.4167
2.4167
2.4166
2.4166
2.4166
2.4166
2.4165
2.4164
2.4163
2.4162
2.4161
2.4159
2.4156
2.4154
2.415
2.4147
2.4142
2.4137
2.4131
2.4124
2.4117
2.4108
2.4099
2.4088
2.4076
2.4063
2.4049
2.4033
2.4016
2.3997

ys_m =

2.4167
2.4167
2.4167
2.4167
2.4167
2.4166
2.4166
2.4166
2.4165
2.4164
2.4163
2.4162
2.416
2.4157
2.4154
2.415
2.4146
2.414
2.4134
2.4126
2.4118
2.4108
2.4097
2.4084
2.407
2.4054
2.4037
2.4017
2.3996
2.3973
2.3948
2.392
2.389
2.3858

Example of
coordinates
passed to CAD
system for
manufacture.

A.9 Calculation of Measurement Errors from a Two Microphone Intensity Probe

Mathcad file: INTEN_ERROR.MCD

MEASUREMENT ERRORS FROM A TWO MICROPHONE INTENSITY PROBE

[INTEN_ERROR.MCD, Mathcad 2000 Professional]

This workspace is for calculation of measurement errors which are associated with two microphone P-P intensity probes.

$$\begin{aligned} Co &:= 343 \cdot \frac{\text{m}}{\text{sec}} && \text{Speed of sound, m/sec} \\ f &:= 5000 \cdot \text{Hz} && \text{Acoustic frequency, Hz} \\ k &:= 2 \cdot \pi \cdot \frac{f}{Co} && \text{Acoustic wavenumber, 1/m} \\ s &:= .0254 \cdot \text{m} && \text{Microphone separation distance, m} \end{aligned}$$

Finite difference approximation error. This is a high frequency limit.

$$FDAE := 10.0 \cdot \log \left(\frac{\sin(k \cdot s)}{k \cdot s} \right) \qquad FDAE = -5.047 \quad \text{dB}$$

To stay within a 1 dB error limit, the upper frequency is:

$$2470 \text{ Hz}$$

An alternative upper threshold is given by the -3 dB point:

$$Fu := 1.9 \cdot \frac{Co}{2 \cdot \pi \cdot s} \qquad Fu = 4083.515 \text{ sec}^{-1} \quad \text{Hz}$$

A low frequency threshold can be developed for a source such as the TBL which has a correlation length associated with it. In Lauchle's INCE paper, he provides an equation:

$$\begin{aligned} &\text{for flow velocity,} && u := 21 \quad \text{m/sec} \\ Fl &:= \left(\frac{11}{8} \right) \cdot 0.7 \cdot \frac{u}{s} && Fl = 795.768 \text{ m}^{-1} \text{ Hz} \end{aligned}$$

Thumbrule for maximum inaccuracy of +/- 1.0 dB is
 $0.15 < k_s < 1.16$.

$$f_1 := 0.15 \cdot \frac{C_0}{2 \cdot \pi \cdot s} \quad f_1 = 322.383 \text{ msec}^{-1}$$

$$f_2 := 1.16 \cdot \frac{C_0}{2 \cdot \pi \cdot s} \quad f_2 = 2493.093 \text{ msec}^{-1}$$

Bias errors for different source fields, Fahy, 102-105

$$i := 0..1250 \quad \text{freq}_i := 4 \cdot i \cdot \text{Hz}$$

Point Monopole field

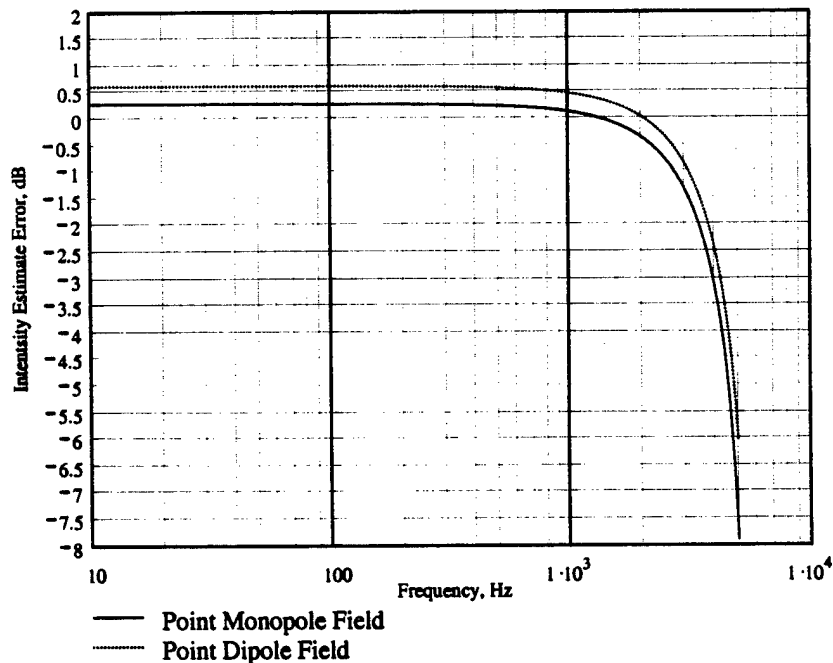
$$r := 5 \cdot \text{cm} \quad h := 1.27 \cdot \text{cm}$$

$$eIM_i := \frac{-2}{3} \cdot \left(2 \cdot \pi \cdot \frac{\text{freq}_i}{C_0} \cdot h \right)^2 + \left(\frac{h}{r} \right)^2$$

$$EIM_i := 10 \cdot \log(1 + eIM_i)$$

Point dipole field intensity bias error

$$eID_i := \frac{-2}{3} \cdot \left(2 \cdot \pi \cdot \frac{\text{freq}_i}{C_0} \cdot h \right)^2 + \left(\frac{h}{r} \right)^2 \cdot \frac{7}{3} \quad EID_i := 10 \cdot \log(1 + eID_i)$$



APPENDIX B

QUIET AIRFLOW FACILITY DEVELOPMENT

This appendix provides some historical perspective of development efforts for the Quiet Airflow Facility. The facility has progressed through many stages during the several years covered by this investigation. All of the efforts have been focused on reducing the background noise levels. Section 5.1 describes the current facility while this appendix describes interim configurations and data acquisition tools.

This facility is basically a quieted air source connected to a flow management nozzle. The original, symmetric nozzle was fitted with an internal contoured ramp to create a semi-circular orifice rather than the circular one that previously existed. This nozzle formed an open jet with an opening axis perpendicular to a planar baffle. A plate mounted in the semi-circular orifice formed a wall jet over the test plate. This configuration is shown in Figure B.1.

B.1 Power Source Improvements

The Buffalo Forge centrifugal blower was originally powered by a 20 HP AC motor driven by a Borg-Warner inverter. This has been replaced by an ABB inverter. This was necessary because of the lack of spare parts for the Borg-Warner system. This old inverter had been used as long as possible because it produced a "sloppy" excitation that was a much smoother sinusoid than the modern, six-step, digitally generated

sinusoidal excitation. This tended to provide a less tonal rich background noise level than the more modern inverters. A series of measurements were made to characterize the impact of this change. One example of the reduction in the tonal levels due to replacement of the Borg-Warner inverter with the ABB inverter is shown in Figure B.2. In some cases, the levels decreased by 30 dB in the frequency range of interest.

B.2 Blower Noise Improvements

The initial blower isolation box did not have a muffler on the inlet. A sheet metal transition section was added from the plenum box intake hole to the blower suction port. A rubber bellows attaches the blower discharge to the attenuation plenum. A Conic-Flow Silencer muffler has been attached to the inlet to the blower. A throttle can be mounted on the muffler intake to provide the coarse adjustment of the suction strength. It is not known if the presence of the branches off the inlet tube between the muffler and the blower intake causes any three dimensional distortions to be ingested into the blower. (These branches are for the suction manifold which has been used in previous tests.) However, some of the low frequency rumble may be attributable to this but the turning at the elbows and probable separated flow is likely a more important source of noise. The air is discharged from the source plenum vertically through a 40 cm diameter flexible vinyl hose and turned with a damped sheet-metal elbow into another piece of flexible hose for entry in the flow management section and nozzle of the wall jet facility. This still didn't prove to be enough quieting, so an additional plenum was added before the flow management section in the final configuration.

B.3 Noise Reduction at the Test Plate

The entire flow management assembly was mounted on pneumatic tires for vibration isolation and ease of movement into and out of the chamber wall opening. In the final configuration, the wheels were not used because the facility did not have to be moved when located on the floor of the anechoic chamber. However, some rubber isolation material is used between the floor and the flow management assembly.

The original configuration for the test plate called for a false bottom to be installed in the existing nozzle so that the discharge orifice could be changed from circular to semi-circular. The plate was to be mounted such that it extended the false wall. This is shown in Figure B.3.

In order to provide for realistic boundary layer growth over the flat plate, as well as to prevent the formation of a free shear layer at the outer edges of the jet orifice, an acoustically transparent, but flow impermeable semi-circular mylar tube was placed over the test plate (Figure B.4). This was engineered by Walter A. Kargus (1997). It is attached to aluminum semi-circular supports at each end and is lightly restrained by a few thin diameter wire hoops in between. During early testing of the acoustically transparent tunnel, it collapsed due to its lack of inherent structural rigidity when subjected to the low pressure region created from the flow. In an attempt to prevent this, cheese-cloth was added across the tunnel termination as a resistance to create a positive gage pressure within the tunnel. This was aerodynamically effective but noisy. A wind sock-like termination was created next, and was found to be much quieter and tended to move exit sources of noise farther away from the sources of interest on the test plate.

The sidewall contamination is reduced by incorporation of suction along the test plate following Motohashi and Blackwelder (1983). A narrow (6 mm) slot along the side of the test plate provides a gap in which some of the over-pressurized air within the mylar tube is allowed to discharge to eliminate secondary flows at the plate-tube junction. Therefore, a much greater percentage of the flow over the test plate remains laminar before wall contamination extends to the center of the plate.

Care was taken to make all corners within the settling chamber and nozzle as smooth as possible to help maintain laminar irrotational flow. Initial measurements indicated that a maximum velocity of 31.7 m/sec at the exit could be achieved. By surveying over the plate with a capillary total head tube on a stethoscope (Figure 5.14), the bursting typical of transition was found to occur about half way down the plate which indicated the beginning of natural transition. Subsequent measurements with a tuft wand indicated that small corner vortices were being created inside the nozzle at the junction of the nozzle wall and the flat bottom. To eliminate this, the test plates were redesigned to include an extension of the plate 15 cm into the nozzle. The entire plate was raised about 2.5 cm from its previous position to create a 1.2 cm high by 30.5 cm wide duct below the plate through which wall flow (including the vortices) could be removed via a suction manifold. Suction for flow management on the test plate was provided by the blower intaking air from a 10 cm hose attached to the duct between the muffler and the rubber isolation hose into the blower. The manifold was developed to provide a more even suction distribution. This is shown in Figure B.4. The manifold itself is shown in Figure B.5. The end plate is removed in one of the photographs to show the rod mechanism for

opening and closing the orifices with wooden cones.

When designing the extension of the test plate into the nozzle care was taken to avoid leading edge separation and premature transition by incorporating a 4:1 elliptical leading edge (as suggested by Gad-el-Hak et al., 1981) and the windsock resistance at the end of the plate. This assured that the stagnation line near the leading edge was on the upper, working surface.

Provision was made for either mechanical or wind puff turbulent structure trips to be attached below the test plate and reside in the laminar region.

Despite all of this effort, it was determined that this configuration did not meet the low background noise levels required to make transition zone noise measurements.

Figure B.6 shows a sound pressure level measurement made above a natural transition zone with a flow velocity of 11.8 m/s. An early version of GLPROG81 was used to calculate predicted levels for transition noise. This required the rather unlikely values of normalized rise time to be between 0.05 and 0.15 in order to match the measurement. Given the shape of the spectrum, it is likely that other contaminating noise sources were measured. Figure B.7 provides the prediction for the same flow conditions using the latest version of GLPROG81.

B.4 Relocation of Test Section and New Nozzle Design

After the success of Brungart (1997) operating with the flow management section and square nozzle located in the anechoic chamber (Figure B.8), it was decided to keep this configuration intact and add an additional plenum. The intention was to further

reduce the low frequency background noise.

However, the 46 cm x 46 cm outlet nozzle needed to be replaced with one that provided a 15.2 cm x 30.5 cm outlet. The design of this nozzle is described in section 5.1.3.

B.5 Diffuser Design

A new diffuser needed to be designed since the Brungart configuration did not utilize one. The intent was to slow the flow and move any possible trailing edge noise sources as far as possible from the test section measurements.

Kline (1959) and Kline, et al. (1959) were used to design the diffuser. The Mathcad file for calculating and specifying the nozzle contours is provided in section A.6. In the design of a straight walled diffuser, one needs to be aware of the potential for a stalled flow to develop in the diffuser. Kline (1959) provided a criterion for determining if stall might exist. This is shown in Figure B.9 as the line on the plot. The diffuser went through several design iterations which are listed in Figure B.9. The open circles refer to the design condition for the side walls and the dark circles refer to the top and bottom walls. A natural diffusion angle, θ , of 7 degrees was designed first; however, a steady stall condition resulted. The diffuser length was decreased by 30% but the stall was still present. The diffuser was then reconstructed with a 4.5 degree diffuser angle. Transitory stall was seen depending on the measurement openings in the test section. When the Soundcoat ® foam was installed, this reduced the effective angle to 3.5 degrees. Transitory stall still occurs at times but it is a very weak circulation. Barlow et al. (1999)

recommend an area ratio of the outlet to the inlet of 5 or 6:1 to avoid separations. This diffuser has an area ratio of 7.3 which may be why it is just on the edge for this transitory flow. However, the desire was to keep any potential trailing edge noise sources as far from the test section as possible.

The possible consequences of a design point being near the stall criterion line are shown in Figure B.10. The steady flow condition should have a uniform flow diffusing following the open area ratio determined by the actual geometry of the diffuser. The transitory stall condition may occur due to any fluctuating disturbance. This is the case when one of the measurement slots in the test section is opened. The steady stall condition effectively reduces the flow area of the diffuser resulting in higher discharge velocities (and more noise). However, the addition of a resistance to the end of the diffuser (in the form of four 1.2 cm thick furnace filters) results in a sufficient pressure rise that eliminates the possibility of this stall under the run conditions for measurements made in this investigation.

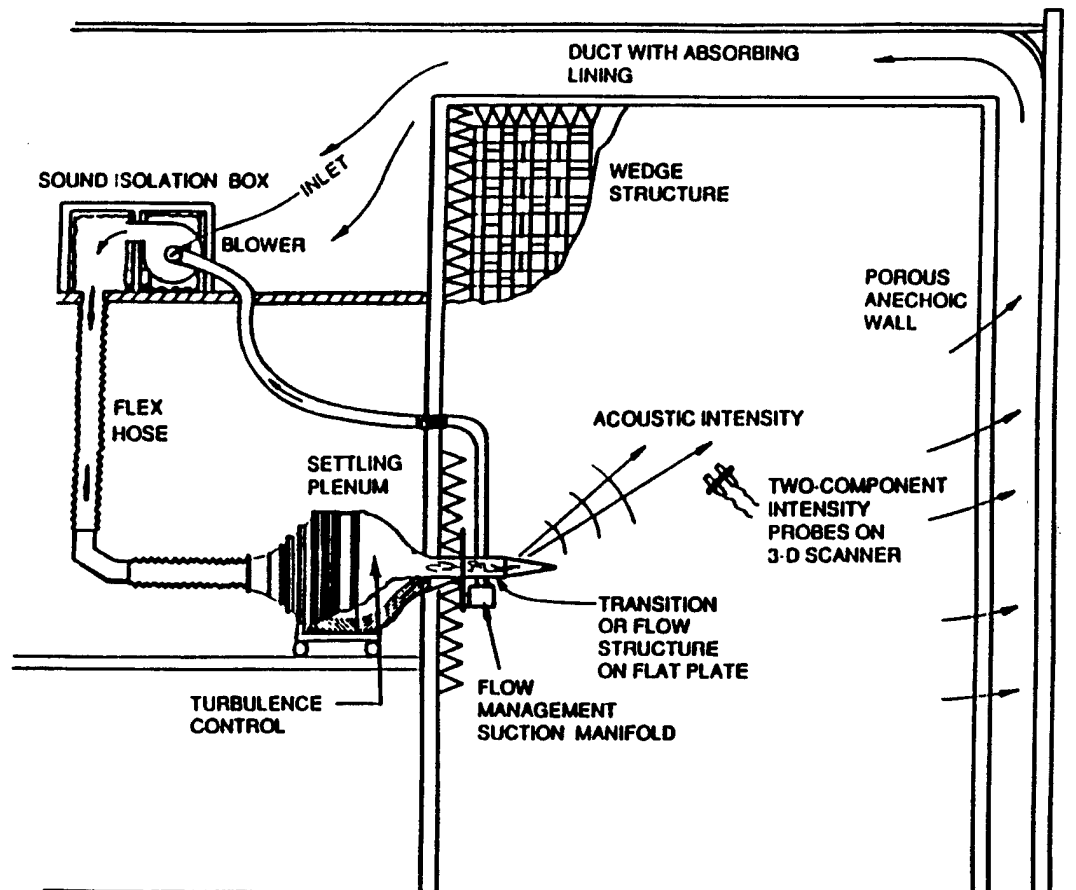


Figure B.1 Original orientation of Quiet Airflow Facility to the flow-through anechoic chamber.

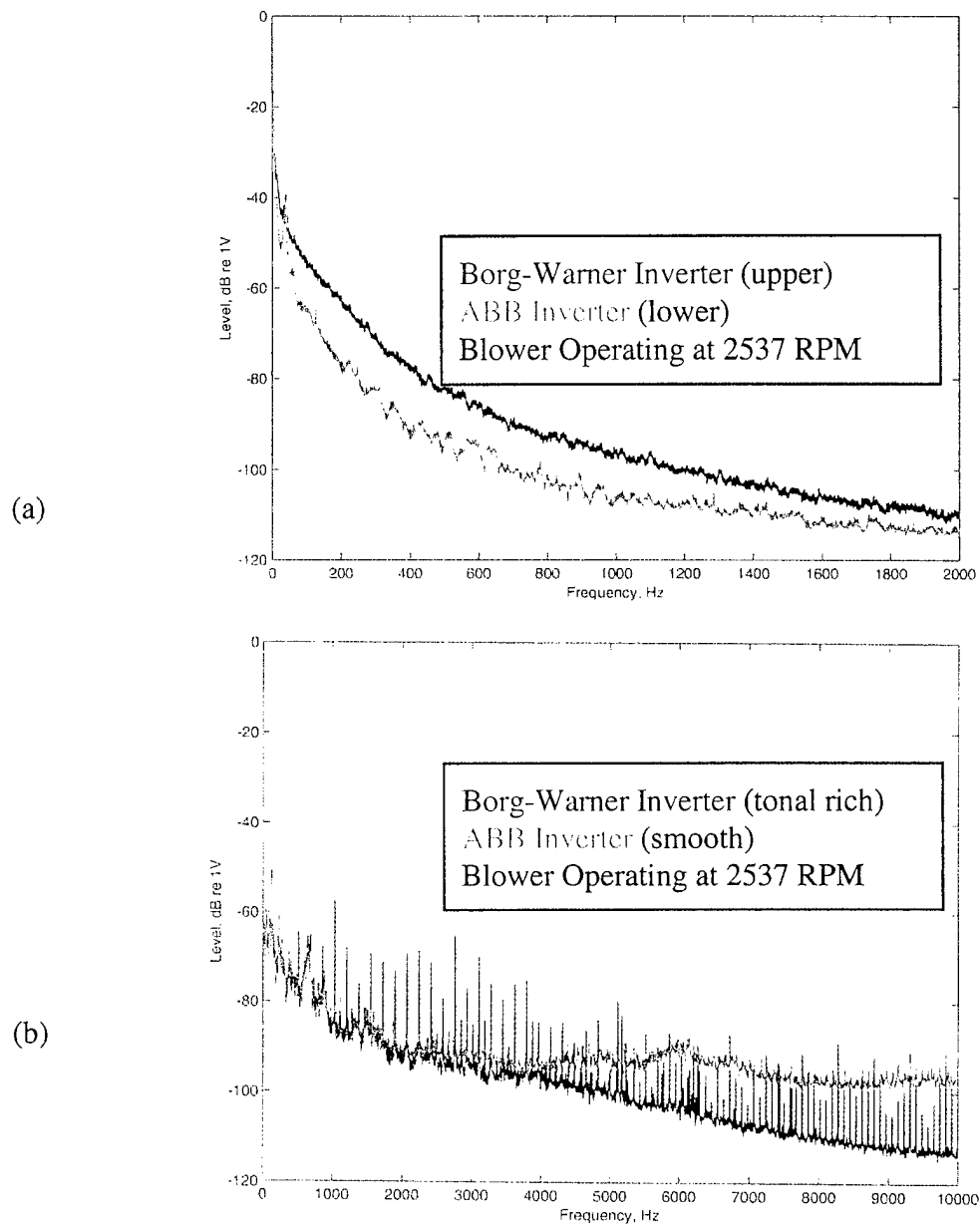


Figure B.2 Comparison of narrowband signature of Borg-Warner inverter and replacement ABB inverter for (a) upstream plenum and (b) airborne noise in control room.

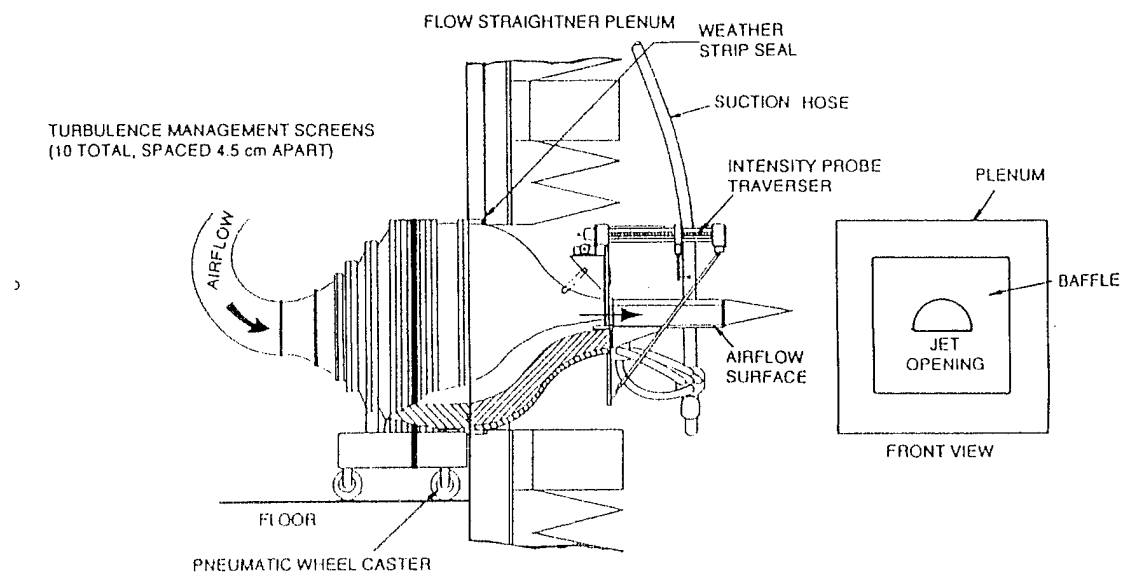


Figure B.3 Original semi-circular wall jet over flat plate configuration.

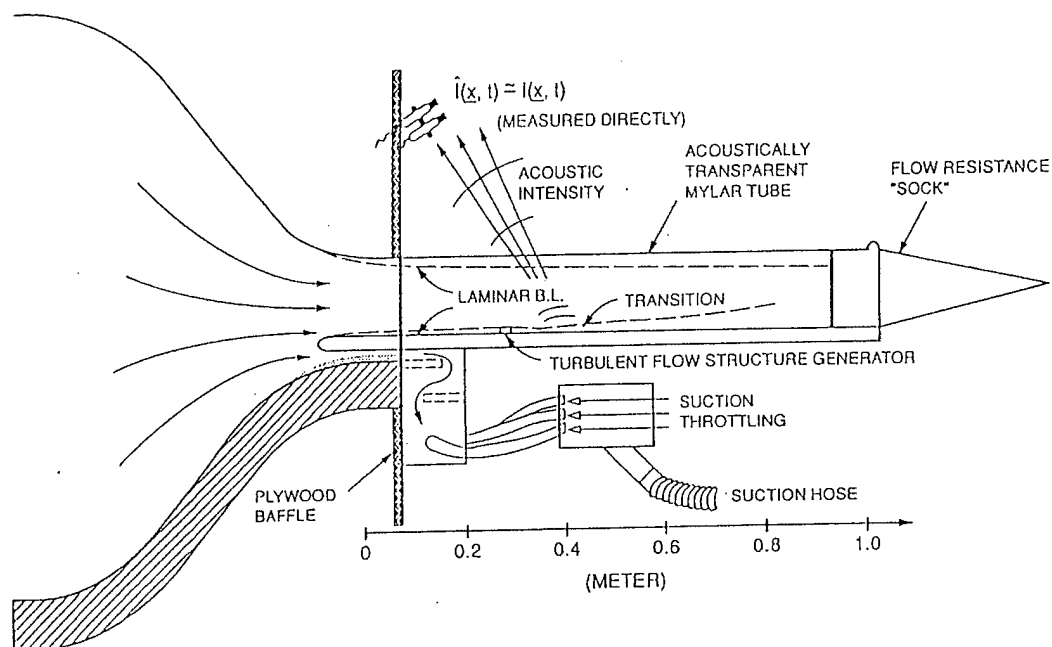


Figure B.4 Addition of mylar tunnel above and suction manifold below test plate.

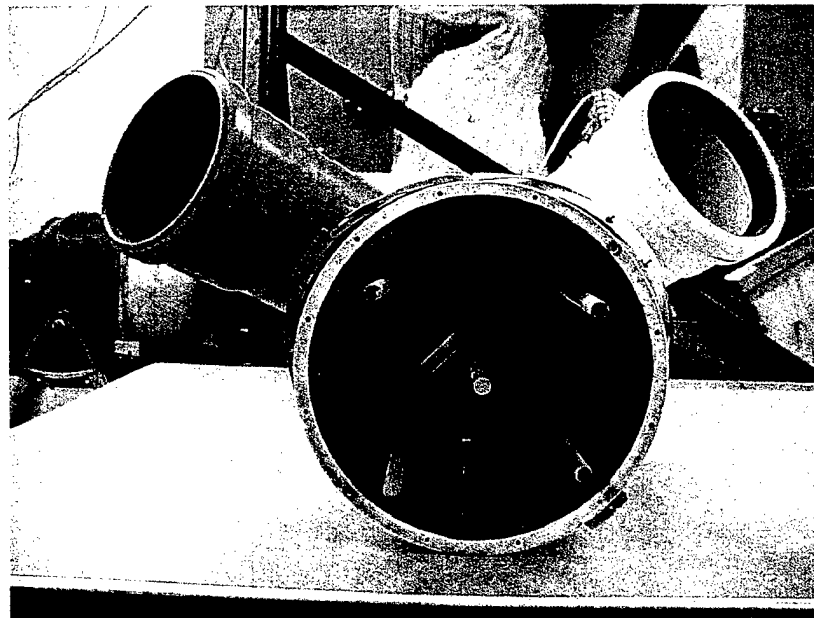
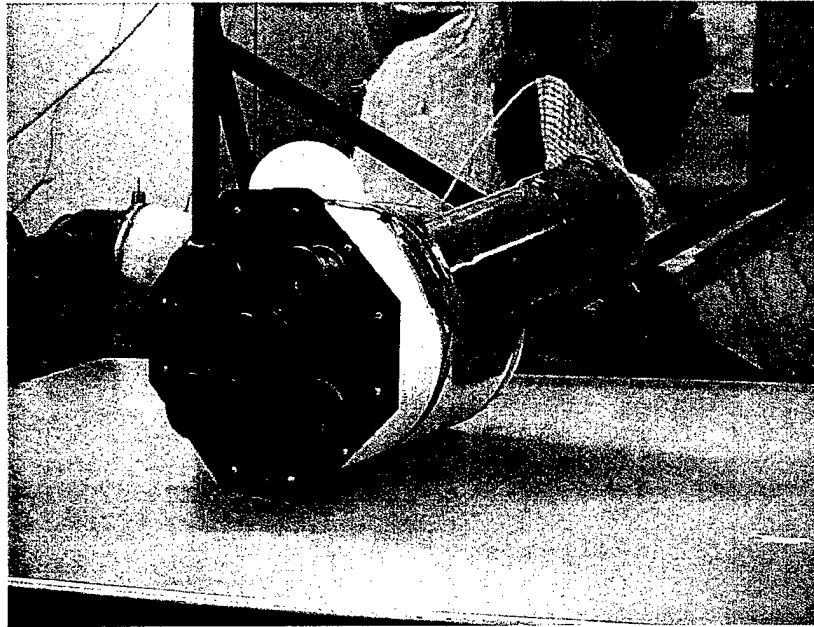


Figure B.5 Views of suction manifold ports and rods with cones.

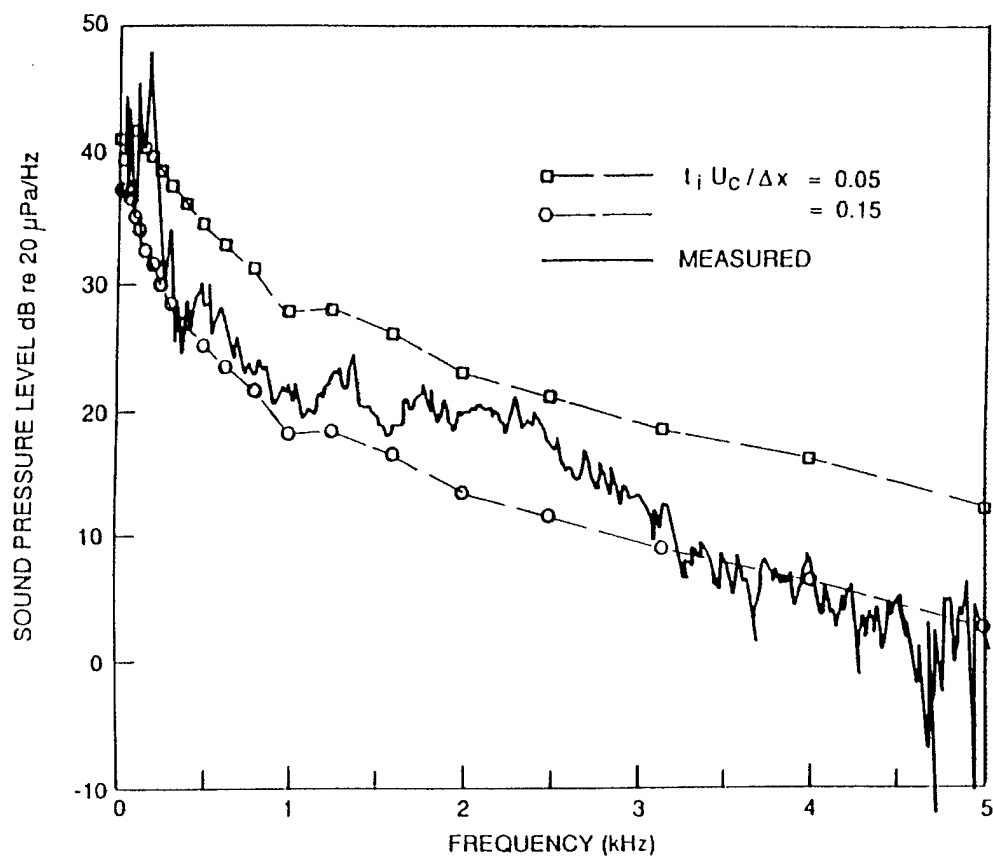


Figure B.6 Measured sound pressure level for assembly in control room running at $U_\infty=11.8$ m/s compared to GLPROG81 predictions for $u_c t_i / \Delta x=0.15$ and $u_c t_i / \Delta x=0.05$.

RADIATED NOISE DUE TO FLUCTUATING DISPLACEMENT THICKNESS FROM BOUNDARY LAYER TRANSITION USING LIEPMANN ANALOGY

GLPROG81.MCD

$\Delta x = 0.66 \text{ m}$	$W = 0.305 \text{ m}$	$c = 343 \text{ msec}^{-1}$
$\Delta \delta_{\text{star}} = 0.00495 \text{ m}$	$r = 0.3 \text{ m}$	$\nu = 0.0000151 \text{ m}^2 \text{ sec}^{-1}$
$U_o = 11.8 \text{ msec}^{-1}$	$\text{rise} = 0.45$	$\rho = 1.21 \text{ kgm}^{-3}$
$U_c = 8.26 \text{ msec}^{-1}$		
$\text{Ret} = 1500000$	$\text{Pref} = 0.00002 \text{ kgm}^{-1} \text{ sec}^{-1}$	$\text{rise} = 0.45 \frac{U_c}{U_o} = 0.7$

SPECTRAL PLOTS

$\gamma(Z) = \gamma_{\text{Farabee}}(Z)$

$B(Z) = B_{\text{Farabee}}(Z)$

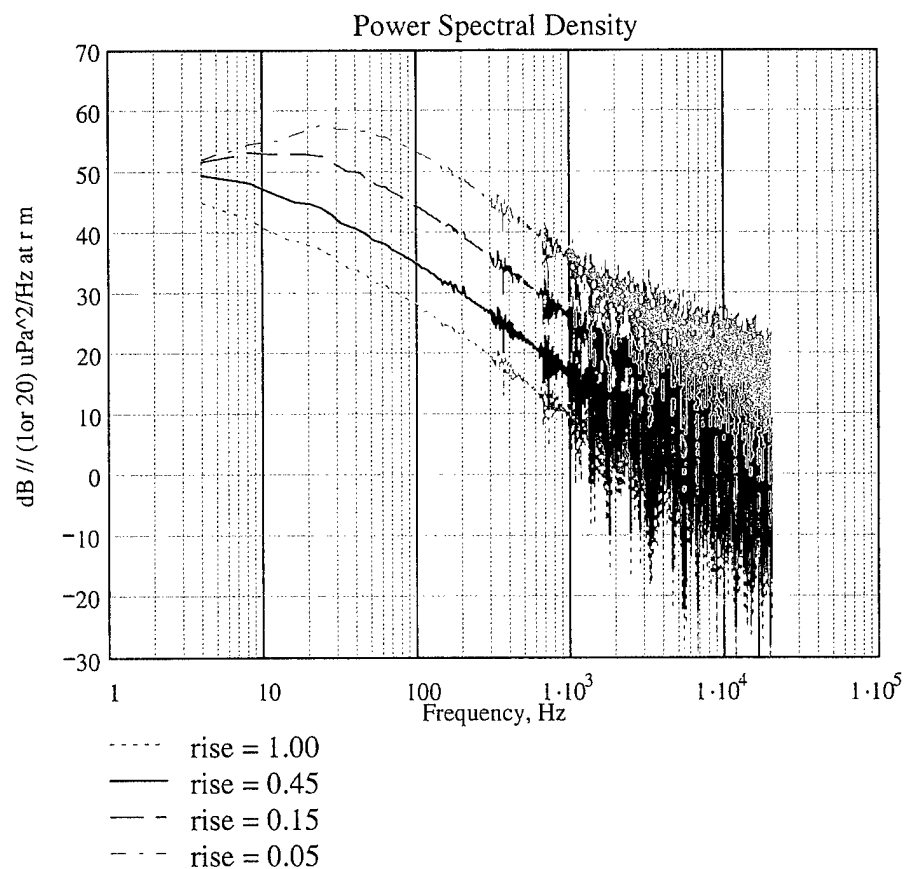


Figure B.7 GLPROG81 sound pressure level predictions for $U_{\infty} = 11.8 \text{ m/s}$ and several $u_c t_i / \Delta x$ values otherwise matching Figure B.6.

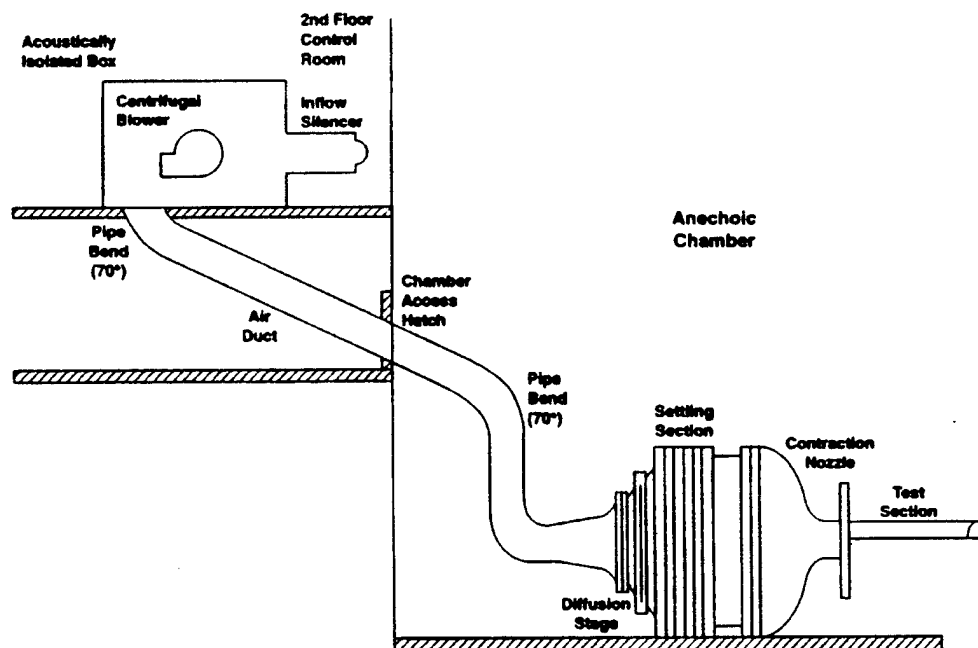
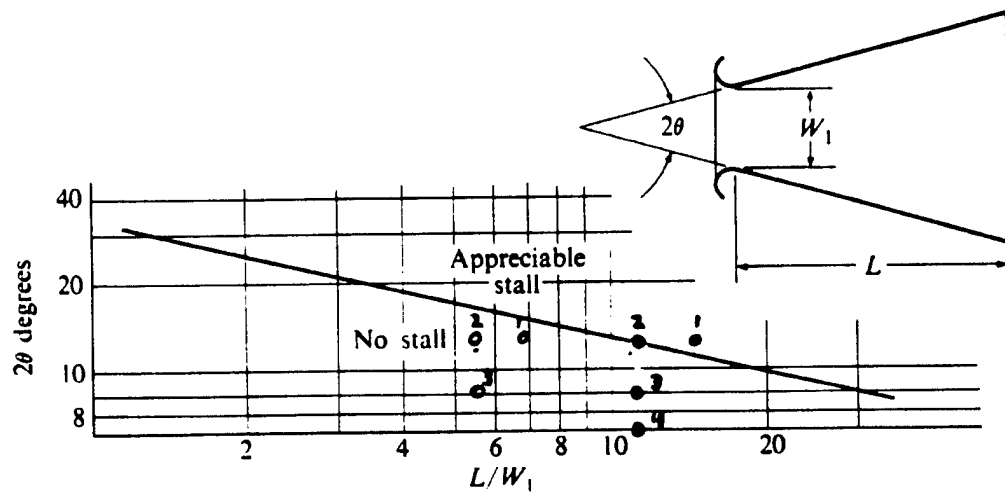


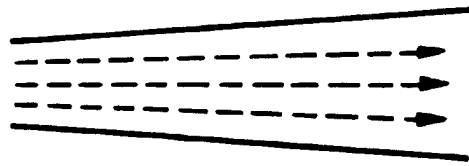
Figure B.8 Relocation of facility and addition of moving wall test plate [from Brungart 1997].



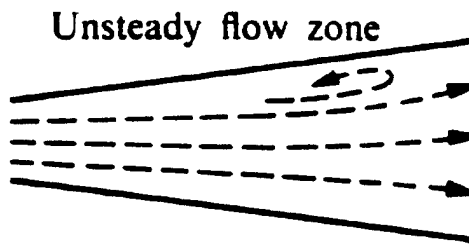
- Condition 1 7 degree, 2.03 m diffuser walls
 Condition 2 7 degree, 1.42 m diffuser walls
 Condition 3 4.5 degree, 1.42 m diffuser walls
 Condition 4 3.5 degree, 1.42 m diffuser walls (after foam panel insertion)

Open circles Diffuser side walls ($W=0.305$ m)
 Dark circles Diffuser top and bottom walls ($W=0.153$ m)

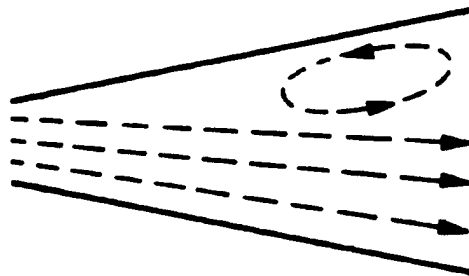
Figure B.9 Diffuser design iterations versus stall design criterion [stall curve from Kline 1959].



(a) Steady flow condition



(b) Transitory stall condition



(c) Steady stall condition

Figure B.10 Possible flow conditions in diffuser.

APPENDIX C

REAL-TIME ACOUSTIC INTENSITY SIGNAL PROCESSING

This appendix describes the real-time acoustic active intensity signal processing performed during the air flow experiment. The processing uses inputs from two microphones using a pressure - pressure (P-P) configuration. The two pressures are averaged to represent the pressure at a location intermediate to the two microphones and acoustic particle velocity is derived by a finite difference integration of the pressures. This is predominately performed in a time-averaged sense. Procedures, governing equations, and uncertainty analysis are well documented in Fahy (1989).

The general concept for making measurements of the acoustic signature of the transition zone or individual turbulent spots is shown in Figure C.1. Transition is allowed to occur naturally or a laminar flow condition is set and a stimulation is used to trigger a turbulent spot. This stimulation can be an acoustic impulse from a speaker or a mechanically generated air puff. A flush mounted hot film is used to provide a spectral conditioning signal. The microphones may be flush mounted as shown in the figure or mounted outside of the tunnel. The idea is to have the microphone separation large enough so that there will be little correlated flow noise between them. Also by orienting the two microphones in a line normal to the tunnel axis, the null of the cosine directivity pattern associated with the intensity probe will reject plane wave tunnel noise propagating along the tunnel axis.

C.1 Time-Averaged Intensity Processing

The traditional method of time-averaged processing a P-P probe is shown in Figure C.2. The active intensity for a time-stationary sound field is obtained from:

$$I_n(\omega) = -\left(\frac{1}{\rho_o \omega d}\right) \text{Im}(G_{p_1 p_2}(\omega)) \quad (\text{C.1})$$

An alternative method often used for handheld 1/3 octave intensity measurement devices is shown in Figure C.3. Here sum and differencing is done to the two analog microphone signals before they are passed through 1/3 octave filters and the difference signal is analog integrated. Analog-to-digital conversion is then performed before multiplication and division by $\rho_o d$. Averaging is often then performed.

C.2 Real-Time Intensity Processing

An approximation for the instantaneous particle velocity taken from the component of the pressure gradient in a direction n is given by:

$$u_n(t) \approx -\left(\frac{1}{\rho_o}\right) \int_{-\infty}^t \left[\frac{\partial p(\tau)}{\partial n}\right] d\tau \quad (\text{C.2})$$

With $I_n(t) = p(t) u_n(t)$, the instantaneous active intensity component is approximated by:

$$I_n(t) \approx -\left(\frac{1}{2\rho_o d}\right) [p_1(t) + p_2(t)] \int_{-\infty}^t [p_1(\tau) - p_2(\tau)] d\tau \quad (\text{C.3})$$

An example of the analog integrator needed to implement Equation C.3 is given in Figure C.4.

The portions of the processing diagram prior to the A/D conversion have been implemented in an electronic circuit. The design of this circuit and its fabrication was performed by Todd D. Batzel of the Applied Research Laboratory at Penn State. The circuit diagram is shown in Figure C.5. The component layout is provided in Figure C.6.

This circuit has two analog inputs which can be up to 5 volts. A high pass filter has been implemented with a cut-off at 30 Hz. The filter is a fourth order Bessel filter with linear phase (Burr-Brown Universal Active Filter, UAF42G). This was chosen for this particular application in order to remove some low frequency tunnel noise that otherwise would have used up about 40 dB of dynamic range. The gains in the circuit are as follows:

multiply by 250	in input
multiply by 295	in integrator
divide by 10	in multiplier
total gain = multiply by 7375 or 38.7 dB	

A reset button is installed for the integrator to allow re-zeroing in case of a built up bias. The circuit can be powered by two onboard 9V batteries or an AC adapter.

The remainder of the processing is performed in the DSP Technologies, Inc SigLab ® 20-42 dynamic signal processor which uses The Mathworks, Inc MATLAB ® software.

It is important for the signal processing of a P-P probe to have two channels well matched in amplitude and phase. The output of the real-time intensity circuit should be zero for the same signal being input to both channels. Any residual intensity is an

indication of an error which consists of random error and bias. The “residual intensity” as compared to the same signal input to channels 1 and 2 of the intensity circuit is shown in Figure C.7. The upper plot shows the phase and amplitude matching of the input signals even with any channel mismatch on the SigLab analyzer. The wide variation in phase and amplitude with frequency indicate problems in the circuitry that were not able to be overcome without a complete redesign. The impact can be seen in Figure C.8 with a comparison of the same measurement for the case of a fully turbulent flow condition between the time-averaged active intensity method and the real-time intensity circuit. A contributing problem may be the closeness of the probe to the source in these measurements. The highly reactive acoustic field may not be conducive to the real-time measurement.

C.3 Conditioning with a Shear Stress Sensor

It is desired to apply the power of coherent output processing to the acoustic measurements. In this case, it is assumed that shear stress due to passage of a turbulent spot is caused by the same physical phenomenon (i.e. growth of the turbulent spot) that results in acoustic radiation (represented by the transfer function $h(\tau)$). Therefore, there should be coherence between those signals. The noise associated with each sensor is assumed to be uncorrelated. These are identified in Figure C.9. It has been demonstrated in other experiments that the shear stress sensor (hot film) is insensitive to background acoustic noise.

This represents a single-input / single-output problem. The measured coherence

function for the shear stress and the active acoustic intensity is (Bendat and Piersol, 1993):

$$\gamma_{\hat{t}_o \hat{f}_r}(f) = \frac{|G_{\hat{t}_o \hat{f}_r}(f)|^2}{G_{\hat{t}_o \hat{t}_o}(f) G_{\hat{f}_r \hat{f}_r}(f)} \quad (\text{C.4})$$

where the hat represents a measured value. Note that this same approach can be used when a single pressure microphone is substituted for the intensity probe microphone pair.

It is assumed that the cross spectral terms

$$G_{\tau_o m}(f) = G_{I, n}(f) = G_{mn}(f) = 0 \quad (\text{C.5})$$

It is also known that

$$|G_{\hat{t}_o \hat{f}_r}(f)|^2 = |G_{\tau_o I_r}(f)|^2 = |H(f)|^2 G_{\tau_o \tau_o}^2(f) = G_{\tau_o \tau_o}(f) G_{I_r I_r}(f) \quad (\text{C.6})$$

When the measured quantities are resolved into true value and added noise, the measured coherence becomes:

$$\gamma_{\hat{t}_o \hat{f}_r}(f) = \frac{G_{\tau_o \tau_o}(f) G_{I_r I_r}(f)}{[G_{\tau_o \tau_o}(f) + G_{mn}(f)] [G_{I_r I_r}(f) + G_{nn}(f)]} \quad (\text{C.7})$$

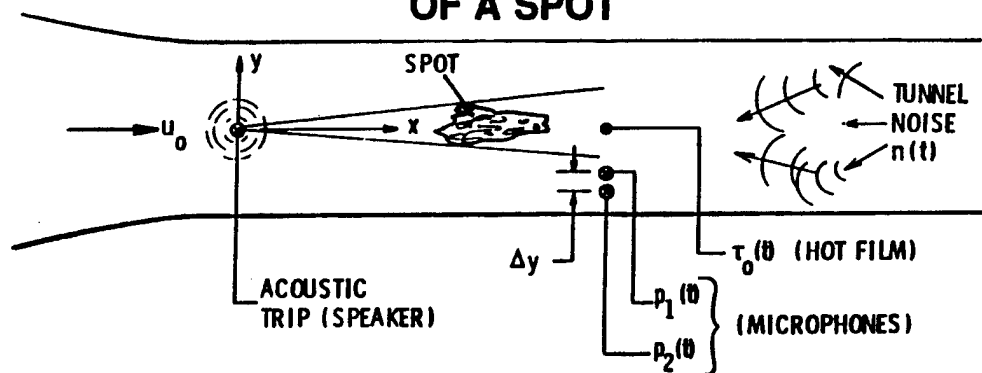
When the measured intensity is multiplied by the coherence function, one gets the

equation:

$$\gamma_{\tau_o \tau_o}(f) G_{\tau_o \tau_o}(f) = G_{\tau_o \tau_o}(f) \left[\frac{G_{\tau_o \tau_o}(f)}{G_{\tau_o \tau_o}(f) + G_{mm}(f)} \right] \quad (C.8)$$

Therefore, a good estimate of the true spectrum of the acoustic intensity is obtained when $G_{mm}(f) \ll G_{\tau_o \tau_o}(f)$ regardless of the amplitude of $G_{mm}(f)$. Josserand's prior measurements (Josserand 1986) and intermittency measurements made during this investigation have shown that the shear stress measurements have a very high signal- to-noise ratio and should meet the criterion well.

MEASUREMENT OF ACOUSTIC SIGNATURE OF A SPOT



$$I_y(t) = u_y(t) p(t)$$

REAL-TIME ACOUSTIC INTENSITY

$$\rho \frac{\partial u_y}{\partial t} = -\frac{\partial p}{\partial y}$$

EULER EQUATION

$$\therefore I_y(t) \cong -\frac{\rho(t)}{\rho \Delta y} \int_{-\infty}^t [p_2(\omega) - p_1(\omega)] d\omega$$

$$\frac{\partial p}{\partial y} \cong \frac{p_2(t) - p_1(t)}{\Delta y}$$

$$\text{WHERE } p(t) = p_1(t) + p_2(t) / 2 \cong p_1(t)$$

$$u_y \cong -\frac{1}{\rho \Delta y} \int_{-\infty}^t [p_2(\omega) - p_1(\omega)] d\omega$$

Figure C.1 General processing diagram.

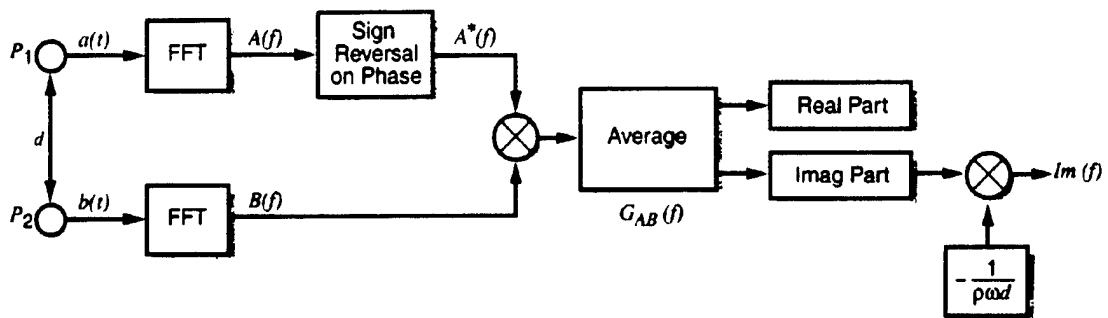


Figure C.2 Traditional method of FFT processing of a P-P intensity probe.

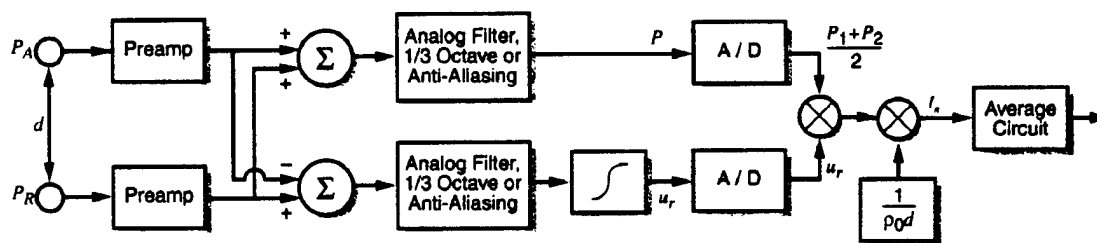


Figure C.3 Processing diagram for analog and digital calculation of intensity from a P-P probe.

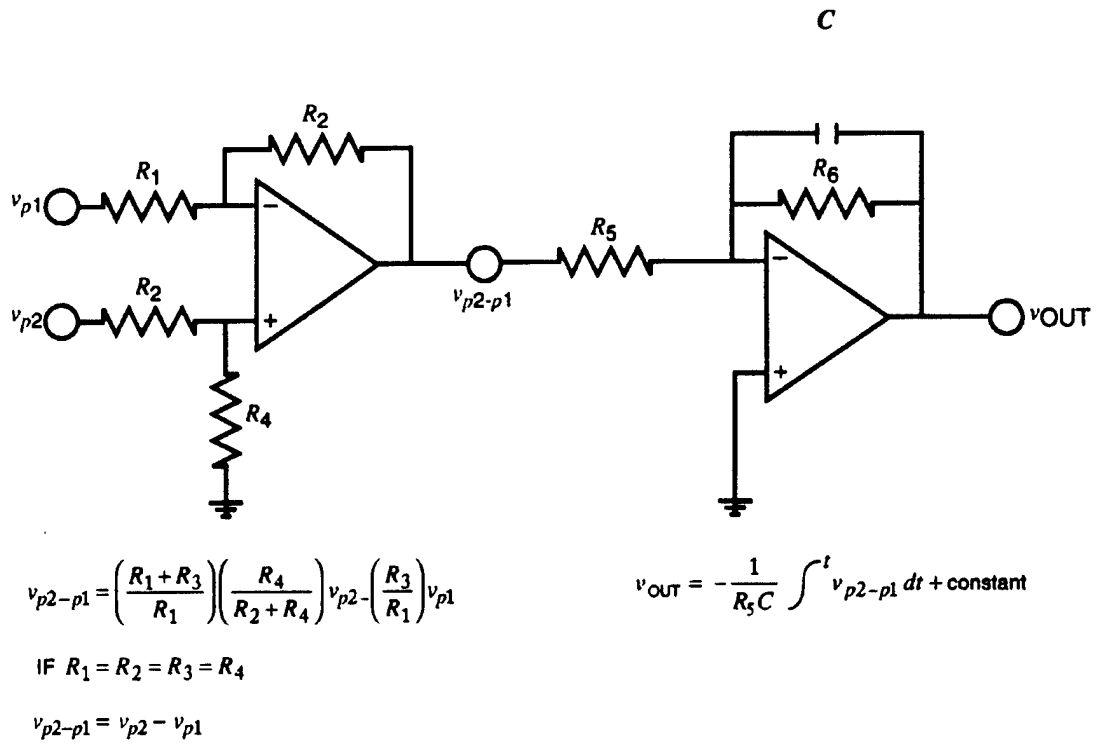
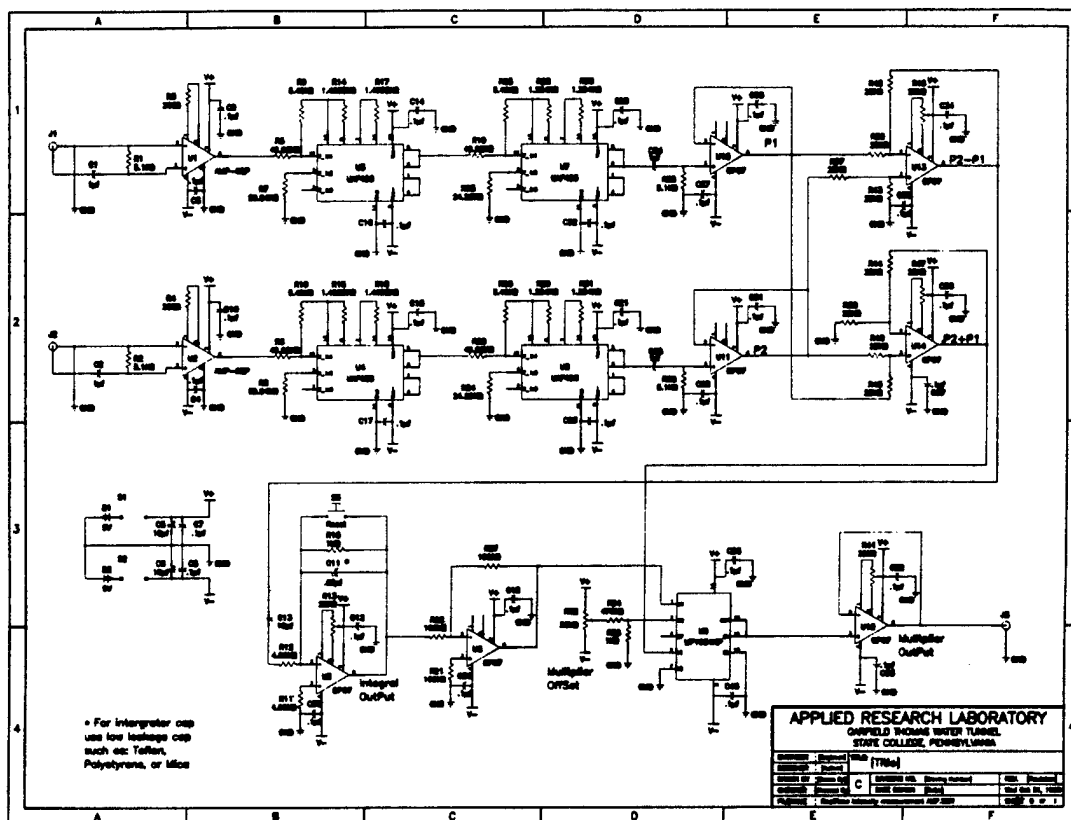


Figure C.4 Processing diagram for integrator.



[Circuit designed and constructed by Todd D. Batzel, Applied Research Laboratory, Penn State University.]

Figure C.5 Circuit diagram for real-time processing of a P-P intensity probe.

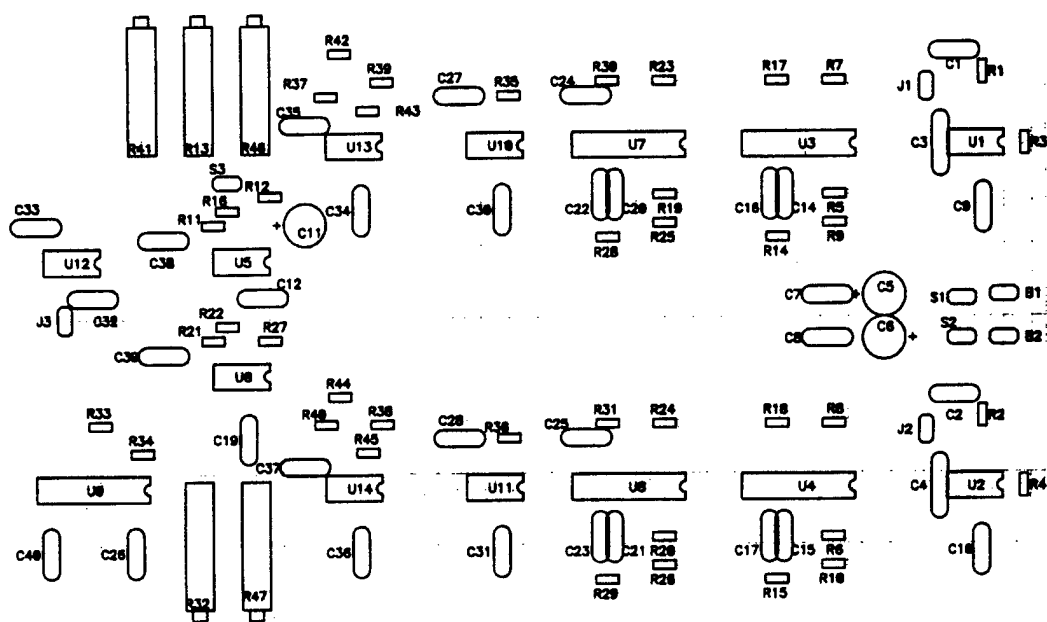


Figure C.6 Component layout for real-time active intensity circuit.

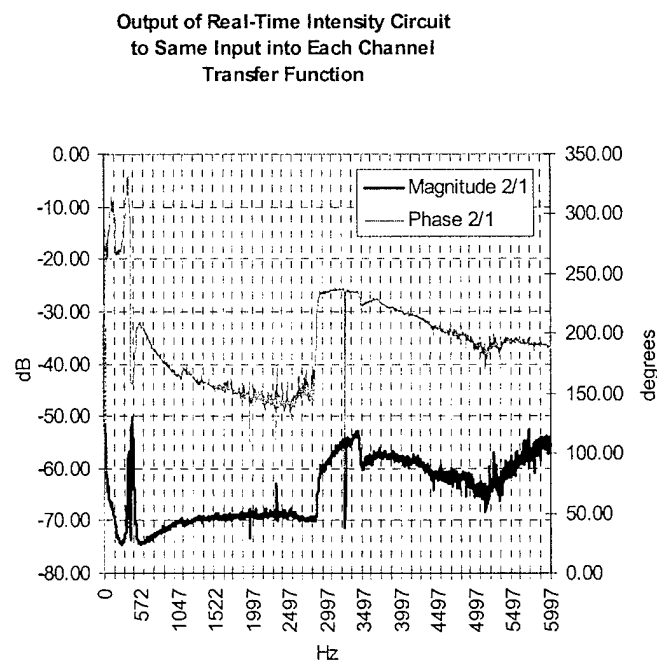
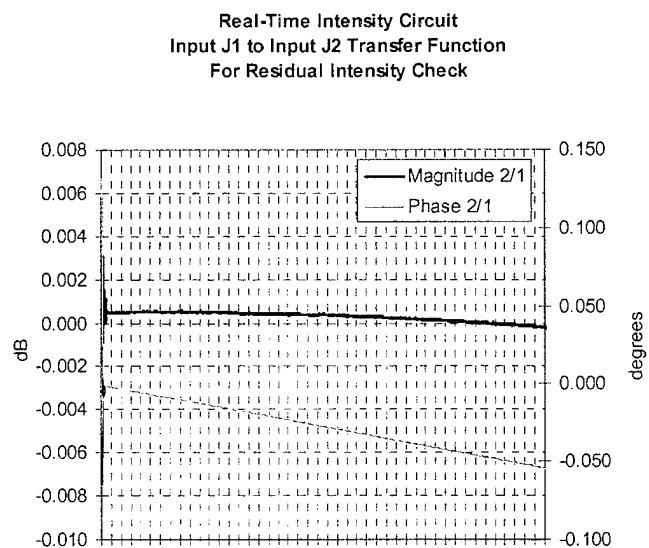


Figure C.7 Residual intensity measured for same signal input to channels 1 and 2 compared. to input signal.

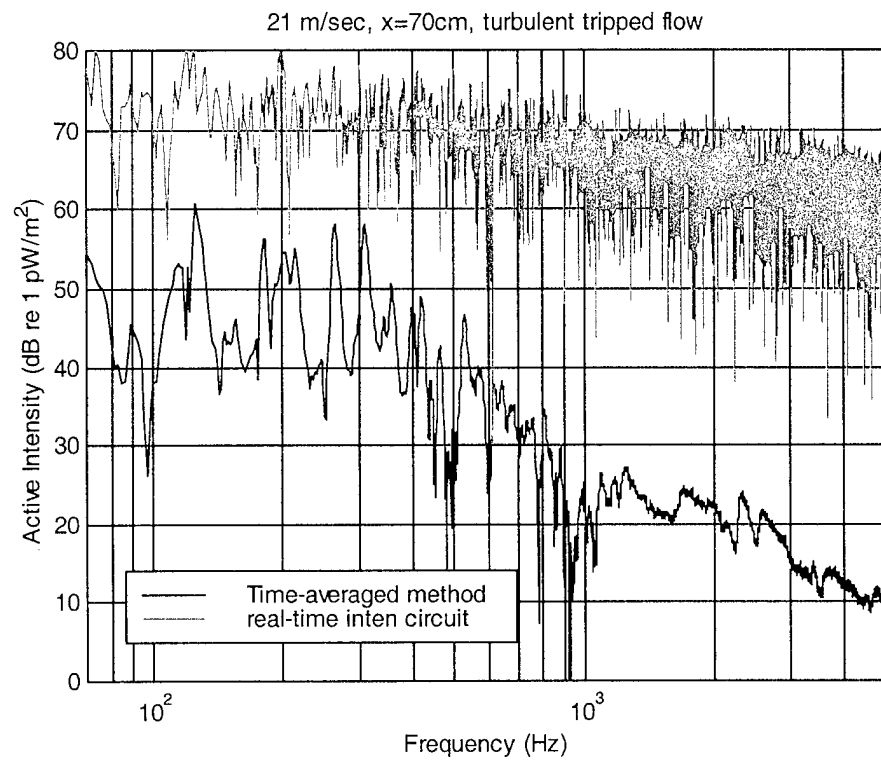


Figure C.8 Comparison of real-time intensity circuit output to time-averaged intensity method for a fully turbulent flow condition.

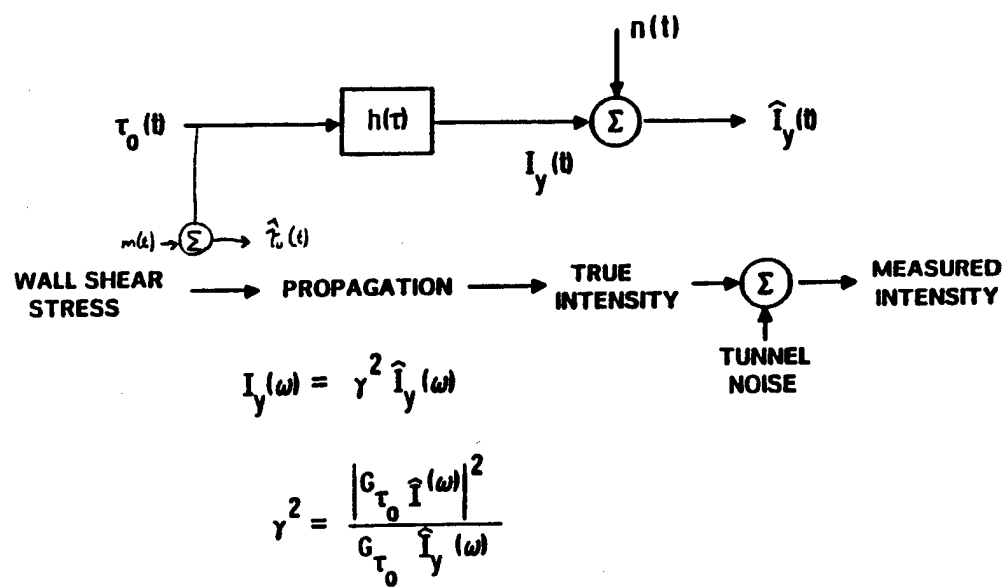


Figure C.9 Processing diagram for conditioning a real-time processing of a P-P intensity probe with a hot film probe.

VITA
RICHARD CHOSTNER MARBOE

Richard C. Marboe was born June 2, 1959 in Spring Township, Pennsylvania. He graduated from State College Area High School in June, 1977. He received his SB in Mechanical Engineering and SM in Ocean Engineering from the Massachusetts Institute of Technology in June, 1982. He joined the research faculty at the Applied Research Laboratory at Penn State after five years as a submarine and engineering duty officer in the US Navy. His ARL management positions have included Program Manager in the Submarine & Ship Technology Office, Deputy Head of the Flow and Structural Acoustics Department, and leader of the Flow Acoustics and the Research Facilitation Groups within that department. His Navy sponsored research has spanned leading propulsor design programs for submarine, surface ship, and weapon propulsors, two-phase flow acoustics (cavitation, bubble excitation, acoustic propagation screening), and hull flow-induced noise. He is a member of the American Society of Mechanical Engineers (Chair of the Turbomachinery Vibration and Noise Technical Comm.) and the Acoustical Society of America. He is the author of several scientific journal and symposia articles and over 35 ARL technical reports.